

**The star formation activity from the centers to the
outskirts in intermediate redshift clusters**

Dissertation
zur Erlangung des Doktorgrades
der Mathematisch-Naturwissenschaftlichen Fakultäten
der Georg-August-Universität zu Göttingen

vorgelegt von
Miguel Aníbal Verdugo Olivares
aus Santiago, Chile.

Göttingen 2008

D 7

Referent: Prof. Dr. Bodo Ziegler

Korreferent: Prof. Dr. Wolfram Kollatschny

Tag der mündlichen Prüfung: 27 März 2008

*Nur wer der Minne Macht entsagt,
nur wer der Liebe Lust verjagt,
nur der erzielt sich den Zauber,
zum Reif zu zwingen das Gold.*

”Der Ring des Nibelungen”

ABSTRACT

The mixture of galaxy types in clusters and the field is different in the local Universe. Going to higher redshifts, the galaxy population is changing also within clusters with look-back time. This may be caused by their late assembly epoch predicted by bottom-up scenarios of structure formation or due to cluster-specific interaction processes.

To disentangle various effects, a project to explore evolutionary status of galaxies from the center of clusters out to their infall regions in $z \approx 0.25$ clusters was initiated.

This thesis describes a panoramic spectroscopic campaign with MOSCA at the Calar Alto observatory. In total, low-resolution ($R \approx 500$) spectra of more than 500 objects were obtained, resulting in 150 member galaxies of six clusters that differ in X-ray luminosities. The wavelength range allows to quantify the star formation activity by using the [O II] and the H α emission lines. This activity is examined on the large-scale environment expressed by the clustercentric distance of the galaxies as well as on local scales given by the spatial galaxy densities.

The general decline of the star formation activity observed in nearby clusters is also seen at $\langle z \rangle \approx 0.25$ and is mainly driven by a significant change in the fraction of active versus passive populations. The global suppression of star formation starts already in the outskirts of clusters (at about $3R_{vir}$), where the galaxy densities are low and the intra-cluster medium is very shallow. Galaxies with ongoing star formation have similar equivalent widths of emission lines independent of local density or clustercentric distances, suggesting that the processes shutting down star formation act on short timescales. Although there is no general trend with velocity dispersion or X-ray luminosity (total mass), each cluster displays a distinct galaxy population. A significant population of red star forming galaxies whose colors are consistent with the red sequence of passive galaxies. They appear to be in an intermediate evolutionary stage between active and passive types.

Different scenarios were evaluated in order to explain those trends. It turned out that ram-pressure stripping can explain to a great extent the previous trends, if the effects of the significant change of the galaxy positions over time, are considered. But additional processes may be necessary as the suppression of the star-formation activity starts at large clustercentric distances and low projected densities. So, as suggested by other studies group preprocessing may play an important role in transforming galaxies before they enter in the cluster environment. This is here supported by the similarities between the group and the population of the outer cluster regions. Starvation, on the other hand, is practically ruled out by the observations under standard assumptions.

It must be noted that different processes may have dissimilar importance in every cluster.

Contents

1	Introduction	1
1.1	Classification of galaxies	1
1.2	The galaxy environment	3
1.3	Galaxy properties and environment	5
1.3.1	The morphology-density relation	6
1.3.2	Galaxy colors and environment	6
1.3.3	Star formation and environment	7
1.4	Galaxy evolution with look-back time	8
1.4.1	Decline of star formation activity with time	8
1.4.2	The Butcher-Oemler effect	8
1.4.3	The abundance of the S0 galaxies	9
1.5	Physical processes that affect galaxy properties	10
1.5.1	Tidal interactions among galaxies	10
1.5.2	Tidal interactions between the cluster potential and galaxies	10
1.5.3	Harassment	10
1.5.4	Galaxy mergers	11
1.5.5	Ram pressure stripping	11
1.5.6	Viscous stripping and thermal evaporation	12
1.5.7	Starvation	12
1.5.8	Group preprocessing	12
1.6	Cosmological context	12

1.6.1	A Λ CDM Universe and the hierarchical scenario	14
2	The Project	17
2.1	Sample Selection	18
2.1.1	Cluster selection	18
2.1.2	Object selection	18
2.2	Observations	19
2.3	Data Reduction	20
2.4	Additional data	21
2.4.1	Additional spectra	21
2.4.2	SDSS data	23
3	Basic measurements	25
3.1	Individual galaxy redshifts	25
3.2	Quality control	25
3.3	Equivalent widths	26
3.4	Star forming galaxies	27
3.5	Selection function	27
3.6	Absolute Magnitudes	28
4	The fields and clusters	31
4.1	Cluster membership	31
4.1.1	The biweight estimators	31
4.1.2	The bootstrap method	32
4.2	Description of the fields	32
4.2.1	R220	33
4.2.2	R265	34
4.2.3	R285	36
4.2.4	Field sample	36
4.3	Dynamical properties of the clusters	36
4.3.1	X-ray luminosities	39
4.3.2	Virial radius	39
4.3.3	Projected density	40
4.3.4	Velocity dispersion profile	42
4.3.5	Probing substructure with dynamics	42
4.4	Spectrophotometric properties of the clusters	44
4.4.1	Luminosity distribution	44

4.4.2	Color-magnitude diagram	44
4.4.3	Fraction of star-forming galaxies	46
5	Environment and star-formation activity	49
5.1	Galaxy colors and environment	50
5.1.1	The sliding bins method	51
5.2	Star-formation via emission lines	51
5.2.1	Comparison with previous work	53
5.3	Origin of the trends	55
5.3.1	The star forming population	55
5.3.2	Subsamples according to membership	56
5.4	Differential evolution with mass	57
5.5	Scenarios	58
6	The properties of the emission line galaxies	63
6.1	Equivalent width distribution	63
6.2	Star formation rates	64
6.3	The case of the red star forming galaxies	67
6.3.1	The AGN connection	68
6.3.2	The effects of dust	69
6.4	Chemical abundances	70
6.4.1	The R_{23} method	71
6.4.2	The $N2$ and the $O3N2$ indices	74
6.5	Star-formation versus stellar mass	75
7	Summary and conclusions	79
8	Outlook & future work	83
8.1	Diagnosis diagrams	84
8.1.1	The $H\alpha$ – $H\delta$ plane	84
8.1.2	The $D_n(4000)$ – $H\delta$ plane	86
8.1.3	The $D_n(4000)$ – $H\alpha$ plane	86
8.2	Infall regions in a massive cluster at $z = 0.45$	86
A	Observations	101
B	Line definitions	103
C	Data for individual objects	105

D Spectrophotometric parameters of the sample	125
Acknowledgments	131
Conferences & PhD activities	133
Publications	135
Lebenslauf	137

List of Figures

1.1	Color picture of the galaxy cluster AbellS 0740.	2
1.2	Hubble fork diagram of galaxy classification	4
1.3	Spatial galaxy distribution as measured by the 2dFGRS	5
1.4	The Dressler's morphology-density relation	6
1.5	The evolution of star formation density.	8
1.6	Constrains of Ω_M and Ω_Λ from different experiments.	14
2.1	Example of an unreduced multi-object spectra image	20
2.2	Typical 1-D galaxy spectra	22
3.1	V-band apparent magnitude versus continuum signal-to-noise ratio	26
3.2	The combined selection function for the whole sample.	28
4.1	Redshift distribution in the three fields	33
4.2	Redshift histograms for each of the investigated clusters	34
4.3	Representation of the R220 field	35
4.4	Representation of the R265 field	37
4.5	Representation of the R285 field.	38
4.6	Bolometric X-ray luminosity plotted against velocity dispersion	40
4.7	Relation between clustercentric distances and projected density	41
4.8	Normalized peculiar velocities versus normalized clustercentric distances	42
4.9	Dressler-Shectman plots for the clusters VMF73, VMF74 and VMF131	43
4.10	Absolute magnitude distribution	44

4.12	Color-magnitude diagrams for the cluster galaxies	45
4.11	Redshift versus absolute magnitudes	46
4.13	Fraction of star-forming galaxies versus bolometric X-ray luminosity	46
5.1	Fraction of blue galaxies versus normalized clustercentric distance and projected density	50
5.2	Fraction of star-forming galaxies and mean equivalent widths of [O II] and H α against normalized clustercentric distances and projected densities to the 5 th neighbor (Σ_5) . . .	52
5.3	Mean equivalent widths of the star-forming population	54
5.4	Cumulative histograms of equivalent widths for field and clusters star-forming galaxies .	55
5.5	Fraction of star-forming galaxies and mean equivalent widths against normalized cluster distance and projected density for the clusters VMF73 and VMF131.	56
5.6	Fraction of star-forming galaxies versus stellar mass	58
5.7	A simple cluster scheme with regions of influence of the different interaction mechanisms	60
6.1	[O II] and H α equivalent widths plotted against restframe $B - R$ color	64
6.2	[O II] and H α equivalent widths for emission lines galaxies in the clusters and in the field	65
6.3	Specific star formation rates based on [O II] and H α versus the respective equivalent widths	66
6.4	Environmental distribution of the different galaxy subtypes	67
6.5	Line ratio diagnostic diagrams to identify AGNs	69
6.6	HST/WFPC2 image of the elliptical galaxy ba_37	70
6.7	O/H abundances versus the R_{23} and O_{32}	71
6.8	O/H abundances versus stellar mass and M_B for field and cluster galaxies based on the R_{23} indicator	73
6.9	Distribution of galaxies in the $N2$ test	74
6.10	Specific star formation rates versus stellar mass	76
8.1	Diagnostic diagrams for the evolutionary status of galaxies	85

List of Tables

2.1	Basic parameters of the cluster sample	18
2.2	Summary of the observations	19
3.1	Set the lines used in redshift determination	26
3.2	Line definitions	27
4.1	Main parameter for the cluster sample	32
4.2	Main parameters for the groups candidates in the studied fields	39
A.1	Observation Log	101
B.1	Line definitions for the strongest features in the galaxy spectra.	103
C.1	Data for individual objects	106
C.1	Continued.	107
C.1	Continued.	108
C.1	Continued.	109
C.1	Continued.	110
C.1	Continued.	111
C.1	Continued.	112
C.1	Continued.	113
C.2	Equivalent widths for individual objects	116
C.2	Continued.	117

C.2 Continued.	118
C.2 Continued.	119
C.2 Continued.	120
C.2 Continued.	121
C.2 Continued.	122
C.2 Continued.	123
D.1 Spectrophotometric data for individual objects.	125
D.1 Continued.	126
D.1 Continued.	127
D.1 Continued.	128
D.1 Continued.	129
D.1 Continued.	130

Introduction

Figure 1.1 shows the center of the galaxy cluster Abell S0740 which is located at a distance of ~ 140 Mpc. This picture is notable for showing different types of galaxies at once. The largest, yellowish object is the central elliptical galaxy present in almost every galaxy cluster, but at least two other objects are worth of attention. They display different sizes, but both of them feature intricate spiral arms, with patchy blue regions and in the case of the galaxy in the lower left corner, also obscured regions. Several other objects with different colors, shapes and sizes are present also in that picture. The Universe in plenty of similar landscapes, and this has triggered a question that has intrigued the astronomers for years. Why the objects, like those seen in Figure 1.1, are so different?

E. Hubble¹ added a fundamental milestone by confirming that those objects (then called “spiral nebulae”) were actually extragalactic objects (the “island universes”, Hubble 1925) containing their own population of stars. This allowed to astronomers to determine distances at least to the nearest galaxies. At the same time, the redshift on the spectral features indicated that most of the galaxies were moving further away, with those at larger distances having larger velocities. In fact, it was found that both quantities are related in a simple mathematical expression,²

$$v = H_0 D \quad (1.1)$$

(Hubble & Humason 1931), where

$$\frac{v}{c} = \frac{\lambda_{observed} - \lambda_{emitted}}{\lambda_{emitted}} \quad (1.2)$$

is the recessional velocity, D is the distance in Mpc and H_0 is the Hubble constant, whose current accepted value is $H_0 = 71 \pm 4 \text{ km s}^{-1} \text{ Mpc}^{-1}$, c is the speed of light and λ is the wavelength of the spectral features used in the calculation.

This relation, called the Hubble’s law, led to the conclusion of an expanding universe and triggered the Big-Bang theory. Furthermore, it allowed to estimate distances to galaxies in a simple and straightforward manner.

1.1 CLASSIFICATION OF GALAXIES

The first starting point in any systematic study is to create a classification scheme able to reveal underlying physical properties. The first classification system of galaxies was again provided by E. Hubble and is still widely used to refer to the main galaxy properties. His scheme was presented as a morphological sequence (see Figure 1.2) based in the visual appearance of galaxies on photographic plates. The galaxies were classified in ellipticals, spirals and irregulars galaxies (the later is not

¹Edwin Powell Hubble, *1889, †1953

²Modern cosmology has determined that this simple relation is not valid at larger distances. This will be discussed in section §1.6.

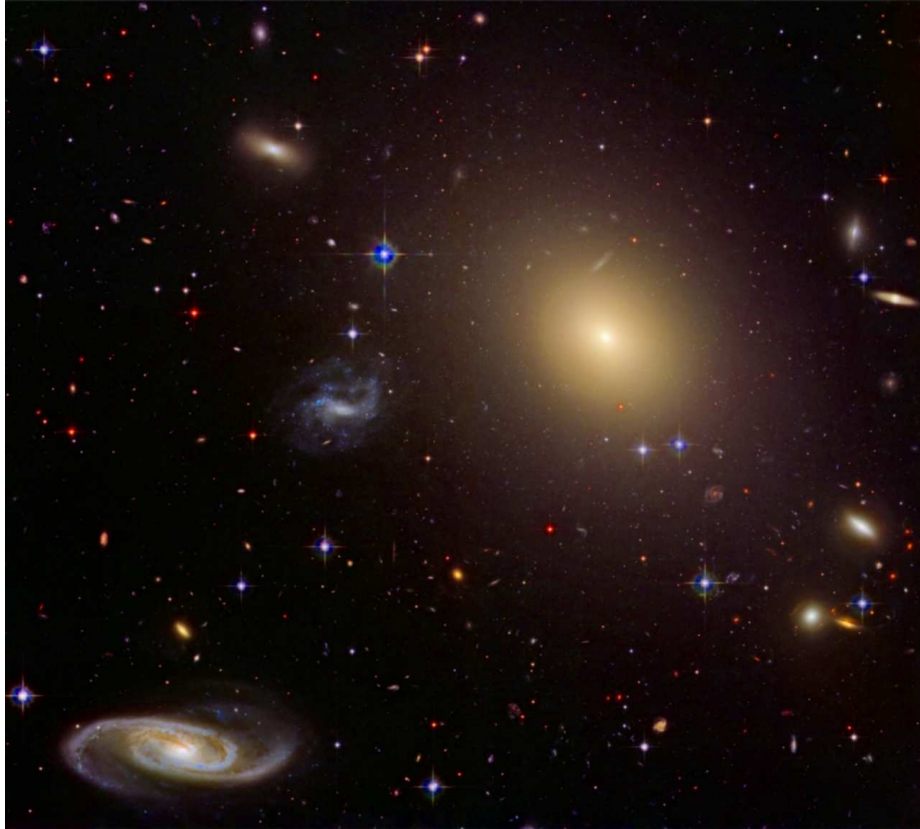


Fig. 1.1: Color picture of the galaxy cluster Abell S0740 at $z=0.0336$ taken with the Hubble Space Telescope.

shown in Figure 1.2). Over the time, those eye-based classifications have been challenged by the improving in the instrumentation which have provided accurate measurements of the morphology, kinematics and spectral properties of galaxies. This has led to the conclusion that galaxies subtypes are objects of very different nature.

Elliptical galaxies are arranged from $E0$ to $E7$, based in their axial ratio, being $E0$ the roundest and $E7$ the most flattened. They appear elliptical in shape, with lines of equal brightness made up of concentric and similar ellipses. Some discussion has existed if ellipticals are oblate, prolate or triaxial objects (*e.g.* Binney 1978), and whether their ellipticities are caused by the galaxy position or by the intrinsic tridimensional shape of the galaxy.

Galaxies of this class have smoothly vary-

ing brightnesses, steadily decreasing outwards from the center and are, in average, proportional to $r^{1/4}$ (where r the galactocentric distance, de Vaucouleurs 1959). These galaxies have all similar colors, with a spectral energy distribution (SED) characterized by a large contribution of light from red giant-branch stars (K and M types).

The motion of stars in elliptical galaxies is random with velocity distributions that emulate molecules in a gas, therefore they have been called dynamically hot galaxies. Velocities, colors and other spectral features distribute with radius and are subject of investigation (for a review see Merritt 1999). Elliptical galaxies have masses from 10^7 to nearly $10^{13} M_{\odot}$, the largest mass range in all galaxies.

Spiral galaxies are generally composed of a bulge, which share many properties with el-

lptical galaxies, and an extended disk with prominent spiral arms. Therefore, their spatial luminosity distribution is described by a combination of the $r^{1/4}$ profile, plus a disk component which has an exponential profile proportional to e^{-r/r_d} (where r_d is the characteristic size of the disk). Spiral galaxies are subclassified according the relation between bulge and disk sizes and the oneness of their spiral arms. In this scheme, *Sa* galaxies have prominent bulges and very closed spiral arms, whereas *Sc* types show small bulges and very open spiral arms.

Many spiral galaxies have a bar that extend between the bulge and the spiral arms and therefore, a “B” is added to their nomenclature (*SBa..SBc*).

Unlike ellipticals, the SED of spiral galaxies shows, normally, a high contribution of light coming from young, hot stars and emission lines caused by the ionizing radiation from this population on their gaseous content. Because of that, the colors of spiral galaxies are bluer than in ellipticals. Kinematically the bulge of the spirals is also supported by dispersion, however at large distances where the disk dominates, the motion is characterized by the ordered rotation of gas and stars (For a review in the spiral galaxy properties see Sofue & Rubin 2001).

S0 galaxies seem to be an intermediate type between ellipticals and spirals³ combining features of both types. They display a large bulge and a small featureless disk. Their stellar populations are also dominated by old, red stars. Together with ellipticals, they are called early type galaxies.

Irregular galaxies As the name indicate, they do not display any regular structure nor central nucleus. They are characterized by patchy luminous areas and generally show blue colors from young stellar populations. These galaxies are generally small in size, but some show

signs of rotation, although asymmetric and often chaotic (*e.g.* Sofue & Rubin 2001).

Some galaxies, however, do not fit in the previous scheme, sharing structures with regular galaxies but severely distorted, often featuring plumes, tails or multiple “regular” structures. Those galaxies are classified as peculiar galaxies (Arp 1966) and are thought to be in a process of interaction.

The early Hubble scheme has been, throughout the years, updated and accommodated in order to include intermediate types as well as to incorporate evidence from new observations (*e.g.* de Vaucouleurs 1959, van den Bergh 1960, Matthews et al. 1964). With the advent of digital imaging and computers, the original visual classification has evolved in automatic processing, mathematically modeling the galaxy luminosity profile (*e.g.* Sersic & Arreguine 1983). This has allowed morphological classification of hundreds of thousand galaxies present in modern extragalactic surveys.

Additionally, observations of galaxies at different wavelengths (from X-ray to radio) have helped to constrain the properties of their stars and interstellar medium (gas and dust) present on galaxies as well as to identify components that play a role in the galaxy evolution, such as the super massive black holes in their centers and their hot gaseous envelopes. Optical spectra, infrared and ultraviolet data provide important information about the stellar mix present on galaxies, such as their rate of formation of stars, their ages and chemical abundances.

1.2 THE GALAXY ENVIRONMENT

Since the Hubble scheme is presented as morphological sequence, and galaxies exhibit a smooth transition between subtypes, the simplest hypothesis was that this diagram represents some sort of evolutionary sequence for galaxies. Additional evidence was provided again by E. Hubble (Hubble 1936), when he noticed that clusters of galaxies are mainly inhabited by elliptical and S0 galaxies, whereas the surrounding field by spiral and irregular galaxies. Therefore, it was suspected that the environment, where galaxies reside, plays some role in their formation and/or evolution.

³Much effort has been done to disentangle whether S0s are truly transition objects or an end-product of galaxy evolution (see Larson et al. 1980, Byrd & Valtonen 1990, Quilis et al. 2000, Bekki et al. 2002, etc.)

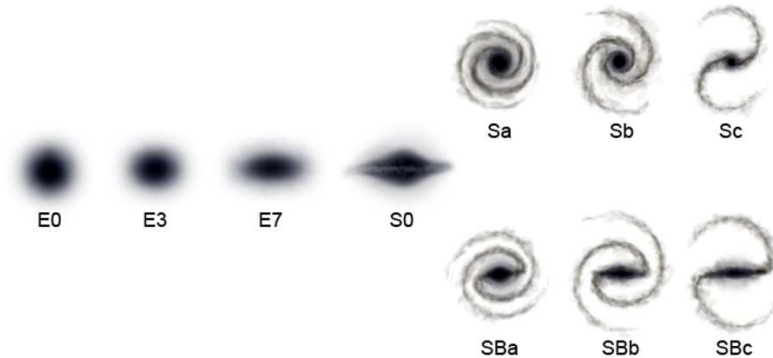


Fig. 1.2: Hubble fork diagram of galaxy classification. It is still a valid scheme to differentiate galaxies, although the evolutionary path proposed has long proved incorrect. Moreover, some the split of different subtypes is somewhat arbitrary, *i.e.* by galaxy ellipticity or barred versus “normal” spirals. Image taken from the Wikipedia website, released under Creative Commons license.

The galaxy environment is often subdivided in cluster, group and field. The distinction among these three is somewhat arbitrary and very thin. In most of the cases, the field is composed of groups which are themselves very diverse in nature. On the other hand, the division between group and cluster can be considered arbitrary but at least is linked to dynamical properties (*i.e.* mass).

Cluster of galaxies are the largest bound structures in the Universe. They are the highest density peaks in the cosmological matter distribution, holding together hundreds or thousands of galaxies. Their velocity dispersions ($\sigma \sim 1000$ km/s) are far too large to be explained only by the gravitational force from the visible matter alone which led to the conclusion of the existence of an invisible component called dark matter (Zwicky 1959).

This was somewhat alleviated by the discovery of a large baryonic component made of hot gas ($10^7 - 10^8$ K) which was detected by its X-ray emission (Gursky et al. 1971, Jones & Forman 1978), but when they are both summed, they make up to the 15% of the necessary mass, the rest is composed of dark-matter with a still unknown nature.

The masses of clusters determined by different techniques⁴ show that they are in ranges of 10^{14} to $10^{15} M_{\odot}$.

Cluster of galaxies are often classified by their optical richness, which relates the number of galaxies in a luminosity range to their spatial distribution (Abell 1958, Zwicky et al. 1961). Although, optical richness correlates with mass (*e.g.* Hansen et al. 2005), more direct parameters, such as velocity dispersion or X-ray luminosity, are commonly used in the present to classify galaxy clusters (Borgani 2006).

Groups of galaxies contain the majority of galaxies in the local Universe (Tully 1987). They usually contain few tens of galaxies and have masses $\sim 10^{13} M_{\odot}$. Their velocity dispersions are substantially lower than clusters ($\sigma \sim 150$ km/s). However many larger system are also classified as groups.

Field The definition of the field is fuzzy. It usually refers to the sparse environment between galaxy groups formed by isolated galaxies or small systems of few galaxies. Since groups

⁴*e.g.* virial theorem, gas hydrostatic equilibrium, gravitational lensing and Sunyaev-Zeldovich effect.

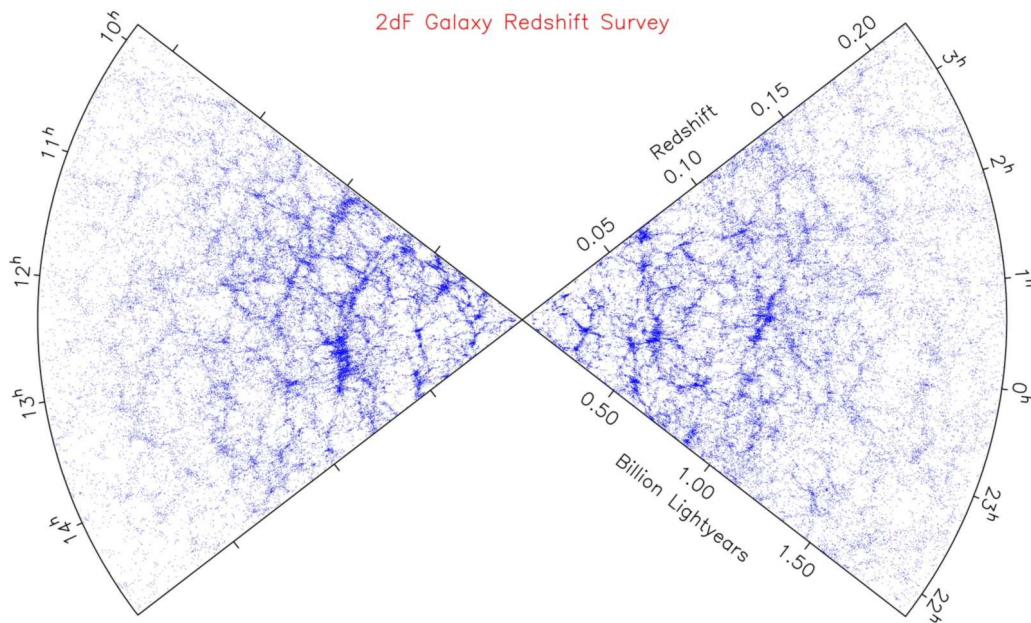


Fig. 1.3: Spatial galaxy distribution as measured by the 2dFGRS (Colless et al. 2001). Beyond $z \sim 0.15$ the survey becomes highly incomplete and the structures cannot clearly be seen anymore (image taken from the survey website).

are difficult to identify at large distances as they show little contrast with the field (except large and compact groups), they usually end being included in the field.

Large redshift surveys, such as CfA⁵, LCRS⁶, 2dFGRS⁷ and SDSS⁸ have revealed the intricate nature formed by galaxy aggregations, with filaments joining clusters and groups. They are structured in super-clusters and large empty regions called voids where few galaxies are found. For instance, the CfA redshift survey was the first in detecting these structures (*e.g.* the very large filament called “the great wall”, Geller & Huchra 1989). In Figure 1.3 a similar map obtained by the 2dFGRS team is shown, where those features can be appreciated.

Those structures appear as a natural product in

⁵ CfA redshift survey (Huchra et al. 1983),
<http://cfa-www.harvard.edu/~huchra/zcat/>

⁶ Las Campanas Redshift Survey (Shectman et al. 1996),
<http://qold.astro.utoronto.ca/~lin/lcrs.html>

⁷ 2dF Galaxy Redshift Survey (Colless et al. 2001),
<http://www.mso.anu.edu.au/2dFGRS/>

⁸ Sloan Digital Sky Survey (York et al. 2000),
<http://www.sdss.org>

hierarchical mass assembly scenarios under the context of Λ CDM cosmologies (see §1.6 for a summary) and have been accurately modeled by the latest *state-of-the-art* simulations (*e.g.* the Millennium run, Springel et al. 2005).

The LCRS found that, at scales larger than 100 Mpc^3 , the anisotropies found in the local Universe are homogenized and isotropized and the cosmological principle could finally be seen (the “end of greatness”).

1.3 GALAXY PROPERTIES AND ENVIRONMENT

One aspect revealed by systematic redshift surveys is that many of the galaxy properties depend strongly on the galaxy concentration. As rich and thus massive galaxy clusters often have very dense cores they also display greater contrast with the field. Whether the mass of the system itself affects galaxy properties is still matter of debate (see Poggianti et al. 2004 and Popesso et al. 2007 for disparate results). It is clear, however, that any correlation with system mass is weaker than with local

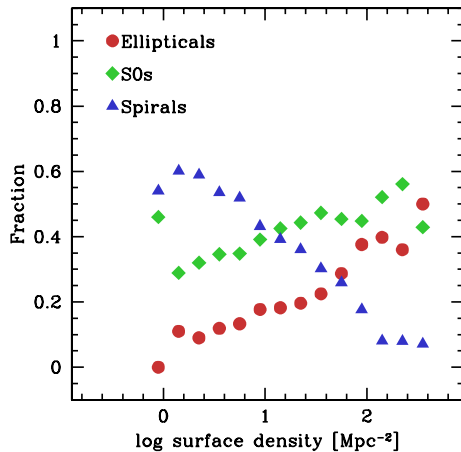


Fig. 1.4: The Dressler’s morphology-density relation (Dressler 1980) for an assemble of local clusters. Galaxy types are subdivided as indicated in the figure (data taken from Dressler et al. 1997).

mass density.

One must keep in mind that the true tridimensional mass density is currently observationally unavailable. However, from simulations, gravitationally bound systems are found to have an “universal” radial mass profile which is well represented by the number density of objects that they contain (Navarro et al. 1996). Mock galaxy catalogs show that physical groups can be also identified by their two-dimensional distribution with high reliability (Eke et al. 2004).

Therefore, in many studies, the environment is expressed by the galaxy number density. Other studies, especially those focused in clusters, represent those trends relative to the clustercentric distance, because galaxy clusters have a mass profile which decreases with radius (*e.g.* Carlberg et al. 1997a). Other mean of studying the environmental evolution of galaxies is simply dividing them according to the class of system where they belong, *e.g.* cluster, group, field, and analyze their general properties.

1.3.1 The morphology-density relation

One of the earliest efforts in quantifying the change of galaxy population with environment was con-

ducted by Dressler (1980), where the change of the morphological mix in nearby galaxy clusters was analyzed (see Figure 1.4). Their results showed that the fraction of elliptical galaxies increases towards higher number galaxy densities, whereas the fraction of spirals decreases. The fraction of S0s galaxies also increases with higher galaxy densities but is less pronounced than for elliptical galaxies.

This result had a big impact on extragalactic astronomy, because it indicated for the first time that some physical mechanism related to the environment affect the galaxy structures. This result has been confirmed by many subsequent studies which have also shown that this relation also extend to poor clusters and galaxy groups (*e.g.* Postman & Geller 1984, Tran et al. 2001, Goto et al. 2003).

1.3.2 Galaxy colors and environment

Optical colors have historically been a useful tool to diagnosis the properties of astronomical objects. Stars placed a color magnitude diagram (CMD) populate special regions⁹ and this distribution is by now well understood in terms of stellar evolution theory. The case for galaxies is more complicated. Unless one is able to resolve individual stars, one only observes the integrated light from their stellar populations, which usually have different ages and metallicities (the main parameters that affect the stellar sequences in the H-R diagram). Therefore, galaxy colors must be understood in terms of star formation histories, but given the number of free parameters (ages, metallicities, dust, initial mass function, etc), they have proved difficult to interpret.

However, it has been noted that galaxies also populate certain regions in a CMD. For example, spheroidal systems, from globular clusters to the giant ellipticals are located in a tight sequence on the CMD, usually few tens of magnitude wide. Smaller systems are normally bluer than larger ones. This distribution has been called the red sequence (*e.g.* Baum 1959, Zepf et al. 1991, Terlevich et al. 2001) as few galaxies are redder than those located there. Spiral and irregulars galaxies normally populate a

⁹The famous Hertzsprung-Russell diagram, circa 1910.

vast region in the CMD located at bluer colors, hence called the “blue cloud”.

The fraction of galaxies populating the red sequence strongly depend on clustering (*e.g.* Zehavi et al. 2002). This should not be a surprise given the strong correlation between morphology and environment, and morphology and colors. So, the question is which of the galaxy properties are correlated independently of the others.

Only recently, thanks to the very large Sloan Digital Sky Survey, the true nature of the color-density relation has been established. First, the galaxy distribution is strongly bimodal and it is well fitted by a double Gaussian (Strateva et al. 2001, Balogh et al. 2004b), which means that any transition between subtypes should occur in short timescales. Secondly, Hogg et al. (2003) and Blanton et al. (2005) pointed out that galaxy colors are more predictive of environment than morphology, breaking the previous degeneracy and indicating that the processes that affect the stellar populations in galaxies are acting in different timescales and likely faster than those that affect the morphology.

Similarly, Haines et al. 2006 using the multi-color photometry in the SDSS found that the mean stellar age is also a strong function of environment, indicating that galaxies in dense environments formed at earlier times.

1.3.3 Star formation and environment

Although blue optical broad-band colors are generally considered an indication of young stellar populations and thus of active star-formation, they are also strongly degenerate as they are affected by both age and metallicity (Worthey 1994). They are also affected by other effects, such as dust and may not reflect eventually the current star-formation activity.

Since it has already been long noted that elliptical galaxies lack emission lines (*e.g.* Osterbrock 1960), it is expected given the morphological-density relation that cluster galaxies have lower average star-formation activity than their field counterparts.

But van den Bergh (1960) identified a popula-

tion of cluster spiral galaxies dubbed “anemic spirals”. They feature weak spiral arms, which indicates that the gas content in those galaxies must be lower as the star-forming regions are the main traces of spiral arms. This was the first indication that galaxies may change their properties in different times scales. Those results have been confirmed by subsequent studies which have detected that many galaxies in clusters are, in fact, deficient in neutral hydrogen (*e.g.* Davies & Lewis 1973, Giovanelli & Haynes 1985, Levy et al. 2007), the building material for a vigorous and continuous star-formation.

The first homogeneous study of the star-formation activity in clusters was conducted by Dressler et al. 1985. They found that ~31% of field galaxies are star-forming whereas in clusters this fraction is as low as ~7%. They also reported that the morphological–density relation can not solely account for this difference.

Active star-forming galaxies in clusters are also peculiar. For example, Chemin et al. (2006) reported that many spiral galaxies in the Virgo Cluster have perturbed kinematics, external filaments and truncated disks. Likewise, Mendes de Oliveira et al. (2003) found that galaxies in compact groups exhibit similar perturbations.

With the advent of large redshift surveys, became possible to study systematically and characterize the dependence of star-formation activity with environment (*e.g.* Hashimoto et al. 1998, Lewis et al. 2002, Gómez et al. 2003, Rines et al. 2005, Haines et al. 2007). All of these studies have found strong suppression of the star-formation activity towards high galaxy density regions and small clustercentric distances. The trends do not seem to be related to the mass of the systems where the galaxies are linked to, no matter if they are poor groups or rich clusters.

Christlein & Zabludoff (2005) have used extensive mathematical modeling in a large local galaxy sample in order to equalize different quantities and have found that even when the morphology, stellar mass and ages are fixed, the relation between environment and star-formation persists. This indicates that this behavior is not another aspect of the well established morphology-density or other similar relations.

1.4 GALAXY EVOLUTION WITH LOOK-BACK TIME

Galaxies, at present times, have ages that are measured in gigayears. This means that most of their stars were formed long time ago. Looking at higher redshift, therefore, permits to probe their evolution with time. At what time galaxies formed the bulk of their stars and how they have changed in morphology and other properties.

Furthermore, as hierarchical scenarios of formation of structures predict that massive systems were assembled only recently in cosmic times, the previous environmental trends are expected to change. However, disentangling the effects of galaxy evolution with those related purely to the evolution of the environment has proved tremendously difficult, and the whole field is matter of active debate.

Nevertheless, the last decade has seen many important findings that put strong constraints to the cosmological and galaxy evolution models. These achievements have only been possible thanks to the advent of the new instrumentation such as more powerful detectors and telescopes (*e.g.* Hubble space telescope and VLT) in combination with large scale simulations.

1.4.1 Decline of star formation activity with time

The global star formation history of the Universe is a key element in understanding the galaxy mass assembly and its study aim to answer the question at what epoch the bulk of the stars were formed. It has been measured by using all available indicators of star-formation activity (*e.g.* X-ray, ultraviolet, optical emission lines, far infrared emission, sub-millimeter and radio). Each of them sample a different related process and all of them are affected by contamination, obscuration, biases and assumptions on the models used to derive the underlying star-formation. This has led to the different measurements of the star-formation density at a given epoch can differ up to a factor three, depending on the method used. Nevertheless, all studies coincide that the cosmic star formation activity has steadily declined since $z \approx 1$ (see Figure 1.5 and Hopkins 2004 for the latest compilation). The decline is well

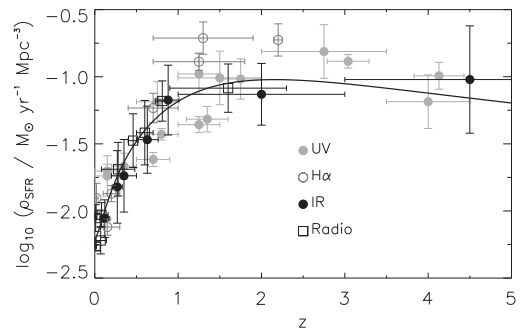


Fig. 1.5: The evolution of the star formation density with cosmic time from the compilation of Hopkins (2004) (data adapted by Bell 2004). Points come from different sources as indicated in the figure. The line is an empirical fit.

characterized by the following function:

$$\psi = \frac{0.006 + 0.072z^{1.35}}{1 + \left(\frac{z}{2}\right)^{2.4}} [M_{\odot} \text{ yr}^{-1} \text{ Mpc}^{-3}] \quad (1.3)$$

For redshift greater than $z = 1$ some controversy persist, specially in the dubbed “redshift desert” ($z \sim 1.5-2$), where the prominent optical emission lines are redshifted to the infrared, and the ultraviolet Lyman- α line is not yet accessible (which occurs at $z \approx 2.5$). Unfortunately, it is at those redshifts where the global star-formation activity is thought to have peaked.

1.4.2 The Butcher-Oemler effect

One of the first pieces of evidence on a change of the galaxy populations with look-back times is the so-called Butcher-Oemler effect (BO effect for short, Butcher & Oemler 1978, Butcher & Oemler Jr. 1984), which is the observed increase on the fraction of blue galaxies in clusters towards higher redshifts. The earlier pure photometric studies have been subsequently confirmed by spectroscopy studies asserting the reality of this effect (*e.g.* Couch & Sharples 1987, Ellingson et al. 2001, Nakata et al. 2005).

There has been much discussion about the in-

terpretation of the effect. At first glance, it could be linked to the overall increase of the star-formation activity with redshift, but galaxy clusters show depleted star-formation activity relative to the field at all redshifts (*e.g.* Balogh et al. 1999, 2002a). Moreover, the increase on the activity in clusters with redshift as measured with emission lines is not as clear as for the general field and shows larger scatter (Balogh et al. 1999, Nakata et al. 2005, Poggianti et al. 2006), although a comprehensive study beyond redshift $z \sim 0.5$ is not yet available.

Ellingson et al. (2001) provided key evidence on the nature of the BO effect. First, when galaxies in the very inner regions of the clusters are selected the effect basically disappears. Second, when only bright galaxies are selected the trend shows larger scatter.

The emerging picture is that recently arrived members to the cluster have shut down their star-formation activity recently and their blue colors is a vestige of their past activity. This confirms the early findings of Dressler & Gunn (1982) who first identified an important fraction of the BO galaxies as post-starbursts. Those galaxies are thought to play an important role in galaxy evolution as their spectroscopy signatures indicate that they have experienced a period of high star-formation activity which was suddenly shut down (Poggianti et al. 1999).

However, recent stellar population models predict that when one galaxy quenches its star-formation it will move to the red-sequence quite quickly (~ 400 Myr, Harker et al. 2006). Evidence of this is provided by the strong galaxy bimodality in observed in galaxy colors (*e.g.* Balogh et al. 2004b), which can not be simply explained otherwise.

Rakos & Schombert (1995) and Andreon et al. (2006) have found caveats in the original BO color criterion which makes the interpretation difficult. They argued that the BO effects can be explained simply by the fact that galaxies at larger redshifts are younger and thus exhibit bluer colors. However, Blanton (2006) found that galaxies experience in average little color evolution between $z = 1$ and $z = 0$, and the red sequence is only about 0.1 mag bluer in the distant Universe.

Andreon et al. 2006 also found positive correlation of the blue fraction with cluster velocity dispersion, similarly to Popesso et al. (2007) at $z = 0$ but De Propris et al. (2004) did not find it in their sample of local clusters. This later study also asserts that the measured fraction of blue galaxies strongly depends on the luminosity cut and aperture radius adopted.

In conclusion, almost 30 years after the Butcher-Oemler effect was first reported, its interpretation is still controversial.

1.4.3 The abundance of the S0 galaxies

An important piece of evidence of the strong evolution of cluster galaxies since moderated look-back times was added by Dressler et al. (1997), who studied a sample of rich, intermediate redshift clusters ($\langle z \rangle \sim 0.5$), finding a strong decrease in the fraction of S0 galaxies in comparison with ellipticals. In local clusters the ratio is approximately 2.5 to 1, whereas in distant systems is 0.5 to 1, a factor five lower. The drop of cluster S0s is accompanied with the increase of the spiral galaxy fraction (see also Couch et al. 1998, Fasano et al. 2000) which fills the gap whereas the elliptical fraction remains almost constant.

The increase of the spiral and blue fraction (as seen in the BO effect) summed to the decrease of a significant population of red galaxies with redshift led to a scheme where the elliptical galaxies were formed at very early times in the cluster life, during the so-called “merger phase” (*e.g.* Ellis et al. 1997). Active infalling spiral galaxies had first their star-formation activity disrupted and later their disks were stripped, slowly being transformed into S0 galaxies. The responsible process is, therefore, very active in relative later phases of the Universe life, in the last ~ 5 Gyr, during the accretion phase.

However, it has proved difficult to witness the relevant processes and several unknowns remains. In particular, which are their timescales and where are more effective. The whole subject has been matter of controversy over the last years, despite considerable observational and theoretical effort.

1.5 PHYSICAL PROCESSES THAT AFFECT GALAXY PROPERTIES

As the years progressed and new and strong evidence was accumulated that galaxies are experiencing strong transformation during the assembly of structures different processes have been proposed in order to explain the change of population with environment and time. They are often classified in two types: 1. Interaction of the gravitational fields between galaxies or clusters, 2. Interaction between the galaxy gas content and the intergalactic media composed of shallower but hot plasma.

1.5.1 Tidal interactions among galaxies

Tidal interactions among galaxy pairs act on dark, stellar and gaseous components of galaxies, producing selective transformations. The efficiency is determined by how bound is the material by gravity. So that, tides are more effective in removing material from the outer parts of the galaxies (Merritt 1984). Although tidal forces act proportionally to M/R^3 , the average separation between galaxies in some environments is comparable to their sizes, so this type of interaction is commonly observed (*e.g.* Hogg et al. 1998, Wehner et al. 2006). Moreover, observations and simulations show that interacting pairs display enhanced star-formation, specially in the central parts (*e.g.* Henriksen & Byrd 1996). However, the efficiencies on morphological change and star-formation busting are dissimilar depending upon the relative masses of the interacting galaxies. If the mass difference is large, the smaller companion may be completely destroyed by the tides and the larger galaxy remains mostly unaffected¹⁰. On the other hand, similar sized galaxies can produce large scale tides that fuel central activity via gas infall into the nucleus, but the effects on the morphology depend on the particular configuration (*e.g.* Icke 1985, Valluri 1993).

Given the high galaxy concentration in clusters, it results intuitive to expect that this effect is stronger in those environments. However, due to the high relative velocities, tidal interactions among cluster galaxies, although more frequent, have sig-

¹⁰The best known example is the Sagittarius dwarf galaxy which is an advanced stage of disruption (Ibata et al. 1994)

nificantly shorter duration than in less massive systems ($t \sim 10^8$ yr); thus, the effects of the perturbation are less severe (Fujita 1998).

1.5.2 Tidal interactions between the cluster potential and galaxies

Given the large mass of clusters, exceeding $10^{14}M_{\odot}$, tidal interactions between galaxies and the whole cluster potential well can effectively perturb cluster galaxies, inducing gas inflow, bar formation, disk heating and star-formation (*e.g.* Merritt 1984, Valluri 1993, Henriksen & Byrd 1996).

Byrd & Valtonen (1990) showed that the gas in the the disk is driven towards the center of the galaxy on timescales of $\sim 3 \times 10^8$ yr, triggering nuclear activity. Also, Bekki et al. (2001) showed that the tides induced by the cluster potential are very efficient in removing the galaxy gas reservoir in the halo, halting its accretion and truncating the star-formation.

1.5.3 Harassment

Although each close encounter among cluster members does not strongly affect the properties of a particular galaxy, due to the short time-scale of the interaction, the effects of many encounters over long periods can produce noticeable effects on the structure. The combined effect of these multiple high-speed galaxy-galaxy and galaxy-cluster interactions has been named "harassment" (Moore et al. 1998, 1999), and may be an effective mechanism in transforming galaxies in clusters.

Recent simulations by Gnedin (2003) show that the accumulated effects of those interactions in spirals galaxies lead to dark-matter halos truncation, thickening of the disk, lost of the outer stellar component (up to $\sim 50\%$) and halting of the star-formation. Low surface brightness galaxies are more affected and can be completely disrupted. If the galaxy to be considered is a spiral, the end-product share many properties with the S0 population

The effect of those tidal interactions can start to affect galaxies at large distances from the cluster core as soon as they get gravitationally bound to

the cluster. The presence of substructure increases the efficiency of this type of interaction.

The time-scale found by Gnedin (2003) is considerably shorter than in the previous simulations performed by Moore et al. (1999), ~ 1.5 Gyr against ~ 4.5 Gyr.

1.5.4 Galaxy mergers

Merger and accretion of substructures are natural results in Λ CDM cosmologies, therefore they are expected to play an important role in galaxy evolution. Much work has been done in characterizing the end-products of those interactions under different configurations since the early works of Toomre et al. (1977). They showed that an equal mass merger of two disk galaxies may end in a spheroidal system. Similar results have been found by several more modern simulations (*e.g.* Barnes & Hernquist 1991, Hernquist 1992, Bekki 2001, González-García & Balcells 2005, etc). Those studies have also shown that the merger of gas rich spirals can produce a starburst, consuming rapidly most of available the gas. Mergers with different mass ratios produce disk heating, growth of the bulge and enhanced star-formation for a short period. Therefore, this process alone can account for most the Hubble sequence (Cavaliere & Menci 1993).

The merger scenario is supported by the frequency of photometric and kinematic disturbances found in elliptical galaxies such as shells, ripples, counter-rotating cores, etc. (*e.g.* Balcells 1997, Hau et al. 1999, Davies et al. 2001).

However, the relative high velocities dispersion found in galaxy clusters and the tides exerted by its gravitational fields prevent the merger occurrence (Makino & Hut 1997), except during the earliest phases of cluster formation (Krivitsky & Kontorovich 1997). Much more friendly is the group environment, where it is expected that most of the merger occurs since $z \sim 0.5$ (Cavaliere et al. 1992).

Depending on particular conditions, the time of relaxation, once the merger started is about 1–2 Gyrs (Bekki 2001, Conselice 2006, Bournaud et al. 2007). These models also show

that mergers had to be much more frequent in the past, with a increasing rate proportional to $\sim (1+z)^3$. However, it is still unclear how important this process is, in the context of galaxy mass build-up, as the observable evolution of the merger rate depends on several assumptions and it is only indirectly inferred (*e.g.* Masjedi et al. 2006, Bell et al. 2006).

1.5.5 Ram pressure stripping

If a disk galaxy moves inside a cluster at $\sim 1000 \text{ km s}^{-1}$ (a typical cluster velocity dispersion), the hot intracluster medium (ICM) may exert a pressure over the gas in the interstellar medium (ISM) with a strength enough to remove it (Gunn & Gott 1972).

The efficiency of the process is mainly determined by how bound the gas to each galaxy is (by gravity) and how strong is pressure over the ISM, which is determined by the galaxy velocity through the cluster and the density of the ICM .

However, as many subsequent studies have shown, the efficiency of the gas removal is altered by each particular configuration (*e.g.* Abadi et al. 1999, Quilis et al. 2000, Vollmer et al. 2000, Kapferer et al. 2007, etc) . For example, galaxies in radial orbits are more affected, because they have higher velocities and pass closer to the denser and hotter cluster core. The efficiency of removal also depends on the inclination of the galaxy disk with respect to the trajectory, with face-on interactions being more efficient than edge-on encounters. Nevertheless, assuming the typical gas densities and velocity dispersion of local clusters, most of the galaxies will have the ISM stripped in times scales comparable to the average cluster crossing times (~ 1 Gyr).

Before complete gas stripping, ram-pressure significantly compresses the ISM and may trigger an episode of enhanced star-formation (Fujita & Nagashima 1999, Bekki & Couch 2003). Such structures have actually been observed by a numbers of studies. For instance, Vollmer et al. (2000) interpreted the distorted $H\alpha$ distribution and kinematics in a Virgo cluster galaxy (NGC4522) as caused by ram-pressure. Similarly, Cortese et al.

(2007) found compelling evidence that two peculiar infalling galaxies in two $z \sim 0.2$ clusters are being affected by ram-pressure. Both galaxies display trails composed of bright knots associated to long stellar streams and show enhanced and depleted star-formation respectively.

1.5.6 Viscous stripping and thermal evaporation

Two other mechanisms may be present in the cores of rich galaxy clusters as they require similar conditions as ram-pressure stripping. One of these is viscous stripping (Nulsen 1982) and the gas removal is mainly due to turbulent momentum transfer and thermal conduction from the hot ICM to the cold ISM, rather than to the pressure alone.

Thermal evaporation, on the other hand, is produced in the interface between the cold ISM and the hot ICM, which produces a rapid increase of the galaxy gas temperature and the galaxy gravity field is not able to retain it (Cowie & Songaila 1977).

The timescales of gas removal of both processes are similar or slightly shorter than for ram-pressure. As the necessary conditions and subsequent effects on the galaxy properties are similar they are often included in the class of strong interactions in clusters.

1.5.7 Starvation

It has been long noted that the amount of gas present in the disks of spiral galaxies is sufficient to sustain the typical star formation rates only for a relatively short period of time (~ 1 Gyr, Larson 1972, Kennicutt 1983). Therefore, it has been proposed that galaxies have a reservoir of gas in the halo which cool down and fall into the disk, keeping the star-formation active. Evidence of existence of this reservoir is found in the diffuse X-ray emission in spiral galaxies (*e.g.* Benson et al. 2000) and the high velocity clouds detected moving towards the halo of our Galaxy via radio emission (see Wakker & van Woerden 1997).

If this thin gaseous component is removed, the galaxy will find itself without the replenishment necessary for a continuous star-formation. Slowly,

the galaxy will consume all the remaining gas in the disk and becomes passive within few gigayears (Larson et al. 1980, Bekki et al. 2002). Some authors have argued that this can explain the decline of the star-formation activity in low density environments and the mild evolution in the morphological mix found in some distant clusters (Balogh et al. 1999, Treu et al. 2003).

1.5.8 Group preprocessing

According to the hierarchical scenario for the formation of large-scale structures, groups of galaxies are the building blocks of rich clusters. It is supported by the frequency of sub-structures seen in X-ray and kinematic studies (*e.g.* Dressler & Shectman 1988). Galaxy groups may therefore represent natural sites for a preprocessing stage in the evolution of cluster galaxies through mergers and tidal interactions, which are otherwise ineffective in high velocity dispersion environments (Fujita 2004). The same study shows that ram-pressure and starvation might already be effective in these groups at $z \sim 0.5$ (see also Hester 2006).

Since preprocessing occurs well outside the core of clusters, this mechanism has been invoked to explain why the star formation activity is suppressed at large clustercentric distances (see §1.3.3).

1.6 COSMOLOGICAL CONTEXT¹¹

Cosmology is the study of the large-scale structure of the Universe as well as its origin and fate. Modern cosmology has its roots in the works of A. Einstein in 1917. According to the fundamentals of general relativity, the evolution of the Universe is determined by the forms of energy it contains and the curvature of space. Einstein's equations can be reduced to a simple form known as the Friedmann equation if isotropy and homogeneity are assumed

$$H^2 \equiv \left(\frac{\dot{a}}{a}\right)^2 = \frac{8\pi G}{3}\rho - \frac{k}{a^2} \quad (1.4)$$

¹¹The preparation of this section has mainly been based in the book of Longair (2007) and the review of Padmanabhan (2005).

where $H = H(t)$ is the Hubble parameter which measures the rate of expansion of the Universe as a function of time, G is the Newton's gravitational constant, $\rho = \rho(t)$ is the energy density, k is the curvature constant (negative, positive or zero) and $a = a(t)$ is the scale factor, which measures how the Universe stretches as a function of time.

The energy density ρ can have several different subcomponents, such as the mass density associated to baryonic and dark matter, the kinetic energy of particles and radiation, the energy associated with fields and the vacuum energy density.

For any value of the Hubble expansion parameter, there is a critical density which solves the previous equation for zero spatial curvature: $\rho_{crit} = 3H^2/8\pi G$. The energy density is conventionally characterized by a density parameter normalized with respect to the critical density: $\Omega = \rho/\rho_{crit}$.

The first precise constraint for the above equation comes from the observations of extragalactic cepheids by the Hubble Key Project, determining that the Hubble constant at $z = 0$ is $H_0 = 72 \pm 8 \text{ km s}^{-1} \text{ Mpc}^{-1}$ (Freedman et al. 2001 and references therein).

Observations of relaxed clusters of galaxies, *i.e.* large scale structures that have collapsed, have led to the conclusion that matter only account the $\sim 30\%$ of the critical density ($\Omega_M = 0.3^{+0.04}_{-0.03}$, Allen et al. 2002). Only $\sim 14\%$ of this, corresponds to baryonic matter ($\Omega_B \approx 0.042$, using the accepted value of H_0 Fukugita et al. 1998, O'Meara et al. 2001). The rest is composed of dark matter.

The Wilkinson Microwave Anisotropy Probe (WMAP) mission, aimed to measure the primordial fluctuations imprinted in the Cosmic Microwave Background (CMB), has found that the temperature anisotropies are compatible with the predictions by inflationary universe scenarios with $\Omega_{total} \approx 1$ and confirming the measurements for Ω_M (Spergel et al. 2007). As this is in concordance with a flat universe, the energy density associated to the curvature of the Universe is $\Omega_k = 0$. Therefore, there is a dark component that makes up to 70% of the energy density of the Universe and does not interact through gravity.

Evidence of it was found years earlier, when

two teams¹², using supernovae type Ia to measure to Hubble constant up to cosmological distances, found compelling evidence of an accelerating Universe (Riess et al. 1998, Perlmutter et al. 1999), *i.e.* cosmological expansion is faster at the present.

This may be better understood by rewriting the equation 1.4 after multiplying by a^2

$$\dot{a}^2 = \frac{8\pi G}{3} a^2 \rho - k \quad (1.5)$$

In an expanding universe, the energy density associated to matter is diluted with time ($\rho_M \propto a^{-3}$). Radiation is also diluted by expansion as well as redshift, so that $\rho_{rad} \propto a^{-4}$. Therefore, the energy density associated to these conventional sources decrease as the Universe expands, therefore, \dot{a} also decreases¹³ (k is a constant). The supernova data imply the energy density needed to make a flat Universe, in concordance with the CMB data, must be varying with time in order to accelerate the Universe, *i.e.* the relative balance between this "dark energy" and matter changes as the Universe expands. The contribution of the dark energy at early times of the Universe life is negligible as matter and radiation were dominant. At the present dark energy dominates. Its current accepted value is $\Omega_{\Lambda_0} = 0.7$ ¹⁴. Therefore, the energy density of the Universe at the present epoch is expressed by,

$$1 = \Omega_M + \Omega_{\Lambda} \quad (1.6)$$

as the energy density due to radiation Ω_R is important only at very early times.

The constrains from different experiments to the values of H_0 , Ω_M and Ω_{Λ} , have led to the so-called "concordance cosmology". This can be appreciated in Figure 1.6, where the results of those studies overlap in a small region in this parameter space. Further constrains come from the baryon acoustic oscillations observed in the galaxy distribution

¹²The High-Z and Supernova Cosmological Project.

¹³Under the energy density from those sources the Universe will continue to expand forever, but at a lower pace.

¹⁴It is, nevertheless, puzzling that two seemingly unrelated processes show similar strength at the current epoch. This has been dubbed as "the coincidence problem".

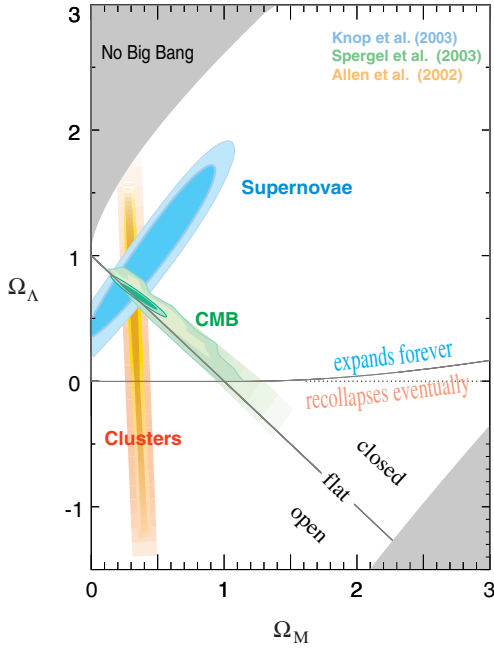


Fig. 1.6: Constrains of Ω_M and Ω_Λ from different experiments. The area of overlapping (marked with a dark green, small ellipse) has led to the “concordance cosmology” term. Taken from the “Supernova Cosmology project” (<http://supernova.lbl.gov/>). The references to the original works are: Knop et al. (2003), Spergel et al. (2003) and Allen et al. (2002).

in large redshift surveys (*e.g.* Cole et al. 2005, Eisenstein et al. 2005), a relic from the original oscillations observed in the CMB, and the abundances of primordial elements which matches the prediction of inflationary models of Big-Bang (Coc et al. 2004).

The form of the Hubble parameter in the concordance cosmology is therefore written as:

$$H(t) = H_0 \left[\Omega_M a^{-3} + \Omega_\Lambda \right]^{1/2} \quad (1.7)$$

The scale factor a can be expressed in the current cosmology as $(1+z) = a_0/a_z$. By making $a_0 = 1$ (normalizing by the present scale), the above equation can be written as:

$$H(z) = H_0 \left[\Omega_M (1+z)^3 + \Omega_\Lambda \right]^{1/2} \quad (1.8)$$

which can be substituted in equation 1.1 to calculate cosmological distances.

The redshift z is defined by:

$$(1+z) = \frac{\lambda_{\text{observed}}}{\lambda_{\text{emitted}}} \quad (1.9)$$

Throughout this thesis, the current standard cosmological model will be used: $(H_0, \Omega_M, \Omega_\Lambda) = (70, 0.3, 0.7)$.

1.6.1 A Λ CDM Universe and the hierarchical scenario

The existence of dark matter has been deduced by the observation of the velocity distribution of galaxies in clusters, the rotation velocities of spiral galaxies and the velocity distribution of stars and globular clusters in particular galaxies. These effects can not be explained in the context of Newtonian dynamics by the masses deduced from their stellar component. The strength of gravitational lensing, the large temperature of the X-ray emitting gas in galaxy clusters and the peaks in the angular spectrum observed in the cosmic background radiation are also evidence of it.

Among the different types of Dark Matter, a cold type, *i.e.* formed by non-relativistic particles, is preferred. This is because of the scales of its effects in the local Universe and the angular spectrum observed in the cosmic background radiation.

Under this scenario, structures began to form under gravitational collapse before matter and radiation decoupled in the last scattering surface. Once the gas fell into those structures, it cooled down and formed stars. The rapid early formation of the structures matches the observation of the oldest stars, which formed in less than a gigayear after the Big-bang.

One important consequence of a CDM dominated universe is that large structures successively are built up from smaller structures. Such framework of structure formation is called hierarchical merging.

This model has been very successful in predicting the overall shape of the large scale galaxy dis-

tribution in scales of ~ 10 Mpc, but some problems still remain. In particular models predict a too large number of dwarf galaxies (cold dark matter gives too much power in small scales) which are not observed (*e.g.* Whiting et al. 2007). Another problem is the observed early formation of massive galaxies which should only occur in a late stage of the Universe life.

This “anti-hierarchical” behavior may not be a shortcoming of the theory itself, but a problem of its modeling, since numerical simulations do not have the sufficient resolution to include individual stars and they are added using standard recipes. Moreover, often several effects related to galaxy evolution are largely ignored due to their still poor understanding.

If some of them are included, specially the effects of AGN and supernova feedback that prevent dwarf galaxies from forming stars, some aspects of this phenomenon disappear (*e.g.* Neistein et al. 2006)

The Project

In the previous chapter, a summary of the different physical processes that may affect the galaxy populations in clusters was given. Several studies, specially in the local Universe, have tried to identify which process is the most relevant. However, the main questions remains unanswered. How much and how fast is the star formation suppressed in infalling galaxies? What is exactly the environmental dependence of the star formation activity? Is it suppressed mainly due to local or global processes? What is the main mechanism?

In order to provide new insights to some of these questions, a project aimed to study the transition between field and cluster environment was initiated.

To tackle down adequately those problems, a photometric only based study is not sufficient, because of the large contamination due to fore- and background objects. This is expected to be much worse in the low density, infall regions around the clusters where the transformation is suspected to take place.

Moreover, studying the star-formation properties of galaxies, using only the inexpensive broadband colors may be misleading because of the assumptions made in the stellar population models. For instance, the relation “blue” colors and star-formation activity is not straightforward in the optical range, because galaxies can have shut down their activity recently and still show blue colors from their new formed stars (*e.g.* Kauffmann 1996, Ellingson et al. 2001). They can also show red colors not due to an

old stellar population but because dust is obscuring the newly formed stars.

Another problem comes from the fact that photometry alone cannot often distinguish transition types, such as the K+A galaxies (Quintero et al. 2004), which may be important in the context of galaxy evolution.

Spectroscopy can effectively solve many of the difficulties mentioned above and provides a much richer wealth of information about the objects studied. On the other hand, it is often expensive, observationally speaking, requiring large amounts of telescope time to obtain a statistically significant sample. Data reduction and interpretation are also more complicated.

The project described in this work is an extensive, panoramic spectroscopy campaign focused in clusters at intermediate redshifts ($\langle z \rangle \sim 0.25^1$). At this epoch a higher galaxy infall is expected (Bower 1991) and thus the chances of observing the responsible interactions increase. As described in the introduction, strong evolution in the cluster galaxy population is observed with lookback time, therefore, the targeted epoch is crucial to understand to current galaxy mix present in local clusters.

Furthermore, it is feasible to obtain a large number of spectra in a relatively short period of time with the available instrumentation.

In this chapter, all observational related issues

¹This is about 3 Gyr of look-back time in the assumed cosmology (*i.e.* $H_0 = 70 \text{ km s}^{-1} \text{ Mpc}^{-1}$, $\Omega_m = 0.3$ and $\Omega_\Lambda = 0.7$).

RIXOS field ^a	Cluster	RA J2000	DEC J2000	f_x [10^{-14} erg s ⁻¹ cm ⁻²]	z	reference
R220	VMF194	17:29:02	74:40:46	17.3	0.213	Mullis et al. (2003)
	XDCS220 ^b	17:23:33	74:44:10	≤ 0.3	0.260	Gilbank et al. (2004)
R265	VMF131	13:09:56	32:22:31	9.0	0.290	Vikhlinin et al. (1998)
	VMF132	13:11:13	32:28:58	46.7	0.245	Vikhlinin et al. (1998)
R285	VMF73	09:43:32	16:40:02	23.1	0.180	Vikhlinin et al. (1998)
	VMF74	09:43:45	16:44:20	21.2	0.256	Vikhlinin et al. (1998)

Table 2.1: Basic parameters of the cluster sample. The coordinates are referred to the X-ray centroid with respect to the J2000 equinox. X-ray fluxes and redshifts were determined by the respective authors in the last column. VMF refers to the Vikhlinin et al. (1998) survey. However, for VMF194, the redshift was determined by Mullis et al. (2003). XDCS220 was detected in the subsequent analysis by Gilbank et al. (2004).

^aMason et al. (2000)

^bThroughout this work this name will be used, however Gilbank et al. (2004) named it as cmJ172333+744410.

will be described, including objects selection, observations and data reduction and how the basic measurements were performed.

2.1 SAMPLE SELECTION

2.1.1 Cluster selection

The clusters were selected from the X-ray Dark Cluster Survey (XDCS, Gilbank et al. 2004), which was focused in the comparison between X-ray and optical identification algorithms of clusters.

For this purpose, they obtained deep optical imaging of RIXOS fields (Mason et al. 2000). These data were obtained with the ROSAT X-ray telescope using the Position Sensitive Proportional Counter (PSPC). Some of the X-ray data were also analyzed by Vikhlinin et al. (1998), and later by Mullis et al. (2003) and Burenin et al. (2007), providing X-ray fluxes and further analysis. Those studies were mainly focused in the detection, characterization and confirmation of X-ray clusters.

The optical observations were performed with the 2.5 m Isaac Newton telescope (INT) located in Canarias², using the Wide Field Camera (WFC), which cover the entire PSPC field (about 30×30 arcmin). The images obtained are in *V* and *I*-bands. Gilbank et al. (2004) performed analysis on the cluster optical properties and compared them with the X-ray properties. In particular, they found

²Observatorio Roque de los Muchachos, La Palma, Spain

several groups and clusters which passed undetected in the X-ray studies. They kindly provided the photometry on what the object selection and additional analysis was based.

From this survey, three fields were selected, each of them containing two clusters in projection, in order to maximize the efficiency of the spectroscopic observations.

The sample was heterogeneously built on purpose, spanning a large range of X-ray luminosities and probably different evolutionary stages. They are at similar redshifts, making them good candidates to probe evolution uniquely due to environmental effects at a cosmological epoch with look-back times of ~ 3.0 Gyr. A basic summary of the cluster sample can be found in Table 2.

2.1.2 Object selection

The selection of individual objects for spectroscopy, was based in the *I*-band apparent magnitude only, in order to avoid any bias against color. During the MOS³ masks design, the objects were selected in such manner that some masks observed preferentially bright objects and thus “short” exposures were needed. Other masks mainly contained faint objects and were observed with substantial longer periods of time. However the mask geometry and the position of the objects in the sky put

³Multi-Object spectroscopy. In contrast with single slit spectroscopy, a mask containing several slits is used, targeting as many objects. Hence the name “Multi Object”

Field	masks	exposure time [s]	N slits
R220	4	3600	83
	4	10800	87
R265	3	3600	64
	4	10800	82
R285	3	3600	78
	4	10800	93

Table 2.2: Summary of the observations with the number of MOS masks in each fields. The exposure time for each type of mask is indicated as well as the total number of slits placed. A detailed log of the observations can be found in the table A.1.

constrains in this selection.

Each MOS mask contains 20 to 25 individual slits, with length enough to perform the sky subtraction process accurately. Some of the slits contained intended bright stars in order to check the astrometric accuracy of the telescope pointing.

2.2 OBSERVATIONS

The observations were performed with the 3.5 meter telescope at Calar Alto Observatory⁴ with the MOSCA optical imager and spectrograph, which cover 11×11 arcmin of field of view (FOV). Thus, 7–8 MOS masks per field are necessary to cover adequately the entire WFC FOV.

The low resolution grism GREEN_500 was selected. This setup gives a resolution of $R \sim 10$ – 15 \AA (8 – 12 \AA at the mean redshift) for a slit width of 1 arcsec. This grism was selected because of its high efficiency and large wavelength coverage ($\lambda \sim 4300 - 9000 \text{ \AA}$), allowing to trace both the [O II] to the $H\alpha$ emission lines at the targeted redshifts. These lines are the most important star-formation indicators available in the optical range (see §6).

The $H\alpha$ emission line is mainly used at $z \sim 0$, whereas [O II] is intensively used in studies at larger redshifts. Having the two indicators in the spectra allow better comparisons with low and

⁴The German-Spanish Astronomical Center at Calar Alto is located in the Sierra de Los Filabres, Andalucía, Spain. It is operated by the Max-Planck-Institut für Astronomie in Heidelberg, Germany.

high redshifts studies, lowering the risk of missing dusty star-forming galaxies or including misclassified AGNs^{5,6}. This advantage is not frequently found in similar studies at similar redshifts.

The observations were performed in February and March, 2002. The conditions were in general good, although many of the nights were non-photometric.⁷

A typical observation requires, besides the science exposures, a number of calibrations, in order to correct unwanted effects introduced by the instruments. The types of exposures used here are:

Science frames: Are those exposures which directly target the objects. In this project, they were varying in duration since during the mask design, sets of objects with different magnitudes were included. A summary of the observations can be found in table 2.2 and a more detailed log in A.1.

Bias frames: Are zero second exposures whose purpose is to account the step level induced by the electronics. This level is usually different each time that the CCD is set on. Ten bias frames were taken at the beginning of each night.

Flat-fields: Have the objective of correcting the CCD pixel-to-pixel variation in sensitivity. They were taken at the beginning or the end of the night by illuminating the spectrograph with a uniform source of light. In this case, a screen mounted in the dome of the telescope was used. For each MOS mask, three frames of 30 s were taken.

Arc lamps: Are spectra produced by illuminating the spectrograph with a source of light with known emission lines. They allow to find a

⁵AGN, active galaxy nucleus, luminous compact regions at the center of many galaxies whose radiation is understood as the result of infalling matter into massive black holes

⁶Studies show that in the great majority of cases AGNs are associated to some level of star formation activity (*e.g.* Heckman et al. 1995, Cid Fernandes et al. 2004), however they can notably contribute to the emission line fluxes, thus, precaution is needed to be taken.

⁷A night is considered photometric (or worth for photometry) when the night is cloudless and the atmospheric extinction varies lineally with the airmass through the object is observed.

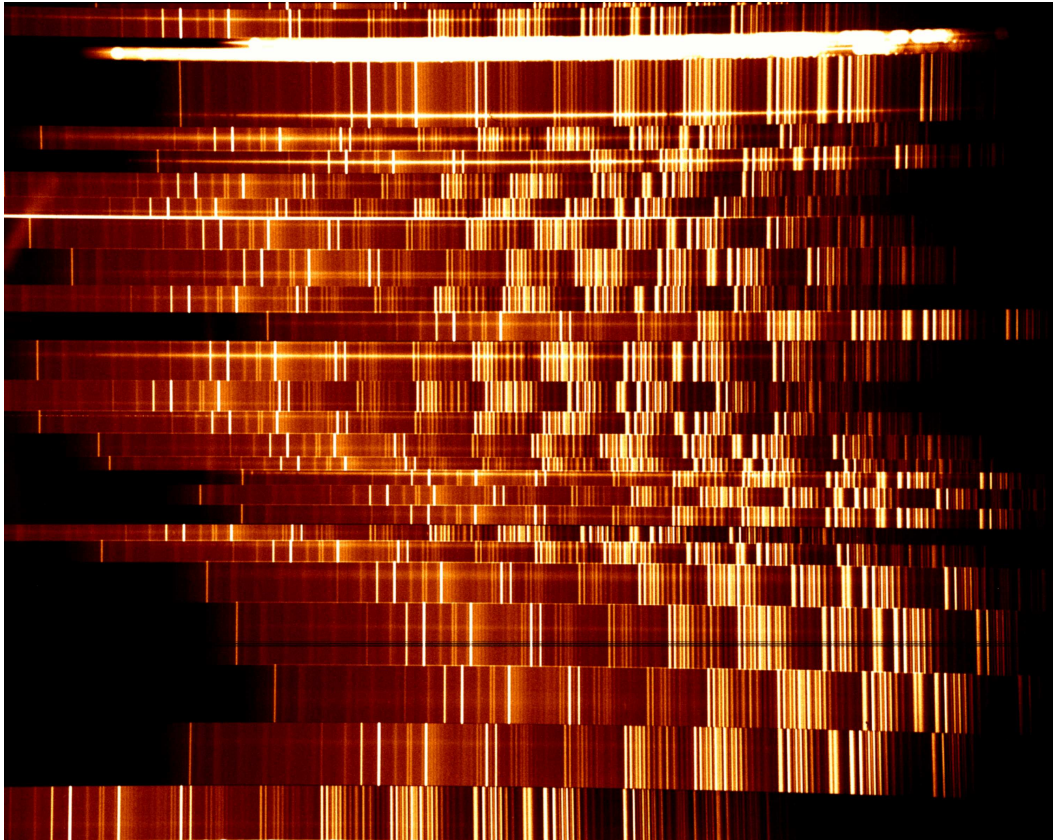


Fig. 2.1: Example of an unreduced multi-object spectra image, containing several objects. The bright horizontal strips are holes centered in stars used to positioning the mask. Some defects in the CCD can be seen, such as the dark line in the fourth spectra (bottom-up). Also, some contamination from reflections is seen at the upper-left. Note that some spectra, specially in the upper and lower parts are severely distorted.

solution that relates the physical position of the spectra in the CCD frame with the wavelength. This process is called wavelength calibration (WLC). These exposures were taken before starting each MOS mask observation, at similar telescope inclinations than the science frames to take in account any possible distortion induced by flexures in the instrument.

Two different arc lamp were used. A 15 s exposure HgAr following with a short Ne burst, therefore called HgAr+Ne. This was augmented by a 120 s exposure of a pure Ar arc in combination with a *BV* filter. This was necessary to make the weak Ar lines at the blue

part of the spectra clearly visible without saturating the chip with the bright red Ar lines.

2.3 DATA REDUCTION

Most of the data reduction was carried out in a standard manner. Each MOS frame was bias subtracted, using the average of ten bias frames, scaled to the overscan level. The overscan region is a set of rows and columns in the CCD, not exposed to the light and thus contains counts only due to the electronics.

The optical design of MOSCA (a focal reducer) induces distortions in the spectra which have to

be corrected before applying other processes (see figure 2.1). Individual spectra were stripped off from the science frames and a third order polynomial function was fitted to the trace of the spectra. Masking bright regions coming from the neighboring slits was necessary. The frame was expanded 20 times in the vertical axis.

Using the information from the fit, each column was moved up- or downwards to take in account subpixel shifts. The spectra was then rebinned to the original size. The same correction was applied to the flat-field and WLC frames to be used them in the next reduction steps. This method was found better than interpolation between pixels in terms of flux conservation.

Each flatfield frame was normalized by the corresponding response curve, which was fitted with a polynomial function to the intensities. Then the individual spectra frames were divided to correct the sensitivity variations. In some few cases, the flatfielding correction was omitted since the flatfield frames showed strong contamination due to scattered light. However, it was found that this was not a big problem, and the spectra appeared as good as the flat-fielded ones. As no flux calibration was attempted, this effect is not considered to be an important problem.

At this point, the subtraction of the sky likes was performed. Two windows, free of contamination, at both sides of the spectrum were defined, and a function was fitted to each column using this information. To each spectra frame, functions with different orders were tested and the one which produced the best result was chosen. In some cases, a constant value was sufficient, in others a third order polynomial was necessary.

In the sky-free spectra frames, normally, the galaxy spectra was clearly visible. It was fitted along the spatial direction with a Gaussian profile. This information was used to weight each row and then they were summed up, obtaining as result the 1D spectra. Individual exposures were then averaged, leaving the final 1D spectra.

At the position of the galaxy spectra a 1D arc-lamp spectra was extracted. Some prominent lines were identified, providing a rough calibration and leaving to a program the task of identifying the rest.

A sixth order polynomial function was fitted to the position of the lines and used to calibrate the wavelength of the final 1D spectra.

Another intermediate process is worth mentioning. A sky spectra was obtained from the original non-subtracted frames. This sky spectra was extracted in an area equal to those used in the 1D spectra fitting (usually a fraction of the windows used to fit the sky level). This sky-spectra is used to create an “error vector”, which is important in the error calculation of equivalent widths (see §3.3).

All the processes mentioned above were made in a semi-automatic, interactive manner, using custom made routines in the MIDAS⁸ environment. In all steps the results were visually inspected in order to check whether they were performed satisfactorily.

No flux calibration was attempted since the weather conditions were variable among the nights (see table A.1) with many non-photometric or bad seeing nights. Also, the slits size covers relatively different fraction of the galaxies, and correcting for this aperture effect is often complicated and inaccurate.

In figure 2.2 some typical 1D spectra are shown. They were de-redshifted to rest-frame to allow an easier comparison among them.

A total of 537 spectra were observed. Some of them turned out to be stars, others were too faint to perform an adequate analysis. In total 318 spectra resulted suitable for analysis. In §3.1 the criteria for their consideration are described.

2.4 ADDITIONAL DATA

2.4.1 Additional spectra

The central parts of the cluster VMF131 (also known as CL1309+32) was previously studied by Balogh et al. (2002a) in a project aimed to study low X-ray luminosity clusters. Their project can be considered as a previous step to the present study because it was aimed to study the star-formation activity in the central regions of clus-

⁸MIDAS, the Munich Image Data Analysis System is developed and maintained by the European Southern Observatory (ESO)

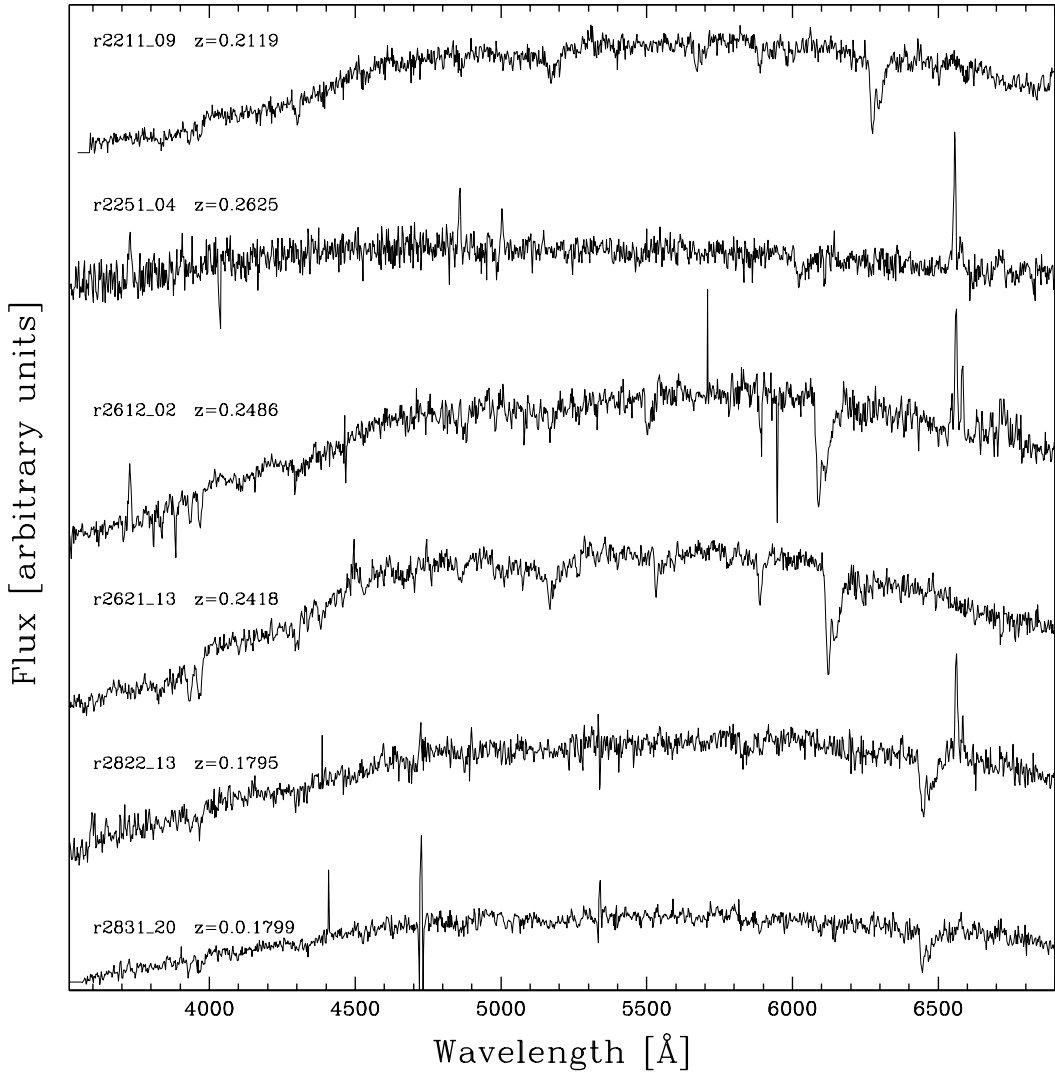


Fig. 2.2: Typical 1-D galaxy spectra. They have been de-redshifted to rest-frame and shifted in the vertical axis for clarity. The identification codes and redshifts are written at the left of each spectra. Note the different quality and differences among the spectra. Some display clear emission lines, others strong absorption lines.

ters at intermediate redshifts, focused in low luminosity X-ray clusters. High luminosity X-ray clusters were previously investigated at similar redshifts by Balogh et al. (1999) using data from the Canadian Network for Observational Cosmology (CNOC, Yee et al. 1996).

They made the observations with the same instrumental setup used in this work and therefore,

adding their data is straightforward. However, their routines to reduce the data as well as their objectives were slightly different and it was decided to look carefully into their data before adding them to the sample used here. From the 45 spectra obtained by them only 17 met the quality standards (see §3.1) used in this work. Few others were repeated observations and therefore excluded since

the observations on which this work was based had, in most of the cases, better quality.

The field R220 was also observed by Gilbank et al. (2004) in order to confirm the suspected clusters, using the same instrumental setup albeit of shorter exposure times. Full access to the original data was granted and the spectra were reduced in the same manner. Given the shorter exposures, few spectra turned out to be useful, and many others were re-observed by this project with better success. Only four of them were finally used in this work.

2.4.2 SDSS data

In the search for additional data to complement the observations was found that the fields R265 and R285 were imaged by the Sloan Digital Sky Survey⁹. The SDSS consists of an imaging survey of π steradian (10^4 square degrees), mostly of the northern sky in five pass-bands (u, g, r, i, z) and medium resolution spectroscopy ($R \approx 1800$). The survey is carried out using a 2.5 m telescope, an imaging mosaic camera with 30 CCDs, two fiber-fed spectrographs and a 0.5 m telescope for the photometric calibration. The imaging survey is taken in drift-scan mode. The imaging data are processed with a photometric pipeline specially written for the SDSS data. The reader is referred to York et al. (2000) for a technical summary of the project and to the webpage for additional information.

None of the fields were spectroscopically observed and unfortunately the R220 field was neither imaged. The available photometry was obtained from the web query form provided by the SDSS site. The g magnitude is the Petrosian magnitude (Petrosian 1976) and the colors are measured in the Petrosian radius, ensuring that the same area is used in all pass-bands. The catalog provided by Gilbank et al. (2004) and SDSS were matched and a visual inspection was made in order to test the reliability of the matching. Two galaxies in the spectroscopic sample were not found in the SDSS database.

⁹SDSS, <http://www.sdss.org/>

Basic measurements

This chapter describes how the main quantities that will be used in the subsequent analyses were obtained.

3.1 INDIVIDUAL GALAXY REDSHIFTS

Individual galaxy redshifts were determined fitting a Gaussian profile to a set of prominent emission and absorption lines (see table 3.1) which are spread over the full wavelength range. The procedure started with an initial guess and was iteratively and interactively refined.

For each galaxy the mean of the individual line redshifts was taken. The error in redshift for each individual galaxy is the standard deviation of mean, when at least four lines were clearly visible. Not all lines were always visible due to the different spectral energy distribution and signal-to-noise of the objects. The error for individual galaxy redshifts usually ranked between 100 to 200 km/s, a reasonable value given the resolution of the instrument used in the observations.

To each spectra, a number representative of its quality was assigned. It was based on the contrast of the lines compared with the surrounding continuum, how many lines were available in the redshift determination and how strong was the contamination of sky-lines residuals.

Spectra with the best quality were ranked with a 0 (zero) and the poorest with a 7 (seven). In general spectra with quality beyond 3 (three) were consid-

ered not trustworthy, and were not included in the final sample.

There are other methods in determining redshifts via, for example, cross-correlation with templates (*e.g.* the task `FXCOR` in IRAF). At low signal-to-noise, the resultant redshifts are only probabilistic, so they may have contaminated the sample. Furthermore, if the lines can not be measured with a certain degree of confidence, they can not be used in the subsequent analysis that this work intends. Therefore, those methods were avoided.

Finally, it resulted in 297 spectra worth for analysis, plus 21 spectra coming from the sources mentioned in §2.4.1 totalizing 318 spectra.

3.2 QUALITY CONTROL

The method mentioned in §3.1, to assign a number according to the quality of the spectra can be highly subjective, because it is based in the eye perception: How clear the different spectral lines are resolved, relative to the surrounding continuum. The main risk is an over-representation of emission line galaxies, since those lines are easily visible and identifiable, biasing the sample towards them, though they can be fainter than passive galaxies.

In order to test this, a better measure of the noise is needed. This was done by fitting a polynomial function to the spectra continuum in the range of interest, from $[O\text{II}]$ to $H\alpha$ at the galaxy redshift. Each spectrum was normalized by that fit, and the

Line	Wavelength [Å]
[O II]	3727
CaK	3930
G-band	4305
H β	4861
[O III]	5007
Mgb	5173
Fe5335	5328
NaD	5885
H α	6563

Table 3.1: Set the lines used in the redshift determination.

standard deviation of the continuum noise was calculated using a $3 - \sigma$ clipping algorithm in five iterations. The algorithm used to fit the continuum ignores emission lines and other small scale prominent features, such as sky lines residuals and telluric lines.

The results are shown in figure 3.1, plotted against V -band apparent magnitude as measure of the total flux. Although the selection of the objects for observing was made using I -band, V -band magnitudes trace better the continuum in the spectroscopic wavelength range, providing a good estimation of the total flux. No significant difference is seen in the distribution of star-forming¹ versus passive galaxies, with the exception of two faint star-forming galaxies.

3.3 EQUIVALENT WIDTHS

Line strengths are measured using equivalent widths, which is defined as the width of a rectangle centered on a spectral line, that on a plot of intensity against wavelength, has the same area as the line. This is calculated in the following way:

$$W = \int \frac{F_C - F_\lambda}{F_C} d\lambda \quad (3.1)$$

where F_C is the continuum flux and F_λ is the flux elsewhere in the line.

¹see next section for the definition of star forming galaxy used in this study

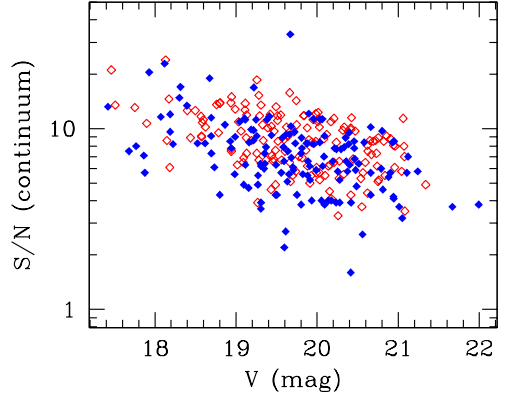


Fig. 3.1: V -band apparent magnitude versus continuum signal-to-noise ratio as measured in §3.2. Open red diamonds are galaxies without emission lines, whereas filled blue diamonds are galaxies with at least one emission line.

Note when the line is in emission (*i.e.* flux higher than the continuum), W is negative.

Using equivalent widths as measure of line strength has several advantages. First, the measurement is independent of the line profile, since the line flux is only summed up. Second, it does not require flux calibration, often complicated and inaccurate for high redshift galaxies, because it is measured comparing to the surrounding continuum. Because of that it is also insensitive to dust extinction, since it affects the line and the surrounding continuum in a similar way.

The estimation of the continuum flux is made by defining two windows free of contamination at each side of the line. In some cases, these windows must avoid other neighboring prominent features, as in the case of the [N II] nebular emission. Nevertheless, the value of W can change depending upon the size of the windows, where the continuum and the line is measured. Several definitions can be found in the literature and the adoption the one in particular basically depends in the characteristics of the data and the comparisons that one pretends to apply. But, in general, it is only a small fraction of the total value (<10%).

The process of calculating W was performed automatically by a custom made program which correct the effects of cosmic expansion on the spec-

Index	Blue continuum [Å]	Line [Å]	Red continuum [Å]	Reference
[O II] λ 3727	3653 – 3713	3713 – 3741	3741 – 3801	Balogh et al. 1999
$D_n(4000)$	3850 – 3950	N/A	4000 – 4100	Balogh et al. 1999
H δ	4030 – 4082	4088 – 4116	4122 – 4170	Balogh et al. 1999
H β	4815 – 4845	4851 – 4871	4880 – 4930	González 1993
[O III] λ 4959	4885 – 4935	4948 – 4978	5030 – 5070	González 1993
[O III] λ 5007	4978 – 4998	4998 – 5015	5015 – 5030	González 1993
H α	6490 – 6537	6555 – 6575	6594 – 6640	Balogh et al. 1999
[N II] λ 6584	6490 – 6530	6576 – 6595	6615 – 6640	González 1993

Table 3.2: Line definitions used in this work for the redshift and equivalent width measurements, along the original references. The $D_n(4000)$ is not a line but a continuum index. For the complete set see Table B.1

tra. Several definitions were used for different lines. In the case of H α and [O II] which are used as tracers of ongoing star formation, the Balogh et al. (1999) definitions are used, as well as for H δ and $D_n(4000)$.

In table 3.2 the definitions used through this work can be found, along with the original references. The blue and red continuum are the window two each side of the line where the continuum flux is measured and fitted. The “line” is the window where the line flux is summed up.

The errors in the equivalent widths are calculated using a error vector which gives an estimate of the signal-to-noise at each line, by comparing the line intensity with the sky lines.

The convention used through this work will be that typical emission lines ([O II], [O III], H β , H α , [N II]) have positive values in *emission*. Typical absorption lines (*e.g.* H δ) are also positive in *absorption*. This may be cause of confusion, however most of the literature adopt this convention and therefore it facilitates any comparison. It must be noted that negative values in H δ do not necessarily mean emission, but a continuum lower than the line, which is mainly due to some weak lines related to heavy elements.

The H α definition used, effectively isolates the targeted line from the neighboring [N II] emission.

Each spectrum was inspected visually to find out whether any lines fall into the prominent telluric bands (A & B), are affected by sky subtraction residuals or by artifacts in the spectra. In some of the cases, lines were flagged out to not be used in

the subsequent analysis.

3.4 STAR FORMING GALAXIES

According to Balogh et al. (2002a), who worked with similar data, in spectra with a resolution $R \sim 15 \text{ \AA}$, an emission line can be measured with uncertainty $< 5 \text{ \AA}$ if $S/N > \sqrt{18 + (W/5)^2}$, where W is the equivalent width of the line. Since the uncertainty for weak lines is dominated by the continuum noise, lines as weak as $\sim 5 \text{ \AA}$ can be reliably measured if $S/N > 4.3$. From Figure 3.1 can be seen that over the 90% of the objects satisfy that condition. The few objects with lower S/N show very strong emission lines and cannot be misclassified.

Therefore, galaxies which show equivalent widths larger than 5 \AA either in [O II] or H α (or both) are considered star forming galaxies. This limit also facilitates the comparison with other similar works. Naturally, in some high S/N galaxies, emission lines with equivalent widths lower than 5 \AA are observed, but since similar lines can not be measured in fainter galaxies, it is preferable to set the previous limit, otherwise any comparison would be impossible. However it was found in subsequent analysis that this limit is robust in separating galaxy types.

3.5 SELECTION FUNCTION

In all fields, only part of the galaxies over the spectroscopic limit ($I \approx 19.5 \text{ mag}$) was observed. In order to correct this effect, a selection function was

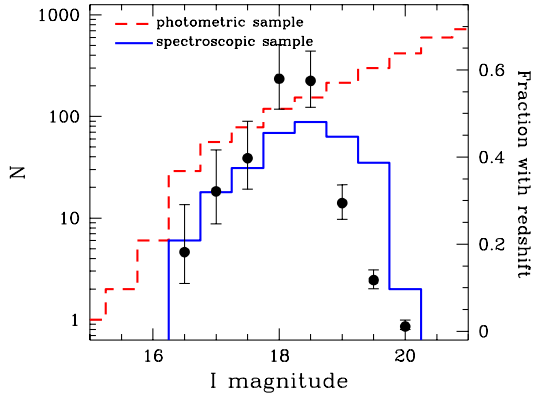


Fig. 3.2: The combined selection function for the whole sample. The histograms show the I -band magnitude distribution for the photometric (dashed red line) and spectroscopic (blue solid line) sample inside of the area covered by the masks. The points show the fraction of galaxies with redshifts. The error bars are Poisson distributed errors (Gehrels 1986).

calculated. It is defined as the fraction of galaxies in the photometric catalog for which redshifts were obtained. The galaxies in the spectroscopic sample are then weighted by the inverse of the fraction to simulate a magnitude limited sample. All statistics in this work are weighted by this function, unless otherwise stated.

As the fields were not homogeneously observed (*i.e.* some parts were observed by two MOS masks, other only by one) and the galaxy distribution neither is uniform, two selection functions were necessary for each field. In the figure 3.2 the combined selection function is shown.

3.6 ABSOLUTE MAGNITUDES

Absolute magnitudes allow to compare the brightness of the objects despite their distances. When measured at different pass-bands they give important information about the spectral energy distribution (SED) of the objects. However, due to the cosmological redshifts, distant galaxies are sampled by local instruments at different rest-frame frequencies, making impossible any comparison. Thus, the absolute magnitudes can not be calculated only using

the distance modulus and an extra term is necessary:

$$m_S = M_Q + DM + K_{QS} \quad (3.2)$$

where m_S is the rest-frame apparent magnitude measured in the band S (arbitrary) and M_Q is the absolute magnitude in the band Q (arbitrary, it can also be S), DM is the distance modulus and K_{QS} is the k-correction term that relate the bands Q and S ².

To calculate the term K_{QS} a good estimation of the object spectral energy distribution (SED) is needed. It can be good constrained via multi-color photometry which sample a large range of wavelengths, allowing to reconstruct the spectra. If it is used in combination with stellar population models, it is possible to obtain better sampled spectra and distinguish types, increasing the accuracy.

Here the IDL-based software `KCORRECT v4_1_4` (Blanton & Roweis 2007) was used to calculate k-corrections. This code is based on the latest stellar population synthesis models of Bruzual & Charlot (2003) and photoionization models of Kewley et al. (2001).

The software algorithm is based on the fact that the seemingly heterogenous galaxy SEDs can be described as a lineal combination of relatively few basic spectral templates. So, with an enough well sampled SED it is possible to find the appropriate combination that best predict the data. Once, the most probable template combination is found, the spectrum is de-redshifted to $z = 0$ and then convolved with the filter transmission curves, obtaining the absolute magnitudes.

Since the fields R265 and R285 have the advantage of having SDSS multi-band photometry, they were also used. Unfortunately, the remaining field (R220) was not observed at this time and only the V and I -band magnitudes provided by Gilbank et al. (2004) are available.

It was found in trial tests that `KCORRECT` is indeed very good in predicting magnitudes in other passbands when they are unavailable. So, for the

²If $S = Q$ does not mean that $K_{QS} = 0$, because band Q is at the object-frame.

fields where magnitudes in both system are present the absolute magnitudes obtained from SDSS were compared against those obtained using solely V and I -band magnitudes.

The magnitudes obtained in either way have scatters of ~ 0.2 mag and offsets of ~ 0.15 mag. The offsets depend on redshift and can be corrected by a linear fitting. The scatter is in agreement with the values found by Blanton & Roweis (2007) for the transformations among different filter systems. These differences are small and hardly change any conclusions in this study.³

For this work B , V and R rest-frame absolute magnitudes were obtained in the Vega system (Johnson & Morgan 1953) using Johnson-Cousins filter definitions (Bessell 1990).

The absolute magnitudes calculated by using the SDSS photometry in the R265 and R285 fields were kept, and the redshift correction was applied for magnitudes obtained from V and I -band photometry solely in the R220 field. All apparent magnitudes were previously corrected for Galactic extinction using the maps of Schlegel et al. (1998). No correction for internal absorption was attempted, since it needs information of galaxy inclination which is in most of the cases is not available, given the low resolution of the ground-based photometry. Similarly, the Balmer decrement can not be used in all cases since $H\beta$ is rarely present in the emission lines galaxies and uncertainties will remain for passive galaxies. No important differences were found between the absolute magnitudes distributions for the field and cluster sample (see Figure 4.10).

As the software uses spectral templates generated by stellar population models, their results can be interpreted in terms of star formation histories, thus, along with the absolute magnitudes, stellar masses were also obtained.

³It turned out, in fact, that one or many bands can be omitted in the input of `KCORRECT` without affecting the results.

The fields and clusters

As described in the previous chapter, six clusters at intermediate redshifts were observed with the main objective of investigating the relation between star-formation and environment from the cluster centers to the outskirts. In this chapter general properties of the clusters will be given including cluster membership, full descriptions of the fields and some physical properties of the clusters as a whole.

4.1 CLUSTER MEMBERSHIP

To determine which galaxies belong to the clusters, the redshift distribution in each field was analyzed (see figure 4.1) first to detect the prominent structures. The clusters studied had already known redshifts, with the exception of those in the R220 field whose redshifts were unclear (see §4.2.1 for details), and therefore were confirmed.

4.1.1 The biweight estimators

The mean cluster redshift (z) and velocity dispersion (σ) were calculated by using the biweight estimators of Beers et al. (1990) and iteratively excluding galaxies beyond $3\text{-}\sigma$ of the mean redshift, until the solution converges. These estimators are more robust than the classical mean and the standard deviation, being less sensible to outliers and asymmetries in the velocity distribution.

The biweight estimator of location (the “mean” z) is defined as

$$C_{BI} = M + \frac{\sum_{|u_i| < 1} (x_i - M)(1 - u_i^2)^2}{\sum_{|u_i| < 1} (1 - u_i^2)^2} \quad (4.1)$$

where M is the median of the individual redshifts x_i , and u_i are given by

$$u_i = \frac{(x_i - M)}{cMAD} \quad (4.2)$$

where c is known as the tuning constant. According to Beers et al. (1990), $c = 6$ gives to C_{BI} high efficiency for a broad range of distributions. MAD is the median absolute deviation from the sample median and is defined by

$$MAD = \text{median}(|x_i - M|) \quad (4.3)$$

and gives high resistance to outliers.

On the other hand, the biweight estimator of scale (σ) is defined as

$$S_{BI} = n^{1/2} \frac{\left[\sum_{|u_i| < 1} (x_i - M)^2 (1 - u_i^2)^4 \right]^{1/2}}{\left| \sum_{|u_i| < 1} (1 - u_i^2)(1 - 5u_i^2) \right|} \quad (4.4)$$

Field	Cluster	z	$L_{X,bol}$ [ergs/s]	σ [km/s]	R_{vir} [Mpc]	N
R220	VMF194	0.210	5.01×10^{43}	282 ± 52	0.629	8
	XDCS220	0.261	1.40×10^{42}	621 ± 271	1.347	14
R265	VMF131	0.294	6.03×10^{43}	476 ± 110	1.014	29
	VMF132	0.247	2.45×10^{44}	774 ± 150	1.692	19
R285	VMF73	0.254	1.23×10^{44}	661 ± 65	1.439	44
	VMF74	0.180	4.79×10^{43}	481 ± 79	1.090	34

Table 4.1: Main parameter for the cluster sample. $L_{X,bol}$ is bolometric X-ray luminosity. R_{vir} is the virial radii and σ the velocity dispersion with the estimated error. N is the number of members identified in each cluster. See the text for details of the calculation of each parameter.

where the u_i are defined as above, but in this case a tuning constant of $c = 9$ is recommended.

To determine C_{BI} and S_{BI} of an individual cluster distribution, the range of redshift was limited in order to not include the other projected cluster present in each field, but this range is far larger than the possible spread due to their velocity dispersions (typically $\Delta(z) \sim 0.2$). Then, galaxies beyond $3\text{-}\sigma$ of the mean redshift were iteratively excluded until the solution converges, which often occurred in few steps.

4.1.2 The bootstrap method

In the paper of Beers et al. (1990) one can also find recipes for how to calculate confidence levels and check the stability of the results using bootstrapping or jackknife resampling techniques, which are specially suitable for small datasets.

A bootstrapping resampling method¹ relies in the creation of a large number of samples drawn from the original population. This is made taking randomly elements from the original sample (with replacement) to create new samples. All statistics (in this case the C_{BI} and S_{BI}) are calculated in each of the 10000 newly created samples. Their distributions were examined and it was found that they were very stable, with a single gravity center and compatible with a Gaussian distribution.

The mean and standard deviation were calculated over the distribution of the bootstrapped values. In the case of the z and σ , the mean of the

¹This method will often be used in this work to check the quality of the respective calculations.

bootstrapped C_{BI} and S_{BI} values coincide with the values calculated using the equations 4.1 and 4.4 as described in the previous section. The standard deviation of the bootstrapped S_{BI} values gives the error in the velocity dispersion calculation. The results for each cluster can be found in table 4.1.

The jackknife method was also tried. It is somewhat similar to the previous method and consists in completely taking out, from the parent sample, only one element at each iteration and calculate the statistics. It was found that it yields errors much lower than the bootstrap technique and, in order to be conservative, it was decided to keep the values calculated with the former method.

All galaxies within the $3\text{-}\sigma$ distance of the mean redshift are considered cluster members. In the next section, a detailed discussion about the characteristic and particularities of each field is given.

4.2 DESCRIPTION OF THE FIELDS

In this section, a detailed description of each field is given, included general properties of the clusters, candidate groups and substructure. Each cluster is represented separately in Figures 4.3, 4.4 and 4.5 with different symbols for star-forming and passive galaxies. The large concentric circles represent one and two virial radii respectively calculated according equation 4.5.

The contours show the distribution of all galaxies with similar colors to the respective red sequences down to $I = 23$ mag. They give some information about the spatial distribution of galax-

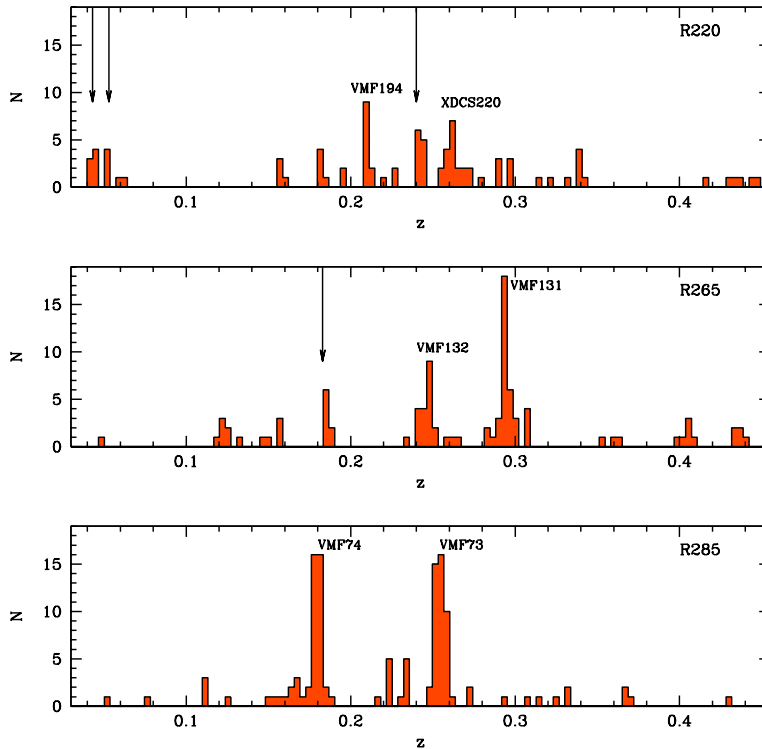


Fig. 4.1: Redshift distribution in the three fields. Big arrows mark the position of the main clusters (see figure 4.2) and the small ones the position of candidate groups in the fields (see section 4.2). Note the different redshift distribution for each the field.

ies without spectroscopy. This technique has been successfully used by other studies to detect substructures around clusters (*e.g.* Kodama et al. 2001, Tanaka et al. 2005).

In this case, it is not possible to firmly state the significance of those structures because only the $V - I$ colors provided by Gilbank et al. (2004) are used and the red sequences have similar colors for each of the projected cluster (see Figure 4.12). Using the SDSS multi-color photometry does not help because their uncertainties are larger at faint luminosities and the red sequences become completely blended. So, the contours plotted in each figure must only be taken as informative. Nonetheless, it is worth to note that many of the spectroscopic identified members are actually associated to structures that show up using this simple color cuts.

4.2.1 R220

The R220 field is a very complex field. There is a larger number of objects than in the other fields. This is maybe due to its lower galactic latitude. The photometric catalog was cleaned of star-like objects, however, the separation is not perfect and many of the slits contained not intended stars, losing the advantage of having an extra MOS mask for this field (8 instead of 7). The redshift distribution also looks more complex (see figure 4.1), with a number of associations besides the two clusters.

The cluster VMF194 was difficult to confirm optically by Vikhlinin et al. (1998) and collaborators. According to Gilbank et al. (2004), it is “a very extended X-ray emission and the galaxy over-density is similarly extended”. Here, VMF194 at $\langle z \rangle =$

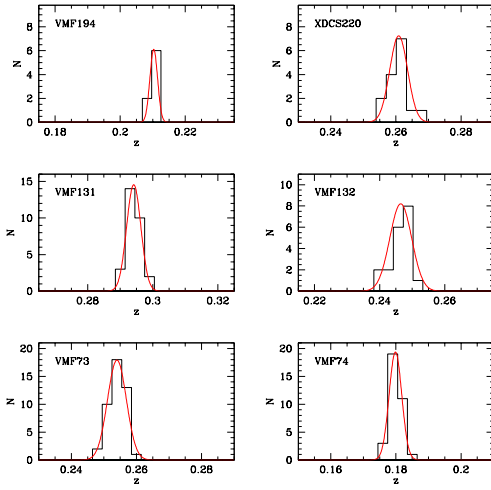


Fig. 4.2: Redshift histograms for each of the investigated clusters, binned at $\Delta z = 0.003$. The red solid curves are Gaussian profiles centered on the median redshift with σ equal to the velocity dispersion.

0.210 (see table 4.1) was unequivocally detected, but the data obtained showed that the cluster has a surprisingly low velocity dispersion for its X-ray luminosity (see figure 4.6). It may be entirely due to selection effects, since only 8 galaxies fall in the redshift range for this cluster. A red-sequence for elliptical galaxies was detected. Three additional galaxies have redshifts compatible with the cluster (within the previous $3\text{-}\sigma$ limits), but lie at very large radii ($> 7R_{\text{vir}}$). When they are included, the velocity dispersion does not change substantially, and thus they were excluded as members, but not included in the field sample (see §4.2.4).

The cluster cmJ172333+744410 at $\langle z \rangle = 0.261$ detected by Gilbank et al. (2004) was confirmed. Here, it is called XDCS220 for short. This cluster has a very low X-ray luminosity and passed undetected in the X-ray analysis of Vikhlinin et al. (1998) and Mullis et al. (2003). Surprisingly, it has a large velocity dispersion (see table 4.1), however, it is likely overestimated due to the existence of a tail in redshift space. Excluding the members which lie at large clustercentric distances does not change the biweight estimate of the velocity dispersion. So, it is possible that it is a real feature of the

cluster, maybe due to that it is in process of assembling or has an extended structure along the line of sight. This cluster shows a clear red-sequence and 5 out of 14 galaxies show on-going star-forming activity.

The contours shown in Figure 4.3 are clearly different for each cluster. VMF194 shows little substructure and the over-density appears offsets of the X-ray centroid. On the other hand XDCS220 shows an extended and irregular over-density in the central parts and several possible substructures in the outer regions. This reinforces the suspicion that it is a cluster in process of formation.

At an angular distance of ~ 4.4 arcmin from VMF194, a clump of galaxies at $\langle z \rangle = 0.243$ was detected. This clump also shows up in the spatial distribution: 8 out of 11 galaxies are clustered in an area smaller than $\sim 0.3 \times 0.7$ Mpc, so both structures almost overlap in the sky. The velocity dispersion of this group is $\sigma = 401 \pm 74$ km/s, which indicates that it is quite massive. No red-sequence was detected and 4 out of the 8 galaxies, show star forming activity. This group likely has been the cause of confusion in all previous studies in this field.

Two other group candidates have been found (see table 4.2), one at $\langle z \rangle = 0.04293 \pm 0.00136$ (390 km/s) with 6 members in 1 Mpc^2 (or 5 in 0.3×0.7 Mpc), all of them being star forming galaxies. The other is at $\langle z \rangle = 0.05274 \pm 0.000445$ (126 km/s), with four members in 0.3×0.4 Mpc.

4.2.2 R265

As reported in §2, the cluster VMF131 was observed in the central parts previously by Balogh et al. (2002a) as a part of their low luminosity X-ray cluster project (and there was known as CL1309+32), using the same instrument and setup, so that their data has been added into this study. This cluster is the most distant ($z = 0.294$) in the sample. The color contours shows little substructure around the cluster but the central over-density is clearly visible in Figure 4.4.

On the other hand, the cluster VMF132 does not show a strong galaxy concentration, despite being the richest cluster in the sample (measured by its X-ray luminosity) and has the largest velocity dis-

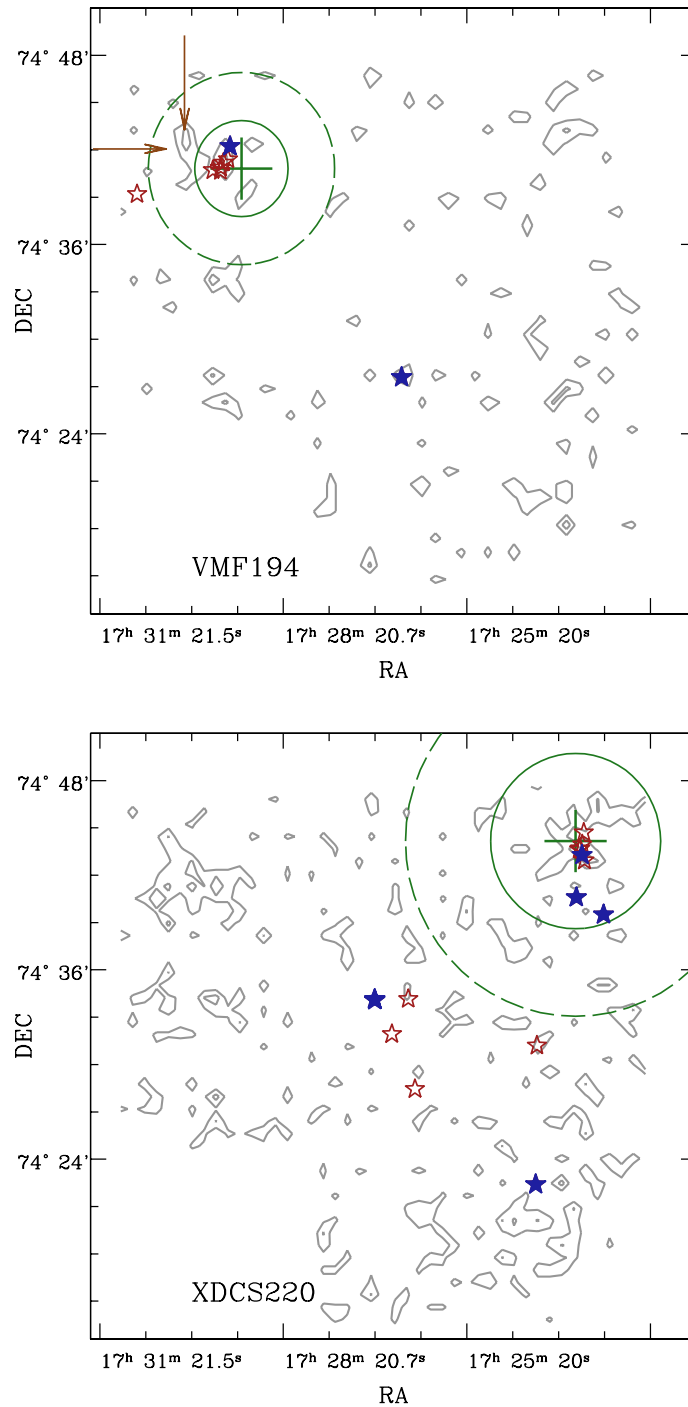


Fig. 4.3: Representation of the R220 field containing the clusters VMF194 (top) and XDCS220 (bottom). The filled blue symbols are star forming galaxies, whereas red open symbols are passive galaxies. The two large green concentric circles represent one and two virial radii respectively, and the vertical crosses the X-ray centroids. The contours show the distribution of all galaxies with colors similar to the respective red-sequence (see text).

persion (and thus the largest virial radii, occupying a large portion of the field). Only sparse and irregular structures are detected by the color cuts in Figure 4.4.

An extended group was also detected at $\langle z \rangle = 0.186 \pm 0.001185$ (349 km/s) with 8 members in an area of 1×2 Mpc, or 0.7×1.5 Mpc if one excludes one galaxy.

4.2.3 R285

The two clusters present in this field almost overlap in their positions on the sky (angular separation ~ 5 arcmin, see figure 4.5). In addition, more masks were placed in the central parts of the clusters, which led into a higher success rate compared with the other fields.

The cluster VMF73 at $z = 0.254$ has the largest number of members identified ($N = 44$). As a consequence of the mask setup, most of the identified members of this cluster are located inside $1 R_{vir}$. They are located in an elongated structure running in the East-West direction, which was also detected by the color cuts (see figure 4.5), despite the strong contamination due to the foreground cluster (VMF74).

There is strong evidence of a second significant structure at $R \sim 1 R_{vir}$. The position of this structure coincide with an extended X-ray source detected by Rasmussen & Ponman (2004) whose X-ray centroid is located at ($\alpha=09^h 43^m 58.5^s$, $\delta=+16^\circ 51' 17''$). At this position a compact group ($\sim 100 \times 100 \text{ kpc}^2$), composed of three bright red passive galaxies, is found. The general galaxy concentration is also higher around them.

The X-ray flux of this structure is $f_{X,1-2\text{keV}} = 3 \times 10^{-14} \text{ erg cm}^{-2} \text{ s}^{-1}$ (Rasmussen, private communication), which yields an X-ray luminosity of $L_{X,bol} = 1.38 \times 10^{43} \text{ erg s}^{-1}$, assuming that the X-ray structure is actually associated to the VMF73 cluster. This structure may be the center of a large, newly infalling group of galaxies, although no peculiarities were detected in the redshift distribution.

The cluster VMF74 has a surprisingly large number of star forming members: 19 out of 34, and many of them have colors similar to the red sequence (see figure 4.12). It is also the closest of

the clusters studied with a mean redshift of $z = 0.18$. The spectroscopically identified members are also distributed in an elongated structure in an almost North-South direction, although less significant than in VMF73. It also shows up using color cuts and the center of the cluster lies close to the extreme of the structure.

According to the *XMM*-Newton X-ray analysis of Rasmussen & Ponman (2004), both VMF clusters do not exhibit peculiarities and are fairly typical for their masses.

4.2.4 Field sample

The field sample consists of all galaxies between $0.15 < z < 0.35$, with at least $6\text{-}\sigma$ of distance from the mean cluster redshifts. The galaxies belonging to the suspected groups are also included (*i.e.* the two low redshift groups are excluded). That yields 90 galaxies. Since the sample is built using the same observations any comparison is straightforward.

4.3 DYNAMICAL PROPERTIES OF THE CLUSTERS

The fundamental parameter that describes the properties of cluster of galaxies is the mass. The cluster mass function and its evolution provide constraints on the evolution of large-scale structure and the cosmology that govern our Universe (for a review see Borgani 2006). For these reasons, over the last ~ 70 years (starting with Zwicky 1937), much effort has been spent measuring the mass of clusters using a number of techniques. These include: (i) dynamical methods applied on the galaxy distributions derived from redshift surveys, (ii) based on the distribution and temperature of the diffuse hot gas in the intra-cluster medium, observed at X-ray wavelength, (iii) gravitational lensing, and (iv) observations of the Sunyaev-Zeldovich effect.

The comparisons among those different methods have been a source of debate specially during the last decade, with agreements and differences up to 1 order of magnitude (*e.g.* Wu & Fang 1996, Smail et al. 1997, Girardi et al. 1998, etc) due to the different assumptions that each method makes.

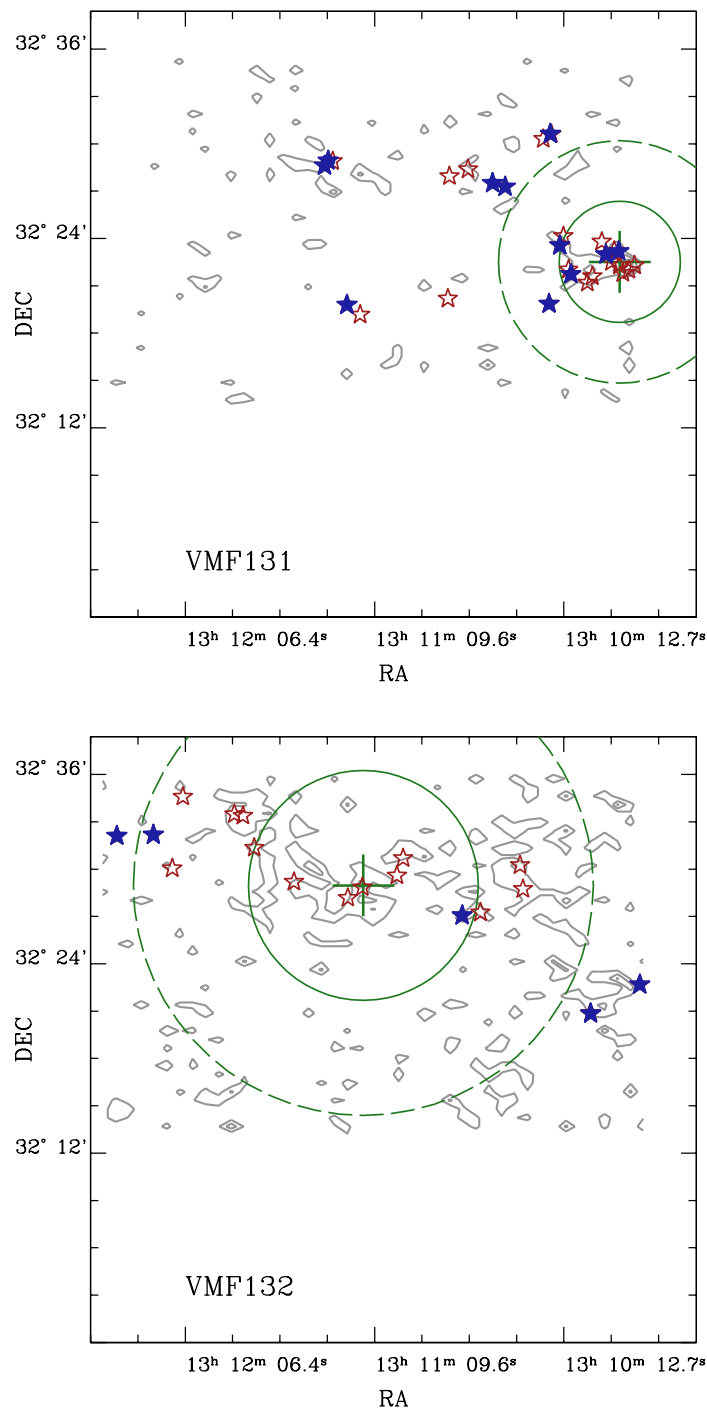


Fig. 4.4: Same as figure 4.3, on top is the VMF131 cluster, bottom VMF132.

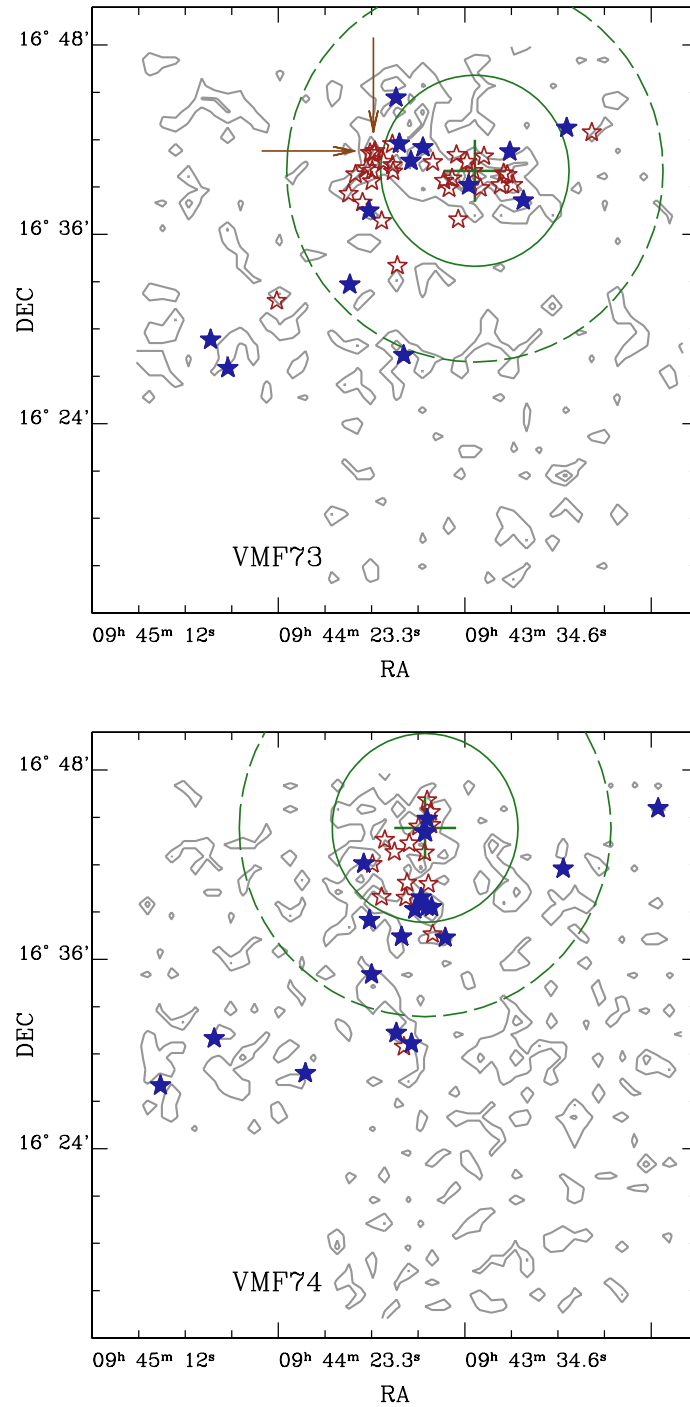


Fig. 4.5: Same as figure 4.3, on top the cluster VMF73 and at the bottom the VMF74 cluster. The arrows in the VMF73 plot indicate the position of the X-ray structure detected by Rasmussen & Ponman (2004) (see text).

Group candidate ID	$\langle z \rangle$	σ [km s ⁻¹]	N
r220_1J 172604+742830	0.053	126	4
r220_2J 172518+742844	0.043	390	6
r220_3J 172958+744204	0.243	401	8
r265_1J 131030+322840	0.186	349	8

Table 4.2: Main parameters for the groups candidates in the studied fields. Their identification codes show the average positions of the members. Mean redshifts (z) and average deviations are shown as velocities (σ). The biweight estimators were used only in groups with at least 8 members. The IDs have been constructed according to the suggestions of the International Astronomy Union (IAU).

However, some latest studies, like Hicks et al. (2006), seem to have solved the differences and have found that the correlation among different methods have little scatter, $M_{dyn}/M_X = 0.97 \pm 0.05$ and $M_{lens}/M_X = 0.99 \pm 0.07$ where M_{dyn} , M_X and M_{lens} are the masses determined via the velocity distribution of galaxies, X-ray analysis and lensing respectively. This has been possible thanks to the latest state-of-the-art instrumentation like large redshift surveys (*e.g.* CNOC, SDSS, 2dFGRS), more powerful X-ray telescopes (*e.g.* Chandra and *XMM-Newton*) and high resolution space based imaging (HST) coupled to deep multi-band photometry.

4.3.1 X-ray luminosities

This work does not have all of these advantages, however, one can be confident, in the light of these latest results, that assuming that clusters of galaxies are in dynamical equilibrium is not, in fact, a bad assumption, despite that they often show evidence of substructures (*e.g.* Ferrari et al. (2005)). In Figure 4.6 the relation between X-ray luminosity and velocity dispersion is shown and compared with the relation of Markevitch (1998), David et al. (1993) and Xue & Wu (2000) measured for $z \sim 0$ clusters. This relation is a test of dynamical equilibrium. Only the clusters in the R220 field are outliers in the relation with VMF194 having a velocity dispersion too low for its X-ray luminosity. As stated before, it may be due the low sampling of this cluster or due to a notable background structure that may have contaminated the X-ray measurements. On the other hand, XDCS220 has a luminosity too low for its velocity dispersion. It is likely not in dynamical equilibrium but in process of assembling.

The X-ray luminosities were taken from Mullis et al. (2003) who used ROSAT data (with the exception of XDCS220 which comes from the re-analysis of Gilbank et al. 2004) and were corrected by the cosmology used here². The fluxes, reported for VMF73 and VMF74 by Rasmussen & Ponman (2004) using the newer *XMM-Newton* mission, also agree within a factor of two with the previous measurements, although direct comparison is difficult because the different models, cosmology and passbands used to calculate them in the later study.

4.3.2 Virial radius

From the results shown in the previous section, it is possible to assume that the clusters sampled in this study are in general in dynamical equilibrium³ and therefore the virial theorem is applicable. The radius where the virial mass is contained is called virial radius. According to the observationally calibrated derivations of Carlberg et al. (1997a) based on a subset of well sampled CNOC clusters, R_{vir} is defined as the distance where the mean inner cluster density is 200 times the critical density $\bar{\rho}(z)$ of the Universe at a given epoch and thus is often called r_{200} . The $200\bar{\rho}(z)$ is the ‘‘critical’’ density for spherical collapse at redshift z and virialization is predicted by models during a Hubble time (Eke et al. 1996). The virial radius r_{200} can be calculated using the velocity dispersion σ using

²They used $H_0=50 \text{ km s}^{-1} \text{ Mpc}^{-1}$, $\Omega_\lambda=0$, and $\Omega_m=1$

³It is probably not true for XDCS220, however for the sake of comparisons it will be assumed that it is. VMF194 is also peculiar, but the differences may arise from other sources.

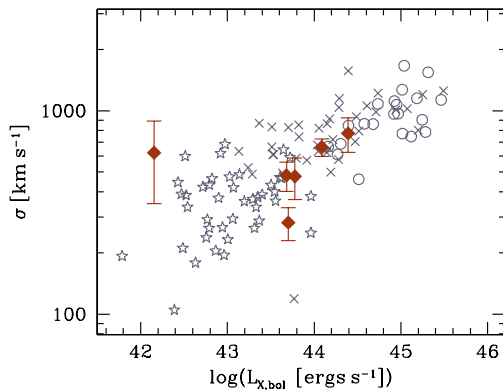


Fig. 4.6: Bolometric X-ray luminosity plotted against velocity dispersion. Open circles (Markevitch 1998), crosses (David et al. 1993) and stars (Xue & Wu 2000) represent the $L_x - \sigma$ relation for local clusters. The six cluster studied here are plotted as diamonds with error bars in the velocity dispersion. Note that, four cluster match quite well the relation, whereas other two (both in the R220 field) do not, being under- and over-luminous for their velocity dispersion. However XDCS220 is the most striking given its large velocity dispersion (see text for a detailed discussion).

$$R_{vir} = r_{200} = \frac{\sqrt{3}}{10} \frac{\sigma}{H(z)} \quad (4.5)$$

where $H(z) = H_0 \sqrt{\Omega_m(1+z)^3 + \Omega_\Lambda}$ with a Hubble constant of $H_0 = 70 \text{ km s}^{-1} \text{ Mpc}^{-1}$ and $(\Omega_\Lambda, \Omega_m) = (0.7, 0.3)$. The density $\bar{\rho}(z)$ can be derived from cosmology models, but direct calculation of r_{200} has proved more difficult and all methods are based in different assumptions. In particular, the dynamical derivation here used is based in the assumption of an universal density profile (see also Girardi et al. 1998 for a slightly different result). Nevertheless, r_{200} correlates very well with other parameters like richness measured via similar dynamical methods (Becker et al. 2007) or weak-lensing analysis (Johnston et al. 2007).

Since r_{200} characterizes the size of clusters in the assumption of a universal mass profile, it is useful to define an environmental parameter given the clustercentric distances of cluster galaxies. Therefore, the distances of galaxies to the center of the cluster are normalized by their respective virial ra-

dius. In such way it is possible to combine the whole sample into an assembled cluster, increasing the statistic significance and erasing cluster-to-cluster variations.

4.3.3 Projected density

Another usual indicator of environment is the local number projected (2-D) density of galaxies. Its calculation does not assume any physical properties of the clusters, but other precautions must be taken. First, the galaxy number density is a function of luminosity. The spectroscopic limit of $I \approx 19.5$ mag corresponds to $M_I \approx -21.4$ for the furthestmost cluster ($z \approx 0.3$) and $M_I \approx -20.2$ for the closest one ($z \approx 0.2$), taking in consideration the typical k-corrections (e.g. Fukugita et al. 1995). So, for each cluster, the photometric catalog was cut using an apparent magnitude that corresponds in average, to the luminosity limit of the farthest cluster, which translates in an apparent magnitude cut of $I \approx 18.3$ at $z = 0.18$ (see Figure 4.12).

The projected density is defined by the area that encircles the fifth nearest neighbor to this galaxy (hence is called Σ_5). However, significant foreground and background contamination is expected and must be corrected before making any statistics. In the literature, several methods of different complexity are described to deal with this problem. Most of them subtract a value (local or global) from the calculated density, making different assumptions. However, those methods often yield unphysical values (i.e. negative numbers) for the density estimates. This case is even more complicated, because besides the field contamination, there is contamination from the other projected cluster. Therefore, another approach was chosen using in combination the photometric and spectroscopic data-set.

If the *true* number density of galaxies in a certain region of the cluster is N (unknown) and the observed one is M , determined from the photometric catalog and including the contamination, one has a relative fraction of $f = N/M$. From the spectroscopic dataset is known that there are n galaxies belonging to the cluster and m is the number of total observed galaxies in the same area with secured redshifts. Since the selection was performed randomly (based only on I -band magnitudes), it is

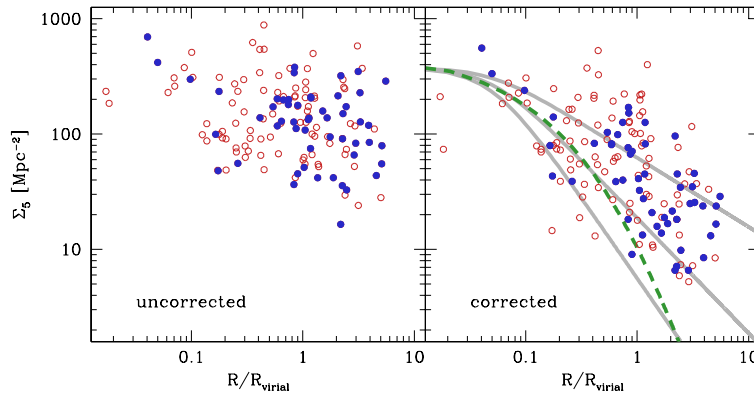


Fig. 4.7: Relation between normalized clustercentric distances and projected density before and after correction for field contamination. Once the correction is made, a tighter relation appears between the two quantities (the right plot), albeit the large dispersion. The open red circles are passive galaxies, whereas filled blue circles are star-forming galaxies. The grey solid lines are King-like profiles and the dashed green line is Hernquist profile (see text for details).

possible to assume that the same fraction now is expressed by $f = n/m$, thus, the observed value M can be corrected, multiplying it by n/m , obtaining as a result N .

The areas used to make these corrections are larger than the areas considered by the individual density calculations. They always encircle 10 galaxies with secured redshifts, and there the number of cluster members versus the non-cluster galaxies is counted. Having a high filling factor helps to the statistical reliability of this simple method, because the areas sampled will have smaller physical sizes, thus smaller deviations from the local density. The results of the correction can be seen in figure 4.7. After this process a correlation between virial radius and projected density becomes evident. Different theoretical density profiles are plotted as comparison.

It is necessary to stress that the densities calculated here and elsewhere are not directly comparable, because the magnitude cuts and approaches to subtract the background are varying among different authors.

Finally, galaxies fainter than the individual cluster magnitude cut were not included in the composite cluster, reducing the sample to ~ 120 galaxies.

The results shown in Figure 4.7 display good

matches with King-like profiles (King 1962) which are described by:

$$\Sigma(R) = \frac{\Sigma_0}{\left[1 + (R/R_C)^2\right]^\alpha} \quad (4.6)$$

where Σ_0 is the central density and here the average density for $R < 0.1R_{vir}$ is used. R_C according Girardi et al. (1998) is $0.005R_{vir}$. The exponent α takes the values 0.3, 0.5 and 0.7, with lower values yielding shallower profiles.

However, Carlberg et al. (1997a) derived r_{200} using instead a profile with the following form:

$$\Sigma_N(R) = 2 \int_R^\infty v(r) \frac{r}{\sqrt{r^2 - R^2}} dr \quad (4.7)$$

with

$$v(r) = \frac{A}{r(r+a)^\alpha} \quad (4.8)$$

the volume density model. The parameter A is made again to match the average central density and a varies between 0.56 and 1.82 for different

galaxy populations with a mean of $a = 0.66$ for the whole CNOC sample (Carlberg et al. 1997c), which is the value here taken.

The different values of α are used to describe the Hernquist profile ($\alpha = 3$, used by Carlberg et al. 1997a) or the NFW profile ($\alpha = 2$, Navarro, Frenk, & White 1996). Here $\alpha = 3$ is taken, although this particular choice is not critical. This profile describes fairly well the combined cluster used by Carlberg et al. (1997a), but their coverage at large radii is poor and here clearly deviates at $R > 1R_{\text{vir}}$.

It is interesting to note that although the density calculation does not assume any theoretical profile, it matches those predicted by different authors.

4.3.4 Velocity dispersion profile

Both, Girardi et al. 1998 and Carlberg et al. 1997b made extensive theoretical and observational analysis of the mass distribution of clusters. Amongst their findings is the almost-universal radial velocity dispersion profile found in clusters (the trumpet profile, Diaferio 1999), where the cluster galaxies are well isolated in the velocity space from the surrounding velocity field. In Figure 4.8 the peculiar velocity (Δv) of each galaxy, with respect to the cluster mean, is normalized to the cluster velocity dispersion and plotted against normalized clustercentric distances. The contours are the results from the cluster mass models of Carlberg et al. (1997a):

$$\sigma_p^2(R)\Sigma_N(R) = \int_R^\infty v(r)\sigma_r^2 \left(1 + \beta \frac{R^2}{r^2}\right) \frac{r}{\sqrt{r^2 - R^2}} dr \quad (4.9)$$

where $\sigma_p(R)$ is the projected velocity dispersion in function of radius (an observable quantity which here is modeled for comparison), β is the anisotropy parameter, with $\beta = 0$ for an isotropic velocity distribution. $\Sigma_N(R)$ is the projected number density profile as equation 4.7 and $\sigma_r(R)$ is the radial velocity dispersion which is modeled as following

$$\sigma_r^2 = \frac{B}{b+r} \quad (4.10)$$

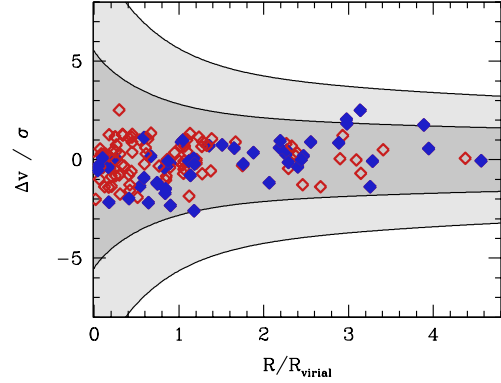


Fig. 4.8: Normalized peculiar velocities versus normalized clustercentric distances for the assembled cluster. The contours are the $3\text{-}\sigma(r)$ and $6\text{-}\sigma(r)$ Carlberg et al. (1997a) cluster mass models (see text).

with B and b adjustable parameters. Carlberg et al. (1997a) used $B = 1/4$ and $b = a$.

The galaxy distribution in this plane is in general quite regular with only few galaxies close to or outside of the $3\sigma(R)$ limits. Those galaxies are expected to be new members of the clusters and probably in process of infall. However, the results based on this diagnosis can not be used to determine the abundance of this population due to its high degeneracy and because it assumes spherical symmetry.

4.3.5 Probing substructure with dynamics

In §4.2 was described that some substructures were detected via color cuts, which show the distribution of galaxies with colors similar to the red sequence ellipticals of the cluster. The main advantage of this method relies in the large number of objects to select, gaining signal. However, it has many disadvantages, as strong contamination due to un-associated fore- and background galaxies in a wide redshift range can not be easily removed. Also, since it is designed to detect elliptical galaxies, structures mainly composed of star-forming galaxies are missed, which is particularly important since at least the $\sim 60\%$ of the galaxies at intermediate redshifts are active (e.g. Hammer et al. 1997).

The ‘‘anomalies’’ detected in the previous test on

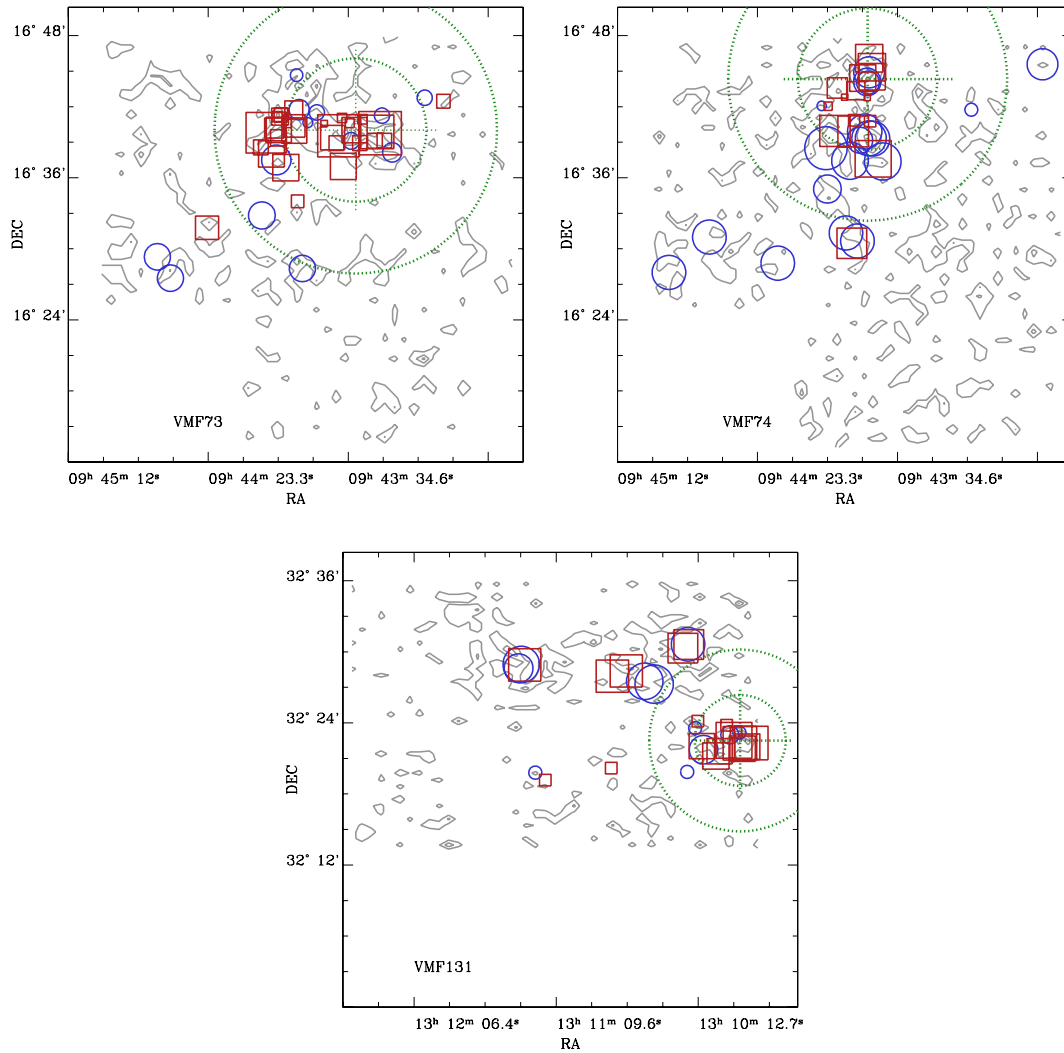


Fig. 4.9: Dressler-Shectman plots for the clusters VMF73, VMF74 and VMF131. The red squares represent passive galaxies and the blue circles are galaxies with detected star-forming activity. The size of the symbols indicates the deviation from the local mean velocity.

the radial distribution of peculiar velocities, likely indicate the presence of dynamically distinct structures. In order to verify this in particular clusters a Dressler-Shectman test was performed (D-S, Dressler & Shectman 1988). This test is based on the following statistics:

$$\delta^2 = \frac{11}{\sigma^2} \left[(\bar{v}_{local} - \bar{v})^2 + (\sigma_{local} - \sigma)^2 \right] \quad (4.11)$$

where line-of-sight velocity \bar{v}_{local} and dispersion σ_{local} are measured with respect to each galaxy's ten nearest neighbors, and \bar{v} and σ are the global cluster values. This statistic measures each galaxy's local deviation from a smooth, virialized velocity and spatial distribution.

Only three clusters are expected to have enough identified members to perform this statistic with significance, since it is required to use ten neigh-

bors to gain enough signal. However, for the most isolated galaxies the local mean velocity can not be measured reliably, and therefore the statistics have little meaning.

In Figure 4.9, the position for all galaxies are plotted. The size of the symbols is related to the value of δ . A single large symbol does not indicate anything statistically significant, but groups of large symbols may indicate the presence of sub-clustering in velocity or dispersion.

It is interesting to note that VMF73, despite of having evidence of substructure (in X-ray and photometry, §4.2.3), does not clearly show it in dynamics, with few galaxies with large symbols in the central well-sampled regions. Perhaps, the notable substructure at the east of the cluster center is heading in a direction perpendicular to the line of sight and thus, will not be detected by this test.

On the other hand, VMF74 shows evidence of many galaxies with δ greater than the central ones. All of them are clustered in the southern region of the main structure defined by the color cuts at a distance of $R \sim 1R_{vir}$. Most of them are also star-forming galaxies.

Little can be said about VMF131. The central regions are well covered, but no systematics are detected. The outer galaxies are too sparse distributed and their δ indicate mostly separation from the main cluster body and not necessarily substructure.

4.4 SPECTROPHOTOMETRIC PROPERTIES OF THE CLUSTERS

4.4.1 Luminosity distribution

The luminosity distribution for cluster and field galaxies in rest-frame B and R bands is shown in Figure 4.10. These two bands are important because they will be used to derive star-formation rates in combination with emission line strengths (§6). As can be seen, both the cluster and the field sample have similar distribution on magnitude, making both of them effectively comparable.

The absolute magnitude distribution peaks at

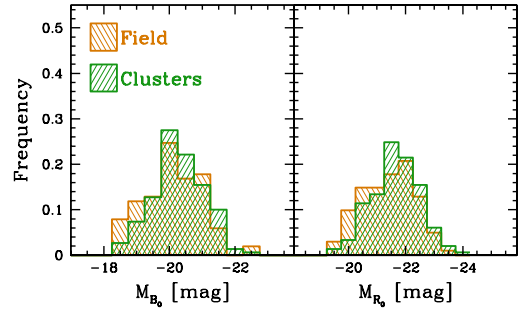


Fig. 4.10: Absolute magnitude distribution in rest-frame B and R for field and cluster galaxies as indicated.

$M_B \approx -20$ and $M_R \approx -21.5$. Since a L^* galaxy at the mean redshift has an absolute magnitude of $M_{B,z=0.25}^* \approx -21.0$ and $M_{R,z=0.25}^* \approx -22.35$ (Gabasch et al. 2004 and Ilbert et al. 2005), the sample is not strongly biased towards high mass galaxies and sample a wide range of galaxy types.

In Figure 4.11, the B -band absolute magnitude versus redshift is plotted. The lower luminosity cutoff is increasing towards higher luminosities as expected from an apparent magnitude limited sample. However, the sample is basically “complete” for magnitudes $M_B \lesssim -20$. The lower magnitude end increases about 1 mag for galaxies of clusters at different redshifts, and ~ 1.5 mag for field galaxies (given their larger redshift span). However, as was pointed out in Figure 4.10, the effects are compensated and both distributions match quite well.

4.4.2 Color-magnitude diagram

In the Figure 4.12 the I versus $V - I$ color-magnitude diagrams for cluster galaxies are plotted. The passive cluster galaxies are distributed in a tight sequence called the red-sequence (or color-magnitude relation, CMR) which was first noted by Baum (1959) and it has been observed in every galaxy cluster so far observed, even at redshifts $z > 1$ (e.g. Mei et al. 2006, Demarco et al. 2007).

⁴ L^* defines the “knee” or turnaround of the galaxy luminosity function, beyond which the number density of galaxies fall sharply. Since the luminosity function and its evolution probes the galaxy mass assembly, the L^* luminosity sets a limit between bright and faint galaxies. For a review, please see Binggeli et al. (1988).

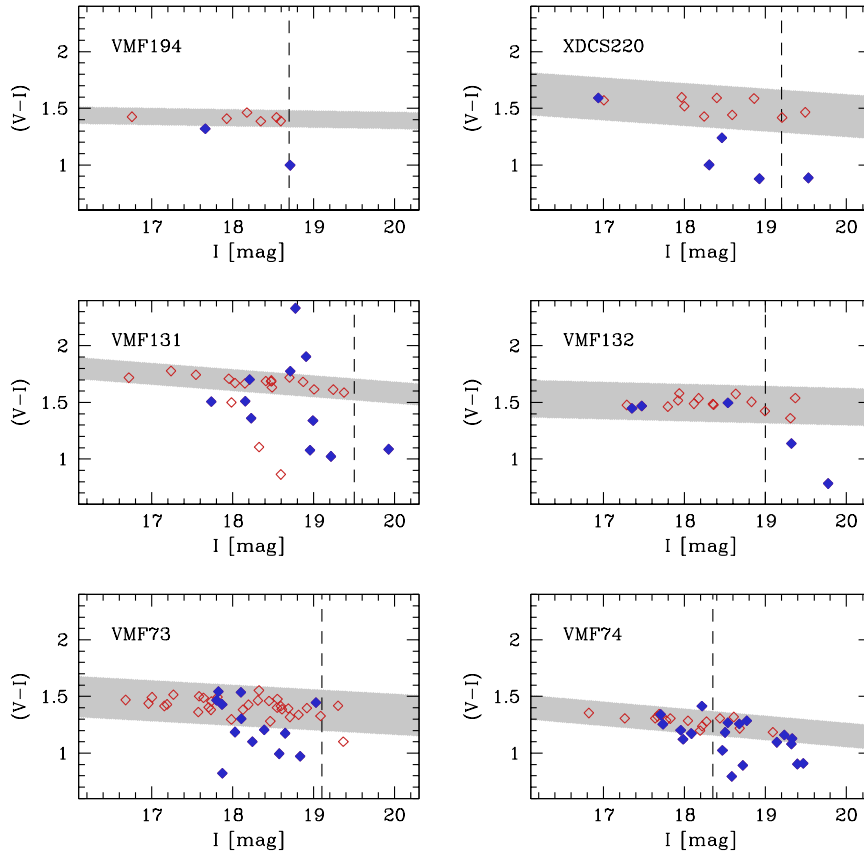


Fig. 4.12: Color-magnitude diagrams for the cluster galaxies. Filled blue diamonds are star-forming galaxies, whereas open red diamonds are passive galaxies. Simple least squares fits were attempted to the red sequences, and the $3\text{-}\sigma$ deviation are shown as a grey shaded region. The weighted mean dispersion of the red-sequence is $\sigma \approx 0.05$ magnitudes. The vertical dashed lines mark $M_I \approx -21.4$ mag used in the density calculation (see §4.3.3). Note the red star-forming galaxies belonging to the red-sequence and even redder in some of the clusters.

The CMR is also present in the field but the number density of early types is not as high as in galaxy clusters and only rises up in large surveys (*e.g.* Strateva et al. 2001). Thus, the red-sequence is a useful tool for detecting cluster of galaxies via over-densities in a color-positions space (Gladders & Yee 2000, Gilbank et al. 2004).

The uniformity of the properties of the red-sequence has been motivated controversy during several years. In this relation, bright galaxies are redder than fainter ones and this relation extends

over a wide range of galaxy luminosities⁵. There is little variation of CMR in colors, slope, scatter for different clusters and look-back times.

Now, it is widely recognized that the slope of the red-sequence can be reproduced as a metallicity sequence with bright galaxies being more metal rich than fainter ones (Arimoto & Yoshii 1987, Kodama & Arimoto 1997), and their uniformity can be explained by an efficient episode

⁵For instance the red sequence extends 8 magnitudes (a factor 10^3 in luminosity) in the Virgo and Coma cluster (*e.g.* Sandage 1972, Thompson & Gregory 1993).

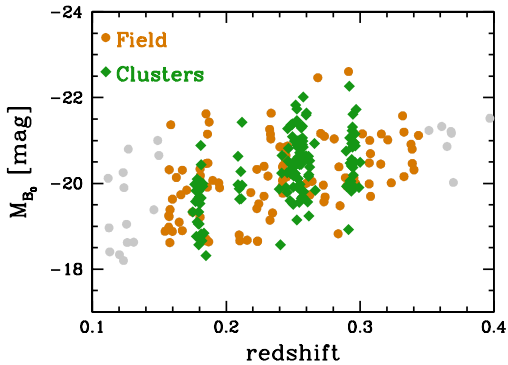


Fig. 4.11: Redshift versus absolute magnitudes for field and cluster galaxies as indicated. The grey dots indicates galaxies outside of the limits of the sample.

of star-formation that occurred at high redshift ($z > 2$) and since then they have evolved passively (Bower et al. 1992). However, recent studies at moderated redshifts ($z < 1$) show evidence of a later build-up of “dwarf” red-sequence galaxies, which have arrived there only recently (e.g. Cucciati et al. 2006, Tran et al. 2007).

The slope and the scatter of the red-sequence may also give clues about the star-formation history of red galaxies and thus of the assembly history of the clusters that host them (Gladders et al. 1998), where larger scatter and steeper slopes indicate younger and older ages respectively (and vice versa).

The red sequence of the clusters studied here are well described by a simple least-square lineal fits to the *passive* galaxies ($W_0([\text{O II}], \text{H}\alpha) < 5 \text{ \AA}$) with their $3\text{-}\sigma$ limits shown as shaded areas in figure 4.12. This allows to classify the galaxies into two types, being *red* galaxies, those with colors as red as the red-sequence (within the $3\text{-}\sigma$ limits) or redder and *blue* galaxies, those with colors bluer than the previous criterion. The scatters of the red sequences are comparable to the error in the photometry ($\sigma \approx 0.05 \text{ mag}$). It is interesting to note that every cluster displays different slope and scatter, and the mean colors are not fully compatible with the cosmological reddening, suggesting a different assembly history.

The small scatter of the red-sequences allows to select galaxies in a narrow redshift range (contam-

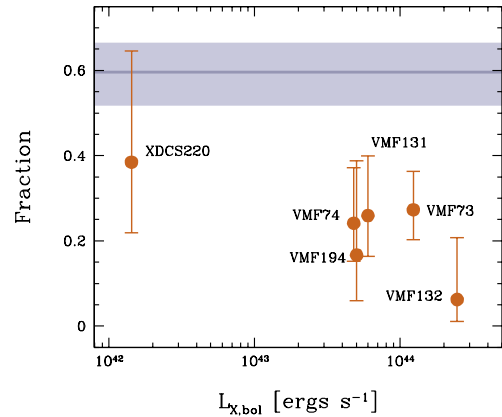


Fig. 4.13: Fraction of star-forming galaxies in each cluster versus bolometric X-ray luminosity as measured with an aperture of $2R_{\text{vir}}$. Note the high fraction in the cluster VMF74 approaching to the field value (shaded area). The error bars are Poisson distributed errors according to the recipes of Gehrels (1986).

ination of course does occur), making possible to create the density maps depicted in Figures 4.3, 4.4 and 4.5.

It is noteworthy the presence of a population of star-forming galaxies belonging to the otherwise passive red-sequence of ellipticals. Most striking is the high number of those galaxies belonging to the cluster VMF74. Some of the characteristics of this sub-population will be described in §6.3.

4.4.3 Fraction of star-forming galaxies

Clusters of galaxies have been historically classified by their optical richness, with those with higher richness being more centrally concentrated and dominated by passive galaxies, and clusters of low richness have a non-depreciable fraction of spiral galaxies (Morgan 1961, Abell et al. 1989). Since galaxy morphology correlates with spectral properties such as star formation activity, and cluster richness correlates with mass, it would be expected that clusters of lower richness display a higher star-formation activity.

The star-formation activity inside of clusters is strongly depleted in comparison to the surround-

ing field at all redshifts (*e.g.* Balogh et al. 1999, Poggianti et al. 2006), however its relation with global cluster properties have often led to conflicting conclusions. In particular, no dependence has been found on the blue galaxy fraction in clusters on cluster velocity dispersions and masses (Goto 2005), nor of the blue fraction with cluster richness, concentration, and degree of sub-clustering (De Propriis et al. 2004).

Goto (2005) has also claimed no dependence on the cluster velocity dispersion and masses of either the total cluster star-formation rate (SFR) or of the total cluster SFR normalized by the cluster mass, in disagreement with Finn et al. (2005), who have shown that the integrated SFR per cluster mass decreases with increasing cluster mass. Wake et al. (2005) have also failed to find any dependence of the fraction of blue cluster galaxies with the cluster X-ray luminosity, L_X . Similarly, Balogh et al. (2002a) have compared the galaxy SFRs in high- L_X and low- L_X clusters and have found no differences. Poggianti et al. (2006), on the other hand, have found that the fraction of emission-line galaxies decreases with increasing cluster velocity dispersion and it also evolves with redshift.

On the other hand, Nakata et al. (2005) have shown that the fraction of star-forming galaxies per cluster has little evolution with redshift, but the cluster-to-cluster scatter is very large and may bias the conclusions. In order to avoid the limitations of similar studies Popesso et al. (2007) used a regression analysis to identify the principal correlations. They found that the cluster properties do not affect the SFR per unit of stellar mass, but the fraction of blue galaxies does show a correlation with velocity dispersion.

All the studies mentioned above noted the large scatter cluster-to-cluster in all of the important parameters, making many of the correlations very weak. This, however, indicates that, despite the finding of some authors, the global cluster properties unlikely affect strongly the properties of galaxies that they host and the scatter is maybe due to more subtle properties like assembly history and large scale environment.

Although, this study has not been designed to investigate this issue, it is illustrative to see which is the fraction of star-forming galaxies per cluster.

This is shown in Figure 4.13 against X-ray luminosity. The fraction of star-forming galaxies has been measured with a fixed aperture of $2R_{vir}$ of radius, larger than the previous studies. Despite the larger aperture sampled in this the values reported here are similar to those found by Balogh et al. (2002a).

With the exception of XDCS220, all clusters are strongly depleted in comparison to the field. One could be tempted to trace a line that would join much of the points, since the brightest X-ray cluster displays the lowest star-forming fraction and the peculiar XDCS220 display the largest. Clusters in between have mid values. However, this can also be due to the afore mentioned scatter rather than a true correlation.

Environment and star-formation activity

As mentioned in the previous chapter, many studies to the date have failed in detecting any correlation between star-formation activity and global cluster properties. The few studies that have detected such correlation, show that it is very weak and has a large scatter. Whether the global cluster properties affect or not the properties of the galaxies that inhabit them, is still matter of controversy, however, any influence is likely weak and perhaps linked to more fundamental relations.

The proposed processes associated to the decline of the star-formation activity are strongly environment dependent, *i.e.* they are effective over a certain threshold of mass density, traced for example by the galaxy concentration. The outcome of these processes varies with the different scenarios (see §1.5). It is necessary to note that probably many of those processes may be active in the cluster environment. This has made the identification of the the most dominant one, difficult, despite the large observational and theoretical effort spent during the last ten years.

The environmental relations of star-formation activity, colors and galaxy morphologies are already well established (see §1.3 for a summary of the most important findings). They have been studied in the local universe by large extragalactic surveys like SDSS or 2dFGRS from the densest regions to the galaxy voids (see Haines et al. 2007 for one of the latest and most comprehensive studies), at higher redshift in clusters (*e.g.* Balogh et al. 1999, 2002a, Ferrari et al. 2005, Poggianti et al. 2006, Sato & Martin 2006b) or in

the low density field in deep redshift surveys (*e.g.* Hashimoto et al. 1998, Gray et al. 2004, Cooper et al. 2006, Franzetti et al. 2007).

The study presented in this thesis aims, for the first time, to study the transition region between the cluster and the field environment at a cosmic significant epoch (~ 3 Gyr of look-back time). At this time, the galaxy infall rate is thought to be about 30–50% larger (Bower 1991, Bower et al. 1998) and therefore cluster-specific interactions were probably more frequent. This increases, in principle, the chances of observing the responsible processes.

In this chapter, the relation between star-formation activity and environment will be studied. The environment will be characterized by cluster-centric distances normalized to the respective cluster virial radius (R_{vir} , see §4.3.2) and the projected density to the fifth nearest neighbor (Σ_5 , see §4.3.3). As shown in Figure 4.7, both quantities are correlated, albeit a large scatter. It can be due to the assumed spherical symmetry in the calculation of R_{vir} , the existence of over-densities at large cluster-centric distances and errors associated to the background correction in the projected density calculation.

All galaxies are combined as they were in a single cluster in order to increase the statistical significance of the trends. Afterwards this sample will be splitted according to different criteria to study particular effects.

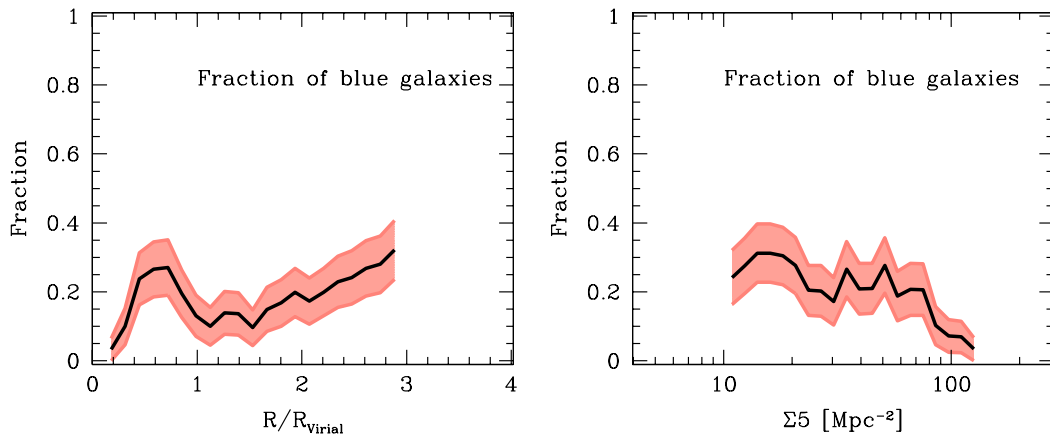


Fig. 5.1: Fraction of blue galaxies versus normalized clustercentric distance and projected density.

5.1 GALAXY COLORS AND ENVIRONMENT

The integrated galaxy color is an indicator of the galaxy stellar populations and thus has been widely used to investigate the evolutionary stage of galaxies. However, the exact parameters are difficult to obtain from the observationally cheap broad-band optical colors due to the strong degeneracy in age, metallicity and dust that produce overlapping effects (Worthey 1994). This problem has been partially solved by observing in multiple photometric bands and including the ultraviolet, infrared and narrow bands in combination with the latest *state-of-the-art* stellar population models (e.g. Bruzual & Charlot 2003).

Although broad-band optical colors can not be used to extract exact parameters of galaxies, it is now clear that galaxies follow an evolutionary sequence evolving from the “blue cloud” to the “red sequence” (e.g. Bell et al. 2004, see also Figure 4.12). Galaxy colors correlate strongly with environment according to the large SDSS-based studies of Blanton et al. (2005) and Hogg et al. (2003) and show strong bimodality (e.g. Balogh et al. 2004b). They were also used for the first time to explore the evolutionary stage of distant galaxies by Butcher & Oemler (1978), leading to the discovering of the controversial Butcher-Oemler effect, which is the observed increase of the fraction of blue galaxies in clusters with increasing red-

shift and it is often interpreted as an increase of the star-formation activity in cluster with redshift (see §1.4.2 for a detailed discussion of this effect).

The environmental dependence of mean colors has been also explored in the distant universe. For example, Kodama et al. (2001) have investigated the blue fraction and mean galaxy color with environment in a $z = 0.41$ cluster, at large distances from the cluster core. Similarly, Tanaka et al. (2005) have focused in the environmental build-up of the red-sequence, comparing two clusters at different redshifts ($z = 0.83$ and $z = 0.55$).

The main caveat of these studies is that they are based solely in broad-band photometry and the membership to the cluster is estimated via probability. This is not a serious issue in the dense central regions of clusters, but is an important problem for the sparsely populated cluster outskirts, where the effects of the contamination are stronger.

Here, the fraction of blue galaxies is investigated in function of environment for *confirmed* cluster galaxies at large cluster-distances and low projected densities. As stated in §4.4.2 a galaxy is considered “blue” if it is bluer than the cluster red-sequence (within the $3\text{-}\sigma$ limits) and “red” otherwise (see Figure 4.12). The results are shown in Figure 5.1.

The fraction of blue galaxies increases in both cases towards large radius and low density regions. A noticeable peak in the fraction of blue galaxies is observed at $R \sim 0.6R_{vir}$. Also, the fraction of blue

galaxies is strongly depleted at $\Sigma_5 \approx 100$ galaxies Mpc^2 , in agreement with Kodama et al. (2001), although it was not possible to test the trend much further of this limit.

Both trends are very similar in shape to the fraction of star-forming galaxies calculated using emission lines as indicators of star-formation activity (Figure 5.2), which should not be surprising since bluer colors often reflect the presence of young stellar populations. However, there is an important fraction of star-forming galaxies with red colors which, in principle, could break down the previous relation. This will be investigated further in the forthcoming sections (see §6.3).

It is important to note that the blue fraction is in average galaxies less than $\sim 30\%$ of the cluster population at $R < 1R_{\text{vir}}$. This result is affected by the peak detected at $R \sim 0.6R_{\text{vir}}$, therefore is an upper limit, however, this is in agreement of what is expected due to the BO effect at those redshifts (Ellingson et al. 2001).

5.1.1 The sliding bins method

The fraction of blue galaxies was calculated over the N nearest galaxies at each point in the plane, *i.e.* inside a moving box centered at each point with a fixed number of elements. Making N too small increase the noise, making it too large shorten the dynamical range covered, because this method truncates the extremes of the lists. It was found that using the nearest 15–25 points is a good compromise between spatial coverage and stability.

In order to check the statistical significance, a bootstrap technique was applied to each box with 2000 iterations, taking the mean and the standard deviation of the bootstrapped values (checking previously if the distributions are compatible with Gaussian) as the final values and their errors respectively.

This procedure is computationally intensive, but it makes the results more robust, because noise can increase or decrease as one includes more or fewer points in the calculations, but the overall shapes of the curves do not change as in the case of choosing arbitrary bins. This method allows to detect small scale variations, for example due to substruc-

ture which can be erased by binning or lead to a misinterpretation of the trends. The bootstrapping method helps to characterize the confidence region, even in the case of unlikely distributions.

This procedure is applied for all similar statistics derived in this thesis (*e.g.* the mean), unless otherwise stated. This method is a variation of the technique used by Balogh et al. (2004a) to create contour plots in a project aimed to study the star-forming properties of galaxies in the local universe.

5.2 STAR-FORMATION VIA EMISSION LINES

Among the star-formation indicators, emission lines are considered very reliable, because they are very sensitive to the ionizing radiation coming from newly formed hot stars (Kennicutt et al. 1994, Kennicutt 1998, Kewley et al. 2004, see §6). So, here the dependence of the star-formation activity on environment is studied using the $[\text{O II}]$ and the $\text{H}\alpha$ emission lines.

In Figure 5.2 the fraction of the star-forming galaxies¹ and the mean equivalent widths of $[\text{O II}]$ and $\text{H}\alpha$ are plotted against normalized clustercentric distances and projected density, respectively, using the method outlined in §5.1.1. Since the detection of emission lines has no dependence on redshift, it is possible to compare the statistics directly with the field sample², applying the same magnitude criteria using for the clusters, *i.e.* a magnitude cut of $M_I \approx -21.4$. However, changing the magnitude cut had little impact in the field statistics, typically $< 5\%$.

The shape of the curves are very similar to those observed in Figure 5.1, both steadily increasing towards large clustercentric distances and low projected densities. The peak at $\sim 0.6R_{\text{vir}}$ is also observed.

In both cases, the fraction of star-forming galaxies is strongly suppressed in the densest regions with less than 20% of the galaxies showing active star-formation. At $R \approx 3R_{\text{vir}}$ the star-forming frac-

¹*i.e.* $W_0([\text{O II}], \text{H}\alpha) > 5 \text{ \AA}$, see §3.4.

²The position of the red-sequence cannot be determined with reliability for the different redshifts that span the field sample, thus this comparison is not possible to make in §5.1.

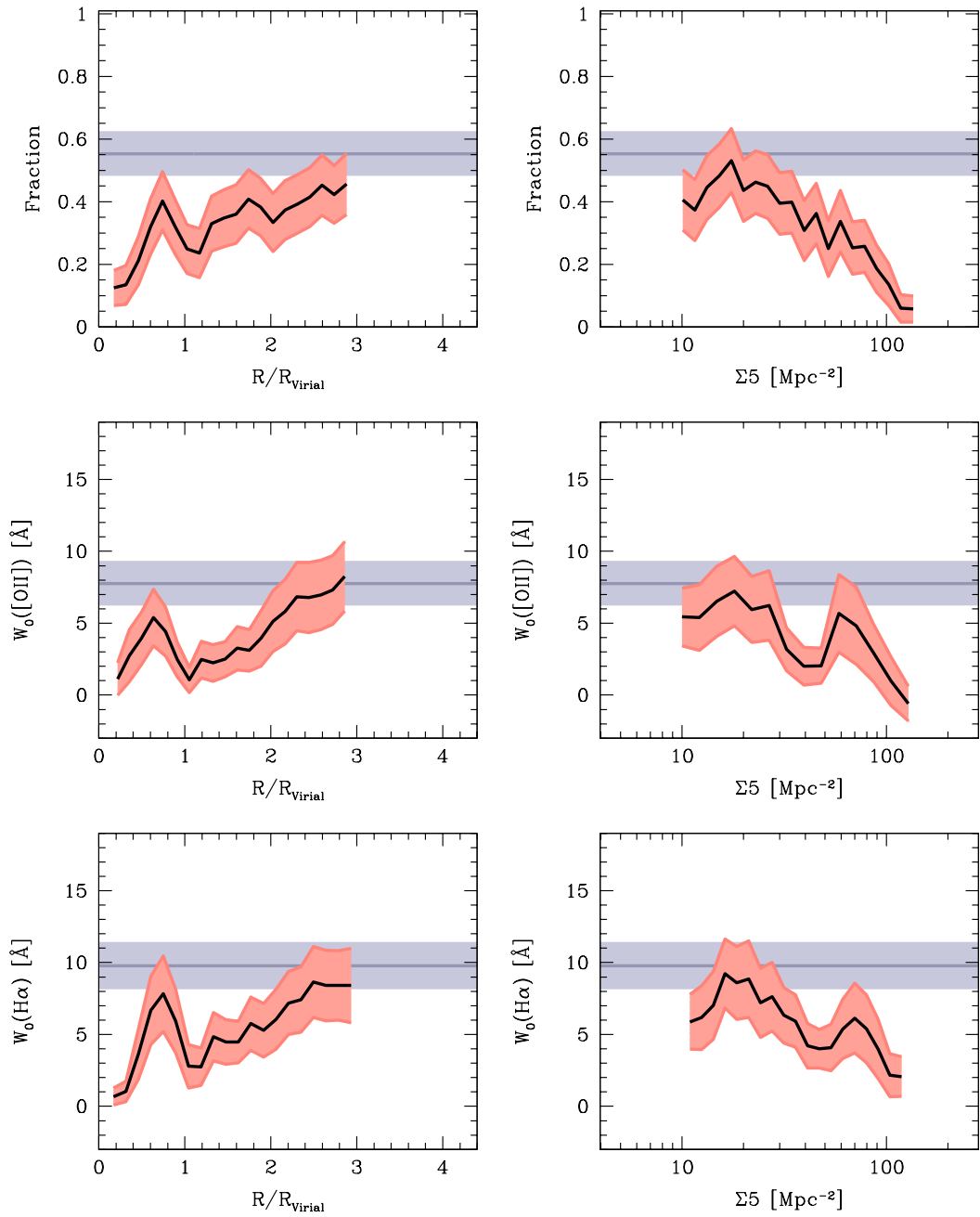


Fig. 5.2: Fraction of star-forming galaxies (top panels) and mean equivalent width of [O II] (middle panels) and H α (bottom panels) against normalized clustercentric distances (left panels) and projected densities to the 5th neighbor (Σ_5 , right panels), plotted as the thick, solid, black lines. The shaded areas around the curve in light blue are the standard deviations of the bootstrapped values. The horizontal areas show the field values for galaxies between $0.15 < z < 0.35$.

tion approaches the field fraction ($\sim 56\%$, shown as a shaded horizontal region), only within the uncertainties, indicating that the processes that stops the star-formation activity was already at work at the environments sampled here, but it is accelerated at smaller cluster centric distances.

The fraction of star-forming galaxies increases linearly towards lower densities reaching the field value at $\Sigma_5 \sim 15 \text{ Mpc}^{-2}$, with a subsequent slight decrease which is also observed for the mean equivalent widths.

The value found for the field fraction is in agreement with previous studies for those redshifts (see Hammer et al. 1997, Balogh et al. 1999, Nakata et al. 2005). Although each author used a different cut to define the star-forming population, the derived values agree within the statistical uncertainties.

The curves for weighted mean of $[\text{O II}]$ and $\text{H}\alpha$ equivalent widths mimic to those for the fraction. All of them reach the field value. In the case of the density relation, the decline at lower densities is also observed. In the case of the radial relation the peak at $R \approx 0.6R_{\text{vir}}$ is also noted. As discussed in §5.3.2 those effects may be due to the different populations present in each cluster.

The averaged $[\text{O II}]$ and $\text{H}\alpha$ equivalent widths behave very similar, except that the mean values for $W_0([\text{O II}])$ are quite high if compared with the local relation where $W_0([\text{O II}]) \approx 0.4W_0(\text{H}\alpha)$ (Kennicutt 1992). This will be discussed further in §6.

5.2.1 Comparison with previous work

It is difficult to compare quantitatively those trends with previously published works, because the methods to subtract the background, the luminosity limit, the selection procedures and cosmologies are varying among the authors. One can, however, make qualitative examinations based on the overall trends.

In the local universe ($z \sim 0$), several studies have investigated the relation of the star-formation activity with environment. For instance, Lewis et al. (2002) and Gómez et al. (2003) in samples drawn from the 2dFGRS and SDSS, respectively, have found that the star-formation activity reaches the

field value approximately at a clustercentric distance $\sim 2R_{\text{vir}}$ and projected densities around ~ 1 galaxy Mpc^{-2} . They also state that the correlation with environment is universal and does not depend on the mass of the system where the galaxies belong. However, the studies based on these two large redshift surveys, typically reach very low projected densities (up to 0.1 galaxies Mpc^{-2}), but do not sample well regions with higher densities due to technical difficulties. Those studies are compatible with the results found here, though those low densities are not reached in this study.

Nevertheless, Rines et al. (2005) in a sample of well known local clusters³ aimed to overcome this caveat, found that the fraction of star-forming galaxies reaches the field value ($\sim 35\%$ at $z = 0$) also at $R \approx 2 - 3R_{\text{vir}}$ and at $\Sigma_5 \sim 1$ galaxy Mpc^{-2} , confirming the previous results. The fraction of galaxies with active star-formation at $R < 0.5R_{\text{vir}}$ is $\sim 10\%$, not much lower than the fraction found here. This is in agreement with studies that have found little or no evolution of the star-formation activity in the inner regions of clusters (*e.g.* Nakata et al. 2005).

As the fraction of field star-forming galaxies is larger at $z \approx 0.25$ ($\sim 55\%$) the star-formation gradient presented in this study is much steeper as the point where the cluster fraction reaches the field value does not appear to be evolving between those two epochs. Therefore, the processes that stop the star-formation activity in clusters were likely more active in the past.

This is also supported by the behavior of the star-formation density relation where the reaching point appear to be at one order of magnitude higher than in the local universe. However, the difficulties in comparing the density values weaken this statement.

At larger redshifts few similar works have been published to the date. Most of them have only sampled the very inner regions of clusters ($R \lesssim 1R_{\text{vir}}$, *e.g.* Balogh et al. 1999, 2002a, Ellingson et al. 2001, Poggianti et al. 2006). The increase of the star-formation activity towards large clustercentric distances, present in the local universe is also ob-

³The Cluster and Infall Region Nearby Survey, CAIRNS (Rines et al. 2003) which include clusters like Coma, Abell 496, etc.

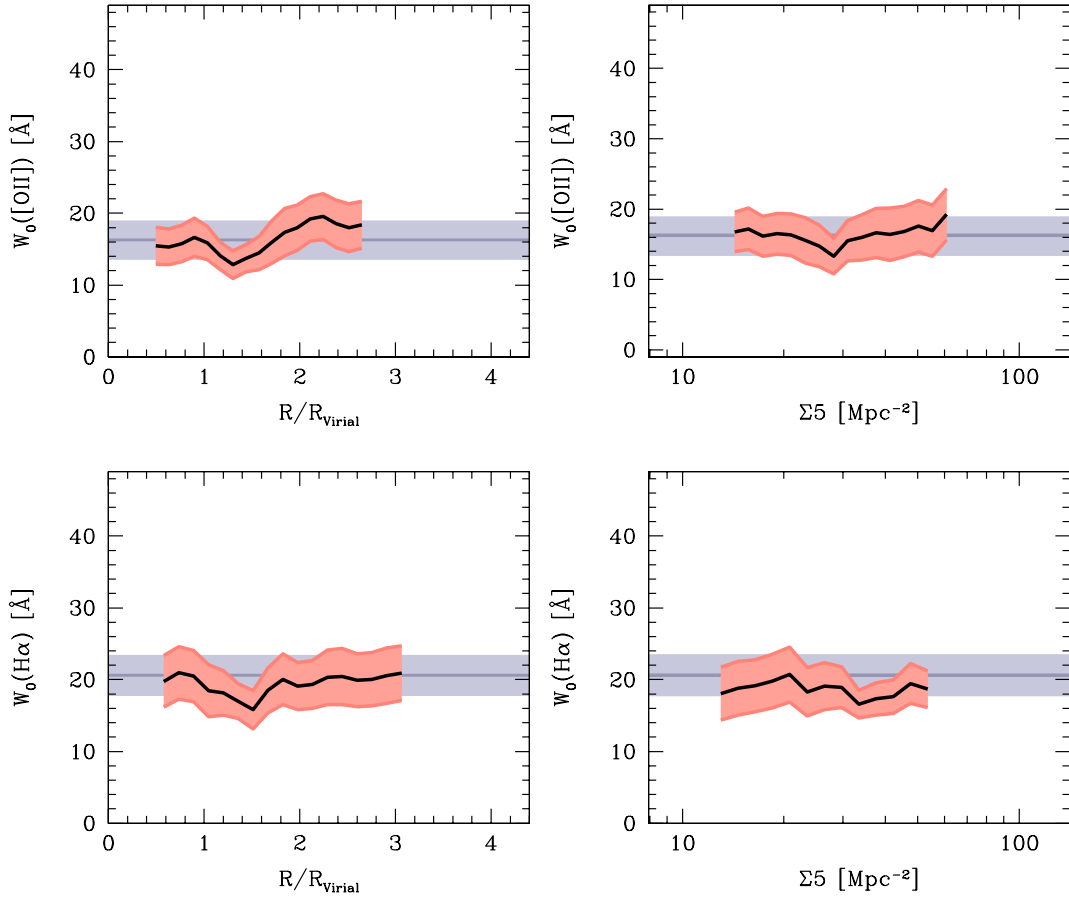


Fig. 5.3: Mean equivalent widths of [O II] and H α of the star-forming population in function of normalized cluster-centric distances and projected density. Horizontal areas represent the mean for field star-forming galaxies.

served at earlier epochs. In the regions covered by their observations, the statistics are similar to those presented here within the uncertainties, despite the different methods used.

Pimblet et al. (2006) studied a sample of 11 clusters between $0.07 < z < 0.16$, with a quite good coverage outside of $1R_{vir}$. Their results point out towards similar conclusions that the studies in the local universe, but the break on the star formation activity appears to be slightly shifted towards higher densities. However, the presentation of their results as well as the focus of that work do not facilitate the comparisons.

Balogh & Morris (2000), Couch et al. (2001), Kodama et al. (2004), Umeda et al. (2004) and

Finn et al. (2005) have all studied the star formation activity in clusters between $0.2 < z < 0.8$ by using narrow-band filters centered in the H α emission line. Similarly, Martin et al. (2000) used a narrow band filter centered in the [O II] emission line in a cluster at $z \sim 0.4$. Those studies are varying in depth and spatial coverage, but have the advantage of being complete over the flux limit. However, this limit is generally quite high and those studies only detected the strongest emitters⁴. Also, they are heavily affected by field interlopers and background sources whose emission lines are redshifted to the targets frame.

⁴with the exception of Kodama et al. (2004), who used the 8 m Subaru telescope.

Nevertheless, all those studies detected differences on the distribution of the emission line emitters and have found that the star-formation is at those redshift already related to the environment.

More recently, Sato & Martin (2006a,b) made spectroscopic observation of the sample of Martin et al. (2000) and were able to confirm many of previous detected emitters as cluster members. But since they focused in studying the previously detected [O II] emitters and their properties, the comparison is not straightforward.

Czoske et al. (2001) initiated a study on the colliding cluster Cl0024+1654 at $z \approx 0.4$, which has been the base of many subsequent, very comprehensive studies on environmental evolution of galaxies (e.g. Treu et al. 2003, Moran et al. 2005, 2007b), though, they only reached clustercentric distances $\lesssim 2 R_{vir}$. However, the current research of this group has been mainly focused on the properties of passive galaxies or morphological selected early types rather than on the change of the star-formation activity with environment.

5.3 ORIGIN OF THE TRENDS

In order to explore the origin of the trends described in the previous section, the sample will be splitted according different criteria. This, however, reduced the number of galaxies sampled in each test and thus is not possible to cover the same dynamical range. The noise is also increased.

5.3.1 The star forming population

First, the environmental distribution of the star-forming population is analyzed, *i.e.* all galaxies with equivalent widths, either in [O II] or $H\alpha$, $< 5 \text{ \AA}$ were excluded.

The results are plotted in figure 5.3. Note that the mean equivalent widths remain quite stable over a large range of galaxy projected densities and clustercentric distances. Those values are statistically similar to those found for field star-forming galaxies, pointing out that both populations do not differ substantially. This is clearly appreciated in Figure 5.4 where the cumulative fraction for each bin of $W_0([O II])$ and $W_0(H\alpha)$ for field and cluster star-

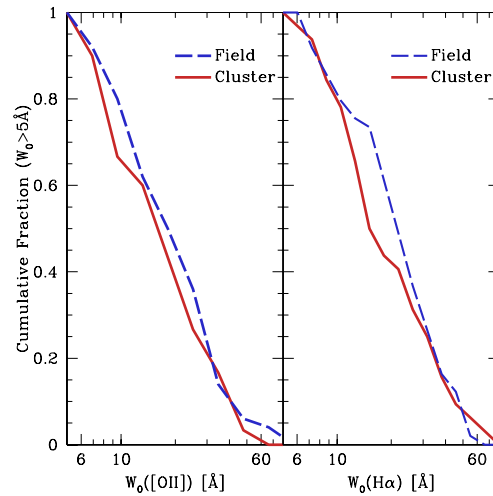


Fig. 5.4: Cumulative histograms of equivalent widths for field and clusters star-forming galaxies as measured by the [O II] and $H\alpha$ emission lines.

forming galaxies is plotted. Both distributions are very similar.

This leads to the conclusion that the trends seen in figure 5.2 are only driven by the change on the relative numbers of star-forming and passive galaxies in different environments.

This result is similar to the findings of Balogh et al. (2004a) at $z \sim 0$ where the distribution of the $H\alpha$ equivalent widths in the SDSS and 2dFGRS was analyzed. They found that this distribution is similar in the “low” and the “high” density environments. The densities sampled by that study are relatively low ($0.1 < \Sigma_5 < 10 \text{ galaxies Mpc}^{-2}$) but Rines et al. (2005) extended this analysis to local clusters and have not found differences in the star-forming population in different environments.

Here, those findings are confirmed at an earlier epoch and the environmental variation was analyzed instead only the distribution of the equivalent widths, finding no change on the properties of the active population.

This is an important finding and puts strong constraints on the mechanisms that affect the star-formation. In particular, it argues against soft processes. Instead of a slowdown of the star-formation over long periods of time, the actual process has to

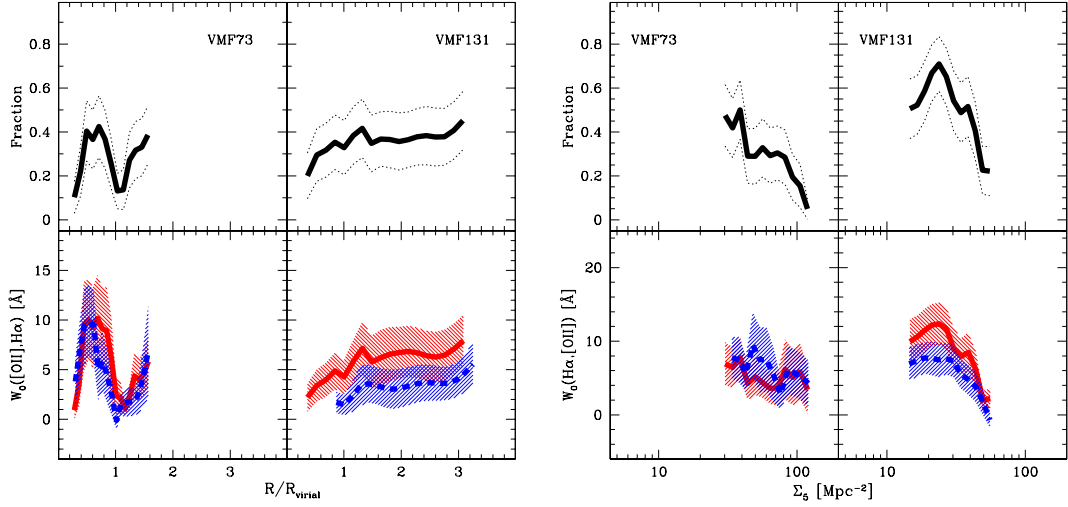


Fig. 5.5: Fraction of star-forming galaxies and mean equivalent widths against normalized cluster distance and projected density for the clusters VMF73 and VMF131 as depicted in the respective panels. In the bottom panels the dashed blue line represent the mean [O II] equivalent widths and the solid red line the H α ones. The respective 1- σ dispersions are marked as hashed areas in the bottom panels and thin dotted lines in top panels.

shut down the activity in short times scales. Furthermore, the processes have to be effective in a wide range of environments.

5.3.2 Subsamples according to membership

Given the relative small sample and some unusual features in the composite cluster, the influence of individual clusters on the averaged trends is investigated. Since two clusters (VMF73 and VMF131) account for an important fraction of the data, they are investigated individually. Here, given the smaller number of galaxies, fewer galaxies are included in each “bin” at expense of increasing the noise.

The results can be seen in figure 5.5. Note the striking differences between the two clusters, especially in the radial distribution. VMF73 shows the peak inside $1 R_{vir}$ which leads to the conclusion that the peak detected in the global trends is exclusively due to this cluster.

This peak, or perhaps better said the depletion at $\sim 1 R_{vir}$, is likely an effect of a secondary structure in this cluster (see §4.2.3) as the radial gradient

is result of the combination of both substructures. This can be taken as additional evidence that the X-ray structure detected by Rasmussen & Ponman (2004) actually belongs to the cluster. It may form part of a large infalling group and clearly has a noticeable effect on the galaxy population, reducing the star-formation activity near the center of this structure. This may be because of its denser intergalactic medium and higher galaxy density than expected at these clustercentric distances.

Additional effects may arise from the geometrical configuration of the cluster at $R < 1 R_{vir}$, given its elongated galaxy concentration. Those features passed unnoticed in the previous analysis of Gerken et al. (2004), as the fixed bins used there eventually erased them.

VMF131 shows, on the other hand, a modest but steady increase in its star-forming activity towards larger clustercentric distances. This cluster is quite well covered at large radii. Thus, the general trends of the composite cluster at those distances are very dependent on it.

As it was noted in §4.2.2, this cluster appears to be centrally concentrated and few substructures

were detected by using the color cuts. Furthermore, the Dressler-Shectman test (§4.3.5) did not show dynamically peculiar structures. It is likely that this cluster is relatively isolated and quite evolved for its mass.

The projected galaxy density probes environment regardless of the cluster geometry, therefore cluster substructure does not affect, in principle, the correlations. Nevertheless, it is observed that the trends for these two clusters are also quite different. VMF73 shows a sharp increase in the fraction of star forming galaxies towards lower projected densities but a modest increase in their overall activity, as measured by their equivalent widths. VMF131 displays an increase in its fraction of star forming members and the average star-formation strength similarly increases.

The scatter of the galaxy population inside of clusters has been already noted, however it does not depend strongly on their X-ray luminosity nor velocity dispersion according to Popesso et al. (2007), although Poggianti et al. (2006) find both a weak correlation between galaxy properties and cluster mass and also evolution of it with redshift.

On the other hand, Rines et al. (2005) also showed that the environmental trends of star-formation are different for each of the clusters sampled by this study. It is unclear whether this difference is related to cluster global properties as measured by classical mass indicators, but at least substructure plays an important role. Therefore, this variation may be related to more subtle properties, such as mass assembly history and large scale structure around the clusters, which is not measurable by standard techniques.

5.4 DIFFERENTIAL EVOLUTION WITH MASS

From the trends presented in the previous section results clear that, from the perspective of star-formation activity, clusters mainly differ from the field in the mix of the galaxy subtypes. This is affected by the cluster substructure but occurs relatively fast, and the relevant processes do not slow but rather quench the star-formation activity.

In order to see what galaxies are being affected

by the cluster environment and thus producing the previous trends, the sample was splitted only between cluster and field galaxies. In this case, galaxies belonging to groups candidates were excluded (see explanation below).

The cluster sample is also splitted in galaxies which lie at clustercentric distances $R > 1R_{vir}$ (“the infalling population”) and those at $R < 1R_{vir}$ (“the inner population”). This division is somewhat arbitrary as it only reflects the galaxy current position, but given the current data and models is not possible to separate both populations. Thus, the previous classification only reflect relative likelihoods.

The fraction of star-forming galaxies was then calculated in function of the galaxy stellar mass (see §3.6). The results are shown in Figure 5.6. The trends are directly compared with recent results of Balogh et al. (2007) who examined groups⁵ and field galaxies between $0.12 < z < 0.55$. The results presented here for field galaxies are consistent with their sample. (within the $1-\sigma$ uncertainties).

The galaxy population in the “infalling” region is very similar to the population found in groups at similar redshifts, pointing out that some sort of pre-processing is already underway before galaxies go much deeper into the cluster potential well. Once those galaxies reach the cluster inner regions other processes act further and only few remain active. This fraction may be even lower as the expected number of infall “interlopers”, *i.e.* galaxies projected over the inner regions, can be as high as the 50% (Rines et al. 2005).

The fraction of star-forming galaxies at the low and the high mass ends are similar in all environments, changing only the characteristic break. However in the case of the “inner” cluster, the fraction remains low over the full range of masses sampled. This fraction is comparable to the typical values found for high mass systems, which is similar in *all* environments.

This can be considered a clear case of “downsizing”, *i.e.* galaxy evolution is shifted towards lower mass systems as cosmic time progresses. The most massive galaxies experienced stronger evolution at earlier times and then become passive de-

⁵Including the group candidates, detected in the present study, may have biased the previous trend.

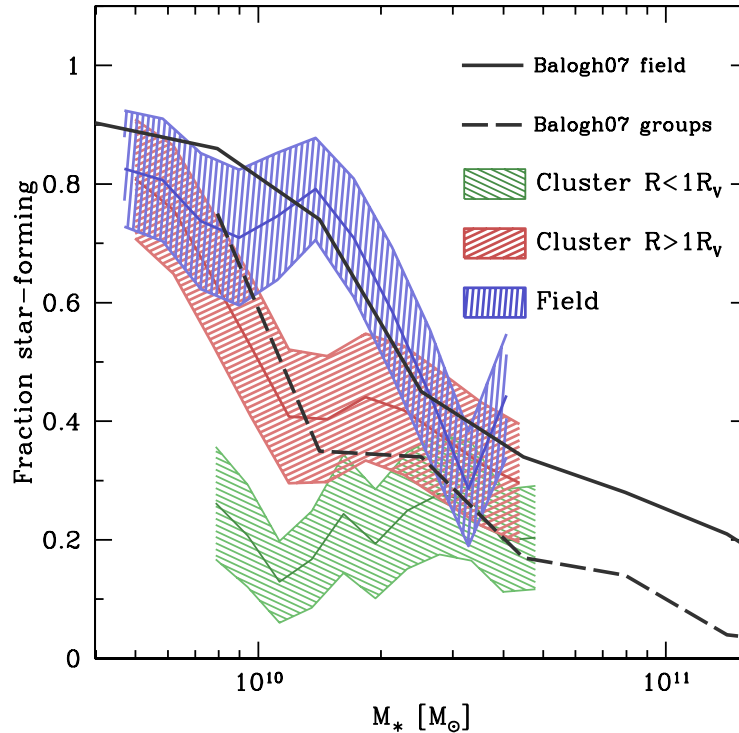


Fig. 5.6: Fraction of star-forming galaxies versus stellar mass for field and cluster galaxies as indicated in the figure. The areas represent the $1\text{-}\sigma$ dispersions. The black solid and dashed lines are field and group galaxies respectively from Balogh et al. (2007) (error bars omitted for clarity).

spite their environment, whereas dwarf galaxies are still evolving. For example, most of the healthy star-forming galaxies at $z = 0$ have low masses (Haines et al. 2007). As the group and cluster environment accelerate galaxy evolution via more frequent interactions, similar effects are expected.

5.5 SCENARIOS

One of the main problems in interpreting the previous results (as well as similar results reported in the literature) is the lack of a consistent scheme able to take into account all the different mechanisms present in the cluster environment that can affect the star-formation activity.

This difficulty arises from different sources. First, in the still poor understanding of the effects of these processes on the different galaxy compo-

nents. Second, in their overlapping spheres of influence and in the fact that some different processes can not easily be disentangled as they produce similar end-products.

The issue of the regions of influence can be seen more clearly in 5.7. This scheme was proposed by Treu et al. (2003) as a very simplified cluster model and defines regions where the different interaction processes are likely to be efficient.

Since galaxies are expected to move considerably during the time that the relevant processes are at work their position in that diagram is only indicative. For example a starburst usually lasts $\lesssim 1$ Gyr which is about the time that a galaxy takes in crossing the cluster ($\lesssim 2$ Gyr for the clusters sampled here).

The efficiency of the relevant processes is also affected by the galaxy properties (specially mass)

and the cluster substructure. Nevertheless, the previous scheme still makes possible to evaluate what processes are affecting the star-formation activity in certain regions.

Ram-pressure stripping is very efficient in quenching the star-formation activity but it only acts in central regions of clusters ($R \lesssim 0.5R_{vir}$, *e.g.* Kapferer et al. 2007). However, star-formation depletion here is detected at distances as far as $\sim 3R_{vir}$. Some of those galaxies may have lost their cold gas due to the scatter in the ram-pressure strength that they experience during the infall as shown by Tonnesen et al. (2007).

It is also possible that many of the galaxies in the outskirts have already passed through the denser intra-cluster media. In fact, models by Gill et al. (2005) predict that as many as half of the galaxies between $1-2.5R_{vir}$ may be “re-bouncing” after a first passage by the cluster core (the so-called “backsplash” population) and thus have experienced strong interactions for sufficient time to become passive. In those models the backsplash galaxies have distinct kinematics compared to the more virialized central ellipticals or the infalling populations. So in principle they could be identified.

The model cluster treated by Gill et al. (2005) is quite realistic but the combined effects of substructure and 2-D projection of the galaxy velocity distribution make difficult to identify this population in real clusters (*e.g.* Rines et al. 2005, Sato & Martin 2006b).

The two individually sampled clusters offer a possibility to test this hypothesis. VMF73 is a luminous X-ray cluster (ranked second after VMF132), taking in account only the central emission. On the other hand, VMF131 is about half as luminous. These clusters display different star-formation profiles. In the case of VMF73, the activity raises sharply and peaks at very small radius ($R \sim 0.6R_{vir}$) and decreases again at $R \sim 1R_{vir}$ where a bright X-ray group is found. It seems clear that both X-ray structures are affecting the star-formation activity of the galaxies embedded therein, but it is not the case for galaxies in between. Those galaxies unlikely have passed through the center of any of both structures.

Although, VMF131 does not have deep modern X-ray imaging but it seems clear from the photometric and dynamical analysis that display much less substructure than VMF73, only marginal evidence of a dynamically decoupled structure just outside $\sim 2R_{vir}$ is found, but it can be due also to those galaxies being simply unrelated to each other. Its star-formation activity shows a much shallower increase towards large radius. It is possible, in this case, that many of the galaxies have passed through the center. The much rounder concentration indicates that, perhaps, is an older cluster, already well assembled. VMF73 on the other hand may be in the way of assembling. But the lack of dynamical peculiarities is puzzling.

However, galaxies infalling into clusters can be also affected by ram-pressure. Under certain circumstances, this process may be important in groups and filaments (Fujita 2004, Hester 2006), but massive and evolved groups are required to affect the properties of relative large galaxies as those sampled in this study. However, since the spatial sampling in the outskirts is low, it is difficult to evaluate whether such groups are present or not, but the characteristics of the infall population indicates that the same process that affect the star formation in groups is active in that region.

Other processes may still be present, since star-formation depletion is observed at distances larger than those predicted by the Gill et al. (2005) simulations and they only account for a fraction of the galaxy population.

Starvation or the strangulation is a softer version of the ram-pressure stripping and thus is able to work at shallower densities. It strips the outer gaseous halo leaving the galaxy without the source of gas to form new stars, so the galaxy slowly consumes the remaining gas in the disk over a long period until exhausted (Bekki et al. 2002).

Since the necessary intergalactic gas densities are much lower, this process is likely to be active in many groups (Kawata & Mulchaey 2008). So, its region of influence in the diagram of Figure 5.7 is only indicative. If this process is active in groups is beyond the objectives of the present study.

Balogh et al. (2000) developed a simple prescription for star-forming galaxies, when no more

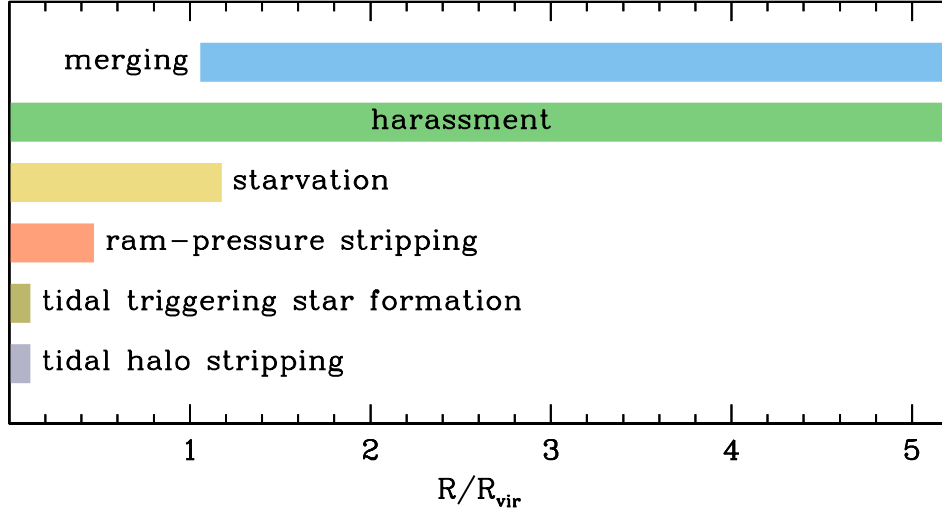


Fig. 5.7: A simple cluster scheme with regions of influence of the different interaction mechanisms (Adapted from Treu et al. 2003).

gas is available for further star formation as in the case of starvation. In this case, the star-formation rate declines as following:

$$SFR(t) = SFR(0) \left(1 + 0.33 \frac{t}{t_e}\right)^{-3.5} [M_{\odot} \text{ yr}^{-1}] \quad (5.1)$$

where $t_e = 2.2(SFR(0)/M_{\odot}\text{yr}^{-1})^{-0.28}$ is the characteristic time and includes the effects of gas recycling due to stellar winds and supernovae.

Elbaz et al. (2007) have determined that at $z \approx 1$, *i.e.* ~ 4 Gyr before the epoch sampled by this study, the star formation rate is a function of stellar mass as: $SFR \approx 7.2 \times (M_{\star}/10^{10}M_{\odot})^{0.9}$. This corresponds to $\log(sSFR) \approx -0.1 \log(M_{\star}) - 8.14$, where $sSFR$ is the specific star-formation rate, *i.e.* SFR divided by the stellar mass. In the next chapter, it is demonstrated that the limit of $W_0([\text{O II}], \text{H}\alpha) = 5 \text{ \AA}$ to select star-forming galaxies sets a $sSFR \sim 2 \times 10^{-11} \text{ yr}^{-1}$. This limit is independent of stellar mass and below it, a galaxy is considered passive.

Assuming that galaxies at $z = 1$ had their outer halo stripped and are only left with their disk reservoir their star formations will behave according to equation 5.1. Galaxies at $z = 1$, with masses $M_{\star} =$

$1 \times 10^{11}M_{\odot}$ have star formation rates $\sim 57M_{\odot}\text{yr}^{-1}$. Under the above prescriptions, they would need about ~ 3.3 Gyr to become passive at $z = 0.25$ under the effects of starvation only, a time scale already longer than the cluster infalling time. On the other hand galaxies sampled in this study with stellar masses of $M_{\star} = 1 \times 10^{10}$ and $M_{\star} = 1 \times 10^9M_{\odot}$ would need ~ 7 and >10 Gyr respectively to become passive under this process. The effect of increased stellar mass as product of star formation are neglected as the effects of gas recycling (Kennicutt et al. 1994) hinder a further growth once the bulk of the stars have been already formed at $z = 1$.

Therefore, only the most massive galaxies sampled in this study may have suffered the effects of starvation for a period of time long enough to become passive, if no other processes are acting altogether.

Another key point is that starvation slows the star-formation in the affected galaxies over a *long* period of time. Unless this process is equally effective in the field and clusters, it would be very improbable that the distribution of the star-forming population appears to be similar in both environments. Moreover, for galaxies infalling into a galaxy cluster, ram-pressure may start to be effective.

tive before the strangulation is completed (Fujita 2004).

Pure gravitational interactions with the cluster potential lead to tides in the mass content of galaxies. They can enhance the star formation activity via compression of the galactic gas (Fujita 1998, Bekki & Couch 2003). But, it can also strip the outer regions such as the dark matter halo (Gnedin 2003) and its gaseous content (Bekki et al. 2001), mimicking starvation, but producing, in addition, a change on morphology.

However, tidal interactions are also present far from the cluster cores, in close galaxy pairs. They particularly affect a galaxies with masses much lower than the parent halo, effectively quenching the star-formation (Cattaneo et al. 2006).

Fast speed encounters of galaxies (*i.e.* harassment) lead to a change of their morphology, as each encounter strip a fraction of the outer part of the galaxies and redistribute it in the dark matter halo. Its effect on the gaseous content is likely be similar to the halo stripping. Harassment has been indicated as the responsible mechanisms in producing S0s galaxies in clusters over long times scales. As the predicted effects in the gaseous content are mild and this process is particularly effective in clusters, likely strong interactions would shut down the star-formation before harassment produces noticeable effects Quilis et al. (2000).

Mergers, on the other hand, are effective on both, star-formation triggering and morphology change. The time scales of this process may be as short as $\sim 1\text{--}2$ Gyr (Bekki 2001, Conselice 2006). They are specially effective in massive galaxies and in groups or cluster outskirts where the relative velocities are low. Given the previous requirement they are likely to constitute part of the group preprocessing.

In conclusion, ram-pressure is able to explain to a great extend the suppression of the star-formation activity in clusters, even in galaxies located at large clustercentric distances. Direct evidence of this process is at work on single galaxies has been shown by some authors (*e.g.* Boselli et al. 2006, Cortese et al. 2007). The galaxies affected by this mechanism display cometary gaseous tidal streams and truncated star-formation disks but their stellar

kinematics are fairly regular, but more modeling is necessary to understand the effects of this process in the general population.

However, additional mechanisms are necessary, because the star-formation activity is already low at larger distances and, specially important, at low projected densities. It is still possible that ram-pressure is affecting galaxies in infalling groups as proposed by some authors. If this is the case, group preprocessing is preferred as denomination, as many other processes (tidal interaction, mergers, etc) are though to be efficient there and thus may play an important role. Evidence of this is found in the fact that the galaxy populations in the outskirts resemble to those found in groups, where they are already evolved with respect to the surrounding field (Figure 5.6). In fact, there is evidence of a sequence where group-like preprocessing in the infalling regions may play an important role before the strong interactions in the inner cluster regions effectively shut down the star-formation of galaxies.

Starvation, on other hand, is found to contribute only marginally to the population mix in clusters under standard assumptions. In the case that it contributes to the galaxy mix in groups, the above denomination is preferred.

It is found in this study that massive galaxies are quite evolved in all environments and the change of the populations between field, groups and clusters is mainly driven by the change of intermediate mass systems. At least in the field, groups and the infalling region dwarf galaxies appear to be unaffected. However, not enough data is present in the current study to support any conclusion of what occur with them in the central regions. Recent studies show that they are resilient to mergers and other interactions in groups but are strongly affected by the effects of ram-pressure or harassment (Haines et al. 2007).

It is important to note that every cluster is a particular entity of its own, and it is likely that different processes have dissimilar importance. They can depend on the cluster history and configuration, as well as on the surrounding environment. These effects may influence the galaxy population that inhabit the clusters as recently shown by Moran et al. (2007a), where the early type populations of two

clusters at $z \sim 0.5$ have different star-formation histories. This is supported here by the different star-formation gradients detected, due mainly to sub-structure and the galaxy populations, with some clusters harboring an important fraction of red-star forming galaxies. They may be important in the scheme of galaxy evolution as shown in the next chapter.

The properties of the emission line galaxies

In the previous chapter, the environmental distribution of star forming galaxies has been shown. It has been described by the equivalent widths of prominent emission lines ($[\text{O II}]$ & $\text{H}\alpha$). However, how are they connected with physical parameters of galaxies? Moreover, it is known that other phenomena can also produce emission lines, specially important in this context are active galaxy nuclei (AGNs), where the material falling into massive black-holes is ionized and produces strong emission. Also, it has been found an important population of star forming galaxies with colors typical of red passive galaxies. Are they “normal” star forming galaxies? In this chapter those questions will be explored.

6.1 EQUIVALENT WIDTH DISTRIBUTION

In Figures 5.1 and 5.2, the environmental distribution of star-forming galaxies is characterized by both, the blue and the emission line galaxy fraction. Both distributions are very similar, indicating that those two indicators are related.

They are, in fact, correlated, although the relation has a large scatter as can be appreciated in Figure 6.1. There, the rest-frame ($B-R$) color is plotted against the equivalent widths of $[\text{O II}]$ and $\text{H}\alpha$. Both cases display a similar distribution. The lines show the mean and the $1-\sigma$ deviation, which is ~ 0.2 mag. This deviation is comparable to the mean color variation between the passive galaxies and the strongest emitters which amounts $\Delta(B-R) \approx 0.4$ mag. No

important differences are found between field and cluster galaxies, except for the larger abundance of non-emitters in the clusters.

The $\text{H}\alpha$ distribution is compared with theoretical tracks calculated by Kennicutt et al. (1994) using Salpeter (1955) and Scalo (1986) initial mass functions (IMF). The data show better agreement with the former IMF.

The scatter in the previous relation arises from many sources. One is purely observational, as the k-corrections have a mean error of the same order of the scatter displayed in the Figure 6.1 (see §3.6).

However, they are also differences in the processes traced by both indicators. Optical colors provide information about the star-formation in timescales of ~ 1 Gyr, because they are more sensitive to the young-to-old stellar population ratios, because the galaxy spectra at optical wavelengths is mostly dominated by intermediate main sequence stars (A to G) and red giants (K and M). On the other hand, emission lines are sensitive to young massive stars (O-B stars) and the amount of gas. Therefore, they are nearly instantaneous indicators of star formation (see next section).

In Figure 5.2, where the environmental variation of the star-formation activity is also addressed via the mean equivalent widths, it can be appreciated that the mean $[\text{O II}]$ and $\text{H}\alpha$ are quite similar for both indicators. However, Kennicutt 1992 found that both indicators are differently related in $z = 0$ star-forming galaxies via the following relation:

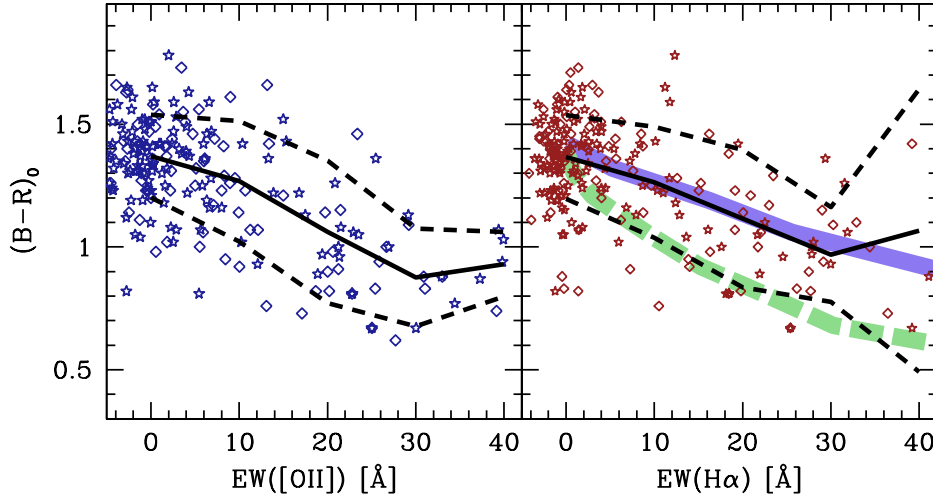


Fig. 6.1: [O II] and H α equivalent widths plotted against restframe $B - R$ color for cluster (stars) and field (diamonds) galaxies. Solid and dashed lines are the mean and the $1-\sigma$ deviations respectively. The thick lines in the right plots are the theoretical tracks of Kennicutt et al. (1994) using Salpeter (1955) (solid purple line) and Scalo (1986) (dashed green line) initial mass functions.

6.2 STAR FORMATION RATES

$$W([\text{O II}]) \approx 0.4W(\text{H}\alpha) \quad (6.1)$$

This deviation can be better appreciated in Figure 6.2, where all galaxies which show both indicators are plotted. The lines show the best least-squares fits and the $1-\sigma$ deviations obtained after 10 iterations. The local relation is also plotted for comparison. The relation for cluster galaxies is $W([\text{O II}]) \approx 0.9W(\text{H}\alpha)$, whereas for field ones is $W([\text{O II}]) \approx 0.7W(\text{H}\alpha)$, but in both cases the scatter is large.

No convincing explanation for this effect has been found, because the instrument setup, line definitions and algorithms are the same than those in Balogh et al. (2002a), where the correlation was indeed found, therefore likely it is an intrinsic characteristic of the sample used here. Hammer et al. (1997) reported the same effect in the Canada-France Redshift Survey galaxies at similar redshifts. They issued some hypothesis that may apply to this work, such as lower extinction, lower metallicities and contamination by AGNs. These possibilities will be investigated throughout this chapter.

In the previous chapter the star formation activity of galaxies has been related to spectral features such as emission lines.

Emission lines in the stellar medium arise whenever an excited atom (or ion) returns to lower-lying levels by emitting discrete photons. There are three main mechanisms which produce atoms (ions) in excited levels: recombination, collisional excitation by thermal electrons and photo-excitation. H α and the Balmer lines belong to the first class, whereas the forbidden lines [O II], [O III] and [N II] are part of the second class.

Hydrogen recombination lines effectively re-emit the integrated stellar luminosity of galaxies shortward of the Lyman limit¹, so, they provide a direct, sensitive probe of the young massive stellar population. Only stars with masses $>10 M_{\odot}$ which have lifetimes <20 Myr, contribute significantly to the integrated ionizing flux (Kennicutt 1992).

In order to estimate the true star formation rate

¹This is the lower limit of wavelengths of spectral lines in the Lyman series ($\sim 912 \text{ \AA}$).

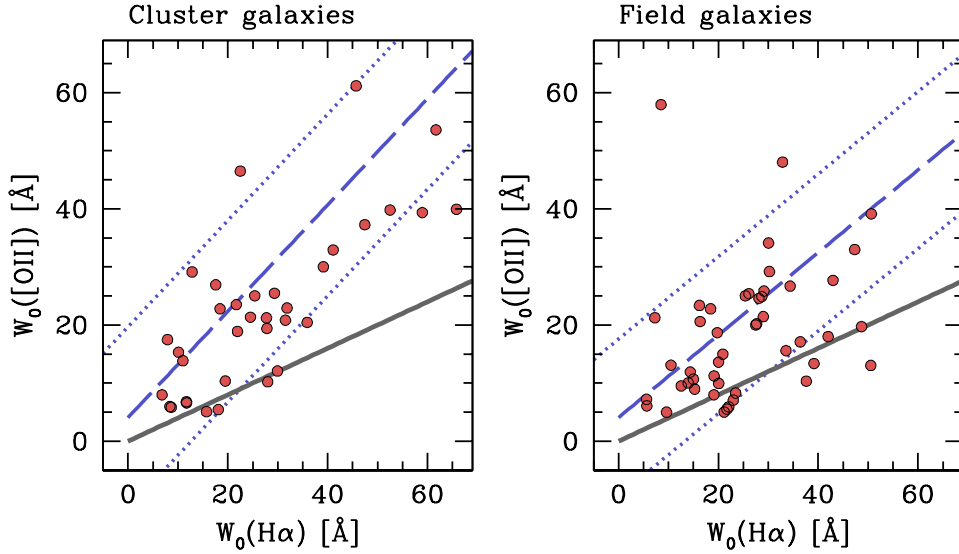


Fig. 6.2: [O II] and $H\alpha$ equivalent widths for emission lines galaxies in the clusters and in the field. Simple least-square fits are plotted (dashed lines) with the scatter accounted (dotted lines). The thick solid line shows the local relation of Kennicutt (1992).

(SFR), a large extrapolation is made to lower stellar masses. This is made assuming a universal initial mass function (IMF), *i.e.* the mass distribution of newly formed stars (*e.g.* Salpeter 1955). According to the calibration of Kennicutt (1992) and Madau et al. (1998)

$$\begin{aligned} SFR[M_{\odot} \text{ yr}^{-1}] &= 7.9 \times 10^{-42} L(H\alpha)[\text{erg s}^{-1}] \\ &= 1.08 \times 10^{-53} Q(H^0)[\text{s}^{-1}] \end{aligned} \quad (6.2)$$

where $L(H\alpha)$ is the luminosity in $H\alpha$ and $Q(H^0)$ is the ionizing luminosity.

The main limitations of this method depend on the uncertainties of the universality of the IMF, the extinction and the assumption that all the ionizing radiation is traced by the gas.

The amount of the ionizing radiation that escape from individual star-forming galaxies is subject of debate, especially its evolution with redshift. Although the values are disparate, they appear to be between 1–6% of the total Lyman photons at low redshifts (Heckman et al. 2001, Inoue et al. 2006).

With respect to the IMF, it has been found that

there is little evidence of variation among normal star-forming galaxies up to moderate redshifts (*e.g.* Kroupa 2001, 2002). However, the SFR depends on the form of adopted IMF. Fortunately, $H\alpha$ equivalent widths and broadband colors are sensitive to the IMF used (Kennicutt et al. 1994). In Figure 6.1, the relation between restframe $B - R$ and $W_0(H\alpha)$ is plotted. Despite the relative large scatter, the mean values are in better agreement with the theoretical tracks of Kennicutt et al. (1994) using a Salpeter (1955) IMF rather than a Scalo (1986) function.

The effects of dust are difficult to quantify without infrared or radio data. Kennicutt (1992), for his sample of bright galaxies used an average of $E(H\alpha) = 1 \text{ mag}$ (values ranged between 0.8 – 1.1). Therefore, the equation 6.2 is written as

$$SFR(H\alpha) = 7.9 \times 10^{-42} L(H\alpha) E(H\alpha) \quad (6.3)$$

However, the spectra used in the present study are not flux calibrated² and $L(H\alpha)$ is not available. But, it is still possible to estimate the $H\alpha$ fluxes

²This is due to the uncertainties in the aperture corrections because the slits sampled different fractions of each galaxy. Also, during some nights poor weather affected the observations.

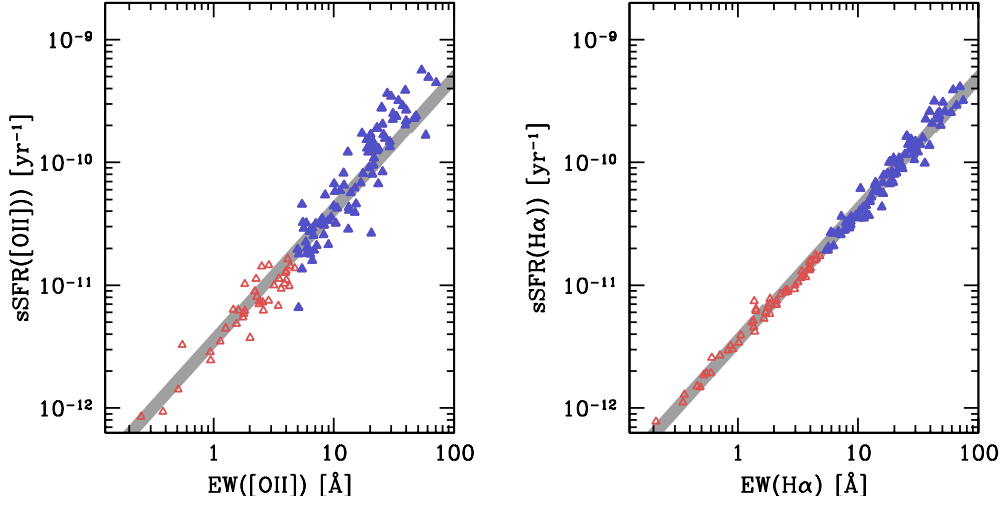


Fig. 6.3: Specific star formation rates based on [O II] and H α versus the respective equivalent widths as calculated using the relations indicated in the text. Blue filled triangles are galaxies with $W_0([\text{O II}], \text{H}\alpha) > 5 \text{ \AA}$, classified here as star forming. The grey lines is the least-squares fit to the H α relation: $\log(\text{sSFR}) \approx 1.07 \log(W_0(\text{H}\alpha)) - 11.4$, which is also plotted in the [O II] panel for comparison.

using the R -band absolute magnitudes and the H α equivalent widths, since

$$W_0(\text{H}\alpha) \approx \frac{L(\text{H}\alpha)}{L_C} \quad (6.4)$$

where L_C is the continuum luminosity in $\text{erg s}^{-1} \text{ \AA}^{-1}$ (see Lewis et al. 2002) and $L_C \approx L_R$, the luminosity in the R -band. For a L^* galaxy $L_C = 1.1 \times 10^{40} \text{ ergs s}^{-1}$, as determined by Blanton et al. (2001), with $M_R^* = -21.8 \text{ mag}$, which leaves

$$L(\text{H}\alpha) = 1.1 \times 10^{40} W_0(\text{H}\alpha) 10^{-0.4(M_R - M_R^*)} \quad (6.5)$$

Therefore,

$$\text{SFR}(\text{H}\alpha) = 0.079 W_0(\text{H}\alpha) 10^{-0.4(M_R + 21.8)} \quad (6.6)$$

Calibrations for other Balmer lines (e.g. H β) are also available, however those lines are much weaker than H α and are only detectable for the strongest emitters. Moreover, they are often affected by underlying absorption from the stellar populations.

As H α becomes out of the optical window beyond $z \sim 0.5$, the [O II] $\lambda 3727$ emission line is often used as indicator of star formation, mainly due to its strength. However, the modeling of the [O II] luminosity is more complicated, because its emission is not directly coupled to the ionizing radiation and its excitation is related to the oxygen abundance and the ionization state of the gas. It is also more affected by dust extinction.

Kennicutt (1992), adopting the H α -derived SFRs, calibrated this indicator as following:

$$\text{SFR}[\text{O II}] = 2.0 \times 10^{-41} L([\text{O II}]) E(\text{H}\alpha) \quad (6.7)$$

Following a similar procedure, the [O II] luminosity can be estimated using the B -band absolute magnitudes.

$$L([\text{O II}]) \sim 1.4 \times 10^{29} \frac{L_B}{L_{B,\odot}} W_0([\text{O II}]) \quad (6.8)$$

where L_B and $L_{B,\odot}$ are the B -band luminosity of the galaxy and the Sun respectively, and $L_B/L_{B,\odot} = 10^{0.4(M_B - M_{B,\odot})}$. Adopting a $M_{B,\odot} = 5.48 \text{ mag}$ and $E(\text{H}\alpha) = 1$ as above, equation 6.7 is then transformed into

$$SFR([\text{O II}]) = 3.4 \times 10^{-12} W_0([\text{O II}]) 10^{-0.4(M_B - 5.48)} \quad (6.9)$$

The SFRs derived from the $[\text{O II}]$ line are expected to be less precise than those from $\text{H}\alpha$ as galaxies exhibit a large scatter in the relation $[\text{O II}]/\text{H}\alpha$, due to the afore mentioned effects. In fact, as shown in Figure 6.2, galaxies in this sample do not follow the Kennicutt (1992) relation, from where the calibration is taken.

However, for the $\text{H}\alpha$ -derived SFRs, uncertainties are also expected due to the crude estimation of the continuum flux.

Using the previous relation star formation rates where obtained for all galaxies with positive equivalent widths. Distinction will always be made for what is considered star-forming galaxies ($W_0([\text{O II}], \text{H}\alpha) > 5 \text{ \AA}$). No attempt was made to obtain SFRs for galaxies with negative equivalent widths, as they yield unphysical values, difficult to interpret if included. This is more a problem for $[\text{O II}]$ than for $\text{H}\alpha$, as the measurement of the former line often yield negative values in absence of emission, values larger than expected from the noise distribution.

In the case that both lines are present, the average of the SFRs derived from either way is taken, otherwise the value from a single line is used, which occurred just in few cases.

Using the stellar masses obtained with `KCORRECT` (see 3.6) specific star formation rates (sSFR) were obtained. This is simply made dividing the SFR by the stellar mass.

In Figure 6.3 the sSFRs obtained in either way are plotted against the equivalent widths. They display strong correlation and a relative small scatter (larger for $[\text{O II}]$), despite the rough estimations made here. The sSFRs obtained from either way are similar, but slightly overestimated for $[\text{O II}]$ at large equivalent widths as evidenced when compared with the $\text{H}\alpha$ fit.

Note that the 5 \AA cut between star forming and passive galaxies has a physical significance as it corresponds to a $sSFR \approx 2 \times 10^{-11} \text{ yr}^{-1}$. A galaxy with such low sSFR will grow only a $\sim 30\%$ in stel-

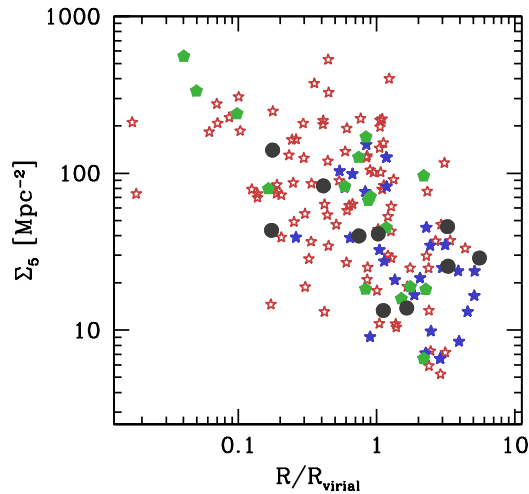


Fig. 6.4: Environmental distribution of the different galaxy subtypes. Red open and blue filled stars represent passive and “normal” star-forming galaxies respectively. Green pentagons are red emission line galaxies, whereas the black circles are AGN candidates.

lar mass during a Hubble time³ if the rate is not altered.

6.3 THE CASE OF THE RED STAR FORMING GALAXIES

It was noted in §4.4.2 the existence of a sub-population of cluster galaxies with emission lines but red colors. 25 out of 56 star-forming galaxies belong to this population. Their average equivalent widths are $\langle W_0([\text{O II}]) \rangle = 14.8 \pm 2.48 \text{ \AA}$ and $\langle W_0(\text{H}\alpha) \rangle = 19.9 \pm 4.90 \text{ \AA}$, similar (within $1-\sigma$) to the mean star-forming population (see Figure 5.3). They do not seem to populate any special environment in the cluster, being more or less evenly distributed over radius and density (see Figure 6.4). They also span the full range of luminosities covered by this study.

Galaxies with a red SED and star-formation activity have been routinely reported at intermediate redshifts either in the field (*e.g.* Hammer et al. 1997) or in clusters (*e.g.* Demarco et al. 2005). In

³ $T_H = (H_0^{-1}) \times 10^{12} \text{ yr} \approx 1.4 \times 10^{10} \text{ yr}$, for the cosmological values here used.

the case of the local Universe, a recent paper by Popesso et al. (2007) reports that red star-forming galaxies make up on average 25% of the whole cluster population. They suggest that those objects are in the process of evolution from late to early types. Wolf et al. (2005) identified hundreds in the field of the supercluster A901/902 ($z \sim 0.17$) based on the information content in their medium-band photometry⁴ of the COMBO-17 survey. They interpret those galaxies as a combination of old-stellar population and dust extinction. Similarly, recently Tanaka et al. (2007) presented indication of red galaxies with younger stellar populations in groups around a $z = 0.55$ cluster. They argue that those red galaxies have truncated their star formation activity recently, on a short time scale, but they host a large fraction of old stars complemented with a reasonable amount of dust.

On the other hand, Martini et al. (2002) based on ROSAT X-ray data, report an unexpectedly high fraction of active galaxy nuclei (AGNs) in red cluster galaxies belonging to a massive $z = 0.15$ cluster, which do not show optical signatures. Although their sample is small, the fraction of obscured AGNs is comparable to the fraction of blue galaxies in the studied cluster. Furthermore, Yan et al. (2006) found that more than half of the red galaxies in the SDSS show emission lines, most of them compatible with low ionization nuclear emission-line regions (LINERs). However, LINERs may not be only due to AGNs, for example, Sarzi et al. (2006) reported *extended* LINER-like emission in several early type galaxies in their spatially resolved spectroscopy. Therefore the question is not clearly settled.

6.3.1 The AGN connection

In order to see whether those galaxies are AGNs or not, and to what degree star-forming galaxies observed here may be contaminated by nuclear activity, some tests based on emission lines were performed (although the obscured AGNs can still be missed). None of the galaxies in the present study show signs of line broadening, typical of Seyferts 1, but Seyferts 2 and LINERs may still be present. For

⁴Their redshifts contain larger uncertainties (cluster membership is probabilistic) and the star-forming status is *model*-based.

that, diagnosis based on the ratios between emission lines ([O II], H β , [O III] λ 5007, H α and [N II]) were performed. However, rarely, all lines are present altogether. Therefore, separate tests were performed to check all possibilities.

The first classical test put the galaxies into the BPT plane (*i.e.* $\log([\text{O III}]/\text{H}\beta)$ vs $\log([\text{N II}]/\text{H}\alpha)$, Baldwin et al. 1981). Each pair of lines are close enough to use the equivalent widths instead of the fluxes. In figure 6.5, all galaxies for which those indexes can be measured, are plotted. The lines are the empirical separation between star-forming galaxies and AGNs of Kauffmann et al. (2003a) defined by

$$\log\left(\frac{[\text{O III}]}{\text{H}\beta}\right) = \frac{0.61}{\log\left(\frac{[\text{N II}]}{\text{H}\alpha}\right) - 0.05} + 1.3 \quad (6.10)$$

and the theoretical one of Kewley et al. (2001)

$$\log\left(\frac{[\text{O III}]}{\text{H}\beta}\right) = \frac{0.61}{\log\left(\frac{[\text{N II}]}{\text{H}\alpha}\right) - 0.47} + 1.19 \quad (6.11)$$

The separation among types is made using $[\text{O III}]/\text{H}\beta > 3$ and $[\text{N II}]/\text{H}\alpha > 0.6$, with the latter test also used independently for all galaxies where these two lines are present. This occurred more often than in the combination of the four lines.

The latest test was proposed by Yan et al. (2006) and only uses the ratio between [O II] and H α equivalent widths and is aimed mainly to detect LINERs.

$$W_0([\text{O II}]) > 5 \cdot W_0(\text{H}\alpha) - 7 \quad (6.12)$$

In total, 10 cluster galaxies show some signs of AGN activity with 6 of them classified as “red star-forming”. Note that all AGN candidates lie close to the boundaries of the respective tests, meaning that their nuclear activity is rather low. The exclusion of those AGNs candidates does not affect the results shown in Figures 5.2 and 5.3, which is expected since AGN frequency is not correlated with environment (Miller et al. 2003 and Figure 6.4).

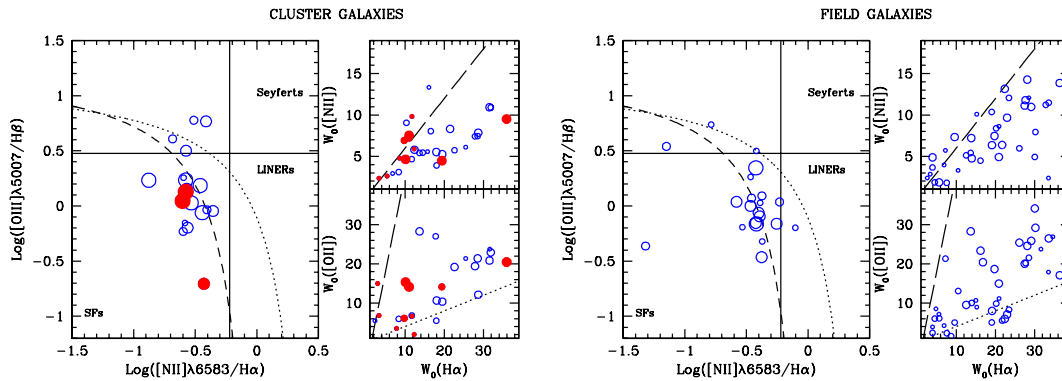


Fig. 6.5: Line ratio diagnostic diagrams for cluster and field galaxies to identify AGNs as indicated at the top of figures. At the left of each panel is BPT plane showing the relation between four important emission lines. The dashed curve is the empirical separation between AGNs and star-forming galaxies, whereas the dotted line is the theoretical one (see text). The vertical and horizontal lines are the approximate separation between types. At lower right of each panel is the [O II]-H α diagram aimed to identify LINERs. The dotted line is the local Kennicutt relation for star-forming galaxies (see also Figure 6.2), whereas the dashed line is the proposed Yan et al. (2006) test. At upper right of each panel is the relation between [N II] and H α equivalent widths. Blue open circles are “normal” star-forming galaxies and red filled ones are the red star-forming galaxies. The size of the symbols is related to the confidence with which each index can be measured, the larger the better.

6.3.2 The effects of dust

Dust extinction is an important contributor to the galaxy SEDs and its effects are measurable in the broad-band colors. However, it does not strongly affect the measurement of the equivalent widths because it obscures similarly the line and the surrounding continuum. So, it is possible that those galaxies have red colors as a consequence of dust extinction.

Extinction is, however, dependent on the galaxy geometry (as well as in the amount of dust content), therefore morphological analysis is necessary to quantify its contribution. The *ground-based* INT images used in this study do not allow to firmly state the morphological properties of the sample at a typical seeing of ~ 1 arcsec. Nevertheless, galaxies in this sample usually have an apparent size of 5–10 arcsec and so basic properties can be obtained. After examination, it was found that out of the 25 “red star-forming” galaxies, 11 are clearly spirals, 11 appear bulge dominated, 2 irregular and one shows signs of interaction (which is also an AGN candidate).

By following the extinction laws for disk galax-

ies of Tully & Fouque (1985), the amount of extinction can be estimated for those disk galaxies. At $z \approx 0.25$, the *V* and *I* filters correspond approximately to resframe *B* and *R*-bands. The extinction in *B*-band is defined by

$$A_B^i = -2.5 \log \left[f \left(1 + e^{-\tau \sec i} \right) + (1 - 2f) \left(\frac{1 - e^{-\tau \sec i}}{\tau \sec i} \right) \right], \quad (6.13)$$

where i is the inclination angle of the galaxy, $f = 0.25$ is the disk thickness, assuming that stars and dust are mixed homogeneously. An optical depth of $\tau = 0.55$ was derived by Tully & Fouque (1985) for a sample of local galaxies using optical and infrared data.

At a given inclination angle, the extinction in the *R*-band is $\sim 0.56A(B)$, therefore only disk galaxies with inclinations larger than 60° will have a correction factor $A(B - R) > 0.2$ mag (e.g. Böhm et al. 2004), a value sufficiently large to pull them out of the red-sequence.

Out of the 11 spirals, 8 are probably edge on

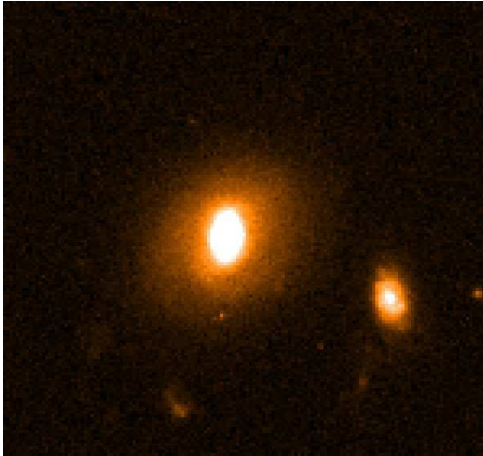


Fig. 6.6: HST/WFPC2 image of the elliptical galaxy ba_37 near the center of the VMF131 cluster, which shows emission lines despite its red colors, likely due to non-thermal emission.

galaxies and the remaining three, face on. As dust properties at $z \sim 0.25$ are not much different than in the local Universe (*e.g.* Clements et al. 2005), extinction can only account for a fraction of the detected red emission lines objects, as highly tilted galaxies are easily distinguished.

The elliptical galaxy ba_37

The cluster VMF131 was observed in the central parts by Balogh et al. (2002b) using the Hubble Space Telescope. Those observations only cover the inner 2.5×2.5 arcmin of the cluster and thus can not be used in the present panoramic study. However, at least, those high-resolution images allowed to identify one of the red “star-forming” galaxies.

This object is identified as ba_37, because it was previously observed by Balogh et al. (2002a) using the same setup (see §2.4.1). It has a $V - I$ color of 1.7 mag, well within the red-sequence for that cluster. In Figure 6.6, it can be appreciated that its morphology is clearly early type. Despite of this, ba_37 shows emission lines. However, it is possible that they are due to non-thermal emission (*i.e.* AGN) as the $\log([\text{N II}]/\text{H}\alpha) \approx -0.07$ (see Figure 6.5). Nevertheless, its activity is rather low as $W_0(\text{H}\alpha) = 11.8 \text{ \AA}$.

6.4 CHEMICAL ABUNDANCES

Emission lines are useful tools to determine several physical parameters of the star-forming regions, such as temperature, density, ionization state and chemical abundances. However, to determine all those parameters with accuracy, is required to observe a full set of sensitive lines, a requirement rarely found in extragalactic surveys given the weakness of many key lines.

However, if the galaxy emission is dominated by giant H II regions ($M > 60M_\odot$), the strong line method can be applied. This method is based on the fact that giant H II regions form a narrow sequence, in which the hardness of the ionizing radiation field is closely linked to the metallicity (*e.g.* Dopita et al. 2000). This is because a higher metal content enhances the metal line blocking of the emergent stellar flux in the extreme ultraviolet and softens the ionizing spectrum (Dopita et al. 2006).

The main advantage of these methods is that emission lines can be measured at higher signal-to-noise than the typical absorption lines used to derive chemical abundances (*e.g.* Lick indices, Trager et al. 1998). Absorption lines methods also have the drawback that in age and metallicity produce similar effects, being necessary extra assumptions in order to break the degeneracy.

The disadvantage of emission line techniques is that the analysis is limited to emission line galaxies, however they reflect the present day metallicity rather than the mean abundances of their integrated stellar populations.

Another key point is that strong line methods are statistical and thus have to be calibrated. The reliability of these methods does not only depend on the choice of an adequate indicator, but also on the quality of the calibration. This calibration can be done by using grids of photoionization models (*e.g.* McGaugh 1991), photoionization combined with stellar population models (*i.e.* IMF, *e.g.* Kewley & Dopita 2002) or from abundances derived from direct methods (*e.g.* Pettini & Pagel 2004) which can be obtained only for the nearby objects.

The strong line method makes use of different combination of strong lines such as $[\text{O II}]\lambda 3727$,

[O III] λ 3869, H β , [O III] λ 4959, [O III] λ 5007, H α , [N II] λ 6584, [S II] λ 6716,6731, [Ar III] λ 7135 and [S III] λ 9069 (*e.g.* Alloin et al. 1979, Pagel et al. 1979, Storch-Bergmann et al. 1994, Dopita et al. 2000, Stasińska 2006, etc).

Each combination has caveats and advantages, and abundances derived from different methods or calibrations may give differences up to 0.5 dex for the same objects. Charlot & Longhetti (2001) and Kewley & Dopita (2002) have proposed to use as many lines as possible in order to disentangle different effects. Tremonti et al. (2004) have done so in the largest galaxy compilation based on bright objects in the SDSS at $z \sim 0$, confirming the tight correlation between galaxy mass and metallicity.

In this section, the abundances for a subset of emission line galaxies will be explored. For this, the AGN candidates were removed from the sample, because their emission may be caused by a completely different mechanism. The sample is much smaller since only few galaxies show all required lines. Indeed, few of them even show the [O III] or the H β emission lines. So, the conclusions may be affected by incompleteness.

The abundances will be expressed in terms of $12 + \log(\text{O}/\text{H})$, where O/H is the oxygen abundance relative to hydrogen. Oxygen is an important sub-product of stellar evolution and displays a relevant peak in the element abundances. Its ions produce very bright lines in the spectra of star-forming regions.

Metallicity is a popular term in the literature to refer to the chemical enrichment. It is more often found in studies that use stellar population synthesis models, as it mainly refers to the iron abundance.

The relation between oxygen abundances, obtained via gas-phase models, and iron metallicities, from stellar population models, has proven problematic. This is in part due to that gas-phase abundances are more firmly determined for strong star-forming galaxies, whereas absorption lines methods work better in passive galaxies. For example, Gallazzi et al. (2005) examined the sample of Tremonti et al. (2004) obtaining metallicities from absorption lines. They found that gas-phase abundances are ~ 0.5 dex higher than those obtained

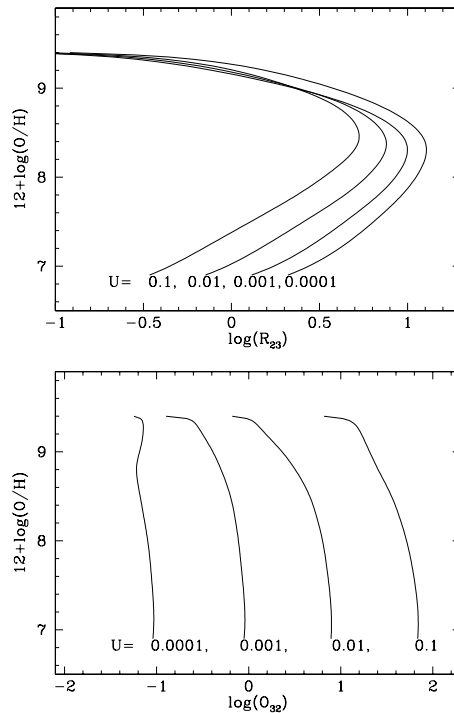


Fig. 6.7: O/H abundances versus the R_{23} and O_{32} in McGaugh (1991) models for several ionization states (U). Note the degeneracy on O/H for single values of R_{23} .

from stellar population models.

This result is expected as the metallicity from stellar light is the average from the whole stellar population, including the first generation of metal poor stars. However, a large fraction of “oxygen” rich galaxies shows a large variation on “iron” metallicity, which may be due to the saturation of gas phase abundances models (some are not very sensitive to high metallicities) or to physical processes like gas inflow and outflows, putting constraints on closed-box models of galaxy evolution.

6.4.1 The R_{23} method

This method was first proposed by Pagel et al. (1979) and subsequently has been developed by many authors. It makes use of the intensity ratio of [O II] λ 3727, H β , [O III] λ 4959 and [O III] λ 5007. Those lines are generally strong and are accessible by optical spectrographs up to large redshifts which

has made it very popular.

The abundances derived from those lines are obtained with a combination of the abundance sensitive parameter

$$R_{23} = \left(\frac{I[\text{O II}] + I[\text{O III}]_{\lambda 4959} + I[\text{O III}]_{\lambda 5007}}{I_{\text{H}\beta}} \right) \quad (6.14)$$

and the ionization sensitive parameter

$$O_{32} = \left(\frac{I[\text{O III}]_{\lambda 4959} + I[\text{O III}]_{\lambda 5007}}{I[\text{O II}]} \right) \quad (6.15)$$

where I is the intensity (flux) of the respective line.

The main caveat of this method is the degeneracy of the O/H ratio for reasonable values of R_{23} (see Figure 6.7). Via alternative models, it has been found that galaxies with $M_B < -18$ in the local Universe generally lie in the upper branch of the relation (see §6.4.2).

The Figure 6.7 shows the O/H dependence versus R_{23} and O_{32} for various values of the ionization parameter U , according the models of McGaugh (1991). There, U relates the ionizing photon density to the gas density. The grids provided by McGaugh (1991) include values of $U=0.1, 0.01, 0.001, \text{ and } 0.0001$, which cover the full range of values found in galactic H II regions (intermediate values are typical). Note that for low metallicities, O/H is almost insensitive to O_{32}

Based on those models, Kobulnicky et al. (1999) parameterized those tracks dividing them into the “upper” metal-rich and “lower” metal-poor branches. Since, all galaxies in the sample used in this work have $M_B < -18$, only the “upper” branch parameterization will be used. A further test is described in the next section. The parameterization is given by,

$$\begin{aligned} 12 + \log(\text{O}/\text{H}) = & 12 - 2.939 - 0.2x - 0.237x^2 - \\ & - 0.305x^3 - 0.0283x^4 - y(0.0047 \\ & - 0.0221x - 0.102x^2 - 0.0817x^3 \\ & - 0.00717x^4) \end{aligned} \quad (6.16)$$

where $x = \log(R_{23})$ and $y = \log(O_{32})$.

The original R_{23} method requires line intensities of which this work lacks, as the spectra are not flux calibrated. This is a caveat found in many other similar works in the distant Universe. With this issue in mind Kobulnicky & Phillips (2003) extended the R_{23} method to be used only with equivalent widths.

The [O III] and the H β lines are sufficiently close to neglect the effect of extinction and variation on the continuum shape, which is not the case for [O II]. So, the above equations can be written as

$$R_{23} = \left(\frac{\alpha_{2\beta} W_0([\text{O II}]) + W_0([\text{O II}]) + W_0([\text{O III}])}{W_0(\text{H}\beta)} \right) \quad (6.17)$$

where $\alpha_{2\beta}$ is the extinction between [O II] and H β .

Similarly the ionization sensitive parameter

$$O_{32} = \left(\frac{W_0([\text{O III}]) + W_0([\text{O III}])}{\alpha_{23} W_0([\text{O II}])} \right) \quad (6.18)$$

where α_{23} is the extinction between the [O II] and [O III] lines.

As H β and [O III] are at similar wavelengths $\alpha_{23} \approx \alpha_{2\beta}$, it is simply called α .

The advantage of using equivalent widths is that they are almost insensitive to extinction, which allows to apply the method, even when reddening corrections are not available. The reason why equivalent widths work well for integrated spectra of galaxies is that there is a very close empirical correlation between line intensities ratios and equivalent widths ratios, meaning that, statistically, galaxy stellar and nebular properties as well as the reddening are closely interrelated. In the presence

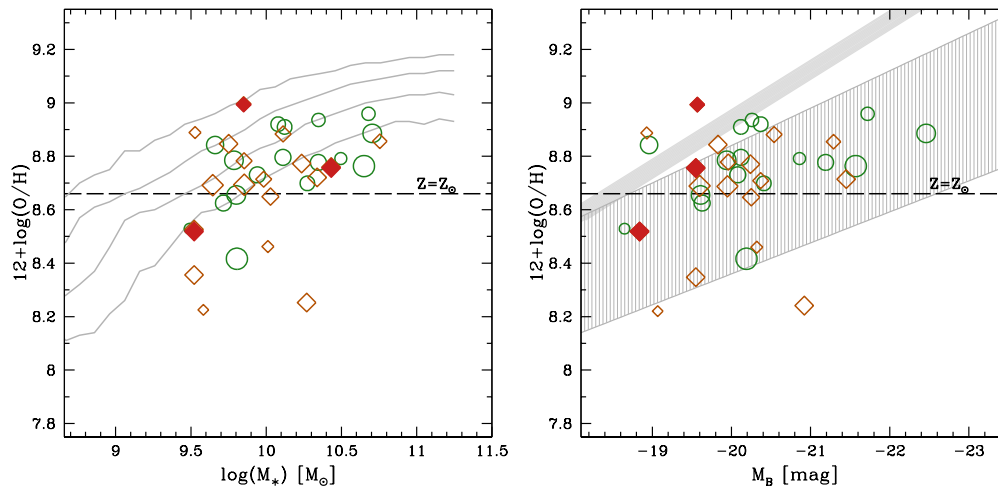


Fig. 6.8: O/H abundances versus stellar mass and M_B for field and cluster galaxies based on the R_{23} indicator (see text). Diamonds and circles are cluster and field galaxies respectively. Galaxies with higher S/N are represented with larger symbols. The three filled red diamonds are “red star-forming” galaxies. The grey contours in the left plot as well as the thick line in the right plot are the SDSS local measurements of Tremonti et al. (2004). The hatched area in the right plot are measurements of Kobulnicky et al. (2003) for distant galaxies. The dashed horizontal line is the solar abundance $12 + \log(\text{O}/\text{H}) = 8.66$ (Asplund et al. 2004).

of gray dust, the extinction is a simple function of wavelength (Charlot & Fall 2000) and therefore the differential extinction between the $H\beta$ –[O III] region and the [O II] line is just a scaling, which is measured, in this case, by α . For a sample of local galaxies spanning a large range of luminosities $\alpha = 1$ is a good assumption and introduces errors not larger than those inherent to the R_{23} method (Kobulnicky & Phillips 2003).

Larger uncertainties are, however, introduced by variations in the continuum, due to the different stellar populations found among galaxies. In order to correct this effect, Liang et al. (2007) analyzed a large subsample of SDSS galaxies finding that α correlates very well with the $D_n(4000)$ continuum index. The break at 4000 \AA is a strong discontinuity mainly produced by the accumulation of several lines in a small part of the spectrum. In old galaxies the light of this region is dominated by type A and G stars, which display this break, whereas young galaxies are dominated by hotter stars in which the elements are multiple ionized and thus the $D_n(4000)$ strength decreases. Because of that, it has been widely used to characterize the stellar pop-

ulations of distant galaxies as it can be measured at higher signal to noise than typical Lick indices used by other works, however, its sensibility to different effects is not straightforward (e.g. Moran et al. 2007a, Tanaka et al. 2007).

The correction for α using the $D_n(4000)$ index is given by:

$$\alpha = 10.88 - 18.31x + 11.18x^2 - 2.34x^3 \quad (6.19)$$

where $x = D_n(4000)$.

Another source of uncertainty not included in the Kobulnicky & Phillips (2003) analysis is the absorption in $H\beta$ from the underlying stellar populations. Young stellar populations as those found in star-forming galaxies contribute to this effect and therefore, $H\beta$ is sometimes used as an indicator of age in stellar systems (Trager et al. 1998), but in galaxies, it is strongly affected by emission filling. The relative contribution of absorption and emission is usually calculated via double Gaussian fitting to the absorption and emission. However, the spectra used in this work do not have the resolution,

and in many cases, neither the signal to perform this analysis adequately.

Fortunately, the contribution in $H\beta$ can be calculated by using the $H\delta$ line. This line is rarely present in emission (except in the strongest starbursts) and for all galaxies in this work it is in absorption. It also suffers of emission filling but to a much lesser degree than $H\beta$.

For a range of ages and metallicities and different star-formation histories is found that both lines scale in emission as

$$W_0(H\delta)_{emi} \approx 0.18W_0(H\beta)_{emi} \quad (6.20)$$

and in absorption as

$$W_0(H\delta)_{abs} \approx 1.3W_0(H\beta)_{emi} \quad (6.21)$$

in the models of González Delgado et al. (1999).

As the measured equivalent widths for those lines are the sum from both contributions the equations can be easily solved and the actual $H\beta$ emission obtained.

Following the above formulae, O/H abundances were obtained for all galaxies where all the lines are available. The results can be seen in Figure 6.8 plotted against stellar mass (M_*) and M_B . They are directly compared with the relation found in the local Universe by Tremonti et al. (2004), and in the case of M_B against the distant relation of Kobulnicky et al. (2003) for galaxies between $0.26 < z < 0.82$.

Tremonti et al. (2004) obtained the metallicities from a more refined method using several emission lines, but subsequent analysis by Liang et al. (2006) using the R_{23} method found slightly lower abundances, well within the uncertainties in Figure 6.8. Kobulnicky et al. (2003) only used the equivalent width R_{23} method, so their results are directly comparable.

The star-forming galaxies in the present study display lower oxygen abundances at fixed mass or luminosity than their local counterparts. The luminosity-metallicity relation found is statistically similar to the one observed in the distant surveys.

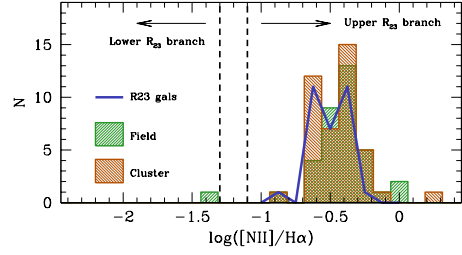


Fig. 6.9: Distribution of galaxies in the $N2$ test aimed to distinguish the “upper” and the “lower” branches. Note that all but one galaxy are in the “upper” branch of the distribution. The R_{23} galaxies are those which have are actually used in that test.

The mass-metallicity relation is present in the sample. No difference is detected between field and cluster galaxies, adding another piece of evidence that both populations are composed of similar objects.

This provides an adequate explanation for the abnormal relation between $[O\text{II}]$ and $H\alpha$ equivalent widths, as the ratio of those lines depends on metallicity. Lower $[O\text{II}]/H\alpha$ ratios imply larger oxygen abundances, because the $[O\text{II}]$ luminosity is sensitive to electron temperature. Lower temperatures are associated with higher abundances (Kewley et al. 2004). This is the reason why the R_{23} method is sensitive to metallicities as it is basically an indicator of the total cooling due to oxygen, one of the principal nebular coolants.

6.4.2 The $N2$ and the $O3N2$ indices

Those tests were first proposed by Alloin et al. (1979) and later calibrated by Pettini & Pagel 2004 using a set of galactic and extragalactic $H\text{II}$ regions. The $N2$ index is simply defined by

$$N2 = \log\left(\frac{[N\text{II}]\lambda 6584}{H\alpha}\right) \quad (6.22)$$

and the $O3N2$ by

$$O3N2 = \log\left(\frac{[O\text{III}]\lambda 5007/H\beta}{[N\text{II}]\lambda 6584/H\alpha}\right). \quad (6.23)$$

As each pair of lines have similar wavelengths, flux calibration and reddening correction are not required and the indicators can easily be worked using equivalent widths. Also, those indicators are not double valued in metallicity as the R_{23} method, allowing to test the full range of galaxy masses without needing extra assumptions.

However, they are not free of problems. The $N2$ index is particularly sensitive to shock excitation or the presence of a hard ionizing radiation field, for example from AGNs. So, it only provides a crude estimation of metallicity (Kewley & Dopita 2002).

Furthermore, those indicators are not very good at high metallicities as the $[N\ II]$ line saturates at super-solar abundances. This is particularly problematic for the $N2$ index as the inclusion of $[O\ III]$ in the $O3N2$ index allow it to gain still some sensibility at high abundances (Kewley & Dopita 2002, Kewley & Ellison 2008). The relation between O/H and indices values is given by simple linear formulae (Pettini & Pagel 2004). Because of that, those indices have found great utility in discerning the branches for emission line galaxies, where the better characterized R_{23} method can be applied.

In Figure 6.9 the distribution of the $N2$ index is plotted for all galaxies where it can be measured, which is a larger sample than those which are used in the R_{23} test. The division between branches is from Kewley & Ellison (2008). Note that all but one galaxy are in the “upper” branch, so, one can be confident on the results shown in the previous section.

6.5 STAR-FORMATION VERSUS STELLAR MASS

In Figure 5.6, the fraction of star-forming galaxies was plotted against galaxy stellar mass. It was found that few massive systems are forming stars, despite the environment, whereas most of the lower mass galaxies display a healthy star-formation activity, except in the inner cluster environment, where the fraction remains low for the whole mass range sampled by this study.

In Figure 6.10, the specific star formation rate (sSFR) is plotted against stellar mass for individual objects. In this case, however, many of passive

galaxies with negative equivalent widths (*i.e.* “negative” star-formation) were omitted.

Star-forming galaxies populate, in this case, a relatively narrow region, a “blue sequence” (Blanton 2006) which has a width of about one order of magnitude in sSFR.

On the other hand, passive galaxies are located in a “red cloud”. This may cause confusion as similar terms (blue cloud and red-sequence) are commonly used in color-magnitude diagrams. However, it is necessary to keep in mind that this red cloud span several order of magnitude on sSFR, due to the low or zero level of activity in cluster ellipticals. This is not clearly appreciated here, because this low activity is difficult to detect and the faint emission lines are erased by the noise. Therefore, the sSFRs for many of the passive objects are only an upper limit.

Here, the “star forming sequence” is compared with the local relation found in the large, UV-selected sample of Salim et al. (2007) at $z \sim 0$,

$$\log sSFR = -0.36 \log M_* - 6.4 \quad (6.24)$$

The “normal” star-forming galaxies are well described by this relation.

On the other hand, the “red” star forming galaxies appear to be transition objects populating the “green valley” (Schiminovich et al. 2007) between the “blue sequence” and the “red cloud”.

The mean sSFR for normal star-forming galaxies is $\sim (1.08 \pm 0.65) \times 10^{-10} \text{ yr}^{-1}$, whereas the red star-forming galaxies have on average $sSFR \approx (2.4 \pm 0.6) \times 10^{-11} \text{ yr}^{-1}$, about an order of magnitude lower. The average upper limit for passive galaxies is $sSFR \approx (4.8 \pm 3.3) \times 10^{-12} \text{ yr}^{-1}$ as galaxies with unphysical star-formation rates were not considered.

Note, that those red star-forming galaxies may also be present in the field, but they are difficult to identify, given the uncertainties in the k -corrections (~ 0.2 mag, larger than the typical red-sequence scatter).

The Figure 6.10 is very illustrative to understand the current galaxy evolution picture. Galaxies along the blue sequence slowly gain mass via accretion and merger processes. They may experi-

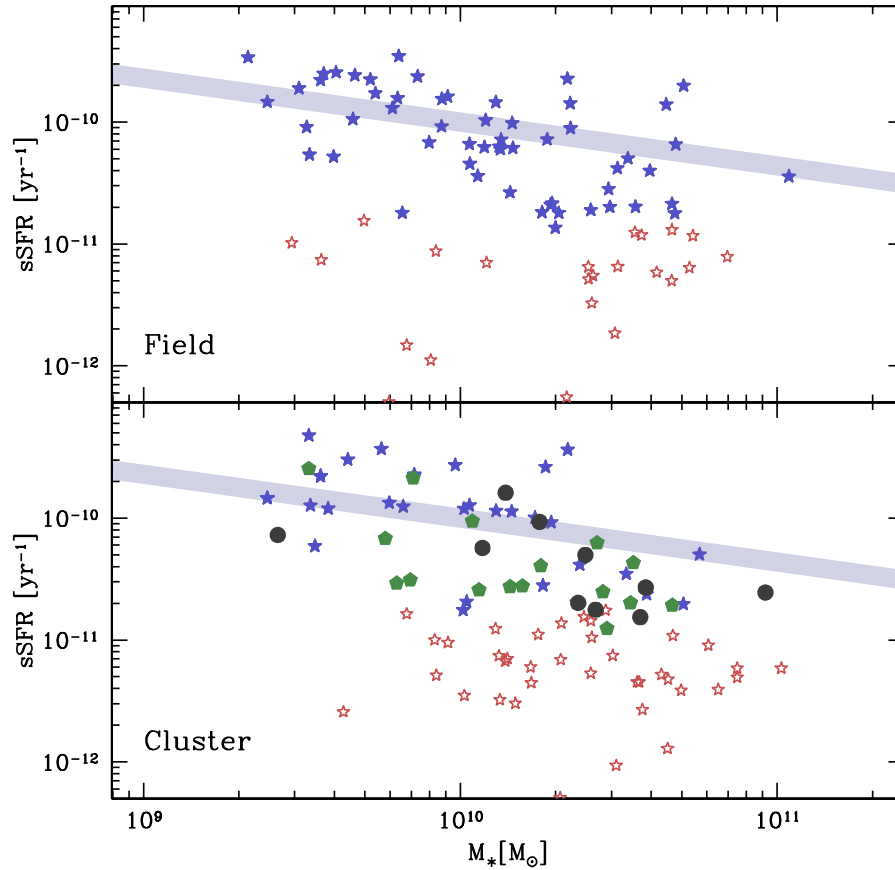


Fig. 6.10: Specific star formation rates for field (top) and cluster (bottom) galaxies versus stellar mass. Normal star-forming galaxies are plotted with blue filled stars and the red star-forming galaxies with green pentagons. The red open stars are passive galaxies with $W_0([\text{O II}], \text{H}\alpha) < 5$ and are shown for comparison. The black circles are the AGN candidates. The thick line is the local relation from Salim et al. 2007.

ence starbursts as results of interactions, or a partial slowdown in their activity. This may produce of the scatter in the relation. But, in the global terms, their sSFR is reduced as their masses increase.

This is likely due to the influence of two effects, *i*) Feedback mechanisms, specially AGN activity (Croton et al. 2006) which prevents further cooling of the hot galaxy halo and becomes more important as the mass of the system increases. *ii*) Environmental processes as larger systems tend to be located in regions of higher galaxy density (Hogg et al. 2003). Note that galaxy overdensities can be also present in the rare-field and some of the

processes that shut down the star-formation may be still effective there.

On the other hand, gas exhaustion or gas removal via interactions or feed-back processes lead to a quenching of the star-formation, moving the galaxy into the red cloud. There, it can experience small episodes of star-formation if cold gas is still available or accrete more gas and move again into the blue sequence. However, it will stay, permanently, in the red cloud if the environment is hostile, as occurs in galaxy clusters.

In this picture, those red “star-forming” galaxies

appear to be in an intermediate stage between the two main types with lower but a still appreciable amount of star-formation.

Those galaxies, however, do not appear to be a homogeneous class of objects. They are composed by dusty spirals, bulge dominated objects and low luminosity AGNs. A larger and more careful study would be necessary to determine their abundance with cosmic times. As the assembly of the red-sequence and the star-formation decline are subject of continuous investigation (*e.g.* Bell et al. 2005), this population may provide a link between this two effects. However, much caution must be taken in the treatment of dust extinction and AGN activity.

Summary and conclusions

The mixture of galaxy types in clusters and the field is different in the local Universe. Going to higher redshifts, the galaxy population is also changing within clusters with look-back time. This may be caused by their late assembly epoch predicted by bottom-up scenarios of structure formation or due to cluster-specific interaction processes.

In this thesis, the main findings of a panoramic spectroscopic campaign are presented. It has been focused in 6 clusters at $z \approx 0.25$ (~ 3 Gyr of look-back time). The spectra cover a large wavelength range, allowing to explore the galaxy properties using different indicators. The observations targeted galaxies from the cluster cores to the outskirts, allowing to study the galaxy evolution in the interface between cluster and field.

Almost 600 spectra obtained with MOSCA at the 3.5m telescope at Calar Alto Observatory were examined, including those from previous projects. Approximately 300 were useful for further analysis. They are splitted in ~ 150 cluster galaxies and about the same number for field galaxies. In order to equalize the sample only ~ 90 field and ~ 120 cluster galaxies were used for direct comparison.

Multicolor photometry has also been used to complement the spectroscopy as well as X-ray analysis from previously published studies.

This work has made use of the automatic and interactive algorithms which have permitted to characterize better the properties of the sample. State-of-the-art codes have been used to calculate absolute magnitudes and stellar masses.

The long wavelength range covered by the spectra permitted an unbiased differentiation among galaxy types.

The main findings can be summarized as following:

1. During the analysis of the redshift and spatial distribution of the galaxies in the studied fields four group candidates were serendipitously found. One and the largest of them overlaps in its position with the cluster VMF194, resolving thereby the doubts about its redshift. This large group may have contaminated the X-ray measurements of previous authors.
2. According to standard techniques most of the clusters appear to be in a virialized state with the notable exception of XDSCS220. Nevertheless, there are differences among them. Some exhibit a great deal of substructure, either evidenced by dynamical or photometric analysis.

For example, a X-ray structure, detected by previous studies in the field of one of the clusters (VMF73), is likely part of it, as its position coincides with spectroscopic and photometric structures and has a noticeable effect on the galaxy population of this cluster.

This difference is not only restricted to the dynamic but also to their galaxy content. The fraction of star-forming galaxies is different among the clusters, but is not possible to establish with the current data whether there is a correlation with global cluster properties.

An important fraction ($\sim 45\%$) of the cluster star-forming galaxies has red colors compatible with those typically found in ellipticals. The abundance of those galaxies is also varying among the clusters.

3. Those red “star-forming” galaxies are not composed of a homogeneous class of objects. Some are ellipticals with low levels of AGN activity. Others appear to be obscured highly inclined objects but otherwise normal spirals. These two classes are not able to fully explain the abundance of these rare objects, as some are face-on spirals whereas others appear to be bulge dominated objects. They are not preferentially located in any environment. They appear to be in an intermediate stage between “normal” star-forming galaxies and passive ones, as their levels of star formation activity is about one order of magnitude lower than the typical star-forming population, but still much higher than the bulk of passive galaxies.

Some authors have also found those objects at different redshifts. They are often interpreted as galaxies with a large component of old stellar populations and dust extinction. However, it is intriguing that otherwise normal star-forming objects have the precise amount of dust and old stellar populations to make them fall into the passive sequence. It is an issue that surely warrant further investigation.

Those galaxies may also exist in the field, but they can not be identified precisely, as the errors associated to the measurements are larger than the scatter of the red-sequence which was used to identify them in clusters.

4. It has been found that emission line galaxies in the field and in the clusters have abnormal [O II]-to- $H\alpha$ ratios. Possibilities suggested by previous authors were explored. High levels of AGN activity has been discarded as an important cause. It has been found, in fact, that the lower chemical abundances displayed by those galaxies compared to local counterparts are possibly the main source of this peculiarity.

The chemical abundances are function of mass

and luminosity and are compatible with the values found by other authors. No difference is detected between field and cluster star-forming galaxies.

The effect of lower metallicity does not appear to have an impact in the derived star-formation rates, although there is marginal evidence that the [O II]-derived SFRs are slightly overestimated at large values when they are compared with $H\alpha$ SFRs.

5. Analyzing the distribution of star-forming galaxies, it was found that it depends strongly on environment. The star-formation activity is strongly depleted at small clustercentric distances and high projected densities. At $R \approx 3R_{vir}$ and $\Sigma_5 \approx 10 \text{ Mpc}^{-2}$, the activity approaches to typical field values. This can be seen either in the fraction or in the mean equivalent widths (which were found to correlate extremely well with specific star formation rates).

Although, it is difficult to make direct comparisons with published works at $z \sim 0$, the star-forming-density appear to be evolving. The trend appears to be steeper as the star-forming activity in the field is higher at $z \approx 0.25$ (35% at $z = 0$ versus $\sim 55\%$ at $z \approx 0.25$).

However, once the star-forming population is analyzed, it was found that it is similar in *all* environments (including the field) and therefore, the change in the average equivalent widths is only driven by the relative abundance of the passive versus active population (the fraction) found in different environments. This puts strong constraints to the possible processes responsible of the suppression of the star-formation activity, arguing against soft mechanisms of galaxy transformation.

6. Nevertheless, the field, the infall and the cluster galaxy populations are different. The fraction of star forming galaxies depends on the stellar mass, but this fraction shows a different behavior for each environment. Galaxies with higher masses are strongly suppressed in all environments, but intermediated mass ones display the largest change with few of them forming stars in the inner cluster. Dwarf

galaxies appear unaffected between the field and the infall region.

Comparing this with published results at similar redshifts, it was found, that the galaxy population in the infall regions is indeed very “group-like” indicating that group preprocessing may play an important role in the galaxy evolution in clusters. Once that some galaxies are transformed by this environment, they enter deeper in the cluster core, which further quench the star-formation.

7. Much caution must be taken with the universality of the environmental trends. At least two clusters display a very different environmental distribution. In the light of the evidence, appears that cluster of galaxies are unique objects whose characteristic ,and those of their galaxy populations, may depend of more subtle properties rather than purely processes related to the mass, such as their X-ray luminosity. It is possible that the cluster assembly history as well as the surrounding environment in large scales play an important role. This may explain the large scatter on galaxy populations cluster-to-cluster reported by several authors.

Several possible scenarios were analyzed in order to explain the environmental trends. It was found that starvation is unable to stop the star-formation in the necessary time-scales and unlikely would be able to reproduce the trends. It is possible that this mechanism is at work in groups as a form of preprocessing, but this is beyond of the scope of this work.

The current understanding of ram-pressure stripping, as well as the other strong interactions between galaxies and the intracluster media, may be able to explain to a great extent the environmental trends, as their times scales match better. The main constraint for this scheme is the low density environment where the decrease of the star-formation is detected. It is still possible that ram-pressure is acting in filaments and groups as suggested by some authors, although this hypothesis is difficult to test here.

In that case, additional processes may be acting. In particular, mergers are thought to be effective in groups. Possible evidence of this, is found in the

fact that the star-formation activity for low mass galaxies remains unchanged between the field and the infall environment. Those galaxies are thought to be sensitive to ram-pressure , but are resilient to merger. It was not possible to study their fate in the inner cluster core.

Galaxies with larger masses display the opposite behavior and it was detected that intermediate mass galaxies do experience a change in their star-formation activity between the field and the infall region. They are further processed in the inner core. Galaxies at the high mass end display low level of star-formation despite their environment.

Therefore, there is still room left for mergers as an important mechanism in “pre-processing” galaxies before they enter in the inner cluster core.

It is important to stress again that galaxies in each cluster may evolve differently as the processes may have dissimilar importance.

Outlook & future work

This thesis has been mainly focused on the properties of cluster galaxies with current star-forming activity at a single cosmologic epoch. They have been characterized in terms of environmental distribution, star formation activity, types and chemical content. Based on that, constraints about the possible processes that stop the star-formation activity in clusters have been set.

However, emission lines tell little about the past star-formation history (SFH) and, therefore, the processes that have shaped the passive galaxy populations. This information is contained in the stellar populations and can be accessed studying, for example, the absorption lines.

The spectra obtained for this project have some advantages and disadvantages for this type of study. The main advantage is the large wavelength span, which allows to study the stellar populations by using several absorption lines.

The disadvantages are the low spectral resolution and signal-to-noise of the data. For example, one of the most popular methods for studying the stellar content on galaxies, the Lick/IDS system (Worthey 1994, Trager et al. 1998), requires $S/N > 20$ and resolution $R > 8$ in order to accurately measure the lines and correct the line broadening induced by the stellar motions inside of galaxies. Those requirements are not present in this sample.

Nonetheless, there are some ways to overcome those caveats. The line broadening can be empirically corrected by using the already measured scaling relations for early type galaxies. In some of

those relations, the velocity dispersion of galaxies correlates with luminosity (among other parameters). Those relations have been already measured for galaxies at similar redshifts and little evolution with respect to the local relation has been found (Fritz et al. 2005). The parameters obtained from several lines can be also averaged to increase the signal.

Furthermore, in the very last years, new algorithms that fit SFHs to the whole spectra (*i.e.* continuum fitting) have become available (*e.g.* the `STARLIGHT` code, Cid Fernandes et al. 2005). In those codes a combination of spectral templates are fitted to the galaxy spectra and therefore ages, stellar masses, metal and dust content can be extracted from data with relatively low signal-to-noise.

All these analyses require exhaustive modeling in order to probe the whole parameter space and obtain reliable results. Even in that case, the results may be not useful as several processes contribute to the formation of the absorption lines. In particular the degeneracy between age and metallicity is very well known.

Furthermore, if the lines are particularly weak (as much in the sample), the $[\alpha/Fe]$ ratio may be not reliable obtained. This parameter is particularly important as α -elements (*e.g.* Mg) are though to be produced by core collapse supernovae, *i.e.* massive stars, whereas Fe is mainly produced by SNe Ia, whose progenitor are relatively low mass stars. As the explosions of SNe Ia are delayed with respect to the starburst for at least 2 Gyr, they do not con-

taminate the interstellar media immediately. Therefore, an α -enhancement in passive galaxies, *i.e.* a high $[\alpha/Fe]$ ratio, indicates that most of the stars were formed in a short period of time, likely in a strong starburst rather than in continuous formation (*e.g.* Thomas et al. 1999).

Due to all those difficulties this investigation was avoided in order to keep the focus on galaxies with current star-formation activity, but it is still considered a fundamental step and will be investigated in the future.

Nevertheless, some aspects of the stellar populations were explored by using diagnosis diagrams based on three important spectral features. They are shortly described in the next section.

8.1 DIAGNOSIS DIAGRAMS

The diagrams presented in Figure 8.1.1 reveal the galaxy distribution in the planes defined by the combination of the $D_n(4000)$ spectral index, the $H\delta$ absorption line and the $H\alpha$ emission line. Those features are widely used to probe the evolutionary state of galaxies as they can be usually observed up to larger redshift (except for the $H\alpha$ line) with good signal-to-noise.

In general, those diagrams are made using the $[O\text{II}]$ emission line as indicator of star-formation activity instead of $H\alpha$, as the latter line is rarely observed in distant redshift surveys. But, as indicated by Goto (2007) using only the $[O\text{II}]$ line may miss several obscured star-forming galaxies and thus the $H\alpha$ line should be used when present. In the figures, the opposite effect is also observed. Some star-forming galaxies have detectable $[O\text{II}]$ emission but no $H\alpha$.

The $H\delta$ absorption line is considered mainly an indicator of mean stellar age (Worthey & Ottaviani 1997), but this dependence is complex (Poggianti & Barbaro 1997), because its values are also affected by metallicity (Gallazzi et al. 2005). This makes this line to take negative values¹ even if no emission is present, as weak lines due to heavy elements are present in the

¹Note that $H\delta$ is defined as positive in absorption and negative in emission, however no galaxy in the sample exhibits emission in $H\delta$.

surrounding continuum.

The $D_n(4000)$ index presents further complexities. It depends on age and metallicity (*e.g.* Poggianti & Barbaro 1997), and it is also sensitive to the present to mean past star-formation rate (Kauffmann et al. 2003b). Despite of these problems, it is widely used because it is a strong feature in the galaxy spectra. It can be measured at higher signal-to-noise than other key features due to the longer wavelength span of the index, which is, however, not large enough to make important the effects of flux calibration. It can be considered a narrow band “color”, but since it is measured directly on the spectra, no k-correction is needed.

Galaxies in which those indexes were measured are plotted in a plane whose axes are two of these spectral features. The plane is subdivided according to the criteria of Balogh et al. (1999).

8.1.1 The $H\alpha$ – $H\delta$ plane

This is one of the most used schemes to distinguish galaxy spectral types. This plane is subdivided in the following subtypes.

- *Passive* – This is a galaxy that does not show significant levels of star-formation. Note, that some star-forming galaxies are still present in this region. They were detected by their $[O\text{II}]$ emission.
- *SF* – Star-forming galaxies. They are “normal” star-forming galaxies in the models of Poggianti & Barbaro (1997), *i.e.* the star-formation has lasted several hundred of millions of years.
- *SSB* – Short starburst. In the models of Poggianti & Barbaro (1997) those galaxies present emission in $H\delta$ and $[O\text{II}]$ (and therefore in $H\alpha$) as a consequence of a strong burst of star-formation. Few field galaxies are present in this region, but as stated before, none of the galaxies show $H\delta$ in emission, therefore the interpretation of them is unclear.
- *K+A* – They are galaxies that do not show emission but strong $H\delta$ absorption. Their

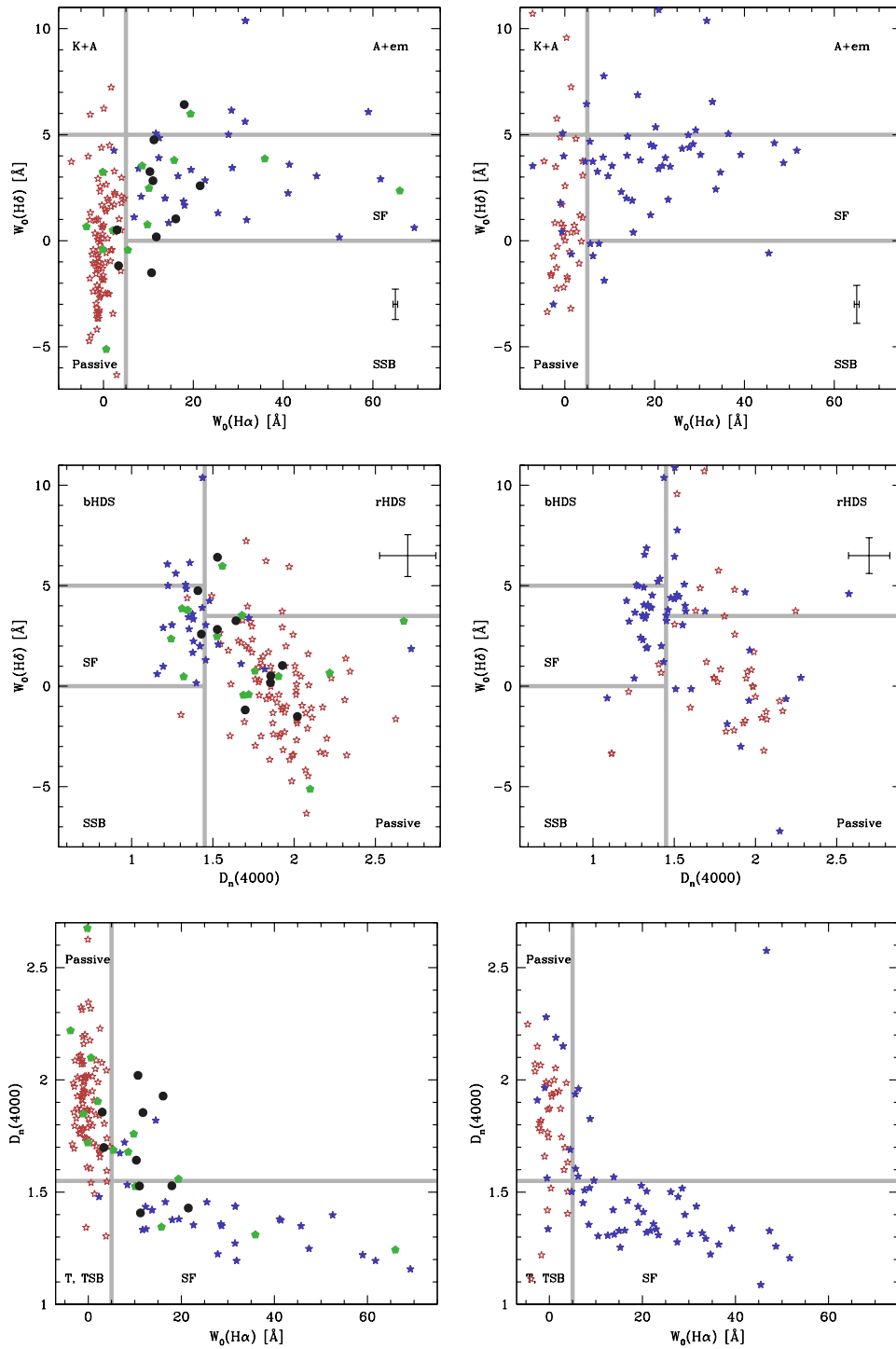


Fig. 8.1: Diagnostic diagrams for the evolutionary status of cluster (left) and field (right) galaxies, probed by their distribution in planes made of the combination of $D_n(4000)$, $\text{H}\delta$ and $\text{H}\alpha$ spectral indices. The open red and blue filled stars are passive and star-forming galaxies respectively. The green pentagons are the so-called red star-forming galaxies whereas the black circles are the AGN candidates. The subdivisions of the planes are described in the text.

spectra contain strong Balmer lines from A-type stars (hence the “A”). Therefore, they are often considered that they experienced a starburst in the last gigayear, which was which was suddenly truncated. This interpretation has led to numerous studies to determine their abundances and thus the importance of the processes that have taken them to this state. The conclusions have been often conflictive. For example Balogh et al. (1999) were not able to confirm the results of Dressler et al. (1999) who found a quite large fraction of K+A galaxies in distant clusters. In this study, the fraction of K+A galaxies appear to be small and similar in clusters and the field, which is in agreement with the large SDSS study of Hogg et al. (2006) who found little correlation between the post-starburst galaxy frequency and environment.

- *A+em* – The evolutionary status of these galaxies is unclear. They present both $H\alpha$ emission and strong $H\delta$ absorption. The active star-formation indicate the presence of O and B-type stars, which have weaker Balmer lines. Furthermore, the $H\delta$ line suffers of emission filling. Poggianti et al. (1999) suggested that they are dusty star-burst or alternatively AGNs. In the diagrams, it can be seen that most of them are “normal” star-forming galaxies in terms of their emission line ratio (only one cluster galaxy may be an AGN) and colors (one red star-forming galaxy), therefore those hypotheses appear, in principle, to be incorrect.

8.1.2 The $D_n(4000)$ – $H\delta$ plane

This diagram has been also used to diagnostic the evolutionary state of galaxies. Besides some of the classes described in the previous section, two more classes are added. They are the *bHDS* (blue $H\delta$ strong) and *rHDS* (red $H\delta$ strong).

Balogh et al. (1999) interpreted *bHDS* galaxies as post-starburst galaxies. However, in the diagram of Figure 8.1.1 they all show star-formation. On the other hand, galaxies classified as *rHDS* are considered as post star-formation galaxies, *i.e.* galaxies that had rather normal star-formation activity but

was quenched rather recently.

It can be seen in the diagrams, that the classification of the star-formation status of galaxies based solely in $D_n(4000)$ and $H\delta$ is far from perfect. Several low level star-forming galaxies (such as the red emission line objects) are located in the same regions as the passive galaxies.

8.1.3 The $D_n(4000)$ – $H\alpha$ plane

This is the latest diagram which can be considered roughly an spectral “color-magnitude” diagram, as the $D_n(4000)$ index correlates with stellar mass (Kauffmann et al. 2003b) and the $H\alpha$ emission line is a good indicator of star-formation activity.

Passive galaxies usually show strong $D_n(4000)$ break as a consequence of their old stellar populations, whereas activity star-forming galaxies display $H\alpha$ emission and weak $D_n(4000)$ indices. There are few galaxies with weak $D_n(4000)$ and no star-forming activity. Moran et al. (2007a) interpreted them as galaxies with truncated star-formation (T) and/or truncated star-burst (TSB), due to, for example, to the effects of ram-pressure stripping.

Few galaxies are found in the large upper right quadrant. Most of them are peculiar, some AGN candidates and red star-forming galaxies are present there.

Given the complex distribution of galaxy types in the previous described diagrams, results clear that extensive modeling is necessary to understand the galaxy evolutionary status. Including extra information from other key spectral features appears to be imperative.

8.2 INFALL REGIONS IN A MASSIVE CLUSTER AT $z = 0.45$

The project described in this thesis have proved for first time the infall regions of clusters at moderate redshifts. It has successfully been able to constrain some of the processes that stop the star formation in those environments. But, it is not exempt of weaknesses. The main one is the relative poor numbers

statistics and sampling in the outskirts. For example, it was not possible to investigate the substructure, such groups and filaments, in the infall regions. Those places may play an important role in preprocessing the galaxies before they enter in the clusters.

In order to overcome this caveat a new project was initiated. This exploratory study is focused in the outskirts of RXJ1347.5-1145, the most massive cluster currently known (Schindler et al. 1997). This cluster has been the focus of numerous observational campaigns with the objective of studying the characteristics of this extreme environment, via X-ray analysis (*e.g.* XMM-Newton observations by Gitti & Schindler 2004), strong and weak lensing (*e.g.* Bradač et al. 2005, 2007) and spectroscopic dynamical analysis (*e.g.* Cohen & Kneib 2002).

Those and other similar studies have been focused mainly in the inner regions of the cluster, up to 15 arcmin in X-ray from the center, about $2R_{vir}$.

With the objective of studying the large scale structure around this cluster a collaboration was started. Our partners are mainly interested on the weak lensing analysis in one square degree around the cluster center. For that, they have obtained wide field (1 deg^2) g , r , i and z imaging with the MegaCam wide field camera at the 3.6 m Canada-France-Hawaii telescope. Those images are deeper and have better quality than those used in the present study (seeing $\sim 0.8 \text{ arcsec}$). Full access to the images and catalogs has been granted.

By using similar techniques as those outlined in §4.2 several structures have been already identified. But, in this case, the multicolor photometry and the photometric redshifts allow to have greater confidence that those structures are real.

In order to study the galaxy evolution in those regions a proposal to the European Southern Observatory (ESO) was submitted² and it has been granted with 10 hours at the wide field VIMOS spectrograph mounted in one of the 8 m very large telescopes (VLT). Three fields were chosen for observation, each with two MOS masks. The multiplex³ advantage of the instrument will allow us to have a high filling factor in those structures, with

which we can detect filaments, groups and pairs of galaxies. This also eliminates any uncertainty due to selection function as the completeness is expected to be between 60 and 100% up to $I = 22.5 \text{ mag}$.

Archival spectroscopic observations already present for the central regions will be invaluable for comparing the evolution between field, cluster and infall environments. The larger wavelength range of our observation will permit to un-mistakenly identify the different galaxy types in a similar fashion that has been done in this thesis, as well as to make use of the full set of spectral features to constrain the galaxy stellar populations.

The spectroscopic analysis will allow to our partners to calibrate the photometric redshifts and the dynamics of the structures detected in the weak lensing analysis. The environment can be also probed by the distribution of dark matter obtained from the lensing analyses.

At the time of writing this thesis the required pre-imaging of the fields to be observed has been submitted to ESO.

²ESO program ID 381.A-0823(A), PI: M. Verdugo.

³The capability of placing more than one slit per row.

Bibliography

- Abadi, M. G., Moore, B., & Bower, R. G. 1999, *MNRAS*, 308, 947
- Abell, G. O. 1958, *ApJS*, 3, 211
- Abell, G. O., Corwin, Jr., H. G., & Olowin, R. P. 1989, *ApJS*, 70, 1
- Allen, S. W., Schmidt, R. W., & Fabian, A. C. 2002, *MNRAS*, 334, L11
- Alloin, D., Collin-Souffrin, S., Joly, M., & Vigroux, L. 1979, *A&A*, 78, 200
- Andreon, S., Quintana, H., Tajer, M., Galaz, G., & Surdej, J. 2006, *MNRAS*, 365, 915
- Arimoto, N. & Yoshii, Y. 1987, *A&A*, 173, 23
- Arp, H. 1966, *ApJS*, 14, 1
- Asplund, M., Grevesse, N., Sauval, A. J., Allende Prieto, C., & Kiselman, D. 2004, *A&A*, 417, 751
- Balcells, M. 1997, *ApJ*, 486, L87+
- Baldwin, J. A., Phillips, M. M., & Terlevich, R. 1981, *PASP*, 93, 5
- Balogh, M., Bower, R. G., Smail, I., et al. 2002a, *MNRAS*, 337, 256
- Balogh, M., Eke, V., Miller, C., et al. 2004a, *MNRAS*, 348, 1355
- Balogh, M. L., Baldry, I. K., Nichol, R., et al. 2004b, *ApJ*, 615, L101
- Balogh, M. L. & Morris, S. L. 2000, *MNRAS*, 318, 703
- Balogh, M. L., Morris, S. L., Yee, H. K. C., Carlberg, R. G., & Ellingson, E. 1999, *ApJ*, 527, 54
- Balogh, M. L., Navarro, J. F., & Morris, S. L. 2000, *ApJ*, 540, 113
- Balogh, M. L., Smail, I., Bower, R. G., et al. 2002b, *ApJ*, 566, 123

- Balogh, M. L., Wilman, D., Henderson, R. D. E., et al. 2007, *MNRAS*, 374, 1169
- Barnes, J. E. & Hernquist, L. E. 1991, *ApJ*, 370, L65
- Baum, W. A. 1959, *PASP*, 71, 106
- Becker, M. R., McKay, T. A., Koester, B., et al. 2007, *ArXiv e-prints*, 704
- Beers, T. C., Flynn, K., & Gebhardt, K. 1990, *AJ*, 100, 32
- Bekki, K. 2001, *ApJ*, 546, 189
- Bekki, K. & Couch, W. J. 2003, *ApJ*, 596, L13
- Bekki, K., Couch, W. J., & Shioya, Y. 2001, *PASJ*, 53, 395
- Bekki, K., Couch, W. J., & Shioya, Y. 2002, *ApJ*, 577, 651
- Bell, E. F. 2004, *ArXiv Astrophysics e-prints*
- Bell, E. F., Papovich, C., Wolf, C., et al. 2005, *ApJ*, 625, 23
- Bell, E. F., Phleps, S., Somerville, R. S., et al. 2006, *ApJ*, 652, 270
- Bell, E. F., Wolf, C., Meisenheimer, K., et al. 2004, *ApJ*, 608, 752
- Benson, A. J., Bower, R. G., Frenk, C. S., & White, S. D. M. 2000, *MNRAS*, 314, 557
- Bessell, M. S. 1990, *PASP*, 102, 1181
- Binggeli, B., Sandage, A., & Tammann, G. A. 1988, *ARA&A*, 26, 509
- Binney, J. 1978, *Comments on Astrophysics*, 8, 27
- Blanton, M. R. 2006, *ApJ*, 648, 268
- Blanton, M. R., Dalcanton, J., Eisenstein, D., et al. 2001, *AJ*, 121, 2358
- Blanton, M. R., Eisenstein, D., Hogg, D. W., Schlegel, D. J., & Brinkmann, J. 2005, *ApJ*, 629, 143
- Blanton, M. R. & Roweis, S. 2007, *AJ*, 133, 734
- Böhm, A., Ziegler, B. L., Saglia, R. P., et al. 2004, *A&A*, 420, 97
- Borgani, S. 2006, *ArXiv Astrophysics e-prints*
- Boselli, A., Boissier, S., Cortese, L., et al. 2006, *ApJ*, 651, 811
- Bournaud, F., Jog, C. J., & Combes, F. 2007, *A&A*, 476, 1179
- Bower, R. G. 1991, *MNRAS*, 248, 332
- Bower, R. G., Kodama, T., & Terlevich, A. 1998, *MNRAS*, 299, 1193
- Bower, R. G., Lucey, J. R., & Ellis, R. S. 1992, *MNRAS*, 254, 601
- Bradač, M., Erben, T., Schneider, P., et al. 2005, *A&A*, 437, 49
- Bradač, M., Schrabback, T., Erben, T., et al. 2007, *ArXiv e-prints*, 711

- Bruzual, G. & Charlot, S. 2003, MNRAS, 344, 1000
- Burenin, R. A., Vikhlinin, A., Hornstrup, A., et al. 2007, ApJS, 172, 561
- Butcher, H. & Oemler, Jr., A. 1978, ApJ, 226, 559
- Butcher, H. & Oemler Jr., A. 1984, 285, 426
- Byrd, G. & Valtonen, M. 1990, ApJ, 350, 89
- Carlberg, R. G., Yee, H. K. C., & Ellingson, E. 1997a, ApJ, 478, 462
- Carlberg, R. G., Yee, H. K. C., Ellingson, E., et al. 1997b, ApJ, 485, L13+
- Carlberg, R. G., Yee, H. K. C., Ellingson, E., et al. 1997c, ApJ, 476, L7+
- Cattaneo, A., Dekel, A., Devriendt, J., Guiderdoni, B., & Blaizot, J. 2006, MNRAS, 370, 1651
- Cavaliere, A., Colafrancesco, S., & Menci, N. 1992, ApJ, 392, 41
- Cavaliere, A. & Menci, N. 1993, ApJ, 407, L9
- Charlot, S. & Fall, S. M. 2000, ApJ, 539, 718
- Charlot, S. & Longhetti, M. 2001, MNRAS, 323, 887
- Chemin, L., Balkowski, C., Cayatte, V., et al. 2006, MNRAS, 366, 812
- Christlein, D. & Zabludoff, A. I. 2005, ApJ, 621, 201
- Cid Fernandes, R., Gu, Q., Melnick, J., et al. 2004, MNRAS, 355, 273
- Cid Fernandes, R., Mateus, A., Sodré, L., Stasińska, G., & Gomes, J. M. 2005, MNRAS, 358, 363
- Clements, D. L., Farrah, D., Rowan-Robinson, M., et al. 2005, MNRAS, 363, 229
- Coc, A., Vangioni-Flam, E., Descouvemont, P., Adahchour, A., & Angulo, C. 2004, ApJ, 600, 544
- Cohen, J. G. & Kneib, J.-P. 2002, ApJ, 573, 524
- Cole, S., Percival, W. J., Peacock, J. A., et al. 2005, MNRAS, 362, 505
- Colless, M., Dalton, G., Maddox, S., et al. 2001, MNRAS, 328, 1039
- Conselice, C. J. 2006, ApJ, 638, 686
- Cooper, M. C., Newman, J. A., Croton, D. J., et al. 2006, MNRAS, 370, 198
- Cortese, L., Marcillac, D., Richard, J., et al. 2007, MNRAS, 376, 157
- Couch, W. J., Balogh, M. L., Bower, R. G., et al. 2001, ApJ, 549, 820
- Couch, W. J., Barger, A. J., Smail, I., Ellis, R. S., & Sharples, R. M. 1998, ApJ, 497, 188
- Couch, W. J. & Sharples, R. M. 1987, MNRAS, 229, 423
- Cowie, L. L. & Songaila, A. 1977, Nature, 266, 501
- Croton, D. J., Springel, V., White, S. D. M., et al. 2006, MNRAS, 365, 11

- Cucciati, O., Iovino, A., Marinoni, C., et al. 2006, *A&A*, 458, 39
- Czoske, O., Kneib, J.-P., Soucail, G., et al. 2001, *A&A*, 372, 391
- David, L. P., Slyz, A., Jones, C., et al. 1993, *ApJ*, 412, 479
- Davies, R. D. & Lewis, B. M. 1973, *MNRAS*, 165, 231
- Davies, R. L., Kuntschner, H., Emsellem, E., et al. 2001, *ApJ*, 548, L33
- De Propris, R., Colless, M., Peacock, J. A., et al. 2004, *MNRAS*, 351, 125
- de Vaucouleurs, G. 1959, *Handbuch der Physik*, 53, 275
- Demarco, R., Rosati, P., Lidman, C., et al. 2007, *ApJ*, 663, 164
- Demarco, R., Rosati, P., Lidman, C., et al. 2005, *A&A*, 432, 381
- Diaferio, A. 1999, *MNRAS*, 309, 610
- Dopita, M. A., Fischera, J., Sutherland, R. S., et al. 2006, *ApJ*, 647, 244
- Dopita, M. A., Kewley, L. J., Heisler, C. A., & Sutherland, R. S. 2000, *ApJ*, 542, 224
- Dressler, A. 1980, *ApJ*, 236, 351
- Dressler, A. & Gunn, J. E. 1982, *ApJ*, 263, 533
- Dressler, A., Oemler, A. J., Couch, W. J., et al. 1997, *ApJ*, 490, 577
- Dressler, A. & Shectman, S. A. 1988, *AJ*, 95, 985
- Dressler, A., Smail, I., Poggianti, B. M., et al. 1999, *ApJS*, 122, 51
- Dressler, A., Thompson, I. B., & Shectman, S. A. 1985, *ApJ*, 288, 481
- Eisenstein, D. J., Zehavi, I., Hogg, D. W., et al. 2005, *ApJ*, 633, 560
- Eke, V. R., Baugh, C. M., Cole, S., et al. 2004, *MNRAS*, 348, 866
- Eke, V. R., Cole, S., & Frenk, C. S. 1996, *MNRAS*, 282, 263
- Elbaz, D., Daddi, E., Le Borgne, D., et al. 2007, *A&A*, 468, 33
- Ellingson, E., Lin, H., Yee, H. K. C., & Carlberg, R. G. 2001, *ApJ*, 547, 609
- Ellis, R. S., Smail, I., Dressler, A., et al. 1997, *ApJ*, 483, 582
- Fasano, G., Poggianti, B. M., Couch, W. J., et al. 2000, *ApJ*, 542, 673
- Ferrari, C., Benoist, C., Maurogordato, S., Cappi, A., & Slezak, E. 2005, *A&A*, 430, 19
- Finn, R. A., Zaritsky, D., McCarthy, Jr., D. W., et al. 2005, *ApJ*, 630, 206
- Franzetti, P., Scodreggio, M., Garilli, B., et al. 2007, *A&A*, 465, 711
- Freedman, W. L., Madore, B. F., Gibson, B. K., et al. 2001, *ApJ*, 553, 47
- Fritz, A., Ziegler, B. L., Bower, R. G., Smail, I., & Davies, R. L. 2005, *MNRAS*, 358, 233

- Fujita, Y. 1998, *ApJ*, 509, 587
- Fujita, Y. 2004, *PASJ*, 56, 29
- Fujita, Y. & Nagashima, M. 1999, *ApJ*, 516, 619
- Fukugita, M., Hogan, C. J., & Peebles, P. J. E. 1998, *ApJ*, 503, 518
- Fukugita, M., Shimasaku, K., & Ichikawa, T. 1995, *PASP*, 107, 945
- Gabasch, A., Bender, R., Seitz, S., et al. 2004, *A&A*, 421, 41
- Gallazzi, A., Charlot, S., Brinchmann, J., White, S. D. M., & Tremonti, C. A. 2005, *MNRAS*, 362, 41
- Gehrels, N. 1986, *ApJ*, 303, 336
- Geller, M. J. & Huchra, J. P. 1989, *Science*, 246, 897
- Gerken, B., Ziegler, B., Balogh, M., et al. 2004, *A&A*, 421, 59
- Gilbank, D. G., Bower, R. G., Castander, F. J., & Ziegler, B. L. 2004, *MNRAS*, 348, 551
- Gill, S. P. D., Knebe, A., & Gibson, B. K. 2005, *MNRAS*, 356, 1327
- Giovanelli, R. & Haynes, M. P. 1985, *ApJ*, 292, 404
- Girardi, M., Giuricin, G., Mardirossian, F., Mezzetti, M., & Boschin, W. 1998, *ApJ*, 505, 74
- Gitti, M. & Schindler, S. 2004, *A&A*, 427, L9
- Gladders, M. D., Lopez-Cruz, O., Yee, H. K. C., & Kodama, T. 1998, *ApJ*, 501, 571
- Gladders, M. D. & Yee, H. K. C. 2000, *AJ*, 120, 2148
- Gnedin, O. Y. 2003, *ApJ*, 589, 752
- Gómez, P. L., Nichol, R. C., Miller, C. J., et al. 2003, *ApJ*, 584, 210
- González, J. J. 1993, PhD thesis
- González Delgado, R. M., Leitherer, C., & Heckman, T. M. 1999, *ApJS*, 125, 489
- González-García, A. C. & Balcells, M. 2005, *MNRAS*, 357, 753
- Goto, T. 2005, *MNRAS*, 356, L6
- Goto, T. 2007, *MNRAS*, 381, 187
- Goto, T., Yamauchi, C., Fujita, Y., et al. 2003, *MNRAS*, 346, 601
- Gray, M. E., Wolf, C., Meisenheimer, K., et al. 2004, *MNRAS*, 347, L73
- Gunn, J. E. & Gott, J. R. I. 1972, *ApJ*, 176, 1
- Gursky, H., Kellogg, E., Murray, S., et al. 1971, *ApJ*, 167, L81+
- Haines, C. P., Gargiulo, A., La Barbera, F., et al. 2007, *MNRAS*, 381, 7
- Haines, C. P., La Barbera, F., Mercurio, A., Merluzzi, P., & Busarello, G. 2006, *ApJ*, 647, L21

- Hammer, F., Flores, H., Lilly, S. J., et al. 1997, *ApJ*, 481, 49
- Hansen, S. M., McKay, T. A., Wechsler, R. H., et al. 2005, *ApJ*, 633, 122
- Harker, J. J., Schiavon, R. P., Weiner, B. J., & Faber, S. M. 2006, *ApJ*, 647, L103
- Hashimoto, Y., Oemler, A. J., Lin, H., & Tucker, D. L. 1998, *ApJ*, 499, 589
- Hau, G. K. T., Carter, D., & Balcells, M. 1999, *MNRAS*, 306, 437
- Heckman, T., Krolik, J., Meurer, G., et al. 1995, *ApJ*, 452, 549
- Heckman, T. M., Sembach, K. R., Meurer, G. R., et al. 2001, *ApJ*, 558, 56
- Henriksen, M. & Byrd, G. 1996, *ApJ*, 459, 82
- Hernquist, L. 1992, *ApJ*, 400, 460
- Hester, J. A. 2006, *ApJ*, 647, 910
- Hicks, A. K., Ellingson, E., Hoekstra, H., & Yee, H. K. C. 2006, *ApJ*, 652, 232
- Hogg, D. E., Roberts, M. S., Schulman, E., & Knezek, P. M. 1998, *AJ*, 115, 502
- Hogg, D. W., Blanton, M. R., Eisenstein, D. J., et al. 2003, *ApJ*, 585, L5
- Hogg, D. W., Masjedi, M., Berlind, A. A., et al. 2006, *ApJ*, 650, 763
- Hopkins, A. M. 2004, *ApJ*, 615, 209
- Hubble, E. & Humason, M. L. 1931, *ApJ*, 74, 43
- Hubble, E. P. 1925, *The Observatory*, 48, 139
- Hubble, E. P. 1936, Yale University Press
- Huchra, J., Davis, M., Latham, D., & Tonry, J. 1983, *ApJS*, 52, 89
- Ibata, R. A., Gilmore, G., & Irwin, M. J. 1994, *Nature*, 370, 194
- Icke, V. 1985, *A&A*, 144, 115
- Ilbert, O., Tresse, L., Zucca, E., et al. 2005, *A&A*, 439, 863
- Inoue, A. K., Iwata, I., & Deharveng, J.-M. 2006, *MNRAS*, 371, L1
- Johnson, H. L. & Morgan, W. W. 1953, *ApJ*, 117, 313
- Johnston, D. E., Sheldon, E. S., Wechsler, R. H., et al. 2007, *ArXiv e-prints*, 709
- Jones, C. & Forman, W. 1978, *ApJ*, 224, 1
- Kapferer, W., Kronberger, T., Weratschnig, J., et al. 2007, *A&A*, 466, 813
- Kauffmann, G. 1996, *MNRAS*, 281, 487
- Kauffmann, G., Heckman, T. M., Tremonti, C., et al. 2003a, *MNRAS*, 346, 1055
- Kauffmann, G., Heckman, T. M., White, S. D. M., et al. 2003b, *MNRAS*, 341, 54

- Kawata, D. & Mulchaey, J. S. 2008, *ApJ*, 672, L103
- Kennicutt, Jr., R. C. 1983, *ApJ*, 272, 54
- Kennicutt, Jr., R. C. 1992, *ApJ*, 388, 310
- Kennicutt, Jr., R. C. 1998, *ARA&A*, 36, 189
- Kennicutt, Jr., R. C., Tamblyn, P., & Congdon, C. E. 1994, *ApJ*, 435, 22
- Kewley, L. J. & Dopita, M. A. 2002, *ApJS*, 142, 35
- Kewley, L. J., Dopita, M. A., Sutherland, R. S., Heisler, C. A., & Trevena, J. 2001, *ApJ*, 556, 121
- Kewley, L. J. & Ellison, S. L. 2008, ArXiv e-prints, 801
- Kewley, L. J., Geller, M. J., & Jansen, R. A. 2004, *AJ*, 127, 2002
- King, I. 1962, *AJ*, 67, 471
- Knop, R. A., Aldering, G., Amanullah, R., et al. 2003, *ApJ*, 598, 102
- Kobulnicky, H. A., Kennicutt, Jr., R. C., & Pizagno, J. L. 1999, *ApJ*, 514, 544
- Kobulnicky, H. A. & Phillips, A. C. 2003, *ApJ*, 599, 1031
- Kobulnicky, H. A., Willmer, C. N. A., Phillips, A. C., et al. 2003, *ApJ*, 599, 1006
- Kodama, T. & Arimoto, N. 1997, *A&A*, 320, 41
- Kodama, T., Balogh, M. L., Smail, I., Bower, R. G., & Nakata, F. 2004, *MNRAS*, 354, 1103
- Kodama, T., Smail, I., Nakata, F., Okamura, S., & Bower, R. G. 2001, *ApJ*, 562, L9
- Krivitsky, D. S. & Kontorovich, V. M. 1997, *A&A*, 327, 921
- Kroupa, P. 2001, *MNRAS*, 322, 231
- Kroupa, P. 2002, *Science*, 295, 82
- Larson, R. B. 1972, *Nature*, 236, 21
- Larson, R. B., Tinsley, B. M., & Caldwell, C. N. 1980, *ApJ*, 237, 692
- Levy, L., Rose, J. A., van Gorkom, J. H., & Chaboyer, B. 2007, *AJ*, 133, 1104
- Lewis, I., Balogh, M., De Propris, R., et al. 2002, *MNRAS*, 334, 673
- Liang, Y. C., Hammer, F., & Yin, S. Y. 2007, *A&A*, 474, 807
- Liang, Y. C., Yin, S. Y., Hammer, F., et al. 2006, *ApJ*, 652, 257
- Longair, M. S. 2007
- Madau, P., Pozzetti, L., & Dickinson, M. 1998, *ApJ*, 498, 106
- Makino, J. & Hut, P. 1997, *ApJ*, 481, 83
- Markevitch, M. 1998, *ApJ*, 504, 27

- Martin, C. L., Lotz, J., & Ferguson, H. C. 2000, *ApJ*, 543, 97
- Martini, P., Kelson, D. D., Mulchaey, J. S., & Trager, S. C. 2002, *ApJ*, 576, L109
- Masjedi, M., Hogg, D. W., Cool, R. J., et al. 2006, *ApJ*, 644, 54
- Mason, K. O., Carrera, F. J., Hasinger, G., et al. 2000, *MNRAS*, 311, 456
- Matthews, T. A., Morgan, W. W., & Schmidt, M. 1964, *ApJ*, 140, 35
- McGaugh, S. S. 1991, *ApJ*, 380, 140
- Mei, S., Holden, B. P., Blakeslee, J. P., et al. 2006, *ApJ*, 644, 759
- Mendes de Oliveira, C., Amram, P., Plana, H., & Balkowski, C. 2003, *AJ*, 126, 2635
- Merritt, D. 1984, *ApJ*, 276, 26
- Merritt, D. 1999, *PASP*, 111, 129
- Miller, C. J., Nichol, R. C., Gómez, P. L., Hopkins, A. M., & Bernardi, M. 2003, *ApJ*, 597, 142
- Moore, B., Lake, G., & Katz, N. 1998, *ApJ*, 495, 139
- Moore, B., Lake, G., Quinn, T., & Stadel, J. 1999, *MNRAS*, 304, 465
- Moran, S. M., Ellis, R. S., Treu, T., et al. 2005, *ApJ*, 634, 977
- Moran, S. M., Ellis, R. S., Treu, T., et al. 2007a, *ApJ*, 671, 1503
- Moran, S. M., Loh, B. L., Ellis, R. S., et al. 2007b, *ApJ*, 665, 1067
- Morgan, W. W. 1961, *Proceedings of the National Academy of Science*, 47, 905
- Mullis, C. R., McNamara, B. R., Quintana, H., et al. 2003, *ApJ*, 594, 154
- Nakata, F., Bower, R. G., Balogh, M. L., & Wilman, D. J. 2005, *MNRAS*, 357, 679
- Navarro, J. F., Frenk, C. S., & White, S. D. M. 1996, *ApJ*, 462, 563
- Neistein, E., van den Bosch, F. C., & Dekel, A. 2006, *MNRAS*, 372, 933
- Nulsen, P. E. J. 1982, *MNRAS*, 198, 1007
- O'Meara, J. M., Tytler, D., Kirkman, D., et al. 2001, *ApJ*, 552, 718
- Osterbrock, D. E. 1960, *ApJ*, 132, 325
- Padmanabhan, T. 2005, 175
- Pagel, B. E. J., Edmunds, M. G., Blackwell, D. E., Chun, M. S., & Smith, G. 1979, *MNRAS*, 189, 95
- Perlmutter, S., Aldering, G., Goldhaber, G., et al. 1999, *ApJ*, 517, 565
- Petrosian, V. 1976, *ApJ*, 209, L1
- Pettini, M. & Pagel, B. E. J. 2004, *MNRAS*, 348, L59
- Pimblet, K. A., Smail, I., Edge, A. C., et al. 2006, *MNRAS*, 366, 645

- Poggianti, B. M. & Barbaro, G. 1997, *A&A*, 325, 1025
- Poggianti, B. M., Bridges, T. J., Komiyama, Y., et al. 2004, *ApJ*, 601, 197
- Poggianti, B. M., Smail, I., Dressler, A., et al. 1999, *ApJ*, 518, 576
- Poggianti, B. M., von der Linden, A., De Lucia, G., et al. 2006, *ApJ*, 642, 188
- Popesso, P., Biviano, A., Romaniello, M., & Böhringer, H. 2007, *A&A*, 461, 411
- Postman, M. & Geller, M. J. 1984, *ApJ*, 281, 95
- Quilis, V., Moore, B., & Bower, R. 2000, *Science*, 288, 1617
- Quintero, A. D., Hogg, D. W., Blanton, M. R., et al. 2004, *ApJ*, 602, 190
- Rakos, K. D. & Schombert, J. M. 1995, *ApJ*, 439, 47
- Rasmussen, J. & Ponman, T. J. 2004, *MNRAS*, 349, 722
- Riess, A. G., Filippenko, A. V., Challis, P., et al. 1998, *AJ*, 116, 1009
- Rines, K., Geller, M. J., Kurtz, M. J., & Diaferio, A. 2003, *AJ*, 126, 2152
- Rines, K., Geller, M. J., Kurtz, M. J., & Diaferio, A. 2005, *AJ*, 130, 1482
- Salim, S., Rich, R. M., Charlot, S., et al. 2007, *ApJS*, 173, 267
- Salpeter, E. E. 1955, *ApJ*, 121, 161
- Sandage, A. 1972, *ApJ*, 176, 21
- Sarzi, M., Falcón-Barroso, J., Davies, R. L., et al. 2006, *MNRAS*, 366, 1151
- Sato, T. & Martin, C. L. 2006a, *ApJ*, 647, 934
- Sato, T. & Martin, C. L. 2006b, *ApJ*, 647, 946
- Scalo, J. M. 1986, *Fundamentals of Cosmic Physics*, 11, 1
- Schiminovich, D., Wyder, T. K., Martin, D. C., et al. 2007, *ApJS*, 173, 315
- Schindler, S., Hattori, M., Neumann, D. M., & Böhringer, H. 1997, *A&A*, 317, 646
- Schlegel, D. J., Finkbeiner, D. P., & Davis, M. 1998, *ApJ*, 500, 525
- Sersic, J. L. & Arreguine, V. M. 1983, *Journal of Astrophysics and Astronomy*, 4, 225
- Shectman, S. A., Landy, S. D., Oemler, A., et al. 1996, *ApJ*, 470, 172
- Smail, I., Ellis, R. S., Dressler, A., et al. 1997, *ApJ*, 479, 70
- Sofue, Y. & Rubin, V. 2001, *ARA&A*, 39, 137
- Spergel, D. N., Bean, R., Doré, O., et al. 2007, *ApJS*, 170, 377
- Spergel, D. N., Verde, L., Peiris, H. V., et al. 2003, *ApJS*, 148, 175
- Springel, V., White, S. D. M., Jenkins, A., et al. 2005, *Nature*, 435, 629

- Stasińska, G. 2006, *A&A*, 454, L127
- Storchi-Bergmann, T., Calzetti, D., & Kinney, A. L. 1994, *ApJ*, 429, 572
- Strateva, I., Ivezić, Ž., Knapp, G. R., et al. 2001, *AJ*, 122, 1861
- Tanaka, M., Hoshi, T., Kodama, T., & Kashikawa, N. 2007, *MNRAS*, 379, 1546
- Tanaka, M., Kodama, T., Arimoto, N., et al. 2005, *MNRAS*, 362, 268
- Terlevich, A. I., Caldwell, N., & Bower, R. G. 2001, *MNRAS*, 326, 1547
- Thomas, D., Greggio, L., & Bender, R. 1999, *MNRAS*, 302, 537
- Thompson, L. A. & Gregory, S. A. 1993, *AJ*, 106, 2197
- Tonnesen, S., Bryan, G. L., & van Gorkom, J. H. 2007, *ApJ*, 671, 1434
- Toomre, A., Tinsley, B., & Larson, R. 1977, *The Evolution of Galaxies and Stellar Populations*, 401
- Trager, S. C., Worthey, G., Faber, S. M., Burstein, D., & Gonzalez, J. J. 1998, *ApJS*, 116, 1
- Tran, K.-V. H., Franx, M., Illingworth, G. D., et al. 2007, *ApJ*, 661, 750
- Tran, K.-V. H., Simard, L., Zabludoff, A. I., & Mulchaey, J. S. 2001, *ApJ*, 549, 172
- Tremonti, C. A., Heckman, T. M., Kauffmann, G., et al. 2004, *ApJ*, 613, 898
- Treu, T., Ellis, R. S., Kneib, J.-P., et al. 2003, *ApJ*, 591, 53
- Tully, R. B. 1987, *ApJ*, 321, 280
- Tully, R. B. & Fouque, P. 1985, *ApJS*, 58, 67
- Umeda, K., Yagi, M., Yamada, S. F., et al. 2004, *ApJ*, 601, 805
- Valluri, M. 1993, *ApJ*, 408, 57
- van den Bergh, S. 1960, *ApJ*, 131, 215
- Vikhlinin, A., McNamara, B. R., Forman, W., et al. 1998, *ApJ*, 502, 558
- Vollmer, B., Marcelin, M., Amram, P., et al. 2000, *A&A*, 364, 532
- Wake, D. A., Collins, C. A., Nichol, R. C., Jones, L. R., & Burke, D. J. 2005, *ApJ*, 627, 186
- Wakker, B. P. & van Woerden, H. 1997, *ARA&A*, 35, 217
- Wehner, E. H., Gallagher, J. S., Papaderos, P., Fritze-von Alvensleben, U., & Westfall, K. B. 2006, *MNRAS*, 371, 1047
- Whiting, A. B., Hau, G. K. T., Irwin, M., & Verdugo, M. 2007, *AJ*, 133, 715
- Wolf, C., Gray, M. E., & Meisenheimer, K. 2005, *A&A*, 443, 435
- Worthey, G. 1994, *ApJS*, 95, 107
- Worthey, G., Faber, S. M., Gonzalez, J. J., & Burstein, D. 1994, *ApJS*, 94, 687

- Worthey, G. & Ottaviani, D. L. 1997, *ApJS*, 111, 377
- Wu, X.-P. & Fang, L.-Z. 1996, *ApJ*, 467, L45+
- Xue, Y.-J. & Wu, X.-P. 2000, *ApJ*, 538, 65
- Yan, R., Newman, J. A., Faber, S. M., et al. 2006, *ApJ*, 648, 281
- Yee, H. K. C., Ellingson, E., & Carlberg, R. G. 1996, *ApJS*, 102, 269
- York, D. G., Adelman, J., Anderson, Jr., J. E., et al. 2000, *AJ*, 120, 1579
- Zehavi, I., Blanton, M. R., Frieman, J. A., et al. 2002, *ApJ*, 571, 172
- Zepf, S. E., Whitmore, B. C., & Levison, H. F. 1991, *ApJ*, 383, 524
- Zwicky, F. 1937, *ApJ*, 86, 217
- Zwicky, F. 1959, *Handbuch der Physik*, Vol. LIII, Clusters of Galaxies (Berlin: Springer), 390, editor S. Flügge
- Zwicky, F., Herzog, E., & Wild, P. 1961, *Catalogue of galaxies and of clusters of galaxies*, Vol. I (Pasadena: California Institute of Technology (CIT), —c1961)

APPENDIX A

Observations

Mask ID	Date	RA DEC (J2000)	Exposure time	Comments
R285_1m2	10 Feb 2002	09:43:53.1 16:41:15.7	4×2700	mostly clear, not photometric
R265_1m2	10 Feb 2002	13:12:05.4 32:32:15.3	4×2700	mostly clear, not photometric
R265_1m1	10 Feb 2002	13:12:04.6 32:32:17.6	3×1200	mostly clear, not photometric
R285_2m2	11 Feb 2002	09:43:39.5 16:39:44.8	4×2700	photometric
R265_2m1	11 Feb 2002	13:11:16.0 32:29:46.6	4×2700	photometric
R285_4m1	12 Feb 2002	09:44:37.0 16:29:45.6	1×3000 + 3×2700	partially photometric
R285_1m1	12 Feb 2002	09:43:54.3 16:41:30.6	3×1200	partially photometric
R265_3m2	12 Feb 2002	13:10:33.9 32:28:35.2	4×2700	partially photometric
R285_5m1	13 Feb 2002	09:43:55.6 16:30:34.0	4×2700	mostly clear, not photometric, seeing~1.5"
R265_3m1	13 Feb 2002	13:10:33.5 32:28:19.4	1×2700 + 2×1200	mostly clear, not photometric, seeing~1.5"
R265_5m1	13 Feb 2002	13:10:55.7 32:18:36.7	4×2700	mostly clear, not photometric, seeing~1.5"
R285_2m1	14 Feb 2002	09:43:38.8 16:39:23.9	3×1500	mostly clear, not photometric, seeing~2.0"
R285_3m1	14 Feb 2002	09:43:03.4 16:42:19.1	3×1500	mostly clear, not photometric, seeing~2.0"
R285_4m1	14 Feb 2002	13:10:07.7 32:21:34.6	3×1500	mostly clear, not photometric, seeing~2.0"
R220_1m1	20 Mar 2002	17:29:44.1 74:41:47.0	3×1200	photometric
R220_1m2	20 Mar 2002	17:29:47.3 74:41:42.4	1×2700	photometric
R220_2m2	21 Mar 2002	17:26:42.5 74:30:45.9	4×2700	mostly clear, not photometric, seeing~1.8"
R220_2m1	21 Mar 2002	17:26:42.7 74:30:06.1	1×1200	mostly clear, not photometric, seeing~1.8"
R220_2m1	22 Mar 2002	17:26:42.7 74:30:06.1	2×1200	photometric
R220_3m1	22 Mar 2002	17:24:37.3 74:29:19.8	3×2700	photometric
R220_4m1	22 Mar 2002	17:23:46.8 74:42:32.6	3×1200	photometric
R220_3m1	22 Mar 2002	17:24:37.3 74:29:19.8	1×2700	photometric
R220_5m1	24 Mar 2002	17:24:23.2 74:18:49.1	3×1200	photometric
R220_4m2	24 Mar 2002	17:23:49.9 74:42:57.3	2×2700	photometric

Table A.1: Observation log summary. With the mask identifier, dates of observation, coordinates at the mask center, exposure times and conditions indicated.

APPENDIX B

Line definitions

Index	Blue continuum [Å]	Line [Å]	Red continuum [Å]	Notes
[O II] λ 3727	3653 – 3713	3713 – 3741	3741 – 3801	Balogh et al. 1999
CaK	3892 – 3914	3914 – 3952	3986 – 4004	Worthey et al. 1994
CaH	3892 – 3914	3961 – 3982	3986 – 4004	Worthey et al. 1994
$D_n(4000)$	3850 – 3950	<i>N/A</i>	4000 – 4100	Balogh et al. 1999
H δ	4030 – 4082	4088 – 4116	4122 – 4170	Balogh et al. 1999
G4300	4266 – 4282	4281 – 4316	4318 – 4335	Worthey et al. 1994
H β	4815 – 4845	4851 – 4871	4880 – 4930	Worthey et al. 1994
[O III] λ 4959	4885 – 4935	4948 – 4978	5030 – 5070	González 1993
[O III] λ 5007	4978 – 4998	4998 – 5015	5015 – 5030	González 1993
Mg <i>b</i>	5142 – 5161	5160 – 5192	5191 – 5206	Worthey et al. 1994
Fe5270	5233 – 5248	5245 – 5285	5285 – 5318	Worthey et al. 1994
Fe5335	5304 – 5315	5312 – 5352	5353 – 5363	Worthey et al. 1994
Na	5860 – 5875	5876 – 5909	5922 – 5948	Worthey et al. 1994
H α	6490 – 6537	6555 – 6575	6594 – 6640	Balogh et al. 1999
[N II] λ 6584	6490 – 6530	6576 – 6595	6615 – 6640	González 1993

Table B.1: Line definitions for the strongest features in the galaxy spectra along the original references. All Worthey et al. (1994) and González 1993 lines are linked to the Lick/IDS system.

Data for individual objects

The tables in this appendix contain information about individual galaxies gathered from different sources. Table C.1 contains general information about the objects, such as coordinates, redshifts, magnitudes and spatial information. Table C.2 contains the measurements on the spectra of the objects.

ID – is the identification code for each galaxy. The galaxies which come directly from this project are denoted with a "r". Galaxies from the Balogh et al. (2002a) project use the "ba" prefix and galaxies from the Gilbank et al. (2004) have the "XDC" prefix. The numbers following the different prefixes depend on the sources. For galaxies with "r" prefix, the first two numbers denote the field (22 for R220, 26 for R265 and 28 for R285). The second couple of numbers are the mask identifier and the numbers following the underscore (_) are the slit identifier. For galaxies with the "ba" prefix, the numbers are kept from this project. In the case of, the two numbers following the "XDC" prefix are the night of the observation and the slit identifier.

membership – Denote to which cluster each galaxy belong according to the criteria of §4.1 or whether they are part of the field sample.

RA , DEC – are the equatorial coordinates of the objects with respect to the year 2000 equinox.

redshift – is the spectroscopic redshift calculated according to the method outlined on §4.1.

$I, V - I$ – is the I -band magnitude and the $V - I$ color provided by Gilbank et al. (2004).

u, g, r, i, z – are the SDSS magnitudes (in the AB system) obtained from the survey website.

D – is the cluster-centric distance in megaparsecs measured from the center of the clusters (see table 2).

$\log(\Sigma_5)$ – is the logarithm of the projected density Σ_5 .

Table C.1: Data for individual objects.

ID	membership	RA	DEC	redshift	I [mag]	$V - I$ [mag]	u [mag]	g [mag]	r [mag]	i [mag]	z [mag]	D [Mpc]	$\log(\Sigma_5)$ [Mpc $^{-2}$]
r2211_07	vmf194	17:29:15.26	+74:41:23.8	0.2099	18.59	1.38	0.22	2.5725
r2211_08	vmf194	17:29:19.77	+74:41:11.2	0.2116	16.75	1.42	0.25	2.3110
r2211_09	vmf194	17:29:22.67	+74:40:39.6	0.2118	18.17	1.46	0.28	2.5144
r2211_10	vmf194	17:29:30.06	+74:40:43.0	0.2110	18.54	1.42	0.38	2.2858
r2212_06	vmf194	17:29:13.37	+74:42:13.8	0.2087	18.71	0.99	0.33	2.0145
r2212_08	vmf194	17:29:22.55	+74:40:52.3	0.2108	17.92	1.40	0.28	2.7246
r2212_23	vmf194	17:30:44.85	+74:39:11.8	0.2098	18.34	1.38	1.44	1.4731
r2221_14	vmf194	17:26:24.27	+74:27:35.2	0.2087	17.66	1.32	3.48	1.4593
r2221_03	xdc220	17:26:50.67	+74:34:04.6	0.2659	18.30	1.00	4.01	1.3976
r2221_03b	xdc220	17:26:50.87	+74:34:08.8	0.2665	19.52	0.88	4.00
r2221_12	xdc220	17:26:11.11	+74:28:26.6	0.2622	18.24	1.42	4.59	1.5703
r2222_03	xdc220	17:26:17.74	+74:34:09.3	0.2571	18.85	1.58	3.59	1.5681
r2222_07	xdc220	17:26:33.92	+74:31:55.8	0.2608	19.20	1.41	4.16	2.0657
r2231_05	xdc220	17:24:11.04	+74:31:12.1	0.2614	18.58	1.44	3.20	1.3937
r2241_05	xdc220	17:23:24.91	+74:44:42.8	0.2616	18.39	1.59	0.18	1.8682
r2241_07	xdc220	17:23:28.45	+74:43:41.7	0.2597	17.00	1.57	0.13	2.4871
r2241_09	xdc220	17:23:26.66	+74:43:16.6	0.2599	16.93	1.59	0.23	2.1478
r2241_10	xdc220	17:23:24.29	+74:42:56.2	0.2595	17.99	1.51	0.32	2.2141
r2241_15	xdc220	17:23:32.26	+74:40:35.7	0.2548	18.46	1.24	0.86	1.5883
r2241_18	xdc220	17:23:05.48	+74:39:30.5	0.2545	18.38	2.56	1.21	1.8511
r2242_06	xdc220	17:23:26.46	+74:43:57.3	0.2616	19.49	1.46	0.11	2.3553
r2251_04	xdc220	17:24:12.22	+74:22:23.8	0.2624	18.92	0.87	5.31	0.9277
XDC29_04	xdc220	17:23:29.37	+74:43:38.7	0.2616	17.96	1.59	0.13	2.2695
r2621_14	vmf131	13:11:22.18	+32:28:53.8	0.2990	19.24	1.61	24.58	21.75	20.39	19.76	19.32	5.08	0.9264
r2621_15	vmf131	13:11:23.60	+32:28:56.3	0.2934	18.95	1.07	21.52	20.75	19.98	19.50	19.57	5.16	1.2192
r2621_16	vmf131	13:11:24.66	+32:28:36.9	0.3001	18.99	1.34	21.77	20.81	19.88	19.55	19.25	5.19	1.3758
r2631_20	vmf131	13:10:41.55	+32:28:23.1	0.2969	17.24	1.77	21.17	19.95	18.41	17.79	17.43	2.97	1.6730
r2632_02	vmf131	13:10:16.57	+32:30:36.6	0.2950	18.70	1.71	22.99	21.47	20.03	19.20	18.87	2.42	0.7717
r2632_02b	vmf131	13:10:16.86	+32:30:38.0	0.2934	19.92	1.08	22.22	21.11	20.69	20.77	20.38	2.43
r2632_03	vmf131	13:10:18.96	+32:30:18.7	0.2938	18.47	1.69	22.91	21.09	19.52	19.03	18.60	2.42	1.1241
r2632_11	vmf131	13:10:30.42	+32:27:16.6	0.2947	17.73	1.50	19.70	19.51	18.62	18.26	18.00	2.29	0.8536

Table C.1: Continued.

ID	membership	RA	DEC	redshift	I [mag]	$V - I$ [mag]	u [mag]	g [mag]	r [mag]	i [mag]	z [mag]	D [Mpc]	$\log_{10}(\Sigma_5)$ [Mpc $^{-2}$]
r2632_12	vmf131	13:10:34.20	+32:27:30.8	0.2946	19.21	1.02	22.31	20.71	20.13	19.84	19.27	2.50	0.9926
r2632_17	vmf131	13:10:47.14	+32:27:56.8	0.2927	19.37	1.58	21.86	21.25	20.19	19.53	19.48	3.18	0.8578
r2641_04	vmf131	13:10:17.22	+32:19:51.8	0.2957	18.90	1.90	20.87	21.41	20.08	19.41	18.94	1.37	1.3197
r2641_05	vmf131	13:10:14.02	+32:23:33.6	0.2961	18.71	1.77	21.42	20.94	19.74	19.09	18.90	1.04	1.6137
r2641_06	vmf131	13:10:12.94	+32:24:09.1	0.2957	18.59	0.86	20.36	19.92	19.54	19.56	19.00	1.03	1.6424
r2641_07	vmf131	13:10:10.66	+32:21:44.2	0.2932	18.77	2.33	20.51	21.33	20.31	19.08	18.75	0.84	1.2614
r2641_12	vmf131	13:10:01.42	+32:23:48.2	0.2961	17.98	1.50	21.38	20.39	19.03	18.44	18.28	0.45	1.5362
r2651_08	vmf131	13:10:47.60	+32:20:11.4	0.2943	18.48	1.63	21.82	20.67	19.34	18.77	18.48	2.94	0.7191
r2651_17	vmf131	13:11:13.98	+32:19:10.5	0.2943	17.54	1.74	25.21	20.46	18.76	18.06	17.80	4.43	1.5212
r2651_19	vmf131	13:11:17.96	+32:19:47.9	0.2940	18.15	1.51	20.79	20.00	19.09	18.62	18.67	4.62	1.1177
ba_07	vmf131	13:10:05.72	+32:21:12.2	0.2965	18.32	1.10	20.51	20.35	19.32	18.99	18.58	0.64	1.7933
ba_09	vmf131	13:10:04.22	+32:21:36.3	0.2900	19.00	1.61	21.96	21.69	19.85	19.40	20.49	0.51	1.6728
ba_12	vmf131	13:09:55.05	+32:21:49.0	0.2938	18.47	1.68	21.77	21.09	19.64	19.00	18.48	0.19	1.8700
ba_14	vmf131	13:09:53.20	+32:21:59.8	0.2912	18.87	1.68	21.29	22.31	20.92	20.30	20.76	0.20	1.8615
ba_18	vmf131	13:10:11.38	+32:22:02.3	0.2938	18.15	1.66	22.40	20.69	19.21	18.67	18.20	0.86	1.3216
ba_25	vmf131	13:09:51.54	+32:22:17.8	0.2924	18.40	1.68	22.47	21.23	19.60	18.87	18.50	0.25	1.7832
ba_28	vmf131	13:09:56.11	+32:22:16.8	0.2920	16.72	1.71	20.01	19.32	17.81	17.16	16.96	0.06	2.2639
ba_30	vmf131	13:09:58.50	+32:22:31.3	0.2946	18.02	1.67	21.44	20.74	19.14	18.59	18.19	0.13	1.8441
ba_36	vmf131	13:10:00.18	+32:22:59.4	0.2943	18.23	1.36	21.61	20.19	19.21	18.83	18.55	0.26	1.5910
ba_37	vmf131	13:09:56.33	+32:23:10.8	0.2894	18.21	1.70	21.93	20.78	19.35	18.71	18.46	0.17	1.6358
ba_39	vmf131	13:09:57.68	+32:23:13.0	0.2923	17.95	1.70	21.67	20.47	19.12	18.49	18.20	0.20	1.5911
r2611_04	vmf132	13:12:07.22	+32:34:35.8	0.2455	18.99	1.42	22.93	21.12	19.90	19.40	19.15	2.95	1.3958
r2611_13	vmf132	13:11:51.74	+32:33:29.2	0.2496	17.79	1.46	21.30	19.86	18.65	18.14	18.02	2.16	1.4590
r2611_14	vmf132	13:11:49.17	+32:33:23.4	0.2465	18.11	1.48	27.05	20.47	19.15	18.50	18.33	2.04	1.4768
r2612_02	vmf132	13:12:27.01	+32:32:06.6	0.2485	18.53	1.49	22.34	20.60	19.63	19.08	18.75	3.69	0.8189
r2612_04	vmf132	13:12:16.07	+32:32:11.0	0.2477	19.32	1.13	21.67	21.07	20.21	19.84	19.73	3.17	1.2237
r2612_06	vmf132	13:12:10.39	+32:30:03.0	0.2495	17.28	1.47	21.59	19.63	18.29	17.76	17.40	2.82	1.2786
r2612_17	vmf132	13:11:45.80	+32:31:21.7	0.2462	17.93	1.57	22.11	20.53	18.95	18.48	17.97	1.69	1.2527
r2621_03	vmf132	13:11:01.05	+32:30:41.6	0.2412	18.35	1.47	21.96	20.57	19.40	18.79	18.57	0.70	1.1164
r2621_04	vmf132	13:11:02.92	+32:29:36.0	0.2406	19.36	1.53	24.21	22.47	20.50	19.85	19.59	0.51	1.2746
r2621_11	vmf132	13:11:13.29	+32:28:50.9	0.2397	18.63	1.57	21.96	20.88	19.72	19.03	18.70	0.03	1.8681

Table C.1: Continued.

ID	membership	RA	DEC	redshift	I [mag]	$V - I$ [mag]	u [mag]	g [mag]	r [mag]	i [mag]	z [mag]	D [Mpc]	$\log_{10}(\Sigma_5)$ [Mpc ⁻²]
r2621_13	vmf132	13:11:17.64	+32:28:11.0	0.2418	17.92	1.51	22.10	20.29	18.90	18.35	17.88	0.29	1.1633
r2621_22	vmf132	13:11:33.84	+32:29:11.9	0.2503	18.17	1.53	21.45	20.51	19.32	18.76	18.33	1.02	1.4310
r2631_21	vmf132	13:10:43.33	+32:27:04.1	0.2459	17.35	1.44	20.29	19.55	18.37	17.93	17.57	1.51	0.9565
r2631_08	vmf132	13:10:25.08	+32:28:44.7	0.2500	19.30	1.36	22.33	20.54	19.41	18.88	18.80	2.34	1.0181
r2632_07	vmf132	13:10:25.93	+32:30:15.4	0.2446	18.82	1.50	22.04	20.86	19.88	19.30	19.10	2.32	1.0385
r2632_13	vmf132	13:10:37.82	+32:27:15.2	0.2456	18.34	1.48	22.25	20.69	19.38	18.92	18.78	1.76	1.0425
r2641_10	vmf132	13:10:04.73	+32:20:51.1	0.2481	17.47	1.46	20.37	19.46	18.37	17.99	17.71	3.84	1.2603
ba_02	vmf132	13:10:04.81	+32:20:52.0	0.2492	17.47	1.46	20.37	19.46	18.37	17.99	17.71	3.83	1.2603
ba_29	vmf132	13:09:49.99	+32:22:41.0	0.2495	19.77	0.78	20.84	20.79	20.43	20.11	20.08	4.32
r2811_06	vmf73	09:43:52.61	+16:44:40.1	0.2538	17.82	1.54	22.02	20.25	18.91	18.35	18.15	1.60	1.1251
r2811_16	vmf73	09:43:58.38	+16:41:09.6	0.2526	16.96	1.43	20.77	19.17	18.11	17.47	17.12	1.52	2.2958
r2811_18	vmf73	09:43:53.52	+16:40:23.1	0.2516	18.32	1.55	25.31	20.90	19.50	18.88	18.62	1.22	2.1096
r2811_19	vmf73	09:43:58.81	+16:40:02.3	0.2538	18.60	1.38	25.26	21.02	19.67	19.17	18.95	1.52	2.3390
r2811_20	vmf73	09:44:03.21	+16:39:48.5	0.2573	18.81	1.33	23.01	21.30	19.87	19.49	18.97	1.77	2.6022
r2811_24	vmf73	09:44:01.37	+16:38:01.1	0.2535	17.73	1.45	21.04	19.97	18.79	18.14	18.02	1.73	1.7239
r2811_25	vmf73	09:43:59.68	+16:37:30.1	0.2542	18.10	1.53	21.51	20.60	19.21	18.63	18.46	1.68	1.6531
r2812_05	vmf73	09:44:05.00	+16:38:34.3	0.2561	18.31	1.46	21.54	20.57	19.34	18.71	18.61	1.90	1.9605
r2812_09	vmf73	09:44:00.32	+16:40:11.5	0.2486	18.70	1.31	26.54	20.89	19.78	19.30	18.68	1.61	2.1931
r2812_12	vmf73	09:43:59.37	+16:41:09.9	0.2570	17.26	1.51	22.62	19.75	18.45	17.97	17.56	1.57	2.3464
r2812_14	vmf73	09:43:53.57	+16:41:43.2	0.2529	17.19	1.43	24.49	19.65	18.20	17.69	17.56	1.29	2.0205
r2821_02	vmf73	09:43:58.08	+16:41:17.0	0.2520	16.67	1.46	21.08	19.28	17.68	17.15	17.17	1.51	2.1606
r2821_08	vmf73	09:43:48.71	+16:40:39.1	0.2545	17.87	0.82	20.05	19.24	18.69	18.41	18.32	0.96	1.9953
r2821_12	vmf73	09:43:43.00	+16:40:34.5	0.2573	17.64	1.48	21.89	20.12	18.61	18.25	18.16	0.63	2.0777
r2821_17	vmf73	09:43:36.34	+16:36:57.3	0.2569	17.58	1.50	20.97	20.00	18.72	18.02	17.81	0.77	1.9530
r2821_14	vmf73	09:43:40.07	+16:39:23.6	0.2578	18.45	1.46	28.19	20.85	19.45	18.88	18.57	0.48	1.5643
r2821_20	vmf73	09:43:33.63	+16:39:06.8	0.2529	17.80	1.46	21.11	20.68	18.99	18.47	18.22	0.23	1.9009
r2821_21	vmf73	09:43:32.42	+16:40:01.0	0.2538	18.55	1.47	22.07	21.23	19.69	19.06	18.79	0.02	2.3243
r2821_27	vmf73	09:43:23.53	+16:39:46.4	0.2576	17.98	1.29	21.10	20.11	18.99	18.50	18.19	0.48	1.9342
r2821_29	vmf73	09:43:19.34	+16:38:08.6	0.2573	17.87	1.43	21.20	20.58	19.15	18.49	18.21	0.84	1.9158
r2822_01	vmf73	09:43:58.93	+16:39:22.0	0.2560	18.91	1.39	25.02	21.52	19.98	19.43	19.19	1.53	2.0053
r2822_03	vmf73	09:43:56.35	+16:36:51.1	0.2552	17.57	1.36	20.95	19.98	18.73	18.20	17.93	1.57	1.8981

Table C.1: Continued.

ID	membership	RA	DEC	redshift	I [mag]	$V - I$ [mag]	u [mag]	g [mag]	r [mag]	i [mag]	z [mag]	D [Mpc]	$\log_{10}(\Sigma_5)$ [Mpc $^{-2}$]
r2822_04	vmf73	09:43:55.89	+16:40:36.0	0.2550	18.68	1.39	21.63	21.24	19.81	19.16	19.09	1.36	2.0049
r2822_05	vmf73	09:43:53.38	+16:39:59.1	0.2510	17.73	1.38	22.52	20.04	18.64	18.25	17.91	1.21	2.1004
r2822_06	vmf73	09:43:51.72	+16:41:45.0	0.2528	18.03	1.18	20.76	19.86	19.00	18.60	18.38	1.19	1.8825
r2822_09	vmf73	09:43:45.55	+16:41:30.9	0.2513	18.83	0.97	21.31	20.43	19.78	19.36	19.50	0.84	1.9077
r2822_14	vmf73	09:43:38.75	+16:38:55.5	0.2533	18.59	1.41	26.97	21.27	19.81	19.15	18.90	0.46	1.4544
r2822_15	vmf73	09:43:37.97	+16:39:32.6	0.2574	17.00	1.49	27.02	19.47	18.00	17.35	17.13	0.35	1.9396
r2822_16	vmf73	09:43:36.80	+16:41:02.7	0.2552	18.19	1.42	29.77	21.42	19.40	18.51	18.93	0.36	1.6899
r2822_17	vmf73	09:43:34.09	+16:40:36.1	0.2500	19.08	1.32	22.43	21.35	20.25	20.03	19.56	0.18	1.8974
r2822_19	vmf73	09:43:30.57	+16:38:56.0	0.2529	19.30	1.41	25.15	21.96	20.52	20.14	19.50	0.27	1.9262
r2822_20	vmf73	09:43:29.64	+16:40:56.8	0.2577	19.36	1.10	22.09	21.08	20.13	19.91	20.20	0.25	1.9012
r2822_22	vmf73	09:43:25.34	+16:39:07.2	0.2549	17.81	1.49	21.57	20.42	18.97	18.29	18.01	0.43	1.7411
r2822_23	vmf73	09:43:24.51	+16:39:52.1	0.2613	18.46	1.28	22.02	20.54	19.34	18.94	18.71	0.42	2.0960
r2822_25	vmf73	09:43:22.06	+16:39:07.9	0.2503	18.54	1.40	23.91	20.81	19.56	19.13	18.86	0.60	1.8024
r2831_03	vmf73	09:43:22.88	+16:41:14.8	0.2482	18.39	1.20	20.64	20.50	19.26	18.91	18.56	0.59	1.9199
r2831_10	vmf73	09:43:08.02	+16:42:45.4	0.2569	18.24	1.10	20.69	19.82	19.11	18.70	18.55	1.50	1.5114
r2831_13	vmf73	09:43:01.49	+16:42:27.7	0.2560	17.15	1.41	20.23	19.79	18.23	17.50	17.45	1.82	1.6307
r2841_07	vmf73	09:44:41.05	+16:29:19.5	0.2500	18.64	1.17	20.82	20.87	19.72	19.17	19.40	4.68	1.6593
r2841_10	vmf73	09:44:36.52	+16:27:31.5	0.2538	18.10	1.30	21.01	20.21	19.18	18.60	18.22	4.72	1.4068
r2841_17	vmf73	09:44:23.76	+16:31:47.1	0.2503	18.12	1.38	21.28	20.58	19.17	18.51	18.51	3.53	0.8670
r2851_04	vmf73	09:43:50.60	+16:28:20.5	0.2506	18.57	0.99	21.09	20.20	19.44	18.90	19.15	2.97	1.3320
r2851_14	vmf73	09:44:04.69	+16:32:49.3	0.2534	19.02	1.44	21.52	20.76	20.09	19.36	19.14	2.52	1.2764
r2851_17	vmf73	09:43:52.24	+16:34:00.8	0.2519	17.70	1.40	20.88	19.97	18.73	18.08	17.89	1.83	1.7885
r2811_01	vmf74	09:43:44.47	+16:46:05.3	0.1783	17.66	1.32	21.54	19.82	18.62	18.13	17.75	0.32	2.3178
r2811_03	vmf74	09:43:43.51	+16:45:20.1	0.1802	18.27	1.27	22.16	20.43	19.17	18.65	18.59	0.19	2.3948
r2811_05	vmf74	09:43:44.49	+16:44:54.2	0.1800	18.50	1.18	21.55	20.09	19.42	18.92	19.12	0.10	2.3784
r2811_07	vmf74	09:43:46.72	+16:44:25.2	0.1791	18.19	1.19	21.91	20.31	19.13	18.80	18.52	0.07	2.3188
r2811_08	vmf74	09:43:45.15	+16:44:05.6	0.1788	18.53	1.26	27.69	20.49	19.80	19.09	18.90	0.04	2.7457
r2811_10	vmf74	09:43:55.55	+16:43:34.6	0.1787	18.04	1.28	20.73	20.26	19.01	18.47	18.15	0.48	1.7345
r2811_11	vmf74	09:43:49.12	+16:43:21.2	0.1808	16.81	1.35	20.72	19.09	17.81	17.29	17.07	0.25	2.1159
r2811_13	vmf74	09:43:53.02	+16:42:48.2	0.1783	18.68	1.21	21.25	20.75	19.62	19.18	18.92	0.44	2.3363
r2811_14	vmf74	09:43:58.75	+16:42:02.5	0.1825	17.82	1.30	21.50	20.05	18.84	18.34	17.97	0.73	1.8032

Table C.1: Continued.

ID	membership	RA	DEC	redshift	I [mag]	$V - I$ [mag]	u [mag]	g [mag]	r [mag]	i [mag]	z [mag]	D [Mpc]	$\log_{10}(\Sigma_5)$ [Mpc $^{-2}$]
r2211_15	field	17:29:53.77	+74:39:44.1	0.1574	17.39	1.22
r2211_16	field	17:29:59.01	+74:41:08.1	0.3318	18.09	1.17
r2211_17	field	17:30:02.07	+74:41:43.3	0.2440	17.85	1.33
r2211_18	field	17:30:05.41	+74:40:00.7	0.1570	18.60	1.32
r2211_19	field	17:30:09.69	+74:42:44.1	0.2451	18.45	1.43
r2211_20	field	17:30:13.48	+74:41:02.5	0.2447	17.89	1.47
r2211_21	field	17:30:16.74	+74:42:26.8	0.2423	18.69	1.51
r2211_22	field	17:30:22.64	+74:39:20.9	0.3402	18.94	1.82
r2211_24	field	17:30:45.34	+74:41:21.3	0.3154	18.73	1.58
r2212_11	field	17:29:40.88	+74:41:23.3	0.2419	18.12	1.46
r2212_12	field	17:29:43.86	+74:41:45.9	0.1598	18.38	0.97
r2212_14	field	17:29:50.08	+74:42:24.7	0.2458	17.73	1.42
r2212_16	field	17:30:00.75	+74:42:09.0	0.2730	19.24	1.51
r2212_19	field	17:30:18.14	+74:41:44.4	0.3381	18.31	1.81
r2221_04	field	17:27:06.87	+74:32:15.8	0.2807	18.32	0.98
r2221_13	field	17:26:25.30	+74:27:56.1	0.2281	18.78	1.34
r2222_02	field	17:27:26.70	+74:34:42.8	0.1805	19.03	1.05
r2222_04	field	17:26:24.13	+74:33:53.7	0.2890	19.12	1.22
r2222_05	field	17:27:22.22	+74:32:27.3	0.2417	19.18	0.88
r2222_08	field	17:26:54.96	+74:31:35.9	0.2705	18.07	1.02
r2222_13	field	17:26:33.10	+74:29:40.5	0.2901	18.91	1.66
r2222_15	field	17:26:10.37	+74:29:09.5	0.1804	18.17	1.04
r2231_06	field	17:24:14.39	+74:29:43.0	0.2183	19.06	0.92
r2231_11	field	17:24:37.73	+74:30:13.6	0.1848	19.49	1.16
r2231_16	field	17:25:12.29	+74:29:40.6	0.2953	19.17	1.21
r2231_23	field	17:25:54.24	+74:26:49.6	0.3436	18.36	1.54
r2241_11	field	17:23:55.07	+74:42:40.0	0.3389	18.45	1.80
r2241_14	field	17:24:12.80	+74:40:47.1	0.1805	17.48	1.38
r2241_21	field	17:23:54.90	+74:38:24.1	0.2684	17.01	0.75
r2241_22	field	17:23:47.22	+74:38:01.9	0.2401	17.91	1.21
r2242_07	field	17:23:37.38	+74:43:40.0	0.2956	18.02	1.61

Table C.1: Continued.

ID	membership	RA	DEC	redshift	I [mag]	$V - I$ [mag]	u [mag]	g [mag]	r [mag]	i [mag]	z [mag]	D [Mpc]	$\log_{10}(\Sigma_5)$ [Mpc $^{-2}$]
r2242_10	field	17:23:51.86	+74:42:56.3	0.2096	19.04	1.69
r2242_11	field	17:24:02.24	+74:42:37.0	0.3390	18.85	1.70
r2242_12	field	17:23:13.33	+74:42:15.4	0.2968	18.90	1.69
r2242_13	field	17:23:17.51	+74:40:37.5	0.1806	18.01	1.09
r2242_18	field	17:24:31.58	+74:37:39.2	0.2419	18.17	1.70
r2251_02	field	17:23:53.84	+74:23:11.3	0.1950	18.20	1.28
r2251_08	field	17:24:12.25	+74:19:17.4	0.2282	18.58	0.90
r2251_16	field	17:24:54.82	+74:15:13.7	0.2914	16.71	1.16
r2611_02	field	13:12:15.56	+32:33:06.4	0.2640	18.93	1.34	22.10	20.96	19.90	19.41	19.04
r2611_11	field	13:11:54.78	+32:30:38.6	0.1571	18.72	0.93	21.09	20.10	19.54	19.17	18.96
r2612_01	field	13:12:28.82	+32:30:27.7	0.2627	19.01	1.60	23.18	21.52	20.03	19.49	19.17
r2621_01	field	13:10:52.83	+32:30:58.0	0.1868	19.30	1.35	20.92	21.10	20.42	19.84	19.69
r2621_05	field	13:11:04.39	+32:32:09.8	0.1580	18.69	0.96	21.09	19.97	19.48	19.05	19.22
r2621_06	field	13:11:05.84	+32:29:57.6	0.3067	18.87	1.87	23.88	21.90	20.02	19.45	19.06
r2621_09	field	13:11:10.48	+32:29:39.1	0.2346	19.41	1.38	22.75	21.36	20.26	19.88	19.59
r2621_10	field	13:11:12.39	+32:32:06.0	0.3017	18.37	1.35	21.53	20.20	19.27	18.76	18.66
r2621_12	field	13:11:14.83	+32:30:59.0	0.3072	18.38	1.63	21.02	20.49	19.28	18.80	18.33
r2631_01	field	13:10:09.80	+32:29:44.2	0.1859	18.05	1.41	21.40	20.08	18.99	18.55	18.26
r2631_02	field	13:10:15.66	+32:27:22.0	0.1849	16.26	1.48	19.78	18.34	17.27	16.76	16.50
r2631_05	field	13:10:19.66	+32:29:34.4	0.2598	18.90	1.51	22.84	20.92	20.02	19.68	19.55
r2631_10	field	13:10:28.21	+32:26:18.3	0.1573	18.66	0.98	20.58	20.08	19.55	19.14	19.17
r2631_11	field	13:10:30.08	+32:29:10.8	0.1872	16.42	1.47	20.23	18.64	17.43	16.93	16.62
r2631_16	field	13:10:37.26	+32:26:37.6	0.1859	17.17	1.01	19.73	18.69	18.02	17.64	17.53
r2651_01	field	13:10:32.47	+32:19:15.3	0.2850	19.42	1.51	21.73	21.65	20.52	20.12	19.49
r2632_06	field	13:10:24.87	+32:27:36.1	0.1850	17.35	1.44	20.93	19.54	18.37	17.88	17.58
r2651_07	field	13:10:46.66	+32:21:16.7	0.3077	18.66	1.31	22.09	20.87	19.70	19.13	19.12
r2632_10	field	13:10:29.29	+32:29:11.4	0.1849	19.07	1.34	22.67	21.24	20.29	19.40	19.28
r2641_11	field	13:10:03.30	+32:21:30.2	0.2841	18.66	1.50	21.50	21.00	19.55	19.11	19.04
r2632_14	field	13:10:38.86	+32:28:04.1	0.3078	19.37	1.57	20.38	21.20	20.53	20.11	20.98
r2632_15	field	13:10:39.83	+32:28:42.5	0.1863	17.39	1.53	20.74	19.51	18.46	17.88	17.69
r2811_12a	field	09:43:58.66	+16:43:04.5	0.1661	18.56	0.94	21.09	19.73	19.32	19.08	18.62

Table C.1: Continued.

ID	membership	RA	DEC	redshift	I [mag]	$V - I$ [mag]	u [mag]	g [mag]	r [mag]	i [mag]	z [mag]	D [Mpc]	$\log_{10}(\Sigma_5)$ [Mpc ⁻²]
r2812_19	field	09:43:51.27	+16:43:11.2	0.1543	18.95	0.65	20.41	20.28	19.85	19.61	19.30
r2812_23	field	09:43:55.30	+16:44:48.9	0.1648	18.46	1.39	23.81	20.56	19.45	19.02	18.75
r2812_25	field	09:43:55.77	+16:45:33.8	0.1578	19.10	1.15	21.81	20.82	19.90	19.59	19.35
r2812_26	field	09:43:51.93	+16:45:45.2	0.2156	19.33	1.74	27.44	22.09	20.26	19.76	19.37
r2821_06	field	09:43:51.14	+16:37:26.3	0.1748	18.72	0.89	20.21	20.20	19.51	19.21	18.73
r2821_13	field	09:43:41.44	+16:40:02.4	0.3068	18.61	1.53	21.03	21.12	19.72	19.17	19.03
r2821_18	field	09:43:35.69	+16:39:41.5	0.2243	18.89	0.94	21.22	20.73	20.14	19.66	19.67
r2821_23	field	09:43:28.76	+16:37:53.2	0.1899	18.08	1.18	20.43	19.81	18.98	18.61	18.11
r2821_28	field	09:43:22.54	+16:38:53.6	0.2733	17.90	1.45	24.52	20.24	18.97	18.35	18.29
r2822_24	field	09:43:23.20	+16:40:38.3	0.1671	18.83	1.23	21.96	20.72	19.81	19.32	19.18
r2831_05	field	09:43:19.89	+16:42:29.8	0.1672	17.58	1.14	20.74	19.27	18.53	18.02	18.00
r2831_08	field	09:43:12.49	+16:44:30.0	0.1704	17.87	1.24	20.85	19.87	18.77	18.31	18.00
r2831_16	field	09:42:56.10	+16:41:13.4	0.2311	18.63	1.25	21.76	20.38	19.53	19.07	19.27
r2831_17	field	09:42:52.23	+16:42:47.2	0.1627	17.88	1.04	20.52	19.35	18.69	18.29	18.19
r2831_18	field	09:42:51.23	+16:41:08.8	0.2335	17.07	1.11	19.94	18.90	18.03	17.56	17.35
r2841_01	field	09:44:58.57	+16:30:07.6	0.2233	19.41	1.42	22.48	21.92	20.55	20.12	19.42
r2841_01	field	09:44:58.57	+16:30:07.6	0.2233	19.41	1.42	22.48	21.92	20.55	20.12	19.42
r2841_09	field	09:44:38.51	+16:27:52.5	0.2331	17.25	1.33	20.05	19.46	18.35	17.84	17.61
r2841_12	field	09:44:33.83	+16:30:53.1	0.2738	19.33	0.75	21.24	21.13	20.35	20.09	19.97
r2841_13	field	09:44:32.35	+16:28:34.4	0.1598	18.91	1.03	21.66	20.55	19.87	19.35	19.43
r2841_18	field	09:44:21.95	+16:30:48.2	0.2326	19.19	1.45	23.90	21.58	20.28	19.78	19.85
r2841_19a	field	09:44:20.04	+16:30:28.5	0.2333	17.51	1.29	21.02	19.66	18.53	17.94	17.85
r2841_20	field	09:44:16.29	+16:28:47.4	0.1798	19.46	0.91	21.39	20.85	20.50	20.21	20.37
r2851_01b	field	09:43:57.19	+16:25:17.4	0.2228	19.09	1.09	21.81	21.04	20.00	19.60	19.15
r2851_02	field	09:43:56.93	+16:27:05.9	0.3328	19.24	1.53	22.51	21.62	20.49	19.78	19.24
r2851_03	field	09:44:00.04	+16:27:29.0	0.3328	18.24	1.71	21.36	20.80	19.33	18.63	18.55
r2851_05	field	09:44:02.36	+16:28:40.6	0.3232	19.34	1.04	22.31	21.54	20.63	19.96	19.83
r2851_06	field	09:44:07.29	+16:29:22.8	0.2324	17.24	1.35	21.03	19.46	18.26	17.71	17.54
r2851_12	field	09:44:04.32	+16:32:00.8	0.3159	18.23	1.50	21.97	20.69	19.25	18.57	18.28
r2851_13	field	09:43:58.24	+16:32:18.3	0.2229	18.11	1.31	21.71	20.27	19.09	18.38	18.23
r2851_18b	field	09:43:48.98	+16:34:44.2	0.2949	18.87	1.49	23.39	21.47	20.08	19.48	19.38

The next table contains the equivalent widths of each of the lines used in this work.

Column (1) – Object ID.

Column (2) – cluster, group or field membership.

Columns (9)–(19) – Equivalent widths and their errors (E) for each object in the following lines: [O II] λ 3727, H δ , H β , [O III] λ 5007, H α and [N II] λ 6583. The superscript in the errors indicate the subjective quality for each line. *c*: the line is clear. *f*: the line is faint but visible. *p*: the line is visible but polluted by *e.g.* sky lines residuals in the continuum windows. *n*: the line is not detected, it may be blended in the noise or simply inexistent. *o*: The line is out of the range covered by the spectra. *u*: The line is completely unusable, it usually falls in the A or B telluric bands or is strongly affected by sky line residuals and other artifacts.

Table C.2: Equivalent widths for individual objects.

(1)	(2)	(9)	(10)	(11)	(12)	(13)	(14)	(15)	(16)	(17)	(18)	(19)	(20)
ID	membership	[O II] [Å]	E([O II]) [Å]	H δ [Å]	E(H δ) [Å]	H β [Å]	E(H β) [Å]	[O III] [Å]	E([O III]) [Å]	H α [Å]	E(H α) [Å]	[N II] [Å]	E([N II]) [Å]
r2211_07	vmf194	9.66	0.75 ⁿ	2.56	0.41 ^f	2.77	0.21 ^c	0.96	0.18 ⁿ	0.75	0.23 ⁿ	0.13	0.26 ⁿ
r2211_08	vmf194	8.95	0.95 ⁿ	-0.44	0.43 ⁿ	3.99	0.24 ^u	0.57	0.18 ⁿ	1.10	0.23 ⁿ	-0.15	0.24 ⁿ
r2211_09	vmf194	0.43	0.48 ⁿ	1.60	0.33 ^c	2.42	0.17 ^p	0.46	0.15 ⁿ	-1.71	0.19 ⁿ	0.80	0.20 ⁿ
r2211_10	vmf194	0.18	0.55 ⁿ	1.00	0.38 ⁿ	2.93	0.21 ^p	1.49	0.18 ⁿ	1.13	0.24 ⁿ	-2.81	0.25 ⁿ
r2212_06	vmf194	-32.93	0.63 ^c	2.24	0.43 ^f	-8.12	0.30 ^c	-4.77	0.27 ^f	-41.10	0.85 ^c	-10.37	0.62 ^f
r2212_08	vmf194	3.93	0.60 ⁿ	-3.35	0.37 ^c	4.75	0.25 ^c	0.82	0.18 ⁿ	1.12	0.28 ⁿ	0.02	0.33 ⁿ
r2212_23	vmf194	8.32	2.22 ⁿ	1.98	0.83 ⁿ	3.77	0.42 ^c	0.16	0.28 ⁿ	-0.87	0.36 ⁿ	-6.03	0.40 ^p
r2221_14	vmf194	-0.02	0.69 ⁿ	3.25	0.46 ⁿ	0.76	0.27 ⁿ	-0.21	0.23 ⁿ	-10.33	0.30 ^c	-9.05	0.35 ^f
r2221_03	xdes220	-39.80	0.67 ^c	0.15	0.46 ⁿ	-4.56	0.28 ^c	-7.80	0.28 ^c	-52.51	0.87 ^c	-6.96	0.63 ^c
r2221_03b	xdes220	-61.16	1.72 ^c	11.08	0.99 ⁿ	-15.67	0.69 ^f	-14.09	0.61 ^c	-45.71	1.66 ^c	-20.15	1.53 ^c
r2221_12	xdes220	-4.34	0.85 ⁿ	-4.18	0.65 ⁿ	2.55	0.33 ⁿ	1.91	0.34 ⁿ	1.46	0.61 ⁿ	0.97	0.53 ⁿ
r2222_03	xdes220	0.21	0.39 ⁿ	0.10	0.26 ^f	2.24	0.13 ^f	1.57	0.14 ⁿ	-0.91	0.17 ⁿ	-2.39	0.20 ⁿ
r2222_07	xdes220	3.07	0.41 ⁿ	-0.01	0.27 ⁿ	4.12	0.15 ^c	0.92	0.15 ⁿ	0.76	0.24 ⁿ	-1.49	0.27 ⁿ
r2231_05	xdes220	4.80	0.35 ⁿ	0.97	0.21 ⁿ	2.27	0.12 ⁿ	1.64	0.13 ⁿ	3.06	0.23 ⁿ	-3.33	0.21 ⁿ
r2241_05	xdes220	-0.02	1.23 ⁿ	3.97	0.68 ⁿ	2.08	0.28 ⁿ	1.60	0.31 ⁿ	3.42	0.52 ⁿ	-1.67	0.45 ⁿ
r2241_07	xdes220	5.64	0.45 ⁿ	-1.56	0.27 ⁿ	1.51	0.12 ⁿ	1.80	0.13 ⁿ	1.65	0.17 ⁿ	-1.27	0.19 ⁿ
r2241_09	xdes220	-14.98	0.51 ^f	0.51	0.37 ⁿ	1.37	0.16 ⁿ	0.41	0.17 ⁿ	-3.00	0.20 ^f	-3.80	0.24 ^f
r2241_10	xdes220	8.83	0.64 ⁿ	-1.05	0.33 ⁿ	2.08	0.14 ⁿ	2.34	0.16 ⁿ	2.30	0.20 ⁿ	1.04	0.24 ⁿ
r2241_15	xdes220	-1.46	0.43 ⁿ	4.84	0.36 ⁿ	-2.10	0.18 ^f	0.63	0.20 ⁿ	-12.41	0.24 ^c	-5.79	0.27 ^c
r2241_18	xdes220	-20.46	0.29 ^c	3.86	0.23 ^f	-3.74	0.13 ^c	-5.03	0.14 ^c	-35.91	0.28 ^c	-9.51	0.22 ^c
r2242_06	xdes220	-3.18	1.04 ⁿ	3.72	0.69 ⁿ	1.70	0.29 ⁿ	-0.02	0.30 ⁿ	7.17	0.62 ^f	-1.89	0.43 ⁿ
r2251_04	xdes220	-37.27	1.09 ^c	3.04	0.62 ⁿ	-8.93	0.29 ^c	-8.25	0.31 ^f	-47.44	0.77 ^c	-18.64	0.67 ^f
XDC29_04	xdes220	0.72	0.58 ⁿ	-1.75	0.41 ^f	2.48	0.22 ^f	0.86	0.23 ⁿ	-1.36	0.31 ⁿ	0.72	0.32 ⁿ
r2621_15	vmf131	0.98	0.30 ⁿ	1.68	0.25 ^f	1.59	0.16 ^f	-1.46	0.14 ⁿ	0.35	0.20 ⁿ	0.40	0.21 ⁿ
r2621_16	vmf131	-20.84	0.24 ^c	5.61	0.22 ^c	-3.02	0.15 ^c	-4.63	0.14 ^c	-31.54	0.33 ^c	-10.92	0.29 ^c
r2631_20	vmf131	2.72	0.48 ⁿ	-0.42	0.38 ⁿ	2.69	0.31 ^p	1.02	0.21 ⁿ	-1.85	0.34 ⁿ	-2.35	0.32 ⁿ
r2632_02	vmf131	2.09	0.23 ⁿ	-0.45	0.19 ⁿ	2.33	0.12 ^c	0.81	0.10 ⁿ	-1.66	0.16 ⁿ	-1.15	0.15 ⁿ
r2632_02b	vmf131	-22.93	0.46 ^c	0.98	0.43 ⁿ	-3.79	0.36 ⁿ	-7.65	0.30 ^f	-31.87	0.78 ^c	-10.91	0.61 ^f
r2632_03	vmf131	-0.38	0.18 ⁿ	0.64	0.15 ^c	1.91	0.09 ^f	-0.19	0.08 ⁿ	0.15	0.13 ⁿ	-0.40	0.12 ⁿ
r2632_11	vmf131	-10.37	0.15 ^c	3.34	0.15 ^c	-1.40	0.10 ^p	-2.00	0.09 ^c	-19.49	0.16 ^c	-5.25	0.15 ^c

Table C.2: Continued.

(1)	(2)	(9)	(10)	(11)	(12)	(13)	(14)	(15)	(16)	(17)	(18)	(19)	(20)
ID	membership	[O II] [Å]	E([O II]) [Å]	H δ [Å]	E(H δ) [Å]	H β [Å]	E(H β) [Å]	[O III] [Å]	E([O III]) [Å]	H α [Å]	E(H α) [Å]	[N II] [Å]	E([N II]) [Å]
r2632_12	vmf131	-19.41	0.21 ^c	5.00	0.19 ^c	-1.87	0.16 ^c	-5.91	0.13 ^c	-27.83	0.33 ^c	-7.41	0.28 ^f
r2632_17	vmf131	-4.03	0.30 ^f	1.77	0.25 ^f	1.44	0.16 ⁿ	0.26	0.15 ⁿ	-3.99	0.20 ⁿ	-0.51	0.22 ⁿ
r2641_04	vmf131	-2.01	1.15 ^f	3.90	0.82 ⁿ	0.22	1.01 ⁿ	-0.34	0.51 ⁿ	-12.32	0.90 ^f	-5.89	0.77 ^f
r2641_05	vmf131	-0.16	1.23 ⁿ	4.75	0.87 ⁿ	-7.05	0.84 ^f	-0.59	0.53 ⁿ	-11.21	0.91 ^f	-7.09	0.82 ^f
r2641_06	vmf131	2.78	0.52 ⁿ	2.92	0.37 ⁿ	2.17	0.26 ^f	1.64	0.19 ⁿ	1.22	0.30 ⁿ	1.15	0.29 ⁿ
r2641_07	vmf131	-5.09	0.38 ⁿ	3.79	0.34 ⁿ	-0.30	0.26 ⁿ	1.09	0.21 ⁿ	-15.73	0.35 ^f	-5.57	0.32 ^f
r2641_12	vmf131 ^o	-1.04	0.45 ⁿ	2.51	0.35 ⁿ	0.52	0.24 ⁿ	-0.36	0.39 ⁿ	-1.11	0.36 ⁿ
r2651_08	vmf131	-2.87	0.25 ⁿ	-0.64	0.21 ⁿ	1.72	0.13 ^f	1.40	0.11 ⁿ	2.55	0.18 ^f	-0.05	0.16 ⁿ
r2651_17	vmf131	-4.27	0.17 ^f	-0.57	0.15 ^f	1.77	0.09 ^f	-0.63	0.08 ⁿ	-0.60	0.11 ⁿ	-2.84	0.11 ⁿ
r2651_19	vmf131	-5.96	0.22 ^f	2.07	0.19 ^f	1.13	0.13 ⁿ	0.95	0.11 ⁿ	-8.38	0.15 ^c	-3.10	0.16 ^f
ba_07	vmf131	5.07	0.80 ⁿ	0.10	0.69 ⁿ	6.16	0.47 ^p	-1.73	0.42 ⁿ	0.24	0.60 ⁿ	-2.00	0.64 ⁿ
ba_09	vmf131	3.28	0.81 ⁿ	5.94	0.75 ⁿ	0.22	0.46 ⁿ	-0.30	0.46 ⁿ	2.95	0.70 ⁿ	-1.90	0.69 ⁿ
ba_12	vmf131	3.51	0.55 ⁿ	-4.73	0.47 ⁿ	0.41	0.25 ⁿ	1.60	0.25 ⁿ	3.18	0.36 ⁿ	3.49	0.37 ⁿ
ba_14	vmf131	4.67	0.68 ⁿ	-3.43	0.58 ⁿ	2.03	0.33 ^u	-2.41	0.32 ⁿ	-2.11	0.43 ⁿ	-2.19	0.47 ⁿ
ba_18	vmf131	6.15	0.49 ⁿ	-1.83	0.42 ⁿ	3.37	0.23 ^f	1.37	0.23 ⁿ	0.20	0.35 ⁿ	-0.41	0.35 ⁿ
ba_25	vmf131	5.13	0.50 ⁿ	-3.14	0.46 ⁿ	3.17	0.25 ⁿ	1.27	0.25 ⁿ	0.13	0.35 ⁿ	0.27	0.36 ⁿ
ba_28	vmf131	5.12	0.35 ⁿ	-2.68	0.29 ⁿ	1.06	0.15 ⁿ	0.56	0.16 ⁿ	0.84	0.22 ⁿ	-2.72	0.23 ⁿ
ba_30	vmf131	2.29	0.48 ⁿ	-3.66	0.43 ⁿ	1.51	0.22 ⁿ	2.04	0.23 ⁿ	1.07	0.34 ⁿ	-1.14	0.35 ⁿ
ba_36	vmf131	-6.82	0.38 ^f	5.05	0.38 ^c	0.04	0.24 ^u	1.24	0.24 ⁿ	-11.69	0.35 ^c	-4.66	0.39 ^f
ba_37	vmf131	-6.66	0.77 ^f	0.17	0.72 ⁿ	0.56	0.38 ⁿ	-0.42	0.40 ⁿ	-11.75	0.59 ^f	-9.82	0.66 ^f
ba_39	vmf131	-2.66	0.46 ⁿ	-2.47	0.42 ⁿ	2.77	0.23 ^f	0.35	0.23 ⁿ	-0.46	0.31 ⁿ	-0.52	0.32 ⁿ
r2611_04	vmf132	6.99	0.54 ⁿ	1.32	0.42 ⁿ	1.20	0.24 ⁿ	3.91	0.24 ⁿ	2.91	0.32 ⁿ	-1.09	0.32 ⁿ
r2611_13	vmf132	6.78	0.35 ⁿ	-3.65	0.29 ⁿ	1.36	0.15 ⁿ	0.56	0.16 ⁿ	1.40	0.21 ⁿ	-0.49	0.21 ⁿ
r2611_14	vmf132	0.91	0.40 ⁿ	0.05	0.33 ^f	2.66	0.17 ^f	0.77	0.17 ⁿ	1.31	0.23 ⁿ	0.23	0.23 ⁿ
r2612_02	vmf132	-15.32	0.23 ^c	2.47	0.20 ^f	0.22	0.11 ^f	-1.37	0.10 ^f	-10.12	0.13 ^c	-4.63	0.13 ^c
r2612_04	vmf132	-39.36	0.31 ^c	6.07	0.24 ^c	-9.19	0.15 ^c	-15.81	0.17 ^c	-58.97	0.39 ^c	-15.59	0.27 ^c
r2612_06	vmf132	1.87	0.14 ⁿ	-0.99	0.12 ^c	2.48	0.06 ^p	1.17	0.06 ⁿ	0.97	0.09 ⁿ	0.56	0.09 ⁿ
r2612_17	vmf132	0.97	0.22 ⁿ	-0.68	0.18 ^f	2.26	0.09 ^c	0.01	0.09 ⁿ	1.33	0.12 ⁿ	-1.27	0.12 ^f
r2621_03	vmf132	1.20	0.21 ⁿ	0.35	0.17 ^f	2.72	0.09 ^c	1.44	0.09 ⁿ	1.89	0.12 ^f	-0.12	0.12 ⁿ
r2621_04	vmf132	0.66	0.40 ⁿ	-1.84	0.29 ⁿ	1.96	0.15 ⁿ	0.51	0.15 ⁿ	-0.07	0.20 ⁿ	0.05	0.20 ⁿ
r2621_11	vmf132	4.32	0.27 ⁿ	-1.16	0.20 ^f	2.34	0.10 ^f	0.72	0.10 ⁿ	1.15	0.13 ^f	0.21	0.13 ⁿ

Table C.2: Continued.

(1)	(2)	(9)	(10)	(11)	(12)	(13)	(14)	(15)	(16)	(17)	(18)	(19)	(20)
ID	membership	[O II] [Å]	E([O II]) [Å]	H δ [Å]	E(H δ) [Å]	H β [Å]	E(H β) [Å]	[O III] [Å]	E([O III]) [Å]	H α [Å]	E(H α) [Å]	[N II] [Å]	E([N II]) [Å]
r2621_13	vmf132	3.18	0.18 ⁿ	0.30	0.15 ^f	1.90	0.08 ^c	1.28	0.08 ⁿ	0.22	0.10 ⁿ	0.09	0.10 ⁿ
r2621_22	vmf132	-2.56	0.23 ⁿ	2.09	0.19 ^f	1.50	0.11 ⁿ	1.71	0.11 ⁿ	-4.01	0.13 ^c	-2.45	0.16 ^f
r2631_21	vmf132	-3.50	0.33 ^f	3.40	0.31 ⁿ	-1.01	0.19 ⁿ	-2.57	0.20 ⁿ	-7.80	0.25 ^f	-3.68	0.27 ⁿ
r2631_08	vmf132 ^o	4.49	0.35 ⁿ	2.14	0.20 ⁿ	1.36	0.21 ⁿ	-1.35	0.28 ⁿ	-3.37	0.32 ⁿ
r2632_07	vmf132	-0.94	0.83 ^p	1.02	0.41 ^f	0.86	0.22 ^p	-1.09	0.25 ^f	-3.46	0.24 ^c	-1.17	0.29 ^f
r2632_13	vmf132	-0.17	0.19 ⁿ	-0.80	0.17 ⁿ	1.93	0.09 ^c	0.34	0.09 ⁿ	1.18	0.12 ^f	-1.26	0.12 ⁿ
r2641_10	vmf132	9.17	1.56 ⁿ	-0.44	0.68 ⁿ	0.11	0.37 ⁿ	2.16	0.48 ⁿ	-5.42	0.54 ^f	-2.61	0.60 ^f
ba_29	vmf132	-53.59	1.20 ^c	2.90	0.84 ⁿ	-11.46	0.63 ^f	-46.52	1.05 ^c	-61.71	2.16 ^c	-12.77	1.54 ^f
r2811_06	vmf73	-6.83	1.17 ^f	-1.18	0.82 ⁿ	1.41	0.36 ⁿ	0.26	0.38 ⁿ	-3.35	0.36 ^f	-2.35	0.41 ^f
r2811_16	vmf73	-0.16	0.65 ⁿ	2.16	0.45 ^f	1.70	0.21 ^f	1.04	0.22 ⁿ	-2.47	0.24 ^f	-0.89	0.28 ⁿ
r2811_18	vmf73	0.80	1.17 ⁿ	0.65	0.69 ⁿ	1.98	0.29 ^f	0.58	0.32 ⁿ	0.43	0.33 ⁿ	-0.83	0.39 ⁿ
r2811_19	vmf73	-1.26	2.62 ⁿ	-2.60	1.28 ⁿ	1.69	0.53 ⁿ	0.94	0.55 ⁿ	0.70	0.67 ⁿ	-0.65	0.73 ⁿ
r2811_20	vmf73	5.85	3.06 ⁿ	-0.96	1.80 ⁿ	1.51	0.73 ⁿ	2.13	1.22 ⁿ	-1.53	0.88 ⁿ	15.29	5.72 ⁿ
r2811_24	vmf73	4.65	1.30 ⁿ	2.32	0.67 ^f	3.24	0.31 ^f	1.84	0.32 ⁿ	0.76	0.35 ⁿ	-0.96	0.37 ⁿ
r2811_25	vmf73	-5.85	1.51 ^f	0.48	1.01 ⁿ	0.86	0.41 ⁿ	1.55	0.41 ⁿ	-2.06	0.46 ⁿ	-3.21	0.52 ⁿ
r2812_05	vmf73	8.83	3.26 ⁿ	6.23	2.27 ^f	0.58	0.47 ^f	2.12	0.78 ⁿ	-0.05	0.45 ⁿ	0.21	0.53 ⁿ
r2812_09	vmf73	5.74	3.73 ⁿ	7.22	1.86 ⁿ	4.04	0.76 ^f	0.15	0.75 ⁿ	-1.70	0.82 ⁿ	-1.99	0.81 ⁿ
r2812_12	vmf73	1.88	1.44 ⁿ	0.40	0.80 ^f	1.45	0.30 ^f	1.09	0.50 ⁿ	-2.53	0.26 ^f	-4.10	0.33 ^f
r2812_14	vmf73	1.48	1.28 ⁿ	-3.43	0.75 ⁿ	1.91	0.26 ^f	1.65	0.27 ⁿ	1.53	0.28 ⁿ	0.21	0.30 ⁿ
r2821_02	vmf73	-0.11	1.40 ⁿ	-1.09	0.80 ⁿ	1.84	0.31 ⁿ	1.19	0.37 ⁿ	1.92	0.37 ⁿ	-1.51	0.42 ⁿ
r2821_08	vmf73	-33.96	0.81 ^c	0.60	0.58 ⁿ	-12.19	0.38 ^c	-10.59	0.43 ^c	-69.22	1.50 ^c	-24.97	1.07 ^c
r2821_12	vmf73	-3.06	1.44 ⁿ	-2.48	0.92 ⁿ	1.69	0.40 ⁿ	-0.53	0.75 ⁿ	-0.93	0.43 ⁿ	2.98	0.66 ⁿ
r2821_17	vmf73	3.38	2.29 ⁿ	-6.33	1.12 ^f	2.23	0.45 ⁿ	0.43	0.86 ⁿ	-2.92	0.58 ⁿ	-2.85	0.78 ⁿ
r2821_14	vmf73	4.93	3.98 ⁿ	0.49	1.70 ⁿ	2.46	0.71 ⁿ	1.16	1.37 ⁿ	-3.89	0.83 ⁿ	-1.42	1.72 ⁿ
r2821_20	vmf73	-13.73	2.82 ^f	0.65	1.50 ⁿ	1.19	0.60 ⁿ	1.59	0.70 ⁿ	3.80	0.80 ⁿ	4.35	0.85 ⁿ
r2821_21	vmf73	0.92	2.23 ⁿ	-2.95	1.61 ⁿ	2.25	0.63 ⁿ	2.53	0.66 ⁿ	1.63	0.74 ⁿ	-1.24	0.82 ⁿ
r2821_27	vmf73	-0.29	1.31 ⁿ	-1.42	0.90 ^f	1.10	0.48 ^f	-2.68	0.78 ^f	-3.83	0.54 ⁿ	-0.25	0.95 ⁿ
r2821_29	vmf73	-5.97	1.61 ^f	-0.41	1.05 ⁿ	1.19	0.48 ⁿ	2.87	1.14 ⁿ	0.11	0.69 ⁿ	3.17	1.05 ⁿ
r2822_01	vmf73	-0.27	0.96 ⁿ	0.19	0.58 ^f	2.11	0.27 ^c	1.77	0.40 ⁿ	1.26	0.34 ⁿ	-0.72	0.40 ⁿ
r2822_03	vmf73	2.69	0.64 ⁿ	-1.32	0.42 ⁿ	1.60	0.21 ⁿ	1.59	0.27 ⁿ	1.52	0.36 ⁿ	-0.12	0.39 ⁿ
r2822_04	vmf73	0.97	1.08 ⁿ	-0.42	0.56 ⁿ	2.92	0.25 ^f	1.57	0.30 ⁿ	2.27	0.32 ^f	-1.39	0.34 ⁿ

Table C.2: Continued.

(1)	(2)	(9)	(10)	(11)	(12)	(13)	(14)	(15)	(16)	(17)	(18)	(19)	(20)
ID	membership	[O II] [Å]	E([O II]) [Å]	H δ [Å]	E(H δ) [Å]	H β [Å]	E(H β) [Å]	[O III] [Å]	E([O III]) [Å]	H α [Å]	E(H α) [Å]	[N II] [Å]	E([N II]) [Å]
r2822_05	vmf73	-0.15	0.45 ⁿ	1.70	0.31 ^c	1.69	0.14 ^c	1.00	0.16 ⁿ	-2.38	0.17 ^f	-1.20	0.21 ^f
r2822_06	vmf73	-2.82	0.50 ⁿ	3.04	0.37 ^c	-0.77	0.21 ⁿ	-0.28	0.23 ⁿ	-16.58	0.30 ^c	-8.04	0.38 ^f
r2822_09	vmf73	-19.19	0.67 ^c	2.84	0.49 ^f	-0.77	0.30 ^f	-1.39	0.36 ^p	-22.61	0.55 ^c	-5.74	0.60 ^f
r2822_14	vmf73	3.89	0.90 ⁿ	-2.38	0.49 ⁿ	2.15	0.22 ^c	0.54	0.23 ⁿ	2.31	0.29 ^f	0.57	0.31 ⁿ
r2822_15	vmf73	4.35	0.56 ⁿ	-3.40	0.31 ^f	1.83	0.13 ^c	1.39	0.21 ⁿ	1.01	0.16 ⁿ	0.21	0.23 ⁿ
r2822_16	vmf73	0.76	0.82 ⁿ	-1.73	0.45 ⁿ	2.68	0.20 ^c	1.68	0.24 ⁿ	0.47	0.25 ⁿ	-1.24	0.25 ⁿ
r2822_17	vmf73	-1.62	0.88 ⁿ	3.20	0.58 ^f	1.12	0.28 ^f	0.66	0.32 ⁿ	-0.11	0.35 ⁿ	-2.76	0.44 ⁿ
r2822_19	vmf73	2.32	1.27 ⁿ	-1.78	0.77 ⁿ	1.65	0.32 ^f	2.76	0.36 ⁿ	3.04	0.48 ^f	-0.07	0.53 ⁿ
r2822_20	vmf73	1.58	0.65 ⁿ	4.38	0.57 ⁿ	1.65	0.27 ⁿ	3.89	0.60 ⁿ	0.46	0.40 ⁿ	1.36	0.66 ⁿ
r2822_22	vmf73	2.17	0.52 ⁿ	-1.30	0.31 ^f	1.29	0.13 ^f	1.10	0.16 ⁿ	0.26	0.17 ⁿ	-1.23	0.18 ⁿ
r2822_23	vmf73	13.14	1.26 ⁿ	0.94	0.49 ^f	3.48	0.25 ^c	1.42	0.32 ⁿ	1.88	0.50 ⁿ	0.47	0.50 ⁿ
r2822_25	vmf73	-1.78	0.67 ⁿ	1.99	0.43 ^f	2.60	0.23 ^c	0.13	0.25 ⁿ	-4.66	0.26 ^f	-1.75	0.33 ^f
r2831_03	vmf73	-24.22	5.22 ⁿ	1.03	2.52 ⁿ	-0.15	1.31 ⁿ	-8.07	2.14 ⁿ	-16.09	1.77 ^f	-13.34	2.52 ^f
r2831_10	vmf73	-10.66	1.02 ^c	1.67	0.87 ^f	-2.12	0.50 ^f	-3.17	0.86 ⁿ	-18.04	0.78 ^c	-3.89	0.94 ^f
r2831_13	vmf73	4.92	1.29 ⁿ	1.88	0.67 ⁿ	2.25	0.31 ⁿ	0.42	0.45 ⁿ	-1.09	0.36 ⁿ	-0.84	0.43 ⁿ
r2841_07	vmf73	-45.76	2.52 ^c	2.59	1.11 ⁿ	-2.52	0.50 ^f	-14.72	0.75 ^c	-21.50	0.73 ^c	-8.31	0.85 ^c
r2841_10	vmf73	-14.14	0.75 ^c	2.82	0.51 ^f	0.18	0.23 ^f	-3.42	0.23 ^f	-11.00	0.28 ^c	-7.53	0.33 ^c
r2841_17	vmf73	1.61	0.98 ⁿ	-2.10	0.46 ^f	2.48	0.18 ^c	0.56	0.20 ⁿ	1.43	0.22 ^f	-0.77	0.24 ⁿ
r2851_04	vmf73	-12.13	0.56 ^c	3.43	0.47 ^f	-2.35	0.30 ^c	-1.49	0.37 ^f	-28.68	0.72 ^c	-7.86	0.74 ^c
r2851_14	vmf73	3.75	2.19 ⁿ	11.55	1.57 ⁿ	0.79	0.66 ⁿ	1.04	0.70 ⁿ	-4.63	0.66 ^p	-0.86	0.78 ⁿ
r2851_17	vmf73	1.31	0.55 ⁿ	-0.20	0.35 ⁿ	1.73	0.14 ^c	0.34	0.17 ⁿ	0.78	0.18 ⁿ	-0.20	0.20 ⁿ
r2811_01	vmf74	4.45	0.72 ⁿ	-2.38	0.45 ⁿ	1.94	0.19 ^f	0.94	0.23 ⁿ	1.37	0.24 ^f	-0.38	0.26 ⁿ
r2811_03	vmf74	2.27	0.97 ⁿ	-2.28	0.58 ⁿ	1.97	0.25 ^f	-0.00	0.27 ⁿ	0.85	0.33 ⁿ	0.83	0.34 ⁿ
r2811_05	vmf74	-21.52	1.18 ^c	0.47	0.85 ⁿ	-13.90	0.47 ^c	-2.73	0.47 ^f	-77.27	1.12 ^c	-28.71	0.84 ^c
r2811_07	vmf74	-2.13	1.22 ⁿ	3.27	0.74 ⁿ	3.44	0.34 ^f	-1.30	0.39 ⁿ	-2.40	0.40 ⁿ	-1.67	0.45 ⁿ
r2811_08	vmf74	-8.10	1.85 ⁿ	3.53	1.21 ⁿ	0.49	0.49 ⁿ	1.69	0.65 ⁿ	-8.58	0.53 ^f	-4.77	0.65 ^f
r2811_10	vmf74	0.93	1.33 ⁿ	-3.28	0.73 ⁿ	1.50	0.29 ⁿ	1.97	0.37 ⁿ	0.97	0.34 ^p	-2.00	0.37 ⁿ
r2811_11	vmf74	0.70	0.64 ⁿ	-2.51	0.38 ⁿ	1.69	0.15 ^f	1.06	0.16 ⁿ	-1.23	0.18 ⁿ	-1.55	0.18 ⁿ
r2811_13	vmf74	2.84	2.04 ⁿ	-3.17	1.09 ⁿ	2.19	0.46 ⁿ	0.89	0.61 ⁿ	1.52	0.59 ⁿ	-1.86	0.64 ⁿ
r2811_14	vmf74	5.52	1.71 ⁿ	1.00	0.73 ⁿ	2.34	0.29 ^f	1.68	0.31 ⁿ	1.56	0.36 ⁿ	0.59	0.35 ⁿ
r2811_22	vmf74	-21.35	2.32 ^f	1.30	1.09 ⁿ	-2.12	0.48 ^f	1.19	0.69 ⁿ	-25.48	0.99 ^f	-6.10	1.01 ^f

Table C.2: Continued.

(1)	(2)	(9)	(10)	(11)	(12)	(13)	(14)	(15)	(16)	(17)	(18)	(19)	(20)
ID	membership	[O II] [Å]	E([O II]) [Å]	H δ [Å]	E(H δ) [Å]	H β [Å]	E(H β) [Å]	[O III] [Å]	E([O III]) [Å]	H α [Å]	E(H α) [Å]	[N II] [Å]	E([N II]) [Å]
r2811_23	vmf74	-2.49	0.96 ⁿ	1.10	0.54 ⁿ	1.54	0.25 ⁿ	1.12	0.32 ⁿ	-6.81	0.28 ^p	-2.92	0.34 ^p
r2812_02	vmf74	-0.22	1.36 ⁿ	1.38	0.65 ⁿ	1.81	0.20 ^f	-0.97	0.22 ⁿ	-0.52	0.21 ⁿ	-1.93	0.21 ⁿ
r2812_16	vmf74	-16.80	4.23 ⁿ	-1.51	1.97 ⁿ	3.12	0.72 ⁿ	3.29	1.09 ⁿ	-10.69	0.60 ^c	-7.19	0.77 ^f
r2812_17	vmf74	6.09	1.68 ⁿ	2.97	0.71 ^f	2.28	0.25 ^f	0.94	0.28 ⁿ	-4.01	0.24 ^f	-2.21	0.25 ^f
r2812_22	vmf74	8.73	3.08 ⁿ	-1.63	1.05 ⁿ	2.61	0.33 ^f	0.46	0.36 ⁿ	0.07	0.36 ⁿ	0.48	0.35 ⁿ
r2812_21	vmf74	-6.10	1.10 ^f	0.75	0.69 ^f	2.29	0.28 ^f	-1.05	0.33 ^f	-9.78	0.25 ^c	-6.92	0.29 ^f
r2821_03	vmf74	10.57	3.86 ⁿ	0.73	1.56 ⁿ	4.39	0.58 ^f	0.28	0.62 ⁿ	-0.03	0.71 ⁿ	-0.46	0.65 ⁿ
r2821_06	vmf74	-23.75	2.87 ^p	10.37	2.14 ⁿ	-4.23	0.99 ^f	-4.40	1.28 ⁿ	-31.60	2.05 ^p	-7.92	1.74 ⁿ
r2821_07	vmf74	-3.49	4.05 ⁿ	-4.47	1.99 ⁿ	3.13	0.74 ⁿ	0.00	0.85 ⁿ	2.84	0.91 ⁿ	-0.15	0.81 ⁿ
r2821_09	vmf74	-5.83	6.46 ^f	3.23	2.33 ⁿ	8.57	1.09 ^f	4.91	1.11 ⁿ	0.17	1.12 ⁿ	-0.68	1.10 ⁿ
r2821_10	vmf74	-16.78	7.64 ^f	-10.11	2.82 ^f	2.70	1.15 ⁿ	3.15	1.63 ⁿ	1.04	1.10 ⁿ	-0.57	1.38 ⁿ
r2821_11	vmf74	-6.26	2.14 ^f	-5.12	1.01 ⁿ	1.68	0.34 ⁿ	0.26	0.44 ⁿ	-0.59	0.49 ⁿ	-1.11	0.50 ⁿ
r2822_07	vmf74	4.17	0.58 ⁿ	-1.33	0.29 ⁿ	2.35	0.12 ^c	1.00	0.13 ⁿ	1.07	0.15 ^c	0.05	0.14 ⁿ
r2822_10	vmf74	-0.03	0.80 ⁿ	1.48	0.43 ^c	1.91	0.17 ^c	0.29	0.19 ⁿ	-0.40	0.20 ⁿ	-1.45	0.21 ⁿ
r2822_13	vmf74	1.35	1.87 ⁿ	0.84	0.77 ⁿ	0.59	0.35 ⁿ	-0.04	0.45 ⁿ	-14.50	0.45 ^c	-5.44	0.51 ^f
r2831_09	vmf74	-14.13	2.55 ^f	5.98	1.83 ⁿ	0.06	0.70 ⁿ	0.32	0.77 ⁿ	-19.38	0.88 ^c	-4.47	0.87 ^c
r2831_20	vmf74	-5.48	1.19 ^f	4.24	0.81 ^f	2.57	0.38 ^f	-0.72	0.41 ⁿ	-2.32	0.60 ^f	-1.71	0.57 ⁿ
r2841_03	vmf74	-27.04	8.74 ^p	1.85	2.29 ⁿ	-1.03	0.59 ^f	-3.99	0.58 ^f	-17.81	0.82 ^c	-0.45	0.90 ⁿ
r2841_08	vmf74	-21.39	1.97 ^c	6.14	1.23 ⁿ	-3.96	0.53 ^f	-2.77	0.56 ^f	-28.51	0.92 ^c	-7.44	0.86 ^f
r2841_20	vmf74	-28.28	2.91 ^c	1.99	1.19 ⁿ	-0.32	0.61 ⁿ	-3.10	0.64 ⁿ	-13.70	1.07 ^c	-5.40	1.27 ^f
r2851_09	vmf74	0.54	2.14 ⁿ	2.64	1.15 ^f	4.01	0.53 ^f	2.12	0.54 ⁿ	-0.59	0.77 ⁿ	1.38	0.71 ⁿ
r2851_10	vmf74	-29.97	0.65 ^c	3.59	0.43 ^f	-4.47	0.24 ^c	-4.77	0.29 ^c	-41.39	0.65 ^c	-12.15	0.56 ^c
r2851_11	vmf74	-39.42	1.39 ^c	2.35	0.74 ⁿ	-6.63	0.36 ^c	-7.37	0.39 ^c	-65.98	1.24 ^c	-16.46	0.80 ^c
r2851_19	vmf74	-5.48	1.62 ^f	6.41	1.04 ^f	-0.27	0.47 ^f	-1.62	0.50 ^f	-17.97	0.64 ^c	-5.53	0.64 ^c
r2211_01	field	-10.68	0.38 ^f	1.89	0.36 ^f	0.01	0.21 ⁿ	-2.59	0.21 ⁿ	-15.00	0.40 ^f	-6.45	0.44 ⁿ
r2211_02	field	-10.03	0.38 ^f	4.91	0.29 ^c	1.87	0.17 ^f	-1.29	0.17 ⁿ	-13.96	0.25 ^c	-4.75	0.28 ^c
r2211_04	field	6.43	0.75 ⁿ	-0.71	0.47 ⁿ	1.86	0.20 ^c	0.95	0.21 ⁿ	-6.25	0.30 ^p	1.14	0.29 ⁿ
r2211_11	Group3	-14.98	0.38 ^c	3.38	0.31 ^f	-1.68	0.18 ^c	-1.01	0.18 ⁿ	-20.88	0.24 ^c	-4.92	0.24 ^c
r2211_12	field ^o	-1.23	0.26 ^c	1.91	0.10 ^c	0.88	0.10 ⁿ	12.34	0.19 ⁿ	8.03	0.15 ⁿ
r2211_13	Group3	3.07	1.35 ⁿ	-0.74	0.68 ⁿ	2.59	0.33 ^c	0.71	0.35 ⁿ	2.55	0.38 ⁿ	3.46	0.43 ⁿ
r2211_15	field ^o	3.73	0.43 ^f	-1.28	0.23 ^c	-0.96	0.22 ^f	-6.20	0.25 ^p	0.63	0.26 ⁿ

Table C.2: Continued.

(1)	(2)	(9)	(10)	(11)	(12)	(13)	(14)	(15)	(16)	(17)	(18)	(19)	(20)
ID	membership	[O II] [Å]	E([O II]) [Å]	H δ [Å]	E(H δ) [Å]	H β [Å]	E(H β) [Å]	[O III] [Å]	E([O III]) [Å]	H α [Å]	E(H α) [Å]	[N II] [Å]	E([N II]) [Å]
r2211_16	field	-29.21	0.52 ^c	4.05	0.61 ^c	-6.75	0.30 ^c	-7.36	0.29 ^c	-30.22	1.14 ^c	-7.94	1.31 ^f
r2211_17	Group3	-5.01	0.70 ^f	3.04	0.52 ^f	0.89	0.27 ⁿ	0.98	0.29 ⁿ	-9.60	0.30 ^c	-7.33	0.35 ^c
r2211_18	field ^o	3.07	0.91 ⁿ	0.24	0.49 ⁿ	0.15	0.42 ⁿ	-3.98	0.41 ^p	5.35	0.57 ⁿ
r2211_19	Group3	-6.01	0.45 ^f	3.73	0.35 ^f	2.19	0.18 ^f	-0.72	0.19 ⁿ	-4.50	0.21 ^c	-1.85	0.22 ^f
r2211_20	Group3	7.76	1.19 ⁿ	-1.70	0.59 ⁿ	2.39	0.25 ^f	0.06	0.26 ⁿ	-0.52	0.28 ⁿ	0.76	0.31 ⁿ
r2211_21	Group3	5.14	0.64 ⁿ	-1.64	0.41 ⁿ	2.87	0.20 ^f	1.67	0.20 ⁿ	3.05	0.24 ⁿ	0.03	0.25 ⁿ
r2211_22	field	2.62	0.59 ⁿ	2.58	0.50 ⁿ	2.73	0.24 ^f	1.41	0.23 ⁿ	-0.04	0.45 ⁿ	-5.86	0.56 ⁿ
r2211_24	field	0.20	0.46 ⁿ	3.48	0.38 ⁿ	3.36	0.21 ^f	1.85	0.21 ⁿ	2.05	0.41 ⁿ	-1.51	0.36 ⁿ
r2212_11	Group3	4.51	1.89 ⁿ	-2.25	1.01 ⁿ	0.89	0.53 ⁿ	0.85	0.52 ⁿ	1.80	0.64 ⁿ	-2.70	0.59 ⁿ
r2212_12	field	-30.89	0.95 ^c	5.06	0.49 ^c	-2.71	0.28 ^f	-7.97	0.29 ^c	0.48	0.42 ⁿ	4.10	0.49 ⁸
r2212_14	Group3	-6.09	0.50 ^f	-0.14	0.38 ⁿ	0.71	0.21 ⁿ	0.21	0.23 ⁿ	-5.65	0.25 ^c	-1.85	0.26 ^c
r2212_16	field	-2.40	1.02 ⁿ	-1.56	0.66 ⁿ	-0.67	0.35 ⁿ	-1.63	0.37 ⁿ	3.05	0.81 ⁿ	4.59	0.70 ⁿ
r2212_19	field	2.78	0.72 ⁿ	-0.03	0.62 ⁿ	2.01	0.27 ⁿ	1.92	0.25 ⁿ	-3.66	0.65 ^o	-0.64	0.66 ^o
r2221_04	field ^o	4.60	0.51 ^c	-8.77	0.39 ^c	-6.05	0.35 ^f	-46.66	1.04 ^c	-25.93	1.06 ^c
r2221_13	field	-8.97	1.04 ^f	0.39	0.72 ⁿ	-3.04	0.39 ⁿ	0.36	0.38 ⁿ	-15.25	0.47 ^f	-10.10	0.50 ^f
r2222_02	field	-70.67	1.25 ⁸	4.01	0.26 ⁿ	-0.97	0.13 ^f	0.17	0.14 ⁿ	-13.85	0.18 ^c	-7.21	0.19 ^c
r2222_04	field	-7.08	0.30 ^c	1.93	0.27 ^f	-1.51	0.17 ^c	-0.52	0.17 ^f	-22.98	0.37 ^c	-9.66	0.35 ^c
r2222_05	field	-18.68	0.31 ^c	4.45	0.25 ^f	-2.54	0.14 ^c	-5.64	0.15 ^c	-19.77	0.22 ^c	-7.46	0.24 ^c
r2222_08	field	-0.55	0.24 ⁿ	-3.34	0.26 ⁿ	-1.81	0.15 ⁿ	-0.32	0.16 ⁿ	10.24	0.62 ⁿ	-3.10	0.32 ⁿ
r2222_13	field	-5.43	0.36 ^f	-3.00	0.26 ⁿ	2.46	0.13 ^f	1.13	0.13 ⁿ	2.56	0.24 ⁿ	-2.03	0.20 ⁿ
r2222_15	field	-25.86	0.34 ^c	5.21	0.21 ^c	-2.45	0.11 ^c	-1.71	0.11 ^f	-29.13	0.18 ^c	-10.97	0.17 ^c
r2231_06	field	-25.41	0.51 ^c	4.34	0.34 ⁿ	-2.75	0.27 ⁿ	-6.90	0.21 ^f	-26.11	0.43 ^c	-5.96	0.40 ^f
r2231_11	field	-48.04	0.78 ^p	6.54	0.41 ^f	-4.33	0.20 ^f	-7.93	0.21 ^f	-32.86	0.40 ^c	-11.23	0.37 ^f
r2231_16	field	-19.73	0.31 ^c	3.66	0.26 ⁿ	-4.64	0.19 ^p	-4.02	0.16 ^c	-48.69	0.45 ^c	-19.35	0.34 ^c
r2231_23	field	-1.55	0.29 ^c	7.76	0.24 ^c	4.20	0.15 ^c	-0.14	0.13 ⁿ	-8.67	0.00 ^f	2.57	0.00 ⁿ
r2241_11	field	-9.00	0.91 ^f	1.78	0.56 ⁿ	2.16	0.26 ⁿ	-1.91	0.24 ^f	0.97	0.44 ⁿ	2.02	0.47 ⁿ
r2241_14	field	-5.11	2.25 ⁿ	0.42	0.88 ⁿ	2.32	0.27 ⁿ	1.68	0.28 ⁿ	0.67	0.27 ⁿ	-1.50	0.25 ⁿ
r2241_21	field	-17.10	0.32 ^c	5.03	0.26 ⁿ	-5.43	0.16 ^c	-3.73	0.15 ^c	-36.41	0.29 ^c	-13.86	0.28 ^c
r2241_22	field	2.47	0.58 ⁿ	5.75	0.31 ^f	4.68	0.17 ^c	-0.06	0.15 ⁿ	1.78	0.18 ^f	-0.82	0.19 ⁿ
r2242_07	field	1.50	0.67 ⁿ	1.70	0.39 ⁿ	2.14	0.22 ⁿ	1.54	0.17 ⁿ	0.67	0.25 ⁿ	-0.46	0.24 ⁿ
r2242_10	field	3.91	2.31 ⁿ	9.57	0.90 ⁿ	3.51	0.34 ⁿ	1.00	0.25 ⁿ	-0.35	0.28 ⁿ	-0.82	0.32 ⁿ

Table C.2: Continued.

(1)	(2)	(9)	(10)	(11)	(12)	(13)	(14)	(15)	(16)	(17)	(18)	(19)	(20)
ID	membership	[O II] [Å]	E([O II]) [Å]	H δ [Å]	E(H δ) [Å]	H β [Å]	E(H β) [Å]	[O III] [Å]	E([O III]) [Å]	H α [Å]	E(H α) [Å]	[N II] [Å]	E([N II]) [Å]
r2242_11	field	-0.95	0.99 ⁿ	-1.06	0.68 ⁿ	0.59	0.27 ⁿ	0.72	0.25 ⁿ	-3.18	0.40 ⁿ	0.60	0.49 ⁿ
r2242_12	field	-0.22	0.90 ⁿ	4.88	0.60 ⁿ	0.19	0.34 ⁿ	1.20	0.26 ⁿ	1.00	0.36 ⁿ	-1.87	0.35 ⁿ
r2242_13	field	-5.53	0.39 ^f	3.53	0.31 ⁿ	-1.61	0.15 ^f	-1.03	0.15 ⁿ	-21.72	0.21 ^c	-6.37	0.20 ^c
r2242_18	Group3	-13.17	1.00 ^f	-7.21	0.65 ⁿ	3.90	0.26 ^f	-0.74	0.24 ⁿ	-2.97	0.21 ⁿ	-0.09	0.23 ⁿ
r2251_02	field	4.56	2.45 ⁿ	-2.19	0.77 ⁿ	2.30	0.23 ⁿ	0.71	0.22 ⁿ	0.26	0.24 ⁿ	-0.61	0.25 ⁿ
r2251_08	field	-20.21	0.80 ^f	4.40	0.49 ⁿ	-3.68	0.27 ^f	-1.75	0.26 ⁿ	-27.68	0.36 ^c	-11.78	0.33 ^c
r2251_16	field	-12.12	0.75 ⁿ	-0.63	0.48 ⁿ	1.90	0.21 ⁿ	1.03	0.20 ⁿ	-1.42	0.25 ⁿ	-0.71	0.26 ⁿ
r2611_02	field	-8.30	0.40 ^f	3.49	0.37 ⁿ	-1.76	0.23 ^f	-1.20	0.23 ⁿ	-23.45	0.37 ^c	-12.07	0.39 ^f
r2611_11	field	-13.09	0.37 ^c	3.52	0.30 ^c	-2.69	0.17 ^p	-1.90	0.17 ⁿ	-10.49	0.23 ^p	-3.30	0.25 ^p
r2612_01	field	0.00	0.27 ⁿ	0.00	0.24 ⁿ	2.82	0.13 ^f	1.04	0.13 ⁿ	-0.05	0.18 ⁿ	-2.76	0.18 ^f
r2621_01	Group4	-8.00	0.40 ^c	4.51	0.29 ^f	-0.28	0.16 ^f	0.02	0.16 ⁿ	-19.11	0.22 ^c	-6.36	0.24 ^c
r2621_05	field ^c	7.24	0.17 ^c	-2.70	0.10 ^c	-7.08	0.09 ^c	-1.37	0.13 ^u	4.18	0.14 ^u
r2621_06	field	-3.45	0.27 ^c	0.38	0.23 ⁿ	1.24	0.12 ^p	0.37	0.12 ⁿ	-1.38	0.17 ⁿ	-0.83	0.19 ⁿ
r2621_09	field	-2.30	0.30 ^f	-0.13	0.25 ⁿ	-1.28	0.14 ⁿ	-0.22	0.15 ⁿ	-7.58	0.19 ^c	-1.79	0.20 ^f
r2621_10	field	-9.52	0.17 ^c	2.30	0.16 ^f	-1.37	0.10 ^p	-1.46	0.11 ^f	-12.55	0.16 ^c	-5.12	0.17 ^f
r2621_12	field	-3.89	0.15 ^f	1.09	0.16 ⁿ	0.50	0.10 ⁿ	-5.77	0.09 ^c	-3.95	0.13 ^f	-3.66	0.14 ^c
r2631_01	Group4	2.90	0.38 ⁿ	0.40	0.30 ^f	3.03	0.16 ⁿ	0.84	0.16 ⁿ	0.17	0.18 ⁿ	-0.05	0.19 ⁿ
r2631_02	Group4	-4.72	0.21 ^f	-1.84	0.16 ⁿ	1.80	0.08 ⁿ	1.27	0.08 ⁿ	-0.55	0.09 ⁿ	-1.86	0.10 ^f
r2631_05	field	-57.95	1.65 ^p	3.92	0.46 ⁿ	-0.91	0.29 ^f	-0.69	0.39 ⁿ	-8.50	0.40 ^c	-0.73	0.53 ⁿ
r2631_10	field	-31.05	0.58 ^c	3.98	0.37 ⁿ	0.51	0.25 ⁿ	-3.28	0.24 ^f	0.25	0.35 ^u	6.92	0.45 ^u
r2631_11	Group4	0.63	0.28 ⁿ	-1.27	0.22 ⁿ	2.37	0.11 ^c	0.86	0.11 ⁿ	1.87	0.14 ^f	-0.60	0.14 ⁿ
r2631_16	Group4	-20.02	0.25 ^c	4.98	0.23 ^c	-2.96	0.15 ^c	-2.38	0.16 ^p	-27.48	0.30 ^c	-11.13	0.29 ^c
r2632_06	Group4	-1.76	0.27 ⁿ	0.72	0.17 ⁿ	1.91	0.08 ^c	0.50	0.08 ⁿ	-2.10	0.11 ^f	-2.02	0.13 ⁿ
r2632_14	field	-23.37	1.36 ^c	6.87	1.24 ⁿ	-0.87	0.80 ⁿ	-5.33	0.58 ^f	-16.20	1.24 ^c	-4.48	1.48 ^f
r2632_15	Group4	-0.51	0.19 ⁿ	0.43	0.14 ^c	1.69	0.07 ^c	0.33	0.07 ⁿ	-2.62	0.08 ^f	-2.38	0.08 ^f
r2641_11	field	-13.38	1.20 ^c	4.05	0.90 ^f	-4.55	0.69 ^f	-2.22	0.59 ^f	-39.16	2.26 ^c	-10.43	1.99 ⁿ
r2651_01	field	1.53	0.34 ⁿ	0.83	0.27 ^f	0.92	0.16 ⁿ	0.31	0.15 ⁿ	2.22	0.30 ⁿ	-0.59	0.29 ⁿ
r2651_07	field	0.53	0.18 ⁿ	0.67	0.17 ^c	-0.13	0.12 ⁿ	-0.77	0.11 ⁿ	0.38	0.17 ⁿ	0.62	0.21 ⁿ
r2811_12a	field	-152.36	8.85 ^p	-0.59	1.73 ⁿ	-9.48	0.77 ^c	-11.15	0.87 ^c	-45.42	1.74 ^p	-15.83	1.44 ^p
r2812_19	field	-26.92	1.21 ^p	3.22	0.56 ^f	0.97	0.42 ^f	-7.33	0.38 ^c	-34.63	0.75 ^p	5.58	0.69 ^u
r2812_23	field	12.44	7.53 ⁿ	3.74	1.70 ⁿ	1.73	0.61 ^f	-26.01	2.20 ⁿ	4.62	0.50 ^u	1.12	0.50 ^u

Table C.2: Continued.

(1)	(2)	(9)	(10)	(11)	(12)	(13)	(14)	(15)	(16)	(17)	(18)	(19)	(20)
ID	membership	[O II] [Å]	E([O II]) [Å]	H δ [Å]	E(H δ) [Å]	H β [Å]	E(H β) [Å]	[O III] [Å]	E([O III]) [Å]	H α [Å]	E(H α) [Å]	[N II] [Å]	E([N II]) [Å]
r2812_25	field	-1.11	7.84 ⁿ	10.70	3.93 ⁿ	-0.10	1.07 ⁿ	1.09	1.16 ⁿ	7.18	1.17 ^u	8.85	1.27 ^u
r2812_26	field	116.00	46.33 ⁿ	33.77	21.2 ⁸	2.40	1.63 ⁿ	2.65	1.12 ⁿ	-0.58	1.05 ⁿ	-2.40	1.00 ⁿ
r2821_06	field	-23.75	2.87 ^p	10.37	2.14 ⁿ	-4.23	0.99 ^f	-4.40	1.28 ⁿ	-31.60	2.05 ^p	-7.92	1.74 ⁿ
r2821_13	field	-7.15	2.61 ^f	4.67	1.65 ⁿ	3.38	1.00 ⁿ	1.07	0.66 ⁿ	-5.59	0.94 ^f	-1.36	1.41 ⁿ
r2821_18	field	-33.01	5.83 ^f	-14.63	3.11 ⁿ	-6.63	1.63 ^f	-4.43	1.41 ⁿ	-47.31	3.41 ^c	-6.02	1.96 ^f
r2821_23	field	0.77	2.50 ⁿ	-3.35	2.00 ⁿ	0.44	1.14 ⁿ	-0.12	1.03 ⁿ	3.92	1.62 ⁿ	-5.54	1.38 ⁿ
r2821_28	field	-5.03	1.22 ^f	1.21	0.87 ⁿ	-1.08	0.43 ⁿ	-1.40	0.51 ⁿ	-19.08	0.83 ^c	-10.37	0.92 ^f
r2822_24	field	-21.56	1.01 ^c	4.56	0.60 ^f	-3.95	0.26 ^c	-4.88	0.30 ^c	-28.55	0.41 ^p	-12.08	0.37 ^p
r2831_05	field	-11.15	2.29 ^f	10.88	1.74 ⁿ	-2.46	0.59 ⁿ	-0.83	0.63 ⁿ	-20.93	0.78 ^p	-8.63	0.76 ^p
r2831_08	field	199.73	22.11 ⁸	-1.87	1.53 ⁿ	2.54	0.59 ^f	0.34	0.59 ⁿ	-8.77	0.62 ^p	-3.92	0.84 ⁿ
r2831_16	field	-9.85	1.60 ^f	5.35	1.20 ^c	0.25	0.72 ⁿ	-0.89	0.64 ^f	-20.22	0.95 ^c	-8.38	0.90 ^f
r2831_17	field	-21.33	1.13 ^c	3.25	0.71 ^f	-4.17	0.34 ^c	-2.64	0.38 ^f	-7.25	0.45 ^p	-5.72	0.54 ^p
r2831_18	field	-5.96	0.39 ^c	3.90	0.32 ^c	-1.93	0.20 ^f	-2.10	0.19 ^f	-22.38	0.31 ^c	-13.15	0.33 ^c
r2841_01	field	0.31	3.79 ⁿ	-0.27	2.17 ⁿ	-3.22	0.84 ⁿ	-1.14	0.68 ⁿ	1.67	0.85 ⁿ	-1.76	0.73 ⁿ
r2841_01	field	0.31	3.79 ⁿ	-0.27	2.17 ⁿ	-3.22	0.84 ⁿ	-1.14	0.68 ⁿ	1.67	0.85 ⁿ	-1.76	0.73 ⁿ
r2841_09	field	1.08	0.92 ⁿ	1.20	0.50 ^f	2.25	0.24 ^f	-0.10	0.22 ⁿ	-3.37	0.23 ^f	-2.84	0.24 ^f
r2841_12	field	-39.60	1.62 ^c	4.25	1.14 ⁿ	-5.68	0.77 ^c	-14.65	0.80 ^c	-51.65	3.45 ^c	1.19	2.21 ⁿ
r2841_13	field	-8.75	1.07 ^c	3.52	0.62 ^f	-0.38	0.27 ⁿ	-1.71	0.28 ⁿ	7.15	0.40 ^u	5.78	0.35 ^u
r2841_18	field	2.60	1.96 ⁿ	4.80	1.16 ^f	1.11	0.48 ⁿ	-1.67	0.42 ⁿ	-2.44	0.43 ⁿ	-1.94	0.44 ⁿ
r2841_19a	field	-2.40	0.47 ^f	3.75	0.31 ^f	1.62	0.14 ⁿ	1.07	0.13 ⁿ	-3.95	0.15 ^c	-4.88	0.15 ^c
r2841_20	field	-28.28	2.91 ^c	1.99	1.19 ⁿ	-0.32	0.61 ⁿ	-3.10	0.64 ⁿ	-13.70	1.07 ^c	-5.41	1.27 ^p
r2851_01b	field	-26.49	0.94 ^c	2.42	0.70 ⁿ	-4.70	0.50 ^c	-4.70	0.40 ^c	-33.61	0.94 ^c	-11.47	0.80 ^f
r2851_02	field	-8.53	1.37 ^f	6.44	1.34 ^f	1.34	0.61 ⁿ	-0.02	0.52 ⁿ	-4.82	1.25 ^f	-1.09	1.97 ⁿ
r2851_03	field	-3.75	0.73 ⁿ	-0.52	0.55 ⁿ	1.95	0.22 ^f	1.12	0.20 ⁿ	-1.04	0.44 ⁿ	-0.65	0.63 ⁿ
r2851_05	field	-20.40	1.63 ^c	3.79	0.84 ^f	-5.48	0.47 ^c	-2.37	0.47 ^f	-16.82	0.97 ^c	-0.80	0.90 ^p
r2851_06	field	1.15	0.69 ⁿ	-3.20	0.41 ^f	1.82	0.16 ^f	1.01	0.16 ⁿ	-1.32	0.17 ⁿ	-1.89	0.18 ⁿ
r2851_12	field	-1.80	0.64 ⁿ	0.21	0.43 ⁿ	1.33	0.19 ^f	-0.15	0.18 ⁿ	0.35	0.38 ⁿ	2.12	0.43 ⁿ
r2851_13	field	0.25	1.08 ⁿ	0.81	0.60 ^f	2.47	0.22 ^f	0.92	0.19 ⁿ	0.83	0.29 ⁿ	0.01	0.26 ⁿ
r2851_18b	field	-4.23	1.04 ^f	3.23	0.80 ^f	4.05	0.77 ^p	0.22	0.35 ⁿ	-6.89	0.63 ^f	-3.95	0.59 ^f

Spectrophotometric parameters of the sample

This table contains the spectrophotometric parameters for individual derived during the analysis.

ID – Same as in appendix C.

membership – Same as in appendix C.

M_B, M_V, M_R – Absolute magnitud in B, V and R bands respetively obtained with the `KCORRECT` code.

$\log(Mass)$ – Logarithm of the stellar mass obtained with the `KCORRECT` code.

$W_0([O\ II]), W_0(H\alpha)$ – Restframe equivalent widths of $[O\ II]$ and $H\alpha$ emission lines. Note that lines in emission have in this case negative values in order to highlight them

$SFR([O\ II]), SFR(H\alpha)$ – Star formation rates obtained from the emission in $[O\ II]$ and $H\alpha$ respectively according to the method outlined in §6.2. Specific star formation rates can be obtained dividing the SFR by the stellar mass.

Table D.1: Spectrophotometric data for individual objects.

ID	membership	M_B [mag]	M_V [mag]	M_R [mag]	$\log(Mass)$ [M_\odot]	$W_0([O\ II])$ [Å]	$W_0(H\alpha)$ [Å]	$SFR([O\ II])$ [$M_\odot\ yr^{-1}$]	$SFR(H\alpha)$ [$M_\odot\ yr^{-1}$]
r2211_07	vmf194	-19.63	-20.31	-20.94	10.029	9.66	0.75
r2211_08	vmf194	-21.42	-22.16	-22.79	10.783	8.95	1.10
r2211_09	vmf194	-19.96	-20.72	-21.37	10.222	0.43	-1.71	0.100
r2211_10	vmf194	-19.64	-20.37	-21.01	10.068	0.18	1.13
r2212_06	vmf194	-19.96	-20.32	-20.84	9.854	-32.93	-41.10	1.692	1.486
r2212_08	vmf194	-20.27	-21.00	-21.62	10.306	3.93	1.12
r2212_23	vmf194	-19.87	-20.56	-21.18	10.125	8.32	-0.87	0.043
r2221_14	vmf194	-20.62	-21.25	-21.85	10.372	-0.02	-10.33	0.002	0.947
r2221_03	xdfs220	-20.92	-21.33	-21.86	10.269	-39.80	-52.51	4.947	4.830
r2221_03b	xdfs220	-19.83	-20.16	-20.66	9.751	-61.16	-45.71	2.777	1.395

Table D.1: Continued.

ID	membership	M_B [mag]	M_V [mag]	M_R [mag]	$\log(Mass)$ [M_\odot]	$W_0([O\ II])$ [Å]	$W_0(H\alpha)$ [Å]	$SFR([O\ II])$ [$M_\odot\ yr^{-1}$]	$SFR(H\alpha)$ [$M_\odot\ yr^{-1}$]
r2221_12	xdfs220	-20.52	-21.26	-21.89	10.412	-4.34	1.46	0.372
r2222_03	xdfs220	-19.68	-20.52	-21.19	10.174	0.21	-0.91	0.045
r2222_07	xdfs220	-19.56	-20.27	-20.90	10.021	3.07	0.76
r2231_05	xdfs220	-20.16	-20.89	-21.52	10.273	4.80	3.06
r2241_05	xdfs220	-20.20	-21.05	-21.71	10.380	-0.02	3.42	0.001
r2241_07	xdfs220	-21.59	-22.44	-23.09	10.924	5.64	1.65
r2241_09	xdfs220	-21.64	-22.50	-23.16	10.963	-14.98	-3.00	3.593	0.919
r2241_10	xdfs220	-20.64	-21.45	-22.10	10.522	8.83	2.30
r2241_15	xdfs220	-20.43	-21.02	-21.61	10.261	-1.46	-12.41	0.115	0.909
r2241_18	xdfs220	-19.55	-20.83	-21.63	10.432	-20.46	-35.91	0.717	2.671
r2242_06	xdfs220	-19.23	-19.99	-20.63	9.919	-3.18	7.17	0.083
r2251_04	xdfs220	-20.37	-20.74	-21.24	9.984	-37.27	-47.44	2.794	2.467
XDC29_04	xdfs220	-20.63	-21.48	-22.15	10.558	0.72	-1.36	0.164
r2621_14	vmf131	-19.74	-20.59	-21.25	10.195	0.98	0.35
r2621_15	vmf131	-20.44	-20.94	-21.49	10.162	-23.51	-21.69	1.876	1.419
r2621_16	vmf131	-20.24	-20.90	-21.50	10.236	-20.84	-31.54	1.382	2.095
r2631_20	vmf131	-21.58	-22.54	-23.23	11.013	2.72	-1.85	0.604
r2632_02	vmf131	-20.14	-21.06	-21.75	10.412	2.09	-1.66	0.138
r2632_02b	vmf131	-19.46	-19.97	-20.52	9.776	-22.93	-31.87	0.744	0.853
r2632_03	vmf131	-20.38	-21.29	-21.97	10.492	-0.38	0.15	0.029
r2632_11	vmf131	-21.29	-22.07	-22.71	10.755	-10.37	-19.49	1.814	3.917
r2632_12	vmf131	-20.25	-20.69	-21.22	10.029	-19.41	-27.83	1.297	1.422
r2632_17	vmf131	-19.57	-20.40	-21.06	10.111	-4.03	-3.99	0.143	0.176
r2641_04	vmf131	-19.78	-20.83	-21.56	10.367	-2.01	-12.32	0.087	0.859
r2641_05	vmf131	-20.10	-21.06	-21.75	10.427	-0.16	-11.21	0.009	0.938
r2641_06	vmf131	-21.02	-21.35	-21.84	10.219	2.78	1.22
r2641_07	vmf131	-19.59	-20.87	-21.67	10.450	-5.09	-15.73	0.185	1.219
r2641_12	vmf131	-21.07	-21.84	-22.47	10.654	-0.36	0.058
r2651_08	vmf131	-20.43	-21.29	-21.96	10.481	-2.87	2.55	0.226
r2651_17	vmf131	-21.27	-22.22	-22.90	10.874	-4.27	-0.60	0.734	0.144
r2651_19	vmf131	-20.86	-21.64	-22.28	10.588	-5.96	-8.38	0.701	1.142
ba_07	vmf131	-21.08	-21.58	-22.13	10.424	5.07	0.24
ba_09	vmf131	-19.89	-20.73	-21.39	10.254	3.28	2.95
ba_12	vmf131	-20.39	-21.29	-21.97	10.493	3.78	3.18
ba_14	vmf131	-19.97	-20.86	-21.53	10.317	4.67	-2.11	0.143
ba_18	vmf131	-20.74	-21.63	-22.29	10.617	6.15	0.20
ba_25	vmf131	-20.44	-21.35	-22.02	10.512	5.13	0.13
ba_28	vmf131	-22.10	-23.03	-23.70	11.185	5.1	0.84
ba_30	vmf131	-20.86	-21.75	-22.42	10.670	2.2	1.07
ba_36	vmf131	-20.93	-21.60	-22.21	10.524	-6.8	-11.69	0.847	1.487
ba_37	vmf131	-20.60	-21.51	-22.19	10.585	-6.6	-11.75	0.610	1.470
ba_39	vmf131	-20.88	-21.80	-22.47	10.697	-2.6	-0.46	0.310	0.075
r2611_04	vmf132	-19.61	-20.32	-20.95	10.045	6.99	2.91
r2611_13	vmf132	-20.81	-21.56	-22.20	10.545	6.78	1.40
r2611_14	vmf132	-20.42	-21.20	-21.85	10.414	0.91	1.31
r2612_02	vmf132	-20.01	-20.79	-21.44	10.254	-15.32	-10.12	0.824	0.632
r2612_04	vmf132	-19.60	-20.11	-20.67	9.855	-39.36	-58.97	1.442	1.818
r2612_06	vmf132	-21.30	-22.06	-22.70	10.749	1.87	0.97
r2612_17	vmf132	-20.50	-21.35	-22.02	10.503	0.97	1.33
r2621_03	vmf132	-20.12	-20.90	-21.54	10.291	1.20	1.89
r2621_04	vmf132	-19.04	-19.86	-20.52	9.899	0.66	-0.07	0.002
r2621_11	vmf132	-19.73	-20.57	-21.24	10.191	4.32	1.15
r2621_13	vmf132	-20.52	-21.33	-21.98	10.474	3.18	0.22
r2621_22	vmf132	-20.36	-21.17	-21.83	10.415	-2.56	-4.01	0.189	0.358
r2631_21	vmf132	-21.22	-21.97	-22.60	10.704	-3.50	-7.80	0.573	1.423

Table D.1: Continued.

ID	membership	M_B [mag]	M_V [mag]	M_R [mag]	$\log(M_{\text{mass}})$ [M_{\odot}]	$W_0(\text{[O II]})$ [\AA]	$W_0(\text{H}\alpha)$ [\AA]	$SFR(\text{[O II]})$ [$M_{\odot} \text{ yr}^{-1}$]	$SFR(\text{H}\alpha)$ [$M_{\odot} \text{ yr}^{-1}$]
r2631_08	vmf132	-19.41	-20.08	-20.70	9.924	-1.35	0.043
r2632_07	vmf132	-19.68	-20.45	-21.10	10.122	-0.94	-3.46	0.0378	0.159
r2632_13	vmf132	-20.19	-20.95	-21.60	10.315	-0.17	1.18	0.0105
r2641_10	vmf132	-21.10	-21.86	-22.50	10.669	9.17	-5.42	0.902
ba_02	vmf132	-21.12	-21.87	-22.51	10.671	-3.97	-2.55	0.590	0.428
ba_29	vmf132	-19.55	-19.79	-20.25	9.522	-53.6	-61.71	1.879	1.295
r2811_06	vmf73	-20.73	-21.53	-22.20	10.568	-6.84	-3.38	0.713	0.425
r2811_16	vmf73	-21.70	-22.40	-23.04	10.874	-0.25	-2.47	0.0637	0.674
r2811_18	vmf73	-20.21	-21.02	-21.68	10.365	2.12	1.06
r2811_19	vmf73	-20.12	-20.79	-21.42	10.224	-1.26	0.69	0.0747
r2811_20	vmf73	-19.98	-20.63	-21.24	10.142	4.70	-1.78	0.093
r2811_24	vmf73	-20.91	-21.64	-22.28	10.578	4.59	0.76
r2811_25	vmf73	-20.47	-21.27	-21.93	10.463	-6.35	-2.06	0.520	0.203
r2812_05	vmf73	-20.35	-21.10	-21.74	10.371	10.61	-0.13	0.011
r2812_09	vmf73	-20.03	-20.66	-21.27	10.149	5.77	-1.84	0.099
r2812_12	vmf73	-21.35	-22.13	-22.78	10.783	1.89	-2.55	0.548
r2812_14	vmf73	-21.47	-22.17	-22.80	10.775	1.51	1.47
r2821_02	vmf73	-21.95	-22.69	-23.33	11.000	1.96	1.45
r2821_08	vmf73	-21.45	-21.74	-22.22	10.339	-34.42	-70.21	6.942	8.992
r2821_12	vmf73	-21.00	-21.77	-22.42	10.635	-2.41	-0.83	0.322	0.127
r2821_17	vmf73	-21.04	-21.82	-22.46	10.656	-1.14	-1.71	0.158	0.274
r2821_14	vmf73	-20.22	-20.98	-21.62	10.319	6.10	-3.88	0.287
r2821_20	vmf73	-20.83	-21.55	-22.19	10.546	-13.30	3.55	1.512
r2821_21	vmf73	-20.08	-20.82	-21.47	10.267	0.96	1.84
r2821_27	vmf73	-20.85	-21.49	-22.09	10.459	0.37	-4.44	0.504
r2821_29	vmf73	-20.83	-21.55	-22.19	10.537	-6.10	0.09	0.696
r2822_01	vmf73	-19.81	-20.51	-21.14	10.115	-0.11	1.33	0.004
r2822_03	vmf73	-21.19	-21.88	-22.49	10.643	2.58	1.83
r2822_04	vmf73	-20.05	-20.75	-21.38	10.217	0.96	2.18
r2822_05	vmf73	-20.98	-21.67	-22.29	10.565	-0.16	-2.27	0.021	0.311
r2822_06	vmf73	-20.89	-21.39	-21.96	10.377	-2.88	-16.06	0.347	1.628
r2822_09	vmf73	-20.32	-20.69	-21.21	10.012	-18.89	-21.93	1.343	1.113
r2822_14	vmf73	-20.09	-20.78	-21.41	10.225	4.20	2.41
r2822_15	vmf73	-21.64	-22.41	-23.06	10.893	4.34	0.92
r2822_16	vmf73	-20.50	-21.23	-21.87	10.418	1.17	0.28
r2822_17	vmf73	-19.67	-20.30	-20.92	10.013	-1.62	-0.21	0.0641	0.008
r2822_19	vmf73	-19.38	-20.06	-20.69	9.937	2.36	2.90
r2822_20	vmf73	-19.66	-20.14	-20.71	9.868	1.77	0.43
r2822_22	vmf73	-20.81	-21.60	-22.24	10.576	2.59	0.24
r2822_23	vmf73	-20.44	-21.05	-21.65	10.288	13.14	1.88
r2822_25	vmf73	-20.14	-20.83	-21.46	10.246	-1.82	-4.41	0.109	0.282
r2831_03	vmf73	-20.47	-21.01	-21.60	10.250	-29.14	-12.83	2.382	0.929
r2831_10	vmf73	-20.78	-21.25	-21.80	10.287	-10.23	-28.00	1.119	2.455
r2831_13	vmf73	-21.56	-22.28	-22.90	10.814	5.11	-1.06	0.255
r2841_07	vmf73	-20.27	-20.79	-21.37	10.143	-46.50	-22.50	3.170	1.316
r2841_10	vmf73	-20.70	-21.32	-21.92	10.395	-13.86	-11.00	1.408	1.072
r2841_17	vmf73	-20.57	-21.27	-21.88	10.399	1.61	1.28
r2851_04	vmf73	-20.54	-20.95	-21.47	10.113	-12.08	-29.96	1.059	1.924
r2851_14	vmf73	-19.63	-20.34	-20.98	10.059	-7.21	0.295
r2851_17	vmf73	-20.99	-21.68	-22.30	10.570	1.32	0.79
r2811_01	vmf74	-20.18	-20.81	-21.42	10.204	4.41	1.38
r2811_03	vmf74	-19.68	-20.27	-20.87	9.973	2.25	1.09
r2811_05	vmf74	-19.57	-20.08	-20.65	9.851	-21.50	-74.73	0.769	2.266
r2811_07	vmf74	-19.84	-20.34	-20.92	9.961	-2.26	-1.85	0.103	0.071
r2811_08	vmf74	-19.40	-19.96	-20.56	9.842	-8.00	-6.81	0.243	0.190

Table D.1: Continued.

ID	membership	M_B [mag]	M_V [mag]	M_R [mag]	$\log(M_{\text{mass}})$ [M_{\odot}]	$W_0([\text{O II}])$ [\AA]	$W_0(\text{H}\alpha)$ [\AA]	$SFR([\text{O II}])$ [$M_{\odot} \text{ yr}^{-1}$]	$SFR(\text{H}\alpha)$ [$M_{\odot} \text{ yr}^{-1}$]
r2811_10	vmf74	-19.86	-20.45	-21.05	10.042	0.93	1.70
r2811_11	vmf74	-21.03	-21.72	-22.33	10.575	0.67	-0.71	0.101
r2811_13	vmf74	-19.30	-19.84	-20.42	9.774	2.77	2.14
r2811_14	vmf74	-20.11	-20.74	-21.34	10.163	5.52	1.76
r2811_22	vmf74	-19.73	-20.15	-20.69	9.820	-21.35	-24.54	0.880	0.767
r2811_23	vmf74	-20.12	-20.59	-21.14	10.020	-2.52	-5.95	0.149	0.282
r2812_02	vmf74	-20.20	-20.86	-21.47	10.228	0.26
r2812_16	vmf74	-20.03	-20.58	-21.16	10.070	-17.48	-7.91	0.955	0.383
r2812_17	vmf74	-20.66	-21.30	-21.90	10.390	6.52	-3.98	0.381
r2812_22	vmf74	-20.18	-20.80	-21.39	10.183	8.78	0.47
r2812_21	vmf74	-20.14	-20.78	-21.39	10.196	-5.83	-8.66	0.352	0.518
r2821_03	vmf74	-19.77	-20.33	-20.92	9.975	11.65	0.21
r2821_06	vmf74	-19.70	-19.90	-20.37	9.559	-25.02	-25.40	1.009	0.592
r2821_07	vmf74	-19.27	-19.88	-20.49	9.831	-4.13	2.97	0.111
r2821_09	vmf74	-19.29	-19.85	-20.45	9.799	-6.65	0.47	0.184
r2821_10	vmf74	-19.11	-19.73	-20.33	9.763	-16.78	2.48	0.394
r2821_11	vmf74	-20.17	-20.77	-21.36	10.157	-6.31	0.95	0.393
r2822_07	vmf74	-20.28	-20.91	-21.51	10.232	4.27	1.39
r2822_10	vmf74	-19.46	-20.06	-20.67	9.900	-0.03	0.08	0.001
r2822_13	vmf74	-18.85	-19.33	-19.89	9.541	1.22	-13.60	0.205
r2831_09	vmf74	-19.57	-20.29	-20.93	10.038	-25.47	-29.34	0.914	1.149
r2831_20	vmf74	-19.99	-20.50	-21.06	10.009	-5.63	-1.42	0.297	0.063
r2841_03	vmf74	-19.07	-19.52	-20.07	9.583	-26.92	-17.58	0.606	0.311
r2841_08	vmf74	-18.93	-19.39	-19.93	9.527	-21.24	-27.75	0.420	0.435
r2841_20	vmf74	-18.97	-19.29	-19.78	9.391	-22.79	-18.44	0.468	0.251
r2841_20	vmf74	-18.94	-19.24	-19.72	9.359	-22.79	-18.44	0.455	0.238
r2851_09	vmf74	-19.00	-19.53	-20.10	9.631	0.03	-0.61	0.011
r2851_10	vmf74	-19.95	-20.16	-20.62	9.645	-30.02	-39.15	1.524	1.148
r2851_11	vmf74	-18.84	-19.31	-19.87	9.522	-39.92	-65.82	0.727	0.971
r2851_19	vmf74	-19.05	-19.37	-19.86	9.424	-5.45	-18.10	0.121	0.265
r2821_06	vmf74	-19.70	-19.90	-20.37	9.559	-25.02	-25.40	1.009	0.592
r2821_06	vmf74	-19.70	-19.90	-20.37	9.559	-25.02	-25.40	1.009	0.592
r2841_20	vmf74	-18.97	-19.29	-19.78	9.391	-22.79	-18.44	0.468	0.250
r2211_01	field	-21.01	-21.64	-22.24	10.529	-10.68	-15.00	1.437	1.964
r2211_02	field	-20.01	-20.41	-20.93	9.902	-10.03	-13.96	0.536	0.549
r2211_04	field	-19.96	-20.81	-21.47	10.285	6.43	-6.25	0.403
r2211_11	field	-20.41	-21.02	-21.62	10.274	-14.98	-20.88	1.164	1.543
r2211_12	field	-21.36	-22.03	-22.63	10.680	12.34
r2211_13	field	-20.56	-21.33	-21.99	10.475	3.07	2.55
r2211_15	field	-20.31	-20.84	-21.42	10.157	-6.20	0.380
r2211_16	field	-21.57	-22.10	-22.66	10.650	-29.21	-30.22	6.594	5.842
r2211_17	field	-20.83	-21.47	-22.08	10.468	-5.01	-9.60	0.574	1.084
r2211_18	field	-18.97	-19.56	-20.17	9.696	0.00	-3.98	0.077
r2211_19	field	-20.14	-20.86	-21.49	10.258	-6.01	-4.50	0.365	0.295
r2211_20	field	-20.65	-21.39	-22.04	10.488	7.76	-0.52	0.057
r2211_21	field	-19.76	-20.55	-21.21	10.170	5.14	3.05
r2211_22	field	-20.31	-21.26	-21.95	10.498	2.62	-0.04	0.004
r2211_24	field	-20.44	-21.26	-21.91	10.451	0.20	2.05
r2212_11	field	-20.38	-21.14	-21.78	10.386	4.51	1.80
r2212_12	field	-19.63	-20.00	-20.51	9.716	-30.89	0.48	1.165
r2212_14	field	-20.86	-21.59	-22.22	10.553	-6.09	-5.65	0.718	0.727
r2212_16	field	-19.56	-20.35	-21.00	10.083	-2.40	3.05	0.085
r2212_19	field	-20.91	-21.86	-22.54	10.734	2.78	-3.66	0.632
r2221_04	field	-21.03	-21.49	-22.01	10.338	-46.66	4.944
r2221_13	field	-19.70	-20.35	-20.96	10.030	-8.97	-15.25	0.360	0.616

Table D.1: Continued.

ID	membership	M_B [mag]	M_V [mag]	M_R [mag]	$\log(M_{\text{mass}})$ [M_{\odot}]	$W_0(\text{[O II]})$ [\AA]	$W_0(\text{H}\alpha)$ [\AA]	$SFR(\text{[O II]})$ [$M_{\odot} \text{ yr}^{-1}$]	$SFR(\text{H}\alpha)$ [$M_{\odot} \text{ yr}^{-1}$]
r2222_02	field	-19.21	-19.63	-20.16	9.608	-70.67	-13.85	1.808	0.267
r2222_04	field	-20.12	-20.71	-21.29	10.123	-7.08	-22.98	0.422	1.252
r2222_05	field	-19.94	-20.26	-20.76	9.786	-18.68	-19.77	0.935	0.660
r2222_08	field	-21.16	-21.59	-22.14	10.415	-0.55	10.24	0.085
r2222_13	field	-19.93	-20.81	-21.49	10.300	-5.43	2.56	0.271
r2222_15	field	-20.08	-20.49	-21.02	9.942	-25.86	-29.13	1.474	1.241
r2231_06	field	-19.78	-20.11	-20.61	9.732	-25.41	-26.11	1.101	0.759
r2231_11	field	-18.65	-19.18	-19.75	9.491	-48.04	-32.86	0.739	0.433
r2231_16	field	-20.12	-20.68	-21.26	10.112	-19.73	-48.69	1.174	2.592
r2231_23	field	-21.11	-21.89	-22.52	10.677	-1.55	-8.67	0.230	1.467
r2241_11	field	-20.79	-21.72	-22.40	10.668	-9.00	0.97	0.994
r2241_14	field	-20.33	-21.03	-21.65	10.311	-5.11	0.67	0.368
r2241_21	field	-22.46	-22.72	-23.19	10.705	-17.10	-36.41	8.749	11.39
r2241_22	field	-20.84	-21.40	-21.98	10.391	2.47	1.78
r2242_07	field	-20.93	-21.77	-22.43	10.668	1.50	0.67
r2242_10	field	-18.79	-19.75	-20.45	9.907	3.91	-0.35	0.009
r2242_11	field	-20.46	-21.33	-22.00	10.497	-0.95	-3.18	0.077	0.333
r2242_12	field	-19.99	-20.89	-21.57	10.336	-0.22	1.00	0.012
r2242_13	field	-20.18	-20.63	-21.18	10.029	-5.53	-21.72	0.346	1.067
r2242_18	field	-20.06	-21.02	-21.72	10.412	-13.17	-2.97	0.740	0.240
r2251_02	field	-19.89	-20.55	-21.15	10.093	4.56	0.26
r2251_08	field	-20.39	-20.72	-21.21	9.960	-20.21	-27.68	1.543	1.406
r2251_16	field	-22.60	-23.12	-23.67	11.037	-12.12	-1.42	7.095	0.696
r2611_02	field	-19.92	-20.60	-21.21	10.127	-8.30	-23.45	0.410	1.190
r2611_11	field	-19.39	-19.66	-20.15	9.515	-13.09	-10.49	0.396	0.200
r2612_01	field	-19.58	-20.45	-21.11	10.145	-0.05	0.002
r2621_01	field	-18.67	-19.28	-19.90	9.600	-8.00	-19.11	0.125	0.289
r2621_05	field	-19.37	-19.69	-20.19	9.561	-1.37	0.027
r2621_06	field	-19.97	-20.99	-21.70	10.419	-3.45	-1.38	0.178	0.110
r2621_09	field	-19.10	-19.78	-20.41	9.817	-2.30	-7.58	0.053	0.183
r2621_10	field	-20.86	-21.54	-22.14	10.496	-9.52	-12.55	1.119	1.499
r2621_12	field	-20.68	-21.54	-22.19	10.572	-3.89	-3.95	0.386	0.496
r2631_01	field	-19.80	-20.51	-21.15	10.120	2.90	0.17
r2631_02	field	-21.46	-22.27	-22.92	10.843	-4.72	-0.55	0.960	0.134
r2631_05	field	-19.74	-20.55	-21.20	10.164	-57.95	-8.50	2.430	0.426
r2631_10	field	-19.37	-19.69	-20.20	9.569	-31.05	0.25	0.925
r2631_11	field	-21.37	-22.13	-22.78	10.783	0.63	1.87
r2631_16	field	-21.19	-21.58	-22.09	10.347	-20.02	-27.48	3.188	3.144
r2651_01	field	-19.51	-20.30	-20.94	10.058	1.53	2.22
r2632_06	field	-20.43	-21.21	-21.84	10.404	-1.76	-2.10	0.139	0.190
r2651_07	field	-20.67	-21.31	-21.90	10.385	0.53	0.38
r2632_10	field	-18.85	-19.52	-20.14	9.697	-0.50	1.74	0.009
r2641_11	field	-20.26	-21.04	-21.68	10.348	-13.38	-39.16	0.907	3.063
r2632_14	field	-19.74	-20.55	-21.20	10.166	-23.37	-16.20	0.980	0.816
r2632_15	field	-20.30	-21.12	-21.79	10.405	-0.51	-2.62	0.036	0.226
r2811_12a	field	-19.60	-19.92	-20.43	9.667	-152.35	-45.63	1.125
r2812_19	field	-19.31	-19.50	-19.93	9.330	-27.69	-42.97	0.779	0.673
r2812_23	field	-19.12	-19.79	-20.42	9.826	12.51	4.21
r2812_25	field	-18.71	-19.17	-19.73	9.468	-1.82	7.97	0.030
r2812_26	field	-18.53	-19.52	-20.24	9.831	-0.49	0.010
r2821_06	field	-19.70	-19.90	-20.37	9.559	-25.03	-25.40	1.010	0.592
r2821_13	field	-20.53	-21.32	-21.97	10.472	-7.21	-5.60	0.623	0.570
r2821_18	field	-19.98	-20.35	-20.86	9.865	-32.99	-47.31	1.728	1.743
r2821_23	field	-20.09	-20.62	-21.20	10.081	1.25	3.93
r2821_28	field	-20.96	-21.71	-22.34	10.598	-4.01	-18.43	0.517	2.645

Table D.1: Continued.

ID	membership	M_B [mag]	M_V [mag]	M_R [mag]	$\log(Mass)$ [M_\odot]	$W_0([O\ II])$ [Å]	$W_0(H\alpha)$ [Å]	$SFR([O\ II])$ [$M_\odot\ yr^{-1}$]	$SFR(H\alpha)$ [$M_\odot\ yr^{-1}$]
r2822_24	field	-18.96	-19.52	-20.11	9.661	-21.45	-29.00	0.435	0.534
r2831_05	field	-20.31	-20.82	-21.38	10.129	-11.25	-19.13	0.793	1.135
r2831_08	field	-19.98	-20.54	-21.12	10.055	197.74	-8.75	0.410
r2831_16	field	-20.00	-20.55	-21.14	10.076	-9.94	-20.07	0.526	0.955
r2831_17	field	-20.14	-20.53	-21.05	9.941	-21.25	-7.27	1.289	0.318
r2831_18	field	-21.72	-22.23	-22.78	10.680	-5.92	-22.07	1.537	4.740
r2841_01	field	-18.92	-19.64	-20.28	9.775	-0.17	1.87	0.003
r2841_09	field	-21.30	-21.97	-22.57	10.668	1.05	-3.41	0.607
r2841_12	field	-20.19	-20.46	-20.93	9.806	-39.14	-50.65	2.472	1.978
r2841_13	field	-19.01	-19.43	-19.96	9.524	-8.45	7.60	0.181
r2841_18	field	-19.22	-19.98	-20.62	9.923	2.68	-2.49	0.073
r2841_19a	field	-21.09	-21.73	-22.32	10.551	-2.20	-4.02	0.318	0.566
r2841_20	field	-18.97	-19.29	-19.78	9.391	-22.79	-18.44	0.469	0.251
r2851_01b	field	-19.61	-20.06	-20.61	9.802	-26.69	-34.39	0.992	1.004
r2851_02	field	-20.15	-20.93	-21.56	10.290	-8.23	-4.83	0.503	0.337
r2851_03	field	-21.01	-21.90	-22.56	10.723	-3.65	-1.02	0.494	0.180
r2851_05	field	-20.37	-20.82	-21.35	10.080	-20.60	-16.33	1.543	0.944
r2851_06	field	-21.27	-21.96	-22.57	10.667	1.08	-1.31	0.232
r2851_12	field	-21.03	-21.78	-22.40	10.620	-1.78	0.48	0.244
r2851_13	field	-20.35	-20.98	-21.58	10.255	0.30	0.85
r2851_18b	field	-20.17	-20.93	-21.57	10.299	-4.23	-6.96	0.262	0.489

Acknowledgments

I would like to start this section, by expressing my gratitude to my advisor, Prof. Dr. Bodo Ziegler for all his support, encouragement and patience after several delays of this work.

I want also to thank the director of the institute, Prof. Dr. Wolfram Kollatschny for his support and for kindly accepting being my second referee of my thesis. Furthermore, I wish to thank the other members of the disputation committee, Prof. Dr. S. Dreizler, Prof. Dr. U. Christensen, Prof. Dr. A. Bahr, and Prof. Dr. W. Glatzel.

I am also very grateful of Prof. Dr. K. Fricke who accepted me as his student when I arrived.

I am very grateful of all members of the Institut für Astrophysik Göttingen. I want to give especial thanks to Mathias Zetzl for his efficiency in keeping our computers in perfect shape, and to the secretaries for their help in innumerable issues. I am also grateful of A. Fritz who helped me a lot during the first weeks of my stay in Germany.

I thank D. Gilbank for providing the photometric catalog in which part of this work was based. I also thank A. Fritz and K. Jäger for their help with some of the software routines used in the data reduction. I want to thank J. Rassmussen, M. Balogh, and B. Gerken for discussions in different aspects of this project.

I want to give thanks to Cristiano Da Rocha and Thorsten Tepper, who have read the manuscript and helped me to improved it.

I have to give the thanks to all the great friends that I have found during these years, for the great time that we have had and for helping me to grow as a person in ways they can not imagine. Thanks Thorsten, Bruno, Gonzaga, Carlos, Olga, Diego, Iria, Cathy, Vladi, Dori, Ruth, Josu, Cristiano, Klaus, Teresa, Ximena and many, many others, who, surely, will forgive me if I forget them. As I always say, the best people I ever met.

But, I cannot give enough thanks to Frauke Stöckicht, for all her help during the last times, including a thoroughly language correction, but specially for her love and the light with which she fills me.

I also thank the love and support that I have received over the years from my family back home. My thoughts have been always with them.

This work has been mainly based in original data taken with the 3.5 telescope at Calar Alto. The efficient support of the observatory staff is acknowledged. Only publically available data and information (*e.g.* images) are used to complement the analysis or to illustrate some points. Their original authors are, in each case, acknowledged.

This work has been finantially supported by the Volkswagen Foundation (I/76 520) and travel grants to Calar-Alto by DFG (ZI663/5-1). Some of the results of this thesis have been accepted for publication in A&A (preprints at astro-ph/0709.4508). This work has been typeset using L^AT_EX.

Conferences & PhD activities

- Poster presentation at the conference *Galaxy growth in a dark Universe*. July 2007, Heidelberg, Germany.
- Poster presentation at XXVI IAU General Assembly, in symposium 235 *Galaxy Evolution across the Hubble Time*. August 2006, Prague, Czech Republic.
- Poster presentation at the *11th Latino-American IAU Regional Meeting*, December 2005, Pucón, Chile.
- Participation at the Summer School Novicosmo *The Dark and the Luminous Sides of the Formation of Structures*. September 2005, Istria, Croatia
- Talk given at the *Astronomische Gesellschaft* meeting. October 2005, Köln, Germany.
- Poster presentation at the *Astronomische Gesellschaft* meeting. October 2004, Prague, Czech Republic.
- Several talks at the Seminar for Extragalactic Astronomy, Institut für Astrophysik, Göttingen

Publications

Refereed papers

1. **Verdugo, M.**, Ziegler, B. L. and Gerken, B. The galaxy populations from the centers to the infall regions in $z \sim 0.25$ clusters. Accepted for publication in *A&A*, astro-ph/0709.4508.
2. Whiting, A. B. and Hau, G. K. T. and Irwin, M. and **Verdugo, M.** An Observational Limit on the Dwarf Galaxy Population of the Local Group. *AJ*, 133:715–733, Feb. 2007.
3. Guldenschuh, K. A. and Layden, A. C. and Wan, Y. and Whiting, A. and van der Bliek, N. and Baca, P. and Carlin, J. and Freismuth, T. and Mora, M. and Salyk, C. and Vera, S. and **Verdugo, M.** and Young, A. The Intrinsic Colors of RR Lyrae Variables: A Means to Determine Interstellar Reddening. *PASP*, 117:721–725, Jul. 2005.

Conference contributions

4. **Verdugo, M.** and Ziegler, B. L., Galaxy Population in the Infall Regions of Intermediate Redshift Clusters. Proceedings of the International Astronomical Union 2, IAU Symposium No. 235 *Galaxy Evolution Across the Hubble Time*. Cambridge University Press, 2007.
5. Ziegler, B. L., Kutdemir, E., Böhm, A., Jäger, K., **Verdugo, M.**, Peletier, R., Kronberger, T., Kapferer, W. and Schindler, S., Distant Galaxy Transformation Probed by VLT and HST. Proceedings of the International Astronomical Union 2, IAU Symposium No. 235 *Galaxy Evolution Across the Hubble Time*. Cambridge University Press, 2007.
6. **Verdugo, M.** and Ziegler, B. L., Galaxy Population in the Infall Regions of $z \sim 0.25$ clusters. *Revista Mexicana de Astronomía y Astrofísica (Serie de Conferencias) XI IAU Regional Latin American Meeting of Astronomy*, Jun, 2006.
7. **Verdugo Olivares, M. A.**, Krisciunas, K., Suntzeff, N. B., Phillips, M. M. and Candia, P. Infrared studies of Type Ia supernovae. *Bulletin of the American Astronomical Society*, Dec, 2002.

Lebenslauf

PERSÖNLICHE DATEN

Name	Miguel Aníbal Verdugo Olivares
Geburtsdatum	15.02.1976
Geburstort	Santiago, Chile
Familienstand	Ledig
Staatsangehörigkeit	Chilenisch

SCHULBILDUNG

März 1982 – Dez 1988	Grundschule am <i>Liceo Manuel Arriarán Barros, Comunidad Don Bosco</i> , La Cisterna, Santiago
März 1989 – Dez 1993	Weiter führende Schule am <i>American Academy</i> in San Bernardo, Santiago

STUDIUM

März 1996 – Januar 2002	Physikalische Fakultät der Pontificia Universidad Católica de Chile
-------------------------	---

PROMOTION

Februar 2004 – Februar 2008	Promotion an der Universitäts-Sternwarte Göttingen (seit Juni 2005 Institut für Astrophysik Göttingen)
-----------------------------	--

